



A Fluidic Oscillator Based on a New Mechanism: for Microbubble Generation and Developing Microbubble Stripping for Separation Phenomena

By

Pratik Desai AMIChemE AMInstP AMAPS GradEI

Supervised by

Professor William B J Zimmerman BScEng, MSc, PhD, CEng FIChemE

A thesis submitted in partial fulfilment of the requirements for the degree of Doctor of Philosophy

The University of Sheffield

Faculty of Engineering

Department of Chemical and Biological Engineering

Submission Date – July, 2017

Acknowledgements

It is convention to have an acknowledgement section in one's thesis. Personally, I often feel that if one has to pen down one's acknowledgements, then perhaps something has gone wrong as one ought to have expressed oneself *in propria persona* at the time. As an engineering scientist and someone with infinite curiosity, there are four people who have had a rather large effect on my development; I would like to thank my parents, mother and father, for their genetics, wonderful upbringing (memetics), and kindling the curiosity as a child, feeding that insatiable hunger was one of the first things they worked on (I owe you everything and a bit more), my avuncular for the Victorian innovativeness and the ability to be a renaissance man- teaching me that my sprachgefühl with language and love for the arts ought to reinforce my technical/scientific ability and not hinder it; rather than choosing the road not taken, to be like the irreverent photon and go for both roads simultaneously, and my academic father for instilling the ability to act on this curiosity and teach me what research actually meant, what it means when one uses the title – Professor. My academic father has had the biggest contribution in writing this thesis and I wish to thank him for it. The title of this thesis comes from him too. I had a working title that involved Goethe's Faustian deal and it wasn't working well enough and the academic father stepped in and saved the day. Thank you for that. What started off as a single MEng project, collaborating with NPL, has now exceeded over 100 successful projects and many more to come. It's been an absolute pleasure and a superb learning experience. I just have one sentence more for him: WBJZ is, one of Epictetus' purple threads, in a world awash in white.

I would like to thank my grandfather, RBD, for his effusive support whenever I needed it and his training, being the incorrigible inorganic chemist that he was, taught me the formula for Borax and Epsom salts at age 3 and taught me coordination chemistry a year later. It was a bit weird then, to learn some of these things (incorrectly formulated, might I add) in year 7 at school. These five individuals have had a great impact on me and I can't thank them enough for the same. I need to make a special mention to the man who first introduced me to research in the U.K., Professor RWKA. He gave me my first research job, six months in my first year in the UK as an undergrad to work as an RA for the HYTHEC project. Thanks for that. It was rather fun. I have always learnt to learn as much as possible from everyone and therefore referred to as the research hoover by my friends and research whore by my contemporaries, but it has always been to mutual advantage. I would like to thank several others who have helped me in this journey but shan't mention them here for brevity's sake.

Emerson once said "a friend may well be reckoned the masterpiece of nature". He was, as always is the case with him, able to express it with great succinctness but completeness. Cicero would have said '*rem acu tetigisti*' to it (hitting the nail on the head). I have been fortunate to have a small covee of friends, small but an extremely strong set of friends. By friends, I mean people amongst whom I have absolute trust. They are to me as the brook described by Lord Tennyson when he said: "For men may come and men may go, but I go on forever". My friends represent the brook and so do I for them. These are special people in my life who have and would be important to the writing of this thesis through various discussions I have had in the years. Loquacious though I am wontedly, I am rather reticent when I ought to write my thanks, which is a fundamental flaw in me. Thanks go to GRK for forever being the inspiration and for fuelling my dynamo. Being a lover of Cicero's oratorical skills, I would say, the life of the dead is placed in the memory of the living. Special mentions are rare in an acknowledgement but it isn't a rule if there is no exception. I would like to thank Dr. Rahul Sangodkar and the haecceity of our friendship. Seneca once said one of the most beautiful qualities of true friendship is to understand and be understood. RP knows me best and is someone who has always been there. We have been situated thousands of miles apart and yet the distance has never come in the way. He has been there throughout and his inestimable input and our conversations have always been splendid. Dr. Zhao-Yuan Leong for his friendship too and for keeping up with me to have cogent conversations as compared to the otherwise dull mediocrity that pervades this world. Academically, these are my contemporaries and it has been wonderful fun and an honour to do so with these fellow Pratikians. They are also extremely close friends. Thanks for everything. The Dear Fellow Society (DFS)! Thanks for making the world, that much more interesting. The DFS was started for me, by the following wondrous people- Dr. Joss Noirel, Dr. Stephen Jaffe, and Dr. Joseph Longworth. Thank you! Dr. Jags Pandhal and (soon to be Dr.) Samuel Noirel are honorary members added to this group. I would like to thank them all for these splendid years together and the splendiferous fun we have had thus far and lots more to come! Stiffy, Kathy, Sheffi, Neelam, Dr. Neel Rangnekar, and Marie for taking on the role of Atlas and supporting the proverbial centre of the universe. I would also like to thank my students and interns who have worked with me on other projects and on the Desai-Zimmerman Research Internship Scheme. Dr. Michael Hines, for being the brother I never had. Thank you. He has had a huge impact on my work and we make an excellent team. Sorry for making you the bad cop every time! I apologise if I have missed anyone in this endeavour. I promise to make it up to you later. My curiosity is matched in kind with my arrogance and for that, I have to thank myself. I can't lay blame to anyone else for that and wanted to make that clear. I know that this is just the start of my career, as Cicero also says, the higher we are placed, the more humbly we should walk. So, there is much more I have yet to learn.

To those who believe that one can improve oneself by undermining or competing with others, I would like to share my motto: *Transire suum pectus mundoque potiri* – rise above oneself and grab the world. There is no need to compete with others when you have yourself to compete with.

Abstract (429)

Microbubbles, gas-liquid interfaces sized between $1\mu\text{m}$ and $1000\mu\text{m}$, exhibit high levels of transport phenomena due to their high surface-area to volume ratio. The thesis describes the underpinning understanding of bubble generation, the invention and benchmarking of a novel fluidic oscillator, the visualisation dynamics associated with the sizing of high throughput microbubble clouds, and the development and application of hot microbubble injection in thin liquid layers for ammonia-water, and ammonia-rich wastewater). Successful design and implementation of a novel technology relies on developing the field around it. The chapters detailed herein demonstrate the path taken and the understanding developed. New understanding is developed for microbubble generation mediated by oscillator flow that the generation frequency of the bubbles coupled with the amplitude required for bubble detachment is imperative for significantly reducing the bubble size. A “sweet spot” is observed where bubble size reduced dramatically – sweet spot (volume-average size $\sim 60\mu\text{m}$, number-average $\sim 7\mu\text{m}$) reduction in bubble size compared to conventional steady flow (volume-average size $\sim 800\mu\text{m}$, number-average $\sim 300\mu\text{m}$) from oscillatory flow (volume-average-size $\sim 180\mu\text{m}$, number-average $\sim 14\mu\text{m}$) is demonstrated. A new fluidic oscillator is invented-Desai-Zimmerman-Fluidic-Oscillator- (DZFO) which retains all the advantageous properties of other oscillators but has several important features/improvements including –higher pulse amplitude (4-10 times higher), lower frictional losses, new switching mechanism, higher frequency attainable (20kHz), constructive/destructive wave formation, asymmetric gas mixing, and lower onset of oscillation ($<1\text{slpm}$) with crisper momentum pulse transfer. These properties also make the DZFO better at microbubble generation and smaller bubbles are generated compared to other oscillators. A mechanism is proposed for this new oscillator and an experimental campaign carried out to support the mechanism and benchmark it with the other oscillators. The DZFO is based on a new mode of oscillation, acoustic resonant mode, which is different to the ones typically used to categorise different oscillators. Acoustic bubble spectrometry has been compared to laser diffraction and optical methods for visualising high throughput microbubble clouds and has been deemed to be the most effective at inferring bubble size distributions for these scenarios. Hearing bubbles is much better than directly visualising them. Microbubble stripping of ammonia from ammonia-water systems and ammonia rich liquor systems was developed and benchmarked with an industrial comparator (air stripping). The mass transfer rates were over 1000-3000 times higher for microbubble stripping compared to air stripping for ammonia-water systems and over 15000 times higher for ammonia-rich liquor. Stripping of nearly 100% ammonia was achieved in less than 30minutes of contact time (as opposed to 95% in 100h for air stripping), and removal of ammonia at a pH less than 9 was achieved which is a first in literature. A new understanding for the ammonia removal process was developed.

Table of Contents

ACKNOWLEDGEMENTS	2
ABSTRACT (429)	3
CHAPTER 1 OVERVIEW	6
CHAPTER 2 LITERATURE REVIEW	9
CHAPTER 3 EXPERIMENTAL SECTION	70
3.1 MAJOR ASSUMPTIONS AND MAJOR DECISIONS – HYPOTHESES	70
3.1.1 RESONANT PULSING FREQUENCY EFFECT FOR MUCH SMALLER BUBBLE FORMATION WITH FLUIDIC OSCILLATION	70
3.1.2 INVENTING THE NEW OSCILLATOR (DESAI-ZIMMERMAN FLUIDIC OSCILLATOR)	73
MECHANISM FOR SWITCHING AS PROPOSED BY THE HYPOTHESIS FOR THE DZFO	77
3.1.3 COMPARISON OF BUBBLE SIZE DISTRIBUTIONS INFERRED ACOUSTIC, VISUALISATION, AND LASER DIFFRACTION	83
3.1.4 SEPARATION PROCESSES – AMMONIA STRIPPING IN AMMONIA RICH WASTE WATERS	84
3.2 DATA COLLECTION PROCEDURES	85
3.2.1 RESONANT PULSING FREQUENCY EFFECT FOR MUCH SMALLER BUBBLE FORMATION WITH FLUIDIC OSCILLATION	85
METHODS AND MATERIALS	85
3.2.2 INVENTING THE NEW OSCILLATOR (DESAI-ZIMMERMAN FLUIDIC OSCILLATOR)	90
3.2.3 COMPARISON OF BUBBLE SIZE DISTRIBUTIONS INFERRED ACOUSTIC, VISUALISATION, AND LASER DIFFRACTION	93
3.2. 4 SEPARATION PROCESSES – AMMONIA STRIPPING IN AMMONIA RICH WASTE WATERS	101
CHAPTER 4 RESULTS AND DISCUSSIONS	109
4.1 RESONANT PULSING FREQUENCY EFFECT FOR MUCH SMALLER BUBBLE FORMATION WITH FLUIDIC OSCILLATION	109
4.2 INVENTING THE NEW OSCILLATOR (DESAI-ZIMMERMAN FLUIDIC OSCILLATOR)	123
RESULTS AND DISCUSSIONS	123
4.3 COMPARISON OF BUBBLE SIZE DISTRIBUTIONS INFERRED ACOUSTIC, VISUALISATION, AND LASER DIFFRACTION	146
DISCUSSION	149
4.4 SEPARATION PROCESSES – AMMONIA STRIPPING IN AMMONIA RICH WASTE WATERS	157
RESULTS AND DISCUSSIONS	157
RESULTS FOR TRIAL 1	172
TRIAL 2 – EXPERIMENTS WITH DIFFERENT LIQUORS	176
CHAPTER 5 CONCLUSIONS	186
5.1 RESONANT PULSING FREQUENCY EFFECT FOR MUCH SMALLER BUBBLE FORMATION WITH FLUIDIC OSCILLATION	186
5.2 INVENTING THE NEW OSCILLATOR (DESAI-ZIMMERMAN FLUIDIC OSCILLATOR)	188
5.3 COMPARISON OF BUBBLE SIZE DISTRIBUTIONS INFERRED ACOUSTIC, VISUALISATION, AND LASER DIFFRACTION	191
5.4 SEPARATION PROCESSES – AMMONIA STRIPPING IN AMMONIA RICH WASTE WATERS	194
CHAPTER 6 FUTURE WORK	196
REFERENCES	197
APPENDICES	213
APPENDIX A- IONIC LIQUIDS – FORMATION DYNAMICS AND EFFECT OF STAGING	213
THE EFFECT OF OSCILLATORY INJECTED FLOW ON MICROBUBBLE FORMATION DYNAMICS IN VISCOUS IONIC LIQUIDS	213

THE EFFECT OF STAGING OF FLUIDIC OSCILLATION ON MICROBUBBLE GENERATION IN VISCOUS LIQUIDS.....	258
MATERIALS.....	264
APPENDIX B DESAI-ZIMMERMAN MMARP – MICROBUBBLE MEDIATED AMMONIA RECOVERY PROCESSES – ‘WASTE FACTORY’	291
APPENDIX C INNOVATEUK ENERGY CATALYST GRANT - ENHANCING THE METHANE GENERATION FROM FOOD WASTE ANAEROBIC DIGESTION MEDIATED BY FLUIDIC OSCILLATOR GENERATED MICROBUBBLES	293
APPENDIX D SUPPLEMENTARY DATA – CHAPTER 3 – PERACTUATION OF FLUIDIC OSCILLATION FOR CONTROLLED MICROBUBBLE GENERATION.....	295

Chapter 1 Overview

The work described in this document is about invention of an enabling technology and the emerging underpinning science.

Fluidic oscillators have been used for microbubble generation since Tesař and Zimmerman modified a Warren type bistable diverter valve and applied it for microbubble generation – Tesař-Zimmerman Fluidic Oscillator (TZFO). Microbubbles are gas-liquid interfaces between 1-1000 μm and have a high surface area to volume ratio. They exhibit extremely high heat and mass transfer due to their surface area to volume ratio and also have high internal mixing rates.

Microbubble generation mediated by oscillatory flow is still not understood well. There are several conflicting theories for size reduction of microbubbles generated by fluidic oscillation. Chapter 2 is a review of literature, Chapter 3 is the experimental section, and Chapter 4 discusses the results. Conclusions are presented in Chapter 5 and the future work to be done follows as Chapter 6. The major experimental sections include subsections 1, 2, 3, and 4 which deal with different aspects of microbubbles.

Subsection 1 deals with understanding the mechanism behind oscillatory flow mediated microbubble generation. Zimmerman *et al.*, 2011 postulated a higher frequency would generate smaller bubbles and (Rehman *et al.*, 2015, Hanotu *et al.*, 2013, Hanotu *et al.*, 2012, AlMashhadani, *et al.*, 2011, Tesař *et al.*, 2014) have used the highest attainable frequency as a default. Tesař (Tesař *et al.*, 2013a ; Tesař *et al.*, 2014) developed techniques (excitation of the third harmonic) and a new oscillator for capable of generating higher frequencies than conventional oscillators in order to generate smaller bubbles. Tesař in 2014 (Tesař *et al.*, 2014), then noticed the importance of backflow (liquid imbibition) into the pores which resulted in smaller bubble formation by reduced coalescence. Based on this work, Tesař developed a low frequency oscillator in order to reduce the bubble size. This shows that there is a need to study the microbubble generation dynamics mediated by oscillatory flow. As seen in (Tesař *et al.*, 2014), high speed photographic visualisation is not very useful for understanding microbubble cloud dynamics. The hypothesis for the microbubble generation mediated by oscillatory flow is that there ought to exist a resonant frequency state where the

bubble formed leaves the system without associated coalescence. In order for this to occur, an artificial amplitude increase is required.

One of the major findings of this subsection determined specific properties and requirements for the development of a new oscillator devised specifically for microbubble generation. Fluidic oscillators can be generally divided into 2 groups based on their mode of switching – jet deflection type and load switching type. A new oscillator was invented based on a new mode of oscillation which does not fit into these categories. Subsection 2 discusses the invention of the Desai-Zimmerman Fluidic Oscillator (DZFO) and the proposed mechanism of switching and the new mode of oscillation. Subsection 2 also compares the performance with other oscillators and experimental campaigns performed in order to benchmark and validate the hypotheses and mechanism proposed for this oscillator. One of the major hypotheses in this chapter is the mechanism and theory for actuation for the DZFO, which is based on acoustic resonators and acoustic resonance.

Single microbubble visualisation and low throughput microbubble cloud visualisation is fairly straightforward and follows from bubble cloud visualisation. Visualising or inferring the bubble size distribution for a high throughput microbubble cloud presents its own challenges.

There are three major techniques that can be used (each having distinct advantages and disadvantages) and Subsection 3 attempts to reconcile the three methods to determine the best method for inferring high throughput bubble clouds and drawbacks for each of the methods used. It also discusses the statistical analyses used for generating bubble size distributions. The major hypothesis in this chapter is that hearing a bubble, based on an intrinsic property of the bubble, is more accurate than direct optical visualisation or on diffractive/refractive properties of the bubble.

Microbubble mediated evaporation dynamics have been described and modelled by (Zimmerman *et al.*, 2014) and empirical studies have been carried out by (Abdulrazzaq *et al.*, 2015) and (AlYaqoobi *et al.*, 2014) for binary systems of ethanol-water and methanol-water. These separations are based on temperature gradient separation which is relatively straightforward. Ammonia dissolves in water and is extremely hard to separate based on a thermal gradient. However, a concentration gradient ought to be able to separate the ammonia from the water. Subsection 4 discusses the development of a novel unit operation

– microbubble stripping – in order to strip ammonia from an ammonia-water solution and from ammonia rich liquors. It discusses the design of a microbubble separation device and the design principles involved. Subsection 4 also deals with the removal of volatile organic compounds in ammonia-rich liquors which results in a colour change observed for the liquid. One of the major hypotheses for this chapter is the competition between the ammonia removal rate (based on the concentration gradient) and the dewatering rate (based on the thermal gradient) would supplement each other, similar to the Soret effect. The addition of OH^- ions and the dewatering step resulting in the release of ammonia from the dissolved liquid would result in greatly enhanced mass transfer coefficients. Due to the non-coalescent nature of ammonia-rich liquor, the bubbles generated would be smaller and enhance the ammonia stripping substantially.

Chapter 5 is the conclusions chapter and discusses the emerging science from each subsection and the understanding developed. Chapter 6 refers to the future work section.

Chapter 2 Literature Review

Microbubbles

Microbubbles are gas-liquid interfaces ranging from 1 μm to 1000 μm in size. Several applications have been identified for them including microalgal separation (Hanotu *et al.*, 2012) , wastewater clean-up (Rehman *et al.*, 2015, Agarwal *et al.*, 2011b), theranostics (Mulvana *et al.*, 2012, Anderson *et al.*, 2010, Lukianova-Hleb *et al.*, 2010, Cai, 2012), algal growth (Al-Mashhadani *et al.*, 2016, Al-Mashhadani *et al.*, 2015, Kezhen Ying, 2013a, Kezhen Ying, 2013b, Zimmerman *et al.*, 2011b, Al-Mashhadani *et al.*, 2011), oil emulsion separation (Hanotu *et al.*, 2013) and for heat and mass transfer applications (due to vastly increased surface area to volume ratios) (Abdulrazzaq *et al.*, 2015, Desai and Zimmerman, 2015, AlYaqoobi, *et al.*, 2014, Zimmerman, *et al.*, 2014). This increased interest has seen increasing application in industrial settings due to the development of low energy microbubble generating systems using microfluidic devices. In fact, it has resulted in a paradigm shift in technology development for traditional industrial processes and unit operations and led to many interesting studies performed which revolutionise core chemical engineering techniques such as microbubble evaporation (dewatering) and distillation, including breaking the water-ethanol azeotrope.

Bubble formation

We is defined as the ratio of the inertia of the fluid to its surface tension and determines the curvature of the bubble which means smaller the bubble greater is the curvature and higher is the surface tension and higher the We. Sk relates the bubble size to the rise velocity of the system whereas the Sh is used for oscillatory systems and for the FO, helps determine the frequency of bubble generation and the characteristics of the FO , especially the oscillatory flow and its bistability.

Conjunctions occur when either of these values is unbalanced, leading to a bigger bubble size being observed. Greater unbalance leads to coalescence in the system. Tesař *et al.* (Tesař, 2013b) describes the case of the smallness of microbubble being limited due to coalescence.

$$Sh_t = \frac{fL}{v} - \text{(Equation 1)}$$

$$Re = \frac{\rho V D_h}{\mu} = \frac{V b}{\nu} = \frac{\dot{M}}{h \nu} \quad \text{(Equation 2)}$$

$$Sk = \frac{f b^2 L}{V} \quad \text{(Equation 3)}$$

$$We = \frac{w^2 D_b}{2 \nu \sigma} \quad \text{(Equation 4)}$$

$$We = \frac{f^2 D_b^3}{2 \nu \sigma} \eta \quad \text{(Equation 5)}$$

f = oscillation frequency (Hz)

L = length of feedback loop (m)

V = supply nozzle bulk exit velocity (m/s)

b = Constriction width (m)

ρ = density (kg/m³)

η = viscosity (Pa.s)

D_h = Hydraulic diameter (m)

ν = specific fluid volume (m³)

w = bubble rise velocity (m/s)

D_b = bubble diameter (m)

σ = surface tension (N/m)

(Sanada et al., 2009, Shirota et al., 2008a) discusses the coalescence observed in rising bubbles and the interactions between two rising bubbles. This interaction depends on the rise velocity, (therefore size) and the rate of formation of the bubble (oscillation velocity in case of FO). Therefore this means that coalescence is directly related to the We , (bubble formation and size), Sk (bubble rise and size), Sh (bubble formation via oscillation and oscillatory flow) and Re (determining the momentum carried by the bubble due to the pulse). This, coupled with the resultant bubble wake and zeta potential (if any due to presence of

ions or coatings on the system), defines the ultimate bubble size. This does not account for the fact that the surface of the membrane generating the bubble (involves the We and $We_{Oscillatory}$ since surface tension is involved) and the orifice size (dependent on Sh since it's the constriction that determines the bulk exit velocity of the orifice).

A conclusion to be drawn from this is that if there is the appropriate balance in the system, (with respect to rise velocity, frequency of bubble generation, bubble size and orifice diameter), analogous to a resonant mode of the system where these conditions are balanced just about correctly, then bubble conjunctions would be avoided leading to a significant size reduction in the bubbles. This is a substantial reduction in size by optimising the parameters of an existing system without any modifications or retrofitting. The amplitude of the pulse is also important as it increases the Sk and Sh which results in lesser conjunctions and coalescence.

Balancing the forces on the bubble being formed:

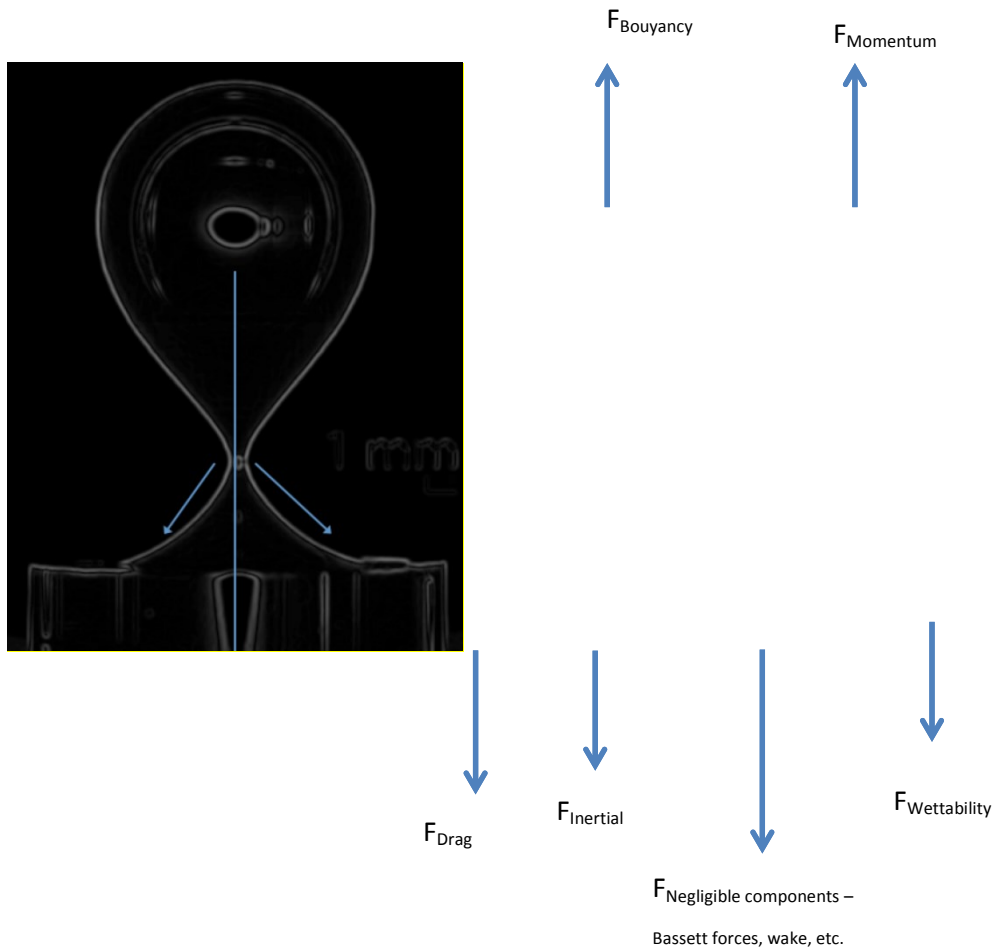


Figure 1 Bubble forces resolved [adapted from [50]]

The buoyancy force and momentum force act upwards, the cosine component of the wettability (anchoring force), drag force, surface tension act downwards.

For an orifice of Diameter D_0 , density of liquid - ρ_L , density of gas - ρ_g Volume of bubble formed - V_b , the following equations are obtained for the forces acting upwards:

Bouyancy force –

$$F_{Bouyancy} = V_b (\rho_L - \rho_g)g \quad (\text{Equation 6})$$

$$V_b = \frac{1}{6} \pi d_b^3 \quad (\text{Equation 7})$$

Resulting in

$$F_{Bouyancy} = \frac{1}{6} \pi d_b^3 (\rho_L - \rho_g)g \quad (\text{Equation 8})$$

Momentum Force –

$$F_{Momentum} = \frac{1}{4} \pi D_o^2 u_o^2 \rho_g \quad (\text{Equation 9})$$

Taking downward forces into account,

Wettability Force –

$$F_{Wettability} = \pi D_o \sigma \cos\theta \quad (\text{Equation 10})$$

Where θ is the wetting angle / contact angle made by the engendering bubble and the surface and σ is the surface tension force / anchoring force/ wetting force and D_o is the diameter of the orifice.

Drag Forces –

$$F_{Drag\ Force} = \frac{1}{2} C_d \rho_L \frac{\pi}{4} d_b^2 u_b^2 \quad (\text{Equation 11})$$

With the rise velocity denoted by u_b

Bubble Inertial Force –

$$F_{IF} = \frac{d(u_b V_b \rho_g)}{dt} = \frac{\rho_g Q^2 V_b^{-\frac{2}{3}}}{12 \pi (\frac{3}{4\pi})^{\frac{2}{3}}} \quad (\text{Equation 12})$$

V_b is the bubble volume, ρ_g is the gas density, ρ_l is the liquid density, g is the acceleration due to gravity, D_b is the bubble diameter, D_o is the orifice diameter, u_b is the rise velocity of the bubble centre, C_D is the drag coefficient and Q is the volumetric gas flow rate.

Fluidic oscillators can be used for the economic and energy efficient generation of microbubbles.

Background and Main Developments in an Oscillator

An oscillator is a transducer that converts a direct input into an alternating output using an energy input which is a parasitic loss. There are mechanical oscillators such as pendulums which oscillate due to the tension in the thread and weight of the bob (with the gravitational force), and balance wheels, used in mechanical clocks, use the spring constant where the energy is stored and generates the oscillations. Electronic oscillators convert the DC power supply into an AC output using a little bit of the input DC voltage to create the oscillation as a parasitic load. Fluidic oscillators use the impinging jet, frictional losses, and compression of the impinging jet via throttling through a nozzle/orifice.

The simplest way to switch a fluid is based on the principle of the Coanda effect (Coanda, 1936). The Coanda effect is the inherent ability of an impinging jet to adhere to the wall of the curved surface. When a pressure differential is introduced in the system, the flow is diverted. If there is another wall on the other side of this diversion, the jet attaches to this wall due to the Coanda effect again. If this 'oscillation' can be maintained, a bistable fluidic oscillator is formed.

Fluidic oscillators have been studied extensively since the

$$1960s V_{av} = \text{Average Volume of bubble formed} = \frac{Q}{A \times N \times f_{eq}} =$$

and were designed to utilise fluid phenomena to act as effective and efficient control devices. The no-moving part approach would ensure that there would be unlimited lifetime, minimal maintenance, controlled switching, and low energy –low failure possibilities. One of the best known examples is the insectohopper designed by the CIA acting as a laser guided fluidic oscillator controlled mechanical grasshopper with listening devices placed in it and devised in 1970s (Agency, 2013)

Fluidic oscillators have been based on hydrodynamic instabilities and perturbations in flowing fluids. Whilst impinging liquids and gases can both be oscillated, this thesis focusses on oscillations induced for gases. Gases can be oscillated by creating the instabilities by a combination of adding a control element via a feedback control. This feedback control is via negative feedback. Most fluidic oscillators are used to either amplify or diminish the impinging jet. The switching is initialised by introducing instability in the form of an opposing

feedback action, *i.e.* positive feedback for a negative feedback control, negative feedback for a positive feedback control. The control of the feedback can be introduced by the path that this flow returns. There can be a single outlet or multiple outlets but typically two outlets are used so that switching can take place with minimal frictional losses.

The switching between the two outlet legs needs to be done by applying a diversion of the flow by applying a return path somewhere in the geometry which can deflect this flow with minimal input of energy or minimal frictional losses. This characteristic of inducing a large scale response for a weak input results in the flow amplification and hence known as fluidic amplifiers (Tesař, 2007b).

Applications of the fluidic oscillators

Fluidic oscillators being no moving part devices, have several advantages over electromechanical devices or mechanical actuators such as a practically unlimited life, reliability, inexpensiveness, lack of maintenance requirements and lack of an electrical power supply. The need for negligible maintenance requirements makes them ideal for industrial applications. Fluidic oscillators have been used for a variety of applications due to the associated low energetics including separation control (Tesař *et al.*, 2013), controlled reactions(Tesař,2010), sequencing samples for compositional analysis (Tesař *et al.*, 2004), modifying boundary layers(Tesař, 2009a), reactor control, heat and mass transfer enhancement for impingent jets (Tesař,2009a) control valves(Tesař,2001) , flow control(Raghu, 2013), vapour detection(Tesař,2007c), reactor flow control (Tesař,2009b), separation control on wind turbine blades (Cerretelli *et al.*, 2010), diagnostics (Weigl *et al.*, 2008,) and flow separation control (Kim, 2011, Tesař *et al.*, 2013), aircraft control (U Gebhardy, 1996), control of microUAVs (Agency,2013), jet mixing (Gregory *et al.*, 2005), Impinging annular jets (Tesař and Trávníček, 2008, Trávníček *et al.*, 2005, Tesař *et al.*, 2004, Trávníček and Tesař, 2004, Trávníček and Tesař, 2003) ,micromixer(Tesař, 2009d), used as measurement devices and several other applications (Kuznetsov, 2010 , Bruus, 2008, Pamme, 2006, Nguyen and Wereley, 2002)

They have also been used for energy efficient microbubble production for various applications. They have been applied towards improving microbubble generation for wastewater treatment such as (Fahad Rehman, 2015; Wafa Ghazlani, 2010; , Tesař and Jilek, 2013) . Additional uses of fluidic oscillators are described in detail by (Tesař, 2017 , Dančová *et al.*, 2016)

There are various types of fluidic oscillators which actuate based on various forms of transduction, i.e. using a basic control terminal perpendicular to the nozzle and various ways to induce pressure differentials to achieve oscillation.

Limitations of Oscillators

Typically, oscillators no-moving part self-actuating devices which are used as backup systems in situations where electronic failure might prove catastrophic – nuclear facilities. As such, they are highly reliable and have been used as backup systems for a variety of purposes. They tend to operate in flow regimes that they are designed for and usually cannot function out of those parameters. Each type of oscillator has its advantages and drawbacks and they are discussed individually.

Types of Fluidic Oscillators

There are various types of fluidic oscillators that can be actuated via a variety of ways. The basic principle of the Coanda type jet adherence remains.

Monostable Oscillator

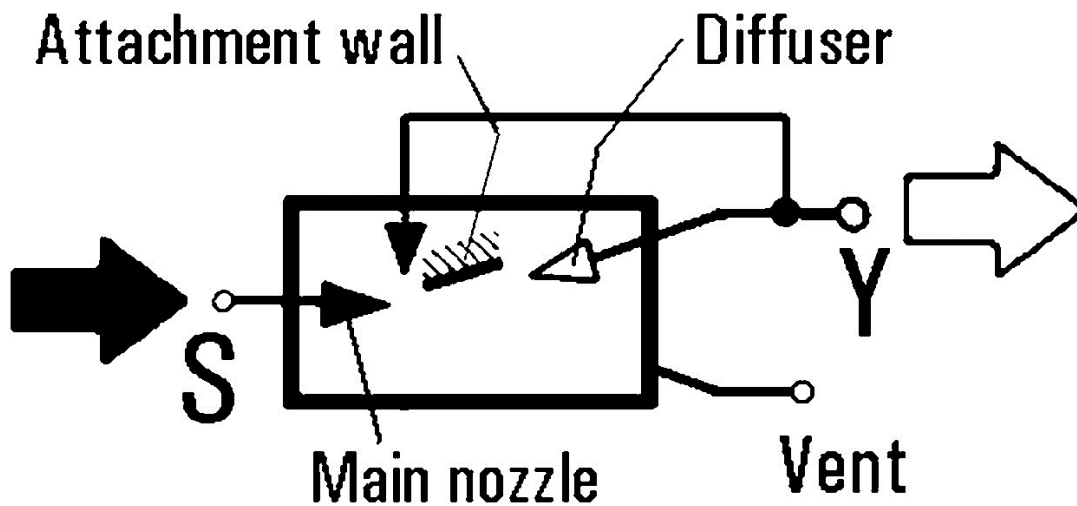


Figure 2 Simplest form of a fluidic oscillator (Tesař, 2013a). S is the supply nozzle , and Y is the output leg.

Figure 2 shows the simplest form of fluidic oscillator with one output leg. There is a supply nozzle from which the impinging jet enters the system and is compressed. The jet adheres to the attachment wall due to the Coanda effect. The diffuser or the output leg, Y, is connected to the control nozzle placed perpendicular to the supply nozzle. The two nozzles, result in entrainment of fluid from the Vent which generates a region of low pressure between the wall and the jet and bends the jet towards the attachment wall which is opposite to the original flow of the jet (which is the Vent). The attached flow leaves the system via output Y. This is a monostable jet deflecting valve with a negative feedback.

Jet deflection and Load switching

The major distinction between types of fluidic oscillators is a jet deflection based and a load based switching oscillator. All fluidic oscillators can be organised by their mechanism of switching as either jet deflection or load based. Both are based on the Coanda effect wall attachment mechanism but whilst one has a control terminal based deflection , the other requires the presence of a load at the output or mechanical device in order divert the flow to the other leg.

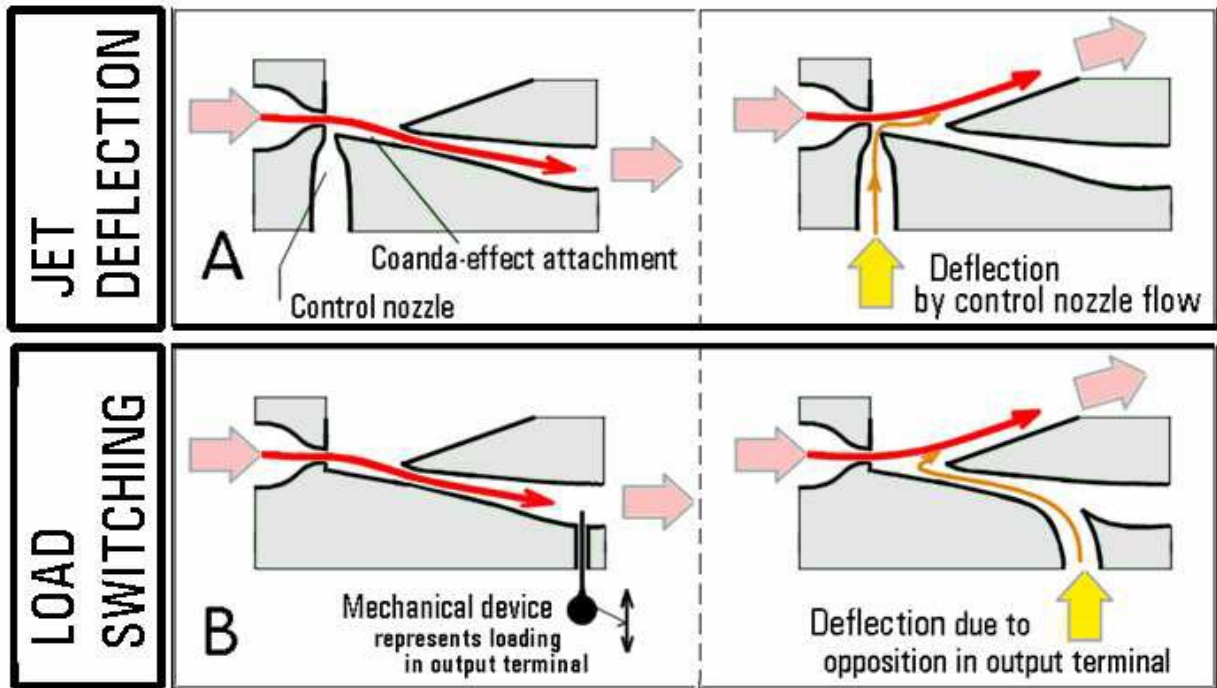


Figure 3 Left - A typical Warren type fluidic oscillator with a control terminal, control nozzles, supply nozzles, Feedback loop channel, and two output channels. Right (A- jet deflection) and (B-Load Switching type) oscillators. (Dančová and Tesař, 2017).

Figure 3 differentiates the two major types of oscillators – Jet deflection and load switching. For a typical jet deflection oscillator, (Warren type, Spyropoulos type, Tesař-Zimmerman fluidic oscillator, and Hartmann Resonator Fluidic Oscillator) the flow enters the supply nozzle and gets amplified at the nozzle. The control terminals are used with the fluid wall attachment (Coanda attachment) acting as an initiator. The control channels are connected between pre and post the nozzle. The flow is partially diverted back due to a pressure differential arising which results in flow switching. An additional mechanism to initiate oscillation is the cusp which acts as a positive feedback by the initial recirculation which is seen in Figure 13. Figure 3 has been taken from (Dančová and Tesař, 2017) Mechanism A and B describe the two types of oscillators.

Load switching is based on a mechanical device in the output terminal for a singular output based on the Zalmanzon principle (Zalmanzon, 1967) or based on recirculation back to the supply nozzle by opposition in the output terminal due to the output load such as the Vortex type fluidic oscillators. Both of these mechanisms require initial pressurisation and the presence of loading in order to switch the flow and therefore are highly load dependent.

Loading is generally classified as adding a pressure drop at the outlet, generally a control valve or diffuser. Higher the load (pressure drop), longer the delay and therefore lower the frequency.

$Sh_t = \frac{fL}{v} \sigma$ Control is severely limited in load switching oscillators unless they are Zalmanzon type fluidic oscillators, due to the heavy dependence on the set geometry for switching. Capacitance type (Zalmanzon type) oscillators are easier to switch but they also involve a pressurisation step in order to initialise the oscillation.

There are other mechanisms of switching for fluidic oscillators but have been neglected here as they cannot be used appropriately as they are too geometry dependent and require a very high pressure drop or have high friction losses.

Certain oscillators that have moving parts are neglected as the main purpose is to have a no-moving part self-actuated fluidic oscillator.

Load Switching Oscillators

The following describes different types of load switching oscillators. These are the oscillators most likely plausible for use with microbubble generation and have been invented for microbubble generation.

Zalmanzon Type Oscillator - Tippetts' Capacitive Fluidic Oscillator (TCFO)

An oscillator designed by Dr. John R. Tippetts based on the Zalmanzon principle *i.e.* a load switched oscillator was designed specifically to generate microbubbles at low flows for viscous ionic liquids (Tippetts,2014).

An important note here is that whilst a jet diversion oscillator usually has a lower pressure drop across it than a load switched oscillator and better control features, it has lower amplitude of pulse than a load switched oscillator (Tesař *et al.*, 2016, Kim, 2011).

This is also known as a capacitance based oscillator due to the fact that the chambre (as seen in Figure 4.3 and Figure 4.3a as 8) acts to compress the incoming wave and reflect it back upon appropriate volumetric conditions. The fixed volume will let the wave compress based

on the impingent wave and the pressure differential between the chambre and the incoming jet. Due to the aerodynamic fluctuations taking place for this process, it is also known as an aerodynamic oscillator. The boundary layer interactions between the wave entering the chambre and filling it up and being reflected back are what cause the oscillation. Figure 4.1 and Figure 4.2 show the different designs that can be based on this same principle where two nozzles are used with a curved surface in order to take advantage of the Coanda effect (Tesař and Bandalusena, 2011, Mirca Boscianu, 2010).

Figure 4.1

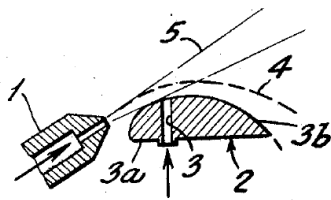


Figure 4.2

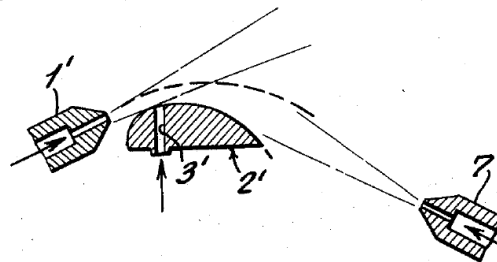


Figure 4.3

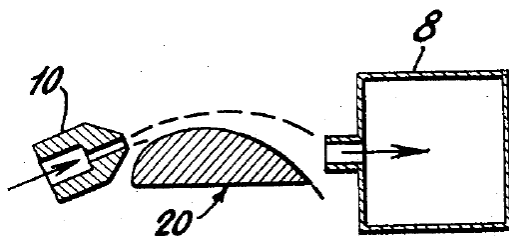


Figure 4.3a

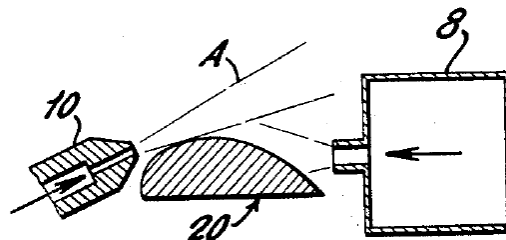


Figure 4 Taken from Zalmanzon(Zalmanzon, 1967).

The oscillator invented by Tippetts and based on the Zalmanzon effect is designated as TCFO – Tippetts’ Capacitive Fluidic Oscillator, because the switching is caused by variations in the

output “capacitive loading” (*i.e* backpressure) in one of the outputs. The backpressure is built up in a small trapped air volume which is the pressurisation step for each oscillation to initialise. Frequency depends on the trapped air volume in the capacitive element C. This is usually a separate container which could have a very large volume if low frequency is required. Conversely its volume can be made very small to produce high frequencies. The high frequency limit is approximately 300 Hz.

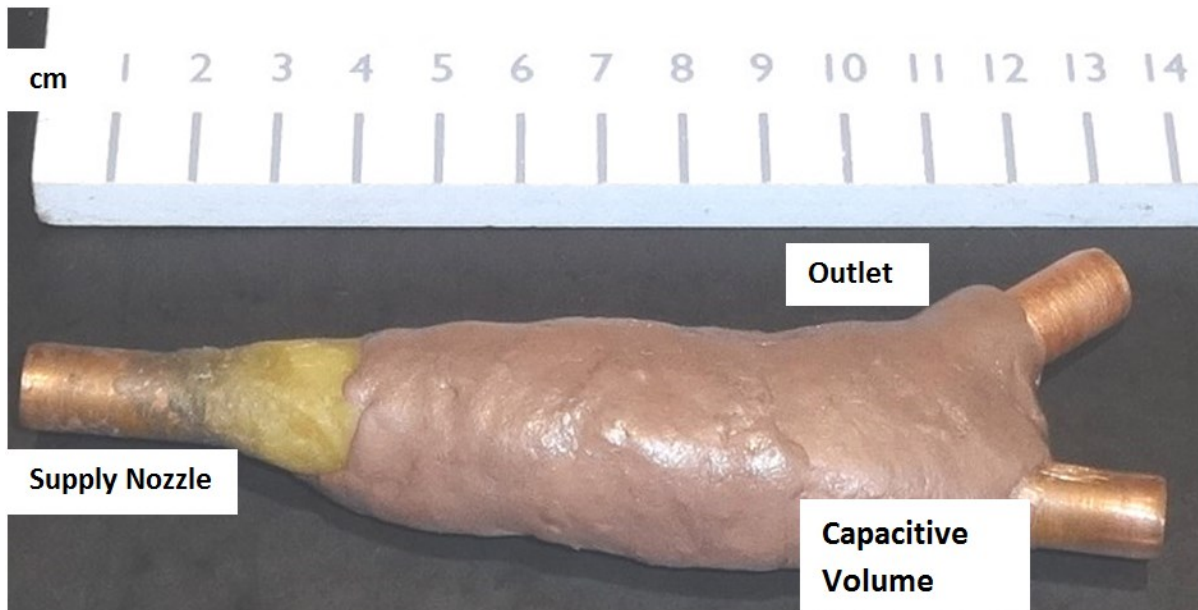


Figure 5 TCFO with feedback connexion (main nozzle 4 x 1 mm). The scale in the figure is in cm.

Figure 5 shows the TCFO with the feedback connexions and the different components for the device.

The resulting device is seen in Figure 6. TCFO with small capacitive volume (plugged tube about 3 cc volume (Figure 6 a), (350 cc volume (Figure 6 b)) power output is from the red nozzle. The scale is in cm It has a supply port (on the left), an outlet port (top right) and a “C”-port (bottom right). All pipe connections are 10 mm OD copper tube. The C-port connects to a trapped volume where the effective capacitive volume is about 3.0 cc. An alternative C-volume is available having a volume of 350 cc as shown in Figure 6b

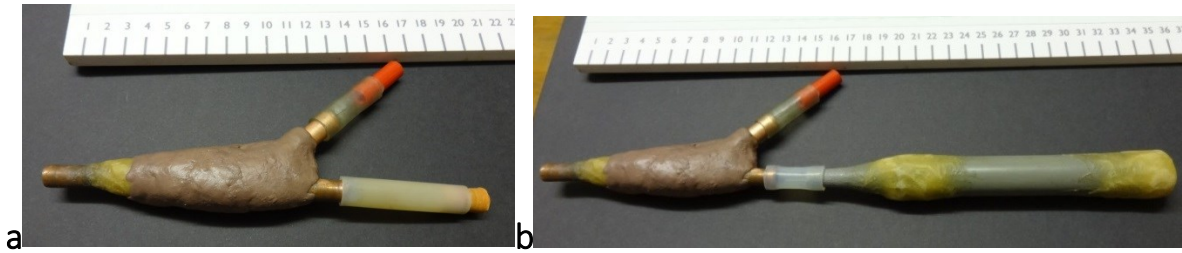


Figure 6 TCFO with small capacitive volume (plugged tube about 3 cc for left(a)), (350 cc volume for right(b)) power output is from the red nozzle. The scale is in cm.

A range of tests showed that TCFO oscillated satisfactorily as shown by a sample oscilloscope trace in Figure 7 from a pressure transducer in the power output port with the small 3cc C-volume. Typically the output ranged between 300 and 250 Hz.



Figure 7 Oscillatory output using the small capacitive volume (3 cc) : Supply pressure 0.5 barg, 275 Hz, flow = 47 slpm(Tippetts, 2014)

As an additional indication of performance, at a frequency of 200 Hz the supply pressure was 0.5 bar(g) and the peak to peak amplitude was 0.22 bar in the pressure across a well matched outlet restrictor. It has a frequency range from 42 Hz to 280 Hz.

280Hz was obtained using a C-volume of 3.2 ml in the form of a 40 mm length of 10 mm ID tube. The main nozzle of the fluidic diverter is 1 mm wide and 4 mm deep giving a flow area of 4 mm². This was then integrated into a single unit by adding a feedback connection in order to provide a diverter and feedback in order to have better control on the system (Tippetts, 2014).

Vortex generated fluidic oscillators

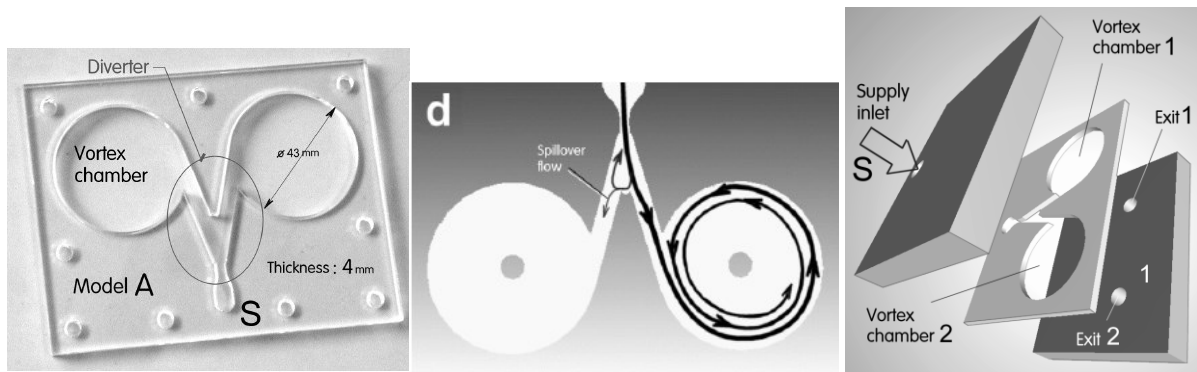


Figure 8 Vortex Generated Fluidic Oscillators (Tesař *et al.*, 2016)

Based on load switched oscillations, these class of oscillators have not been studied in depth until recently (Tesař *et al.*, 2016). They were invented by Tesař, for specifically using with microbubble generation. Tesař (Tesař,2014), using high speed photographic evidence of microbubble generation via fluidic oscillation in order to better understand the mechanism of oscillatory flow generated microbubbles saw that liquid imbibition was an extremely important component. The bubble conjunctions and coalescence associated with high frequency bubble formation via fluidic oscillation would result in larger bubbles.

Tesař, based on his findings, extrapolated that using a low frequency oscillator would be able to generate smaller microbubbles by limiting the conjunctions involved during microbubble generation. This was the motivation for inventing an oscillator which can generate frequencies between 2-10Hz.

This type of oscillator depends on the vortex generated prior to the outlet which induces part of the flow to return to the supply nozzle and switch the flow to the other leg. The frequency of this system depends on the flow through the system, loading at the outlet, and the diameter of the vortex chamber. There is a delay to induce the oscillation in order to initialise the system and is called the spin up delay.

The oscillator faces the problem that the frequencies attained are too low to attain high throughputs and results in a similar throughput as steady flow but smaller bubbles. The pressure drop attained for this system is also much higher due to the high level of liquid imbibition during microbubble generation due to the lower frequency of generation. This makes this oscillator not effective for microbubble generation. Additionally, the presence of

the frequency resonant condition or 'sweet spot' in microbubble generation seen in the previous chapter and the other findings negates the need for this oscillator.

Jet Deflection Oscillators

The following subsection describes jet deflection type fluidic oscillators which are based on the jet deflection principle. The underlying principle of using a small deflection at the control terminal, in order to divert the main flow to the other leg, results in a finer control of the oscillatory pulse and a lower pressure drop across the system. Additionally, there is a no need to include a pressurisation step in order to initialise pressurisation or if needed, much lower than the load switching oscillators. The Warren type, Spyropoulos type, TZFO, microscaled TZFO, and Hartmann resonator type fluidic oscillators fall into this category of oscillators. However, the TZFO and microscaled TZFO will be described separately in later sections.

Warren type and Spyropoulos type Oscillators

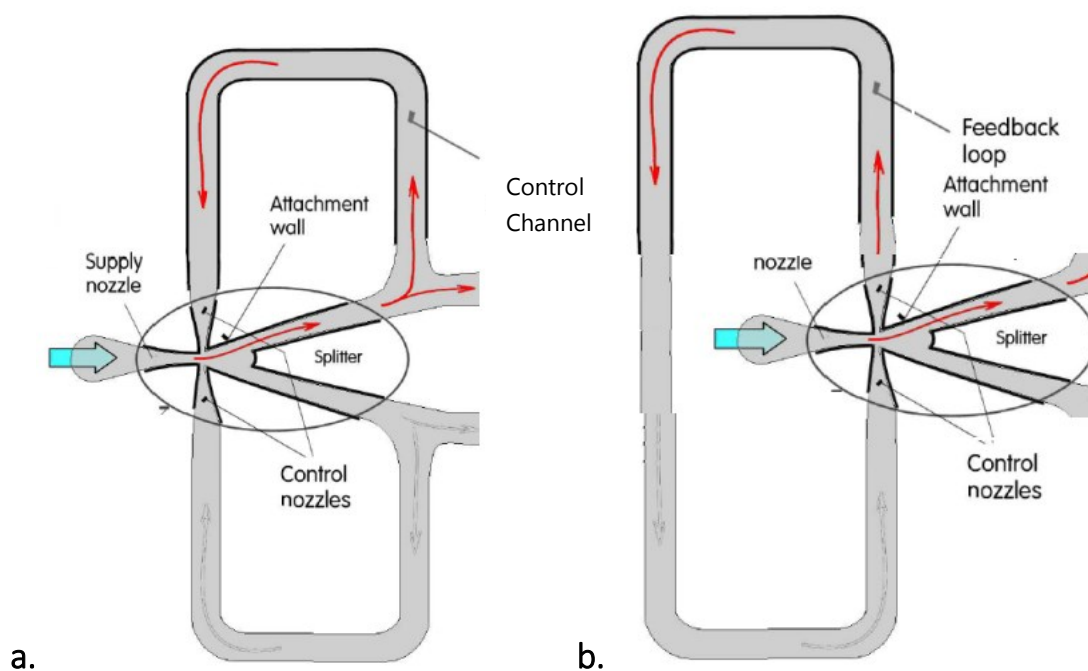


Figure 9 Left(a) Warren type, Right(b) Spyropoulos type Fluidic Oscillator(adapted and modified from Tesař *et al.*, 2016)

They were amongst the first oscillators to have been invented. They consist of a supply nozzle, a pair of control nozzles, a pair of outlets, and positive/negative feedbacks. The splitter region is responsible for the introduction of a small positive feedback in the form of a cusp. The feedback channel or control channel acts as the negative feedback. The flow enters the supply nozzle, gets compressed, and there is a recirculation zone formed in the splitter region due to the cusp. The control terminals are nozzles which are typically 30-60% smaller than the supply nozzle (i.e. control nozzle width= 0.4-0.7 times supply nozzle width) so that only a partial flow enters the control nozzles which then act as a venturi jet. The switching then depends on the configuration, and the length of the control/feedback channel as well as the impinging flowrate. As can be gleaned, the frequency control is easier for a Spyropoulos loop type feedback as opposed to a Warren type feedback.

These configurations are typically introduced by adding a negative feedback by either connecting the two control terminals into a feedback loop feeding into the control nozzles – Spyropoulos type control loop Figure 9b and Figure 10b or connecting the control nozzle to the outlet in order to induce feedback from the amplified output post throat nozzle of the impinging jet -Warren negative feedback oscillator Figure 9a and Figure 10a.

Figure 10 shows a better representation of the components of the fluidic oscillator with S as the supply nozzle, X1 and X2 as the control nozzles (the black shaded triangles representing nozzles) , Y1 and Y2 as the outlets (the white triangles representing partial deflection)

Two configurations can be used to introduce negative feedback in order to destabilise the system – connecting the two control terminals (Spyropoulos type feedback) or by connecting each control terminal with the outlet leg in order to have the outlet flow back into the terminal (Warren type feedback). Both type of configurations have been adequately described in Tesař *et al.* (Tesař, 2012) .

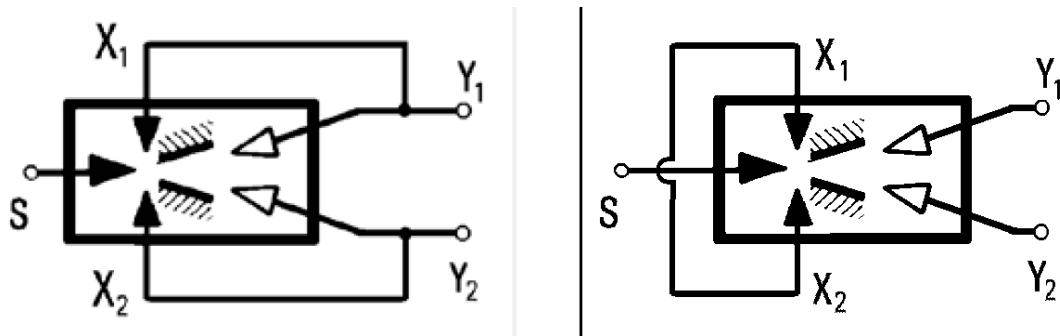


Figure 10(a) Warren Type Negative Feedback (b) Spyropoulos loop feedback (Tesař, 2012)

The TZFO was invented as an adaptation of these two configurations and the switching mechanism will be described in detail in later subsections.

Frequency control is easier for a Spyropoulos loop type feedback control system as there is an additional parameter introduced for frequency control (length of the feedback loop) whereas the Warren type depends merely on the outlet and the supply flowrate. This also means that the Warren type feedback is less responsive to flowrate changes, outlet changes, and manufacturing asymmetries due to this feature. The Spyropoulos loop type feedback on the other hand is very sensitive to these changes and therefore whilst providing an ability to map the frequency domain is not very stable in terms of frequency. Both configurations have achieved a frequency maximum of 300Hz based on previous studies.

Hartmann Resonator Fluidic Oscillator

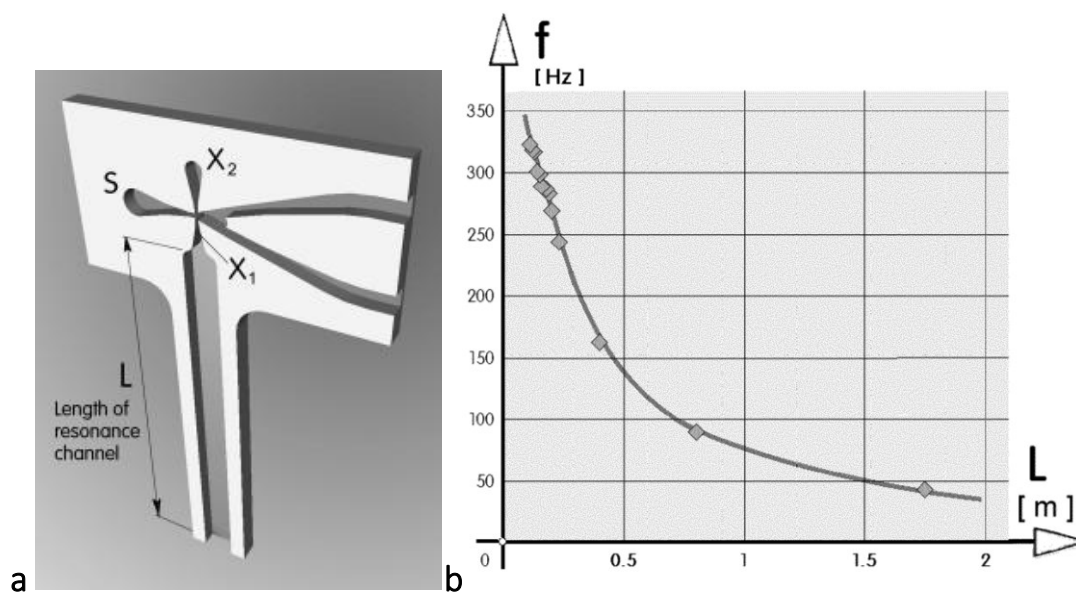


Figure 11 Hartmann Resonator Oscillator – Left a) L is the length of the resonating channel which determines the frequency, S is the supply nozzle and X1 and X2 are the control nozzles. Right b) Frequency response curve (Tesař *et al.*, 2013)

The Hartmann resonator oscillator was invented by Tesař for microbubble generation prior to his work (Tesař, 2014) on the liquid imbibition via fluidic oscillation generated microbubbles which led to his change in focus to aim for lower frequencies for enhanced microbubble generation (Tesař *et al.*, 2016). The focus at the time of the invention of this oscillator was that higher the frequency of the oscillator, smaller the microbubble generated in the system as per (Zimmerman *et al.*, 2009). This oscillator was also invented due to its ease of manufacturability and use for flow separation control systems (Tesař *et al.*, 2013). Higher frequencies are also useful as actuators since they can be used in situations where the mechanical movement and associated friction would cause mechanical failure.

A jet diversion oscillator, the oscillator is based on the principle of the quarter wave, Hartmann resonator placed at the control terminal. The flow deflections are caused by the open channel placed at the control terminal and usually is a single open channel located at X1/X2 as seen in Figure 11a. The wave propagates across the open channel (X1). Upon initialisation of the oscillation, the pressure deflections at the top of the channel deflect back the wavefront which cause it to switch. These are based on the quarter wave resonator, and hence, the wavelength is four times the length of the resonating tube. The frequency response is controlled by the length of the resonator (X1).

Due to the open channel, there is considerable gas loss and the also limits the outlet load for the oscillator since the oscillator will become monostable on higher loads since this is an open channel. The control nozzles are smaller than the supply nozzle as compared to the ratios for the Warren/Spyropoulos type oscillators due to the open resonance control channel. This leads to the control nozzle being 50%-70% smaller than the supply nozzle, thereby increasing the pressure drop and reducing the region of operation for this oscillator.

Although the frequencies achieved by this oscillator are in the range of 350Hz (Figure 11b) , the limitations described above, gas losses, and the higher resultant friction losses make this

oscillator not effective for microbubble generation. Additionally, the finding in the previous chapter, means that smaller microbubble generation requires the right resonant frequency for bubble generation (sweet spot) and sufficient amplitude for bubble detachment. Whilst venting can attain the amplitude for this oscillator and the TZFO, this oscillator will suffer much higher gas losses which cannot be controlled since the vent for this case will have an open unrestricted channel in the form of the resonant channel X1.

The following section describes the first oscillator to be used for generating microbubbles, and the mechanism for switching for this oscillator.

The original microbubble generating fluidic oscillator- Tesař-Zimmerman Fluidic Oscillator (TZFO)

The fluidic oscillator, developed for microbubble generation by Tesař and Zimmerman, and entitled the Tesař-Zimmerman Fluidic Oscillator (TZFO), is based on the Spyropoulos and Warren type fluidic oscillators , both of which depend on the feedback control of the impingent wave in order to induce an oscillation based on the flow switching via the level of feedback imposed.

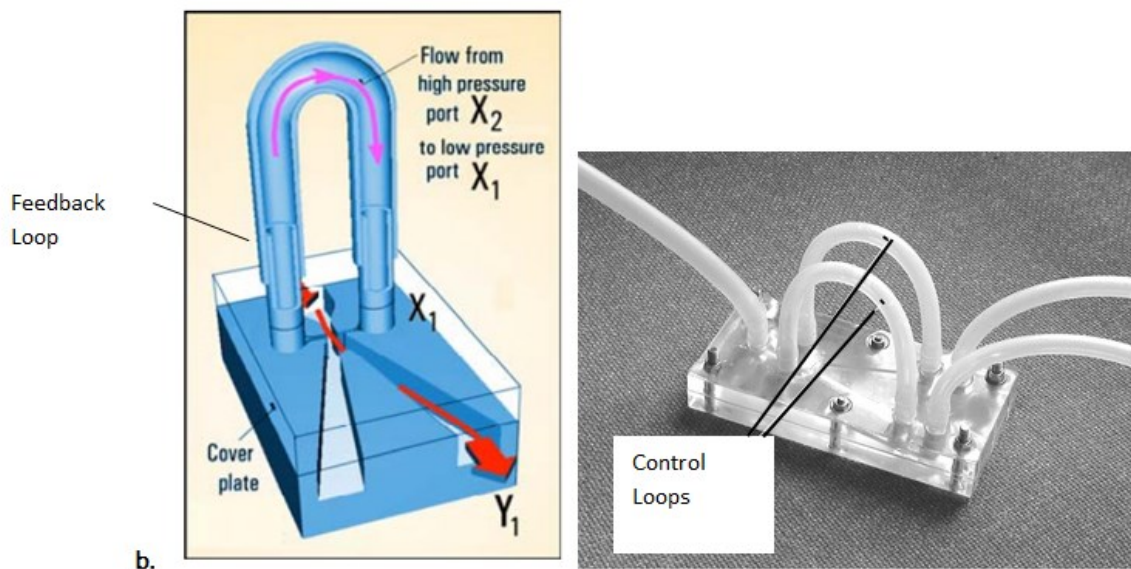
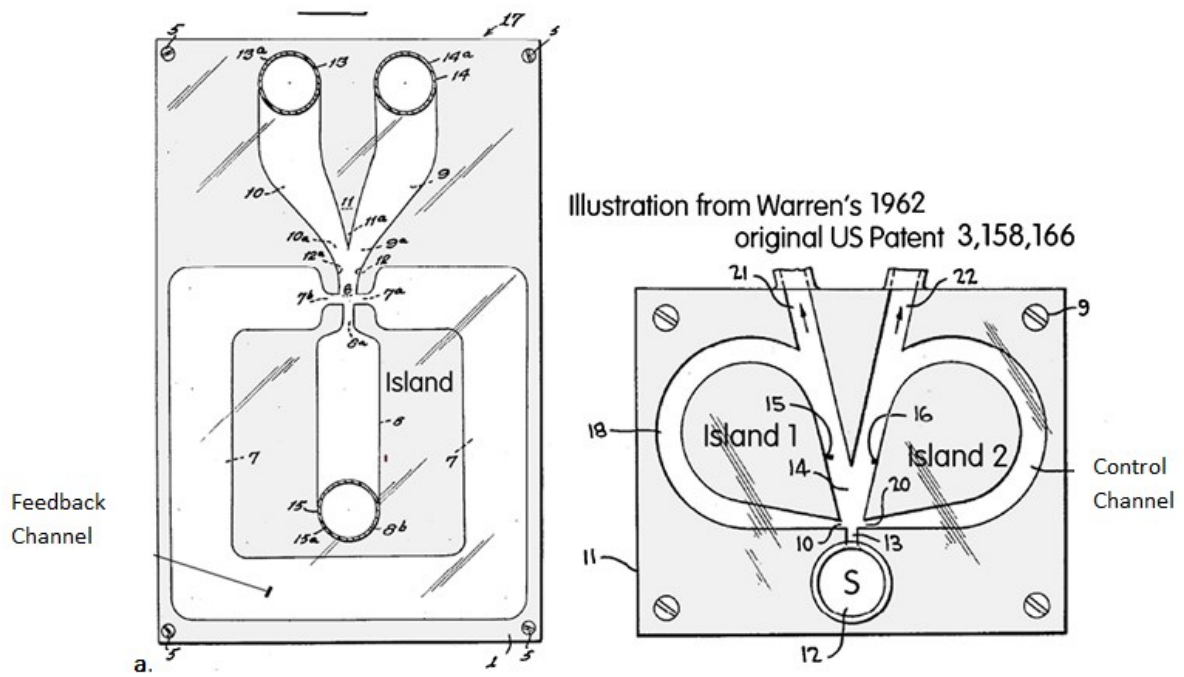


Figure 12 The Spyropoulos type oscillator, or feedback channel type oscillator invented by Warren. a. shows the original fluidic oscillators invented by Warren , (left) Spyropoulos type, (right) Warren type, with control channels or feedback channels inserted as part of the cavity. b. Changing the frequency was easily achieved by changing the feedback channel in third dimension by Tesař and Zimmerman. These two oscillators have been entitled Tesař-Zimmerman Fluidic Oscillators (TZFO) (Tesař,2013a.).

Figure 12 shows some of the first generation fluidic oscillators (Warren type and Spyropoulos type). Both the Warren type and the Spyropoulos type oscillator, or feedback channel type

oscillator were invented by Warren. Figure 12 a. shows the original fluidic oscillators invented by Warren , with control channels or feedback channels inserted as part of the cavity. This meant, changing the frequency required changing the geometry/requiring a new oscillator to be fabricated.

Tesař and Zimmerman modified these oscillators to generate microbubbles by adding the control ports in the third dimension which can be seen in Figure 12 b.

Changing the frequency was easily achieved by changing the feedback channel. These two oscillators have been entitled Tesař-Zimmerman Fluidic Oscillators (TZFO) (Tesař, 2013a.).

The major advance made by Tesař and Zimmerman was the use of the feedback loop in the third dimension which would allow for a better control of the TZFO (adopted from Warren and Spyropolous) and the application of the oscillator for microbubble generation. The Warren type oscillator was first described in a patent, by Warren (Warren, 1962) and adapted after suitable modifications by Tesař – Zimmerman and developed for bubble generation (Zimmerman *et al.*, 2008). The lack of ease in the control of frequency for this device made this configuration less popular than the Spyropoulos type configuration.

The benefits of bubble generation mediated by oscillatory flow were not unknown previously (Shirota *et al.*, 2008b, Tsuge and Hibino, 1983, Pinczewski, 1981, Hibino, 1978, Park *at al.*,1976, 1976, Lanauze and Harris, 1974, La Nauze and Harris, 1972, Ramakrishnan *et al.*, 1969, Satyanarayan *et al.*, 1969, Khurana and Kumar, 1969, Leibson *et al.*, 1956). All of them had noted the advantages of this phenomenon or made relevant comparisons but could not achieve the process in an effective manner. One of the key advantages of using fluidic oscillators aside from their low pressure drop and no-moving parts is the ability to generate hybrid synthetic jets which are useful for generating microbubbles. The hybrid synthetic jet is the key aspect for the reduced microbubble size and the effective microbubble generation by fluidic oscillators as discovered by (Tesař, 2014).

Using an acoustic device (a speaker or piezo system) to create an oscillatory flow without the synthetic hybrid jet component does not generate the same level of bubble size reduction typically associated with the amplified hybrid synthetic jet (Brittle *et al.*, 2015). This is further described in later sections.

The self-excited flow oscillation is produced by the aerodynamic/hydrodynamic instability in fixed wall cavities.

Mechanism of switching for TZFO with microbubble generation

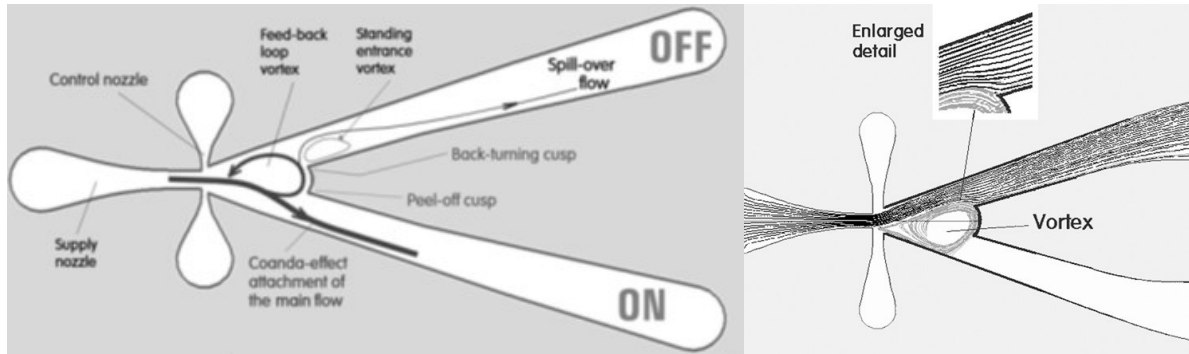


Figure 13 Flow in the TZFO (Tesař and Bandalusena, 2011) and enlarged recirculation zone(Tesař, 2009c) formation due to vortex formation induced by the positive feedback i.e. cusp.

The TZFO creates hybrid synthetic jets (*cf.* Figure 17) which help engender microbubbles in an economical fashion. The switching is achieved via a pulsatile flow and the adherence of the jet to the wall due to the Coanda effect (needed for the bistability of the system) and its subsequent detachment to the other leg due to a switchover created by a cusp (*cf.* Figure 13). This cusp is present in a region known as the splitter region (Tesař *et al.*, 2006). The cusped nose is responsible for resisting switching and acts like a positive feedback for the system. This positive feedback needs to be overcome in order for the switching to take place. This is why there is a need for an introduction of a destabilising negative feedback which can overcome the innate positive feedback. The recirculation vortex that is created due to the cusp, results in the oscillation initialisation. The control terminals help in the switchover and are used to facilitate the change in frequency. It can be thought of as the introduction of negative feedback to the system in order to increase its instability. This instability, in fact, induces a stable oscillatory flow which can also be termed as stable bistability. Both the outlet legs are balanced which results in a stable system by loading the system with equiresponsive spargers for bubble generation.

The Spyropoulos type feedback loop TZFO has been exclusively utilised for microbubble generation in literature. This is likely due to the fact that the frequency control is easier and

this configuration provides finer control and response to changes in the system which improve the ability to measure these changes. This type of negative feedback has several advantages. Firstly, frictional losses are kept to a minimum possible for the configuration (Warren type which requires flow back into the system and via the control terminal will have a higher friction loss and pressure drop) and mechanism in place and secondly, although the onset of oscillation is delayed in this loop when compared to the Warren type oscillator, the frequency of oscillation can be easily controlled with the use of different feedback loop lengths. Since a frequency domain test is required and important, the Spyropoulos type feedback configuration is used exclusively in this document.

As seen in Tesař *et al.* (Tesař, 2007c), the frequency of the TZFO is inversely proportional to the length of the feedback loop. This is due to the delay introduced by the feedback loop. The longer the loop, the longer would be the cycle of delay, which would mean, longer switching time and therefore a lower frequency. Due to the working of the TZFO, each half oscillation engenders a bubble. This led to the hypothesis that *ceteris paribus*, an increase in the frequency will directly result in the increase in the number of bubbles generated by Zimmerman and Tesař, in (Zimmerman *et al.* , 2008, Zimmerman *et al.*, 2009, and Zimmerman *et al.* , 2011)

However, this assumption does not include the effect of conjunctions, bubble size, bubble rise, bubble-bubble interactions, bubble wake and size of the orifice generating the bubble. All these factors increase the bubble size which results in a reduction in the effective bubble number. Since the frequency of the TZFO kept on increasing with the decrease in feedback loop length, it was hypothesised that with the internalisation of the feedback loop, i.e. shortest path created, the frequency would shoot up. This was actually observed and an exemplar of this experiment is present in the thesis.

The feedback loop acts as the negative feedback and introduces a delay to the system. This is immanent to the loop due to the fluid inertia as well as the time for acoustic propagation. Hence this loop is also known as the inertance loop.

The oscillation is generated using a no-moving part actuator driven by air flow. To activate the feedback flow, the pre-requisite amplification is required and this means greater than unity flow as well as a pressure gain between the control and output terminals. In practice,

there is a sudden 'blockage' introduced into the system with the help of valves. In order for the TZFO to oscillate, this 'blockage' is absolutely critical since it provides the greater than unity flow thereby activating the feedback loop. Figure 14 shows the entrainment observed in the TZFO due to the bistability.

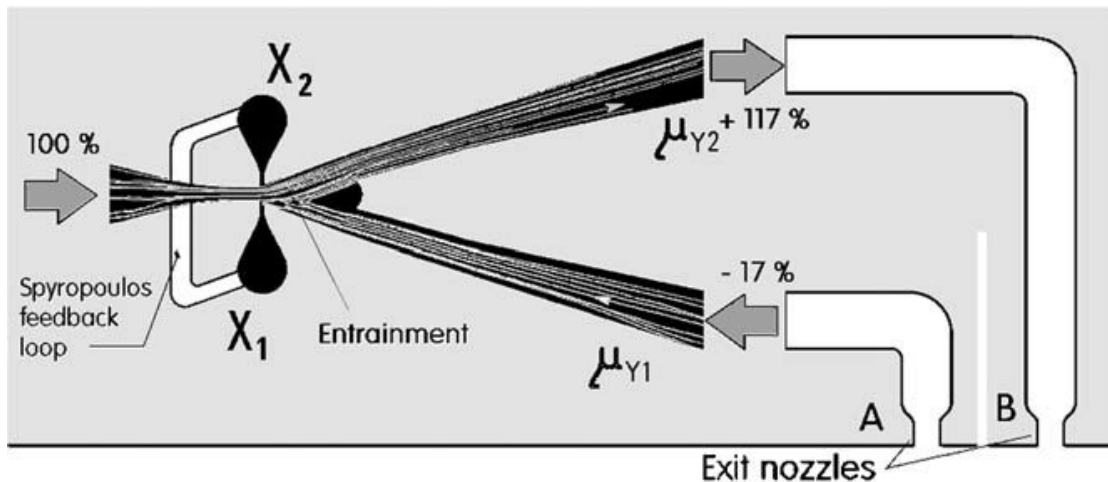


Figure 14 Entrainment observed in the oscillator for a steady state computation (Tesař and Bandalusena, 2011 and Tesař *et al.*, 2006).

There is an entrainment of the jet that results in it being diverted to the second nozzle (B) which then causes the return of flow in to the first nozzle (A) and vice versa. This happens in a periodic fashion, causing the bistability. This figure is taken from Tesař *et al.* (Tesař *et al.*, 2006) and (Tesař and Bandalusena, 2011), and shows the values for a steady state computation. An oscillatory flow requires a transient computation and the values were found to be much higher than those found herein. This means that the effect is amplified which in turn means that the amplitude is higher for an oscillatory flow system. This means that once stability is achieved, each nozzle can engender the bubble cut off individually and therefore, if the two legs are balanced properly, two equi-responsive diffusers can show a balanced performance.

Due to the entrainment observed in the TZFO, the outlet flows cannot be measured using flow meters. This is because of two reasons. Firstly, if the frequency of the switching is high, then the flow meters cannot show a response and therefore will most probably show the inlet flow rate. Secondly, due to the spillover and the entrainment, there is unevenness in the flow regime for each nozzle. This means that one of the nozzles shall have a higher flow out

of it than the other and vice versa. This effect is crucial for the bistability but too much of it leads to the monostable behaviour. This is the control parameter for the amplification factor possible. Once bistability is achieved, this entrainment, still very much a feature of the switchover, is reduced. But due to this, flow out of the oscillator cannot be easily measured. However, this technique can be used for ensuring repeatability of experiments. Several publications have demonstrated the efficacy and bubble size reduction observed upon application of the TZFO over bubble formation under steady state flow; Tesař *et al.* (Tesař, 2007c, Tesař and Bandalusena, 2011, Zimmerman *et al.* (Zimmerman *et al.*, 2009a, Zimmerman *et al.*, Zimmerman *et al.*, 2008, Zimmerman *et al.*, 2011a) and Desai *et al.* (papers submitted). An example is shown in Hanotu *et al.*, (Hanotu *et al.*, 2012) wherein a 40 µm orifice produces 1040 µm bubbles under steady state flow and 90 µm bubbles under oscillatory flow. However this method of producing the bubbles is not for larger scale processes since it relies on meshes and when scaled up produces design difficulties.

Bubble formation via fluidic oscillation

As mentioned previously, fluidic oscillation has shown considerable reduction in bubble size as compared to conventional steady flow. There are certain factors that prevent this: coalescence and conjunction and if this can be avoided, smaller bubbles can be engendered. Tesař *et al.*, (Tesař, 2013b) explains in detail why fluidic oscillation is unable to achieve bubbles sized approximately to the size of the orifice without any change in the formation dynamics.

A simple equation used for the bubble formation developed by Thomas Young and Pierre Simon-Laplace, known as the Young-Laplace equation which describes the pressure difference sustained across the interface between two static liquids and films. Figure 15 shows the spherical cap that happens during bubble formation.

$$\Delta P = \frac{2\sigma}{r} \quad (\text{Equation 13})$$

Where

σ – Surface tension [N/m], ΔP – Pressure difference [N/m²], and r - Radius of the spherical cap [m]

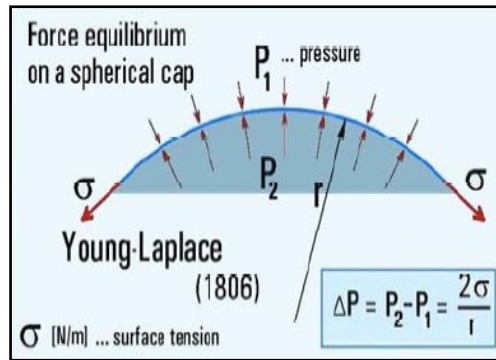


Figure 15 Spherical cap during bubble formation

The switching mechanism generates the pressure difference necessary for the bubble growth to be cut off and the bubble is generated which is smaller than that achievable at constant flow. Taking this into account, the bubble that is actually generated is in the ascending part of the oscillatory cycle. Another interesting point seen in Figure 16 is that waveforms are rectangular in form for the low frequencies. This behaviour has been observed in the oscilloscope for some of the lower frequencies. The rectangularity is due to the jet in the valve remaining attached at one of the attachment walls until the switching occurs.

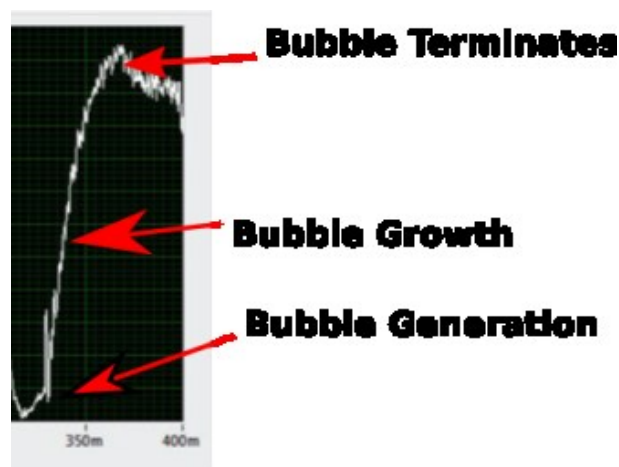


Figure 16 Bubble growth in the oscillatory cycle.

The waveform in Figure 16 shows an oscillatory cycle and marks the point in the detachment cycle where the bubble pinch off would take place. The bubble growth just shows how the hybrid synthetic jet engenders microbubbles for each pulse and how the bubble detachment takes place herein.

The bubbles are detached due to the switchover and the frequency is dependent on a number of parameters namely lengths of the feedback loop, flow rate and velocity / constriction based on the Strouhal number discussed previously (Strouhal, 1878)

The Strouhal number is a dimensionless(Kuneš, 2012b) number that determines the flow and frequency conditions of a fluidic device and enables characterisation of these devices in terms of frequency response (for jet deflected oscillations especially). However, the number is not used usually outside of the fluidics field.

$$Sh_t = \frac{fL}{V} \quad (\text{Equation 14})$$

Where f = oscillation frequency [Hz], L = length of feedback loop [m], and V = supply nozzle bulk exit velocity [m/s]

Hybrid Synthetic Jets

Figure 17 shows the different type of jets that can be introduced in a system. A pulsed and fully pulsed jet can be formed using several waves including acoustic excitation in order to generate an oscillatory wave which are both net zero but could be offset from the mean. A synthetic jet is where an oscillatory flow is introduced with inflow and outflow from two nozzles. The net mean however, is still zero. The most sought after jet, especially for bubble formation is the hybrid synthetic jet which generates a net non-zero pulse deviating from the mean. The amplification ratio and flow conditions including wall cavity geometry determines the deviation from the mean. The reason for the use of a hybrid synthetic jet and the size reduction obtained due to TZFO application is seen in (Tesař, 2014, Vít *et al.*, 2014, Tesař, 2013b, Tesař, 2013c, Jilek, 2013) and is due to this feature.

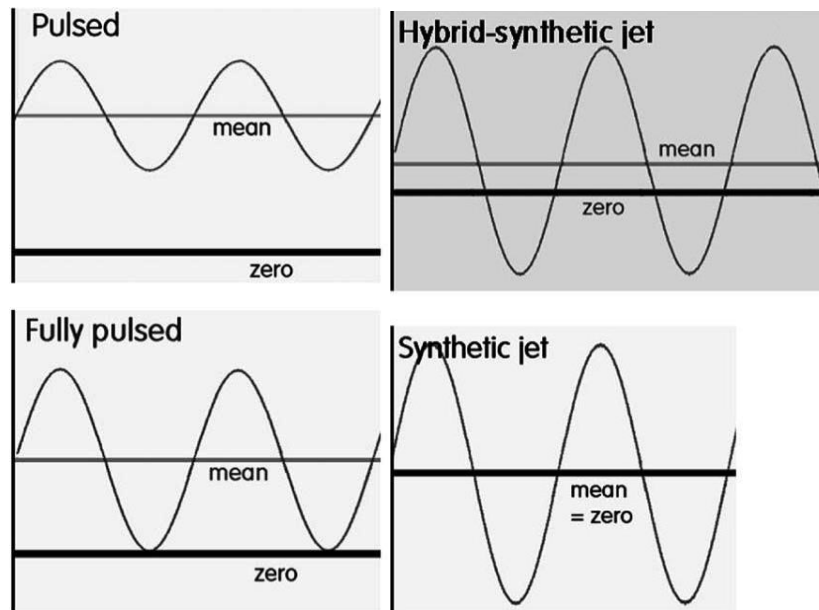


Figure 17 Different types of jets observed (Tesař *et al.*, 2006)

In contrast to usual synthetic jets, the “hybrid-synthetic jets” of non-zero time-mean nozzle mass flow rate are increasingly often considered for control of flow separation and/or transition to turbulence as well as heat and mass transfer. The pulsed and fully pulsed jets can be generated by using several devices and develop (either offset from the mean or at mean) to generate net zero flow. A synthetic jet is different as it is a pulsed jet with periodic alternation of inflow and outflow from an output nozzle thereby causing a pressure differential. This is still net zero i.e. positive and negative pulses cancel each other out. However, a hybrid synthetic jet results in a net deviation from the mean and this is highly sought after for several applications. This has been generated by the fluidic oscillator type devices and is used for bubble formation.

The need for reduced venting and achieve higher frequencies if amplitude could be maintained, was necessitated by the findings in the previous chapter. Microscaling the TZFO was the proposed method approached to simulate an oscillator capable of matching the response rate for the system.

Microscaling the TZFO – Reducing Venting (hydraulic losses) and frequency response

As discussed previously, there is a requirement to reduce the hydraulic losses and increase frequency. Reducing the hydraulic losses can be attained by microscaling the TZFO. This

would in theory, reduce the channel size and therefore reduce the onset of oscillation for the device. Microscaling the system was achieved in a manner similar to the original work for scaling the TZFO by Tesař (Tesař, 2009c). All the ratios were maintained and the TZFO were scaled down from a supply nozzle width (b) of 1mm down to 0.1mm and seen in Figure 18. Tesař (Tesař, 2009c) scaled them down to 0.85mm and up to 6 mm. The microscaled TZFO with a supply nozzle width $b=0.5$ mm was selected to be used for this matching as it had the appropriate flow characteristics for comparison with the other oscillators to be tested. Frequencies upto 2000Hz have been achieved at a maximum depending on the fluidic circuit and the downscaling.

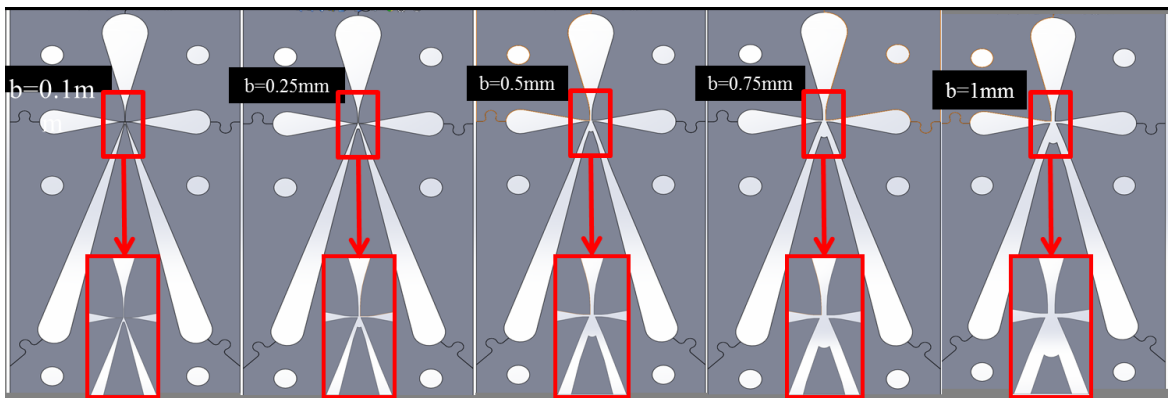


Figure 18 Scaling down the TZFO (Image Courtesy – Pratik Desai and Dr. Michael John Hines, formerly with ACAL Energy).

The problem with simply microscaling the system in order to reduce the hydraulic losses (i.e. initialise oscillation at a lower flowrate and therefore not require venting) is that reducing the channel widths and wall thickness of the fluidic oscillator also results in concomitant increase in backpressure and frictional losses. This is not desirable. Furthermore, due to the higher pressure of the system, it will lead to an increase in leaks which is also not desired.

One of the most important requirements is to develop or identify a microbubble visualisation technique such that high throughput cloud microbubble dynamics can be studied.

Cloud Bubble Visualisation Techniques

Cloud bubble visualisation has always been an extremely difficult prospect. It requires not only the expertise of the technical equipment but also specific analytical inferences derived from understanding of the methods of detection which is why there are very few experts in the field. Microbubbles are harder to visualise than bubbles but for a low throughput system or single microbubble system, the visualisation is straightforward. Microbubble clouds are much harder to visualise than bubble clouds and inferring the bubble size distribution for a bubble cloud is complicated. There are several problems associated with measuring the bubble size distributions since most assumptions about bubble size are based on assumptions such as monodispersity of bubble population, or no interference between different bubbles generated, or a bubbles being present in a singular plane. The DZFO has been able to generate smaller bubbles and in a non-coalescent system, the DZFO will be able to generate much smaller bubbles and therefore, with a much higher throughput as has been seen previously. However, there is no clear method to measure cloud microbubble size. There are three likely possible techniques that might be able to obtain a bubble size distribution for a microbubble cloud and have been used in literature but they need to be compared in order to understand on the advantages and disadvantages imposed by each system.

In order to compare the bubble visualisation techniques, it was important to use different interpretations of bubble size distributions in order to better understand the systems being used. This is developing a technique that provides the underpinning understanding of the bubble formation dynamics and information relating to the various applications of microbubbles. Understanding the bubble sizes for the cloud also helps with the application of hot microbubbles and calculations for the same.

Bubbles ranging from (1 – 1000 μm) in size are termed microbubbles. Although the actual definition of a microbubble is under dispute and depends on its application, for the purposes of this study, the aforementioned definition holds (Parmar and Majumder, 2013). Bubbles have been visualised for over half a millennia with Newton's observation of bubble formation with a pair of lenses whilst the Berthelot tube method long been known as a way to observe cavitation in liquids (Trevena, 1987). Reynolds discovered bubble formation by cavitation via the process of boiling (Leighton, 1994). Bubble visualisation is easier for fine bubbles or for

sparse microbubbles generated by either energy intensive or low throughput yielding. A simple study through a microscope or a lens is sufficient to visualise the bubble. Cloud bubble dynamics is a more onerous task. Common practice is to use optical imaging coupled with the volume fraction of the bubble by juxtaposing a control image (bubble-free) over the bubble cloud image. This is followed by using the pixels to determine the void fraction. However, this does not necessarily provide any more information about the bubble size distribution. Therefore, optical methods were developed with algorithms relying on variety of techniques to estimate bubble sizes(Wesley *et al.*, 2016a, Magintyre, 1986, Ming Yang Su, 1994, Zhen Xu 2007). Interests in bubble cloud dynamics has largely been focussed on marine engineering and oceanic sciences. This is due to the high cost of producing microbubbles, thereby opposing the use of microbubbles for industrial purposes.

Zimmerman *et al.*,(Zimmerman *et al.*, 2011a) has shown a substantial reduction in energy costs for generating microbubbles with concomitant increase of throughput. The Tesař - Zimmerman fluidic oscillator(Tesař, 2012) made it possible to economically use microbubbles for industrial applications and has been used to in several applications for lab scale(Hanotu *et al.*, 2012), pilot scale(Zimmerman *et al.*) and large scale industrial purposes. Several T Junction devices (Martinez, 2009, Hashimoto and Whitesides, 2010), sonication (Schroeder *et al.*, 2009) and other techniques can now be used for generating a cloud of microbubbles with a wide size distribution. With the advent of such techniques, the methods for visualisation have simultaneously shifted from direct measurement using a microscope to indirect techniques for higher accuracy through the exploitation of properties exhibited by bubbles. The bubble size distributions depend on the methods used for obtaining the bubble size and the statistical analyses that accompany these methods. Methods used for inferring bubble size distributions include four point optical probe(Guet *et al.*, 2003, Xue *et al.*, 2003, Xue *et al.*, 2008), capacitance probes(Farag *et al.*, 1997), electrical conductivity(Steinemann and Buchholz, 1984), video imaging (Colella *et al.*, 1999, Mulvana *et al.*, 2012, Spicka *et al.*, 1999, Weber, 1981), acoustical backscatter (Farmer, 1991), acoustic resonator(Farmer, 1998), acoustic pulse propagation sensor(Farmer, 1998), laser diffraction(Xu, 2001), acoustic attenuation(Choi *et al.*, 2006, Czernski, 2012, Elmore and Caruthers, 2003), UCT bubble size sampler(Laskowski, 2002) , and laser attenuation(Murata, 1984).

Figure 19 shows why there is a problem with direct visualisation of a microbubble cloud. Whilst there are several instances of photographic evidence of smaller microbubbles directly visualised in previously published work (Zimmerman *et al.*, 2011, Rehman *et al.*, 2015, Hanotu *et al.*, 2012, Agrawal, 2011) and several other instances, it is not possible to visualise these bubbles easily. This is why there is a need to evaluate and develop the best method and analysis for microbubble cloud visualisation.

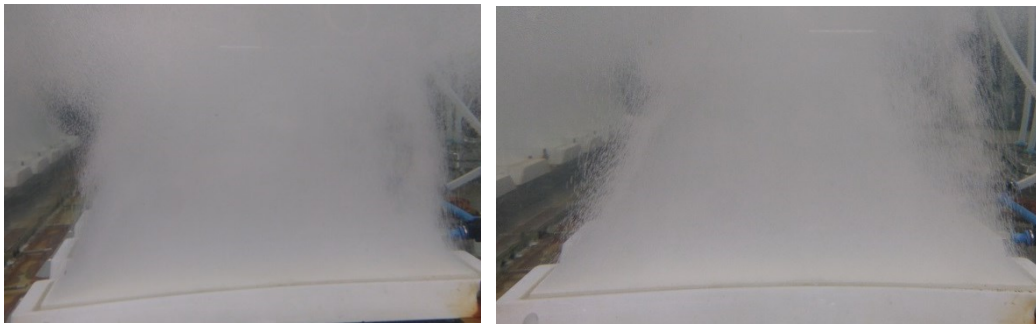


Figure 19 Photographic Visualisation of Cloud Bubble Dynamics (left) –control/steady flow, (right) oscillatory flow. (Courtesy, Dr. Michael J Hines)

Several comparison studies have been performed on bubble visualisation such as MagIntyre *et al.*, (Magintyre, 1986) – work on resolving optical and acoustic methods; Farmer *et al.* (Farmer, 1998), Chahine *et al.* (G.L. Chahine, 2001), Su *et al.* (Ming Yang Su, 1994) and Czernski *et al.* (H. Czernski, 2011) in order to merge the understanding of these techniques and try to obtain a better understanding of these visualisation systems. However, comparison studies for cloud bubble dynamics with an emphasis to smaller bubbles (microbubbles) have not been performed or studied in detail. Statistical analyses performed on the sizing by each method skews the size distribution and therefore the final average bubble size obtained is quite different depending on the actual statistical analysis applied. A comparison study is performed for three classes of bubble sizing techniques - optical, photonic, and acoustic, delving specifically into Dynaflo's Acoustic Bubble Spectrometer (ABS), Malvern Instruments' Spraytec and High Speed Photography using a Photron FastCam S3 high speed optical camera. Acoustic methods and high speed photography have been used by several research groups whilst Spraytec has been used by Tesař *et al.* (Tesař, 2012), in order to

estimate the bubble size. Each method, consequently, offers its own advantages and disadvantages depending on the actual method of estimating the bubble size population.

This section discusses the distinct advantages offered by the different visualisation methods and other capabilities.

Optical Methods

This is a direct form of measurement and visualisation, as well as the simplest method used by several research groups since it is a quick and easy way to engender a bubble size distribution. Optical methods can be usually split into Point Four optical probe (for bubbles $>800\mu\text{m}$)(Guet *et al.*, 2003, Xue *et al.*, 2008) high speed photography or high speed videography.

High Speed Photography

Optical methods usually involve a monochromatic light source and require the liquid to be transparent to light and greater the contrast between the bubble and the background, the more robust it is for the automated image analysis. High speed photography has been used by a lot of research groups due to its ease of use. Most high speed cameras have the ability to capture more than 500 frames per second (fps).

The bubble generator is placed in the centre with the light source and the camera placed opposite each other in order to obtain the best contrast for the bubbles. Figure 20 shows the collinear set up for optical visualisation.

The bubble generating rig is placed in the centre with the camera and diffused light sourced placed antipodal each other in order to obtain maximal contrast. This has been described well in (Brittle *et al.*, 2015, Wesley *et al.*, 2016a).

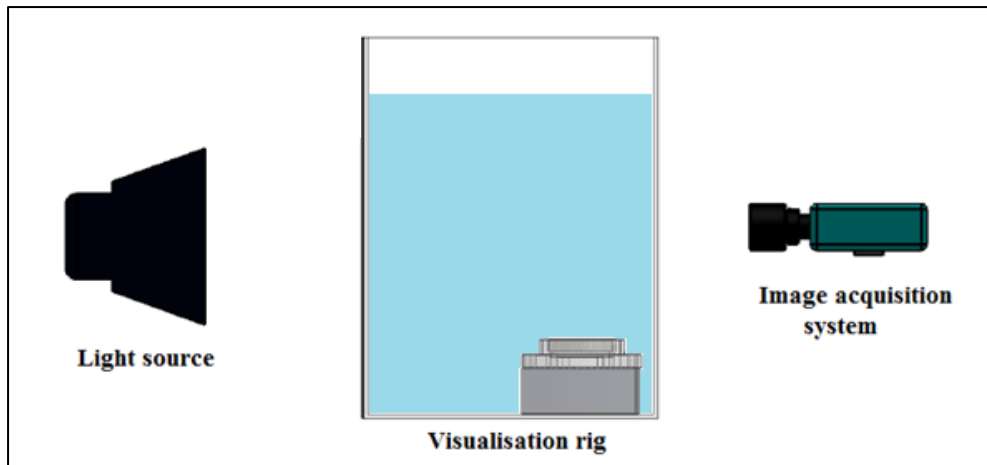


Figure 20 Collinear set up for optical visualisation

Automated image analysis is made easier if there is a good contrast between the background and the bubbles and this is obtained with the configuration described. A quick set up time, this method requires little skill or expertise yet being an effective technique for garnering a bubble size distribution. The camera need not have more than 2000 fps to obtain a bubble size distribution. The simplicity of the system is one of its key advantages and significantly reduces the costs of the system.

Automated image analysis is possible by simple algorithms by using any suitable programming language viz. Octave, ImageJ, Matlab, Mathematica, and LabView.

Image analysis does not require complicated inversions and the ill posed inversions that are a feature for the indirect methods such as photonic and acoustic methods i.e. Resonant Bubble theory or Mie theory is not required for the optical measurements as well. Gail *et al.* (Gail P. Box, 1992) show that Mie inversions are similar to the acoustic inversions as they have a similar ill posed inversion – the solution of the inverse of the Fredholm integral. The inversion of the Fredholm integral is *ill posed* and is quite difficult to invert (Szczuczyski, 2009). This is used by Mie theory to obtain an aerosol distribution.

Image analysis can also be performed manually and therefore would be able to provide bubble sizes without the need of computing power albeit rather cumbersome. Although this technique is convenient for single bubbles, cloud bubble dynamics present their own drawbacks. Automated image analysis cannot be reliably used for overlapping bubbles as well

as non-circular bubbles and when the bubbles are present next to the wall. The bubbles also need to be in a single plane, in focus and non-overlapping. Depending on the angle used, the bubble size obtained is significantly different. A long working length lens could be used, which in turn, makes the process expensive and cumbersome.

This problem could be solved by using multiple cameras at the three focal planes but results in the need to develop a way to accrue information from the three cameras and then collate the information together in order to obtain a bubble spectrum. Bubbles at the wall, partial bubbles, non-circular (spherical for the 3D system) are not detected by automated image analysis. This makes the task tedious, cumbersome and further complicates matters.

Different lenses are required for a particular size range. They cannot be used simultaneously unless another camera is used concomitantly. A comprehensive bubble size distribution is therefore difficult to obtain and only a certain size range can be observed at a given time. Once the appropriate lens has been chosen and the camera focussed, it cannot detect the other bubble size ranges and cannot differentiate between the particles and bubbles if they are too small. Multiple lenses would therefore increase the cost of the system and then one has to make a lot of measurements coupled with several analyses and comparisons.

A number of additional analyses can be made using a high speed camera. If the camera has a high frame rate, such as the Photron FastCam S3, the rise velocity of the bubble can be measured as well as the bubble formation dynamics, growth dynamics, conjunction and coalescence. Alwan *et al.* (Adil A. Alwan, 2012), presents the possibility to use image analysis techniques to calculate the rise velocity of a system with an ordinary camera.

Acoustic Methods

Acoustic methods have been used for bubble sizing for almost half a century. Medwin *et al.* (Medwin, 1977) presents an excellent review on bubble sizing using acoustic methods. The bubble acoustic response is seen through backscatter, attenuation, resonator as well as the change in sound speeds in the medium (Czerski, 2012). This is possible by the substantial effect that a bubble has on the propagation of acoustic waves. According to Medwin,

(Medwin, 1977), the mechanical oscillations observed in the bubble are due to their stiffness and inertia which is due to the gas inside the bubble and the ambient liquid outside the bubble.

Commander *et al.* (Commander and Prosperetti, 1989) demonstrated that it was possible to acoustically determine the bubble sizes in the medium.

The relationship between complex sound speed in a bubbly medium, c_m and bubble free sound speed c_0 is defined by

$$\frac{c_0^2}{c_m^2(f)} = 1 + \frac{c_0^2}{\pi} \int_0^\infty \frac{an(a)}{f_R^2 - f^2 + i\delta f^2} da \quad - \text{(Equation 15)}$$

a is the bubble radius(m) , f is the insonant frequency (Hz), f_R is the natural frequency of the bubble of size a . $n(a)$ is the bubble density function and δ is the bubble damping.

This relationship by itself can be used for obtaining bubble size. However, there is a loss in fidelity which is why other methods have been improved upon. This along with the relation

$$\frac{c_0^2}{c_m^2(f)} = u(f) - iv(f) \quad - \text{(Equation 16)}$$

Where phase speed $v(f)$ is given by

$$\frac{c_0^2}{u(f)} \quad - \text{(Equation 17)}$$

And attenuation constant α is given by

$$\alpha(f) = 20(\log_{10} e) \left(\frac{2\pi f v}{c_0} \right) \quad - \text{(Equation 18)}$$

This combination provides the bubble with a resonant frequency at which to oscillate. According to the solution of the Rayleigh-Plesset equation, the linear response of the bubble under continuous insonation and its non-linear response along with oscillation is a property that is observed only for bubbles (not particles) making this method favoured due to its specificity.

Also, in the Rayleigh region, the insonation frequency is dependent on the 6th power of the radius thereby making it a specific method.

$$f \propto r^6 - (\text{Equation 19}) \quad (\text{Leighton, 1994})$$

The acoustical cross section is greater than the geometric cross section by 3-4 orders of magnitude.

Several authors have used hydrophones to measure bubble size and have used these different properties in order to obtain bubble size distributions for coated and uncoated bubbles but usually for larger bubbles or smaller bubble clouds (Cleveland *et al.*, 2004, DeJong *et al.*, 2010, Jia-Ling Ruan, 2008, Kooiman *et al.*, 2011, Linsey C. Phillips (PhD Student), 2011, Linsey C. Phillips, 2009, Meijering *et al.*, 2007, Phillips *et al.*, 2010, Phillips *et al.*, 2011, Ting *et al.*, 2012, Vos *et al.*, 2008)

The drawback comes in the complicated inversion observed due to the inverse of the *ill posed* Fredholm integral. An *ill posed* problem presents with the problem that small errors in measurement propagate an enormous effect on the solution.

The next subsection discusses the commercially available Acoustic Bubble Spectrometer (ABS) developed by Chahine, (Kalumuck, 2003) for inferring bubble size distributions.

Acoustic Bubble Spectrometry - ABS by Dynaflo

The section shall discuss Acoustic Bubble Spectrometry (ABS) - a method developed by Georges Chahine and based on an assumption known as the resonant bubble approximation (RBA). Wu *et al.* (Wu and Chahine, 2010) describe the system in detail and the algorithm used for the bubble size measurement.

The main development made by Dynaflo is the algorithm based on constrained minimisation. As discussed previously, consider $\int n(a) da$ with limits of minimum and maximum radii of bubbles (*a priori* assumption based on the frequency of the hydrophone being used) defines the actual bubble size distribution.

The resonant bubble approximation produces equations similar to the ones shown above with slight modifications that result in the inversion that would be the resultant bubble size distribution. Further information can be found in Chahine *et al.* (G.L. Chahine, 2001).

Dynaflow developed this system to measure bubble sizes and generate a bubble size distribution and as well as void fraction measurements. A number of papers have been published by Dynaflow over the years on this technique. It is analogous to a spectrophotometer but instead of light uses acoustical methods for the detection and sizing of the bubbles (Wu and Chahine, 2010) and therefore the technique has been defined as acoustic spectrometry.

A hydrophone is a microphone that can be used underwater. As sound travels much faster in water and attenuates slower than with air as the medium, the design of the hydrophone has to be modified accordingly by matching its acoustic impedance in water (Leighton, 1994). An equiresponsive hydrophone pair is used in this system with one utilised for generation and the other for the detection.

It is a device that uses acoustic methods to measure bubble size distribution and void fractions in liquids. The system is known for its durability, simplicity of use, as well as it being quite inexpensive. The ABS is based on the Resonant Bubble Approximation (RBA). This approximation is based upon the fact that bubbles of specific size resonate when insonated by a specific frequency and is related to the 6th power of the radius. Due to this principle the ABS can distinguish between a particle and a bubble and is the only method out of the three that can do it. Most acoustic methods retain this specificity due to the immanent properties of the bubbles.

Microbubbles oscillate linearly upon ultrasonic insonation and if the mechanical index of the insonation ultrasound is high enough, the oscillations become nonlinear which increases the specificity thereby making it more effective for sizing. The acoustic pressure has to be increased to be able to cause a nonlinear response and a compression or expansion which results in the emissions of nonlinear signals and their respective harmonics of the transmitted signal. This also causes the acoustic impedance of the bubble to change with respect to water, improving the signal. This can be thought of as a contrast enhancing effect of the coating on a coated medical microbubble.

The acoustic impedance of an object is a material property and is a product of the speed of sound and the density of the medium and is what determines acoustical properties in the medium. It can be thought to be analogous to the characteristic electrical impedance (Leighton, 1994).

Initially the two hydrophones are placed antipodal to each other with the bubble generator placed in the centre. The transmitter insonates starting from a specific frequency and performing a frequency sweep. This signal may/may not be amplified depending on the conditions. Whilst the receiver amplifies the signal and the data obtained is then inverted by bespoke software provided by the company. A zero calibration reading is taken (analogous to any spectroscopic method). This is taken as P_0 . The production of bubbles causes a change in pressure when the bubble cloud is insonated. This is attenuation and therefore a reduction in the pressure. This change is recorded by the transducers and compared to the initial P_0 case when there were no bubbles being produced.

Short bursts of monophonic frequencies are used at particular intervals and received by the receiving (acquisition) hydrophone.

The bubbles resonate at a certain frequency of sound and there is a pressure loss associated due to the presence of a bubble. There is a reduction in the pressure generated due to the presence of bubbles. This difference between the waves when there are no bubbles present and when there are bubbles present is known as attenuation and is used for the inversion to garner the bubble size distribution.

Figure 21 shows a schematic of the acoustic bubble spectrometer and the corresponding set up.

The hydrophones are placed opposite each other and the bubble cloud is placed in the centre. Each hydrophone pair is composed of equiresponsive transmitters and receivers. A series of frequencies (post amplification) are transmitted across the transmitting hydrophone for a no-bubble and then a bubbling phase. The receiving hydrophone then receives the signal and amplifies it which is then mapped onto what becomes the bubble size distribution.

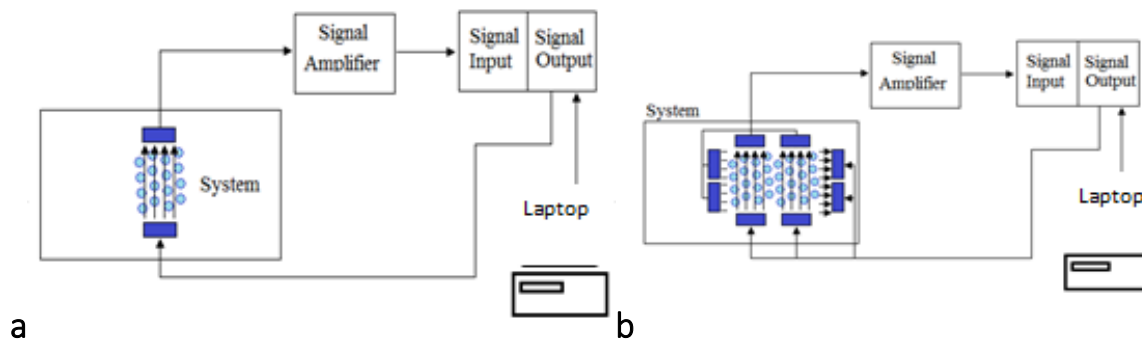


Figure 21 Schematic of the Acoustic Bubble Spectrometer (a) Stereophonic System (b) Octaphonic System.

The ABS provides continuous results and is extremely specific to bubbles. This near real time size distribution makes it a convenient system to use. The ABS with an octaphonic system, due to the four pairs of hydrophones, can infer, after sufficient optimisation, a comprehensive size distribution depending on the hydrophones being used, between 10 μm and 2 mm. The quadraphonic system has 4 pairs of hydrophones, with resonant peaks at 50 kHz, 150 kHz, 250 kHz and 500 kHz. They are driven from 5 kHz to 1000 kHz thereby helping garner a bubble size distribution between radii 3 microns to 600 microns. According to Wu *et al.* (Wu and Chahine, 2010), void fractions of up to 3×10^{-3} can be measured and this has been verified whilst conducting this study.

Although expertise is required to solve problems or use the product beyond the scope of what has been described, the GUI makes it easy to use provides opportunities to expand the repertoire of the system. Skewed results are obtained if bubbles stick to the surface of the hydrophones and since the hydrophones need to be placed in the liquid, even small imperfections act as large centres for bubble coalescence. Therefore the hydrophones need to be regularly wiped and cleaned using water (Stride, 2008).

The distinct advantage of acoustic methods over photonic and optical ones is that bubbles in liquids are more transparent to acoustic waves than to optical ones. The ABS and any other acoustic technique are easier to use with other liquids especially ones which are not transparent to light. Liquids are much more transparent to acoustic waves than to light (G.L. Chahine, 2001).

However, since the hydrophones are quite sensitive and need to be carefully handled, they need to be suitably protected. Large liquid samples can be used with the ABS. Depending on the hydrophone material and the amplification, in theory; the ABS can be used even for large scale industrial process for engendering bubble size distributions without any problems such as in fermenters, bioreactors and large tanks. For small chambers, with appropriate matching, the hydrophones can be placed outside the tank, in an ambient fluid, and measurements can be made to determine the bubble size distribution.

It can measure the sound speed of the medium and this can be used to determine the viscosity or density of the said medium. It can be modified to detect particles by simple attenuation of the signal to detect impedance as well although it will not be as effective and careful calibration would be required. Since this method does not require a transparent tank, it can be easily placed in a free flowing system or in large industrial pipes in order to garner the bubble size distribution. It can be used in a reactor or a sparger in order to determine the bubble size distribution.

Breitz *et al.*, (Breitz and Medwin, 1989) have shown that an *in situ* measurement of bubble spectrum under breaking waves is possible. With sufficient modifications, this could be replicated using the ABS.

Photonic Methods

This is the most common method used in particle sizing aside from optical imaging. Photonic methods are incredibly effective in terms of accuracy and range of the size distributions for small samples. The accuracy of photonic methods reduces for bubbles as compared to particles due to the immanent property of the bubble and the total internal reflection by bubbles upon illumination as compared to particles. Bubbles have the possibility of total internal reflection and bubble opacity is not high which means that the diaphanous behaviour exhibited by the bubbles affects the laser diffraction and scattering. Particles and bubbles interact with light (and sound) in three ways: absorption, emission and scattering. Assuming that the particles are spherical, the intensity of the scatter is measured and the bubble size distribution is inferred using Mie theory. The scatter is dependent on the size of the particles and the intensity on the number of particles.

A bubble can be thought of as a dielectric sphere and an air filled bubble, with water as a medium fits into this category. Mie theory describes diffraction, refraction and reflection (internal and external). Diffraction cannot tell the difference between a particle and bubble since it is independent of particle properties whereas refraction and reflection are dependent on the type of particle and its refractive index, although this property is fairly difficult to measure effectively. When light passes through a particle with an angle of incidence = 0° , there is no change to the incident light. However at all the other angles the three effects can be observed depending on the angle of incidence and total internal reflection is observed for incident angles above the critical angle. Different devices using the photonic methods for particle sizing has been collated by Xu(Xu, 2001). There are plenty of devices that use this phenomenon for particle sizing. Many of them produced by a single company - Malvern Instruments. They have the Mastersizer that uses laser diffraction for particle analysis and for ranges between $0.01 \mu\text{m}$ to $3500 \mu\text{m}$, the Zetasizer, the Resonator and Spraytec amongst others.

Although Malvern Instruments Spraytec has not traditionally been used for obtaining bubble size distribution, Tesař *et al.*, (Tesař, 2012) has used the system for that purpose.

Malvern Spraytec

According to Malvern Instruments, Spraytec uses dynamic light scattering as a principle, and has a range using the 300mm lens between $0.1 - 900 \mu\text{m}$. $Dx(50)$: $0.5 - 600\mu\text{m}$. It is able to measure the aerosol size distribution via laser diffraction. The system measures droplet size distributions and requires the angular intensity of light scattered from a spray to be measured as it passes through a laser beam. This scattering pattern is first recorded and then analysed using a Fraunhofer and Mie scattering to yield a size distribution. Complete resolution of the size dispersion has been obtained through optimisation as well as using a patented multiple scattering algorithm ensuring up to 98 % obscuration (Spraytec, 2013).

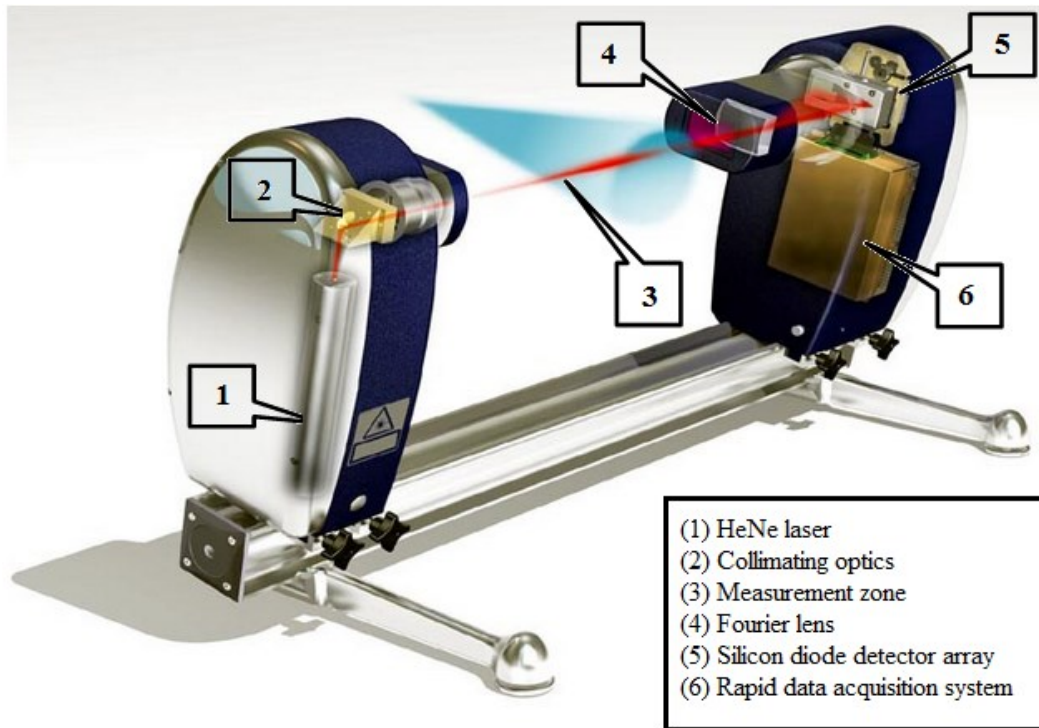


Figure 22 Spraytec Schematic (Spraytec, 2013)

Figure 22 shows a schematic of the Spraytec system. Two lasers are placed antipodal to each other with the test cell placed in the centre. This was a modification made to the original set up as the usual method for measurement is spraying it in the space between the two lasers. Each laser has a lens configuration capable of acquisition at 300 and 750 mm lens and the Mie inversion help helps determine the bubble size between 100 nm and 2000 μm . He-Ne laser is used and the receiving lens adjusts itself and has a self-correcting calibration system for alignment. Alignment is extremely important here and accounts for major errors and inconsistencies if not performed accurately which is why it has a separate collimator as well as an auto alignment feature embedded in its protocol. The lens and laser systems are placed with collimating optics so that there is a small area of interest being measured. The distribution of interest is placed in the middle and zero condition and active principle are recorded. The dispersion due to sample present creates the size distribution and the rapid data acquisition system ensures continuous generation of a bubble size distribution.

The modification made here was to use a glass cell for bubble measurement and using a macro provided by Malvern Instruments to account for changes in refractive index.

Many features of the Spraytec help make it a very useful and easy system to work with. Arguably the best feature of this system is its ability to capture the spray dynamics of the system and how the size changes with time. The results are instantaneous and the analysis performs statistical averaging to provide with accurate results. Bubbles are droplets with the phases inverted. Therefore the Spraytec can be used for bubble size measurements as well.

Cloud bubble sizing might be a difficult phenomenon for laser diffraction techniques since the bubbles would be diffracting far more than a particle and there is a possibility of total internal reflection in a bubble. Since this principle depends on light diffraction and not a property exhibited specifically by bubbles alone, it cannot differentiate between a bubble and a particle. It is also affected by the diffractions caused by bubbles and particles in its vicinity and therefore some bubbles might be 'hidden'. This is less prominent in the acoustic wave due to the large size of the wavefront. This gives rise to some errors in measurement. Photonic methods depend on the liquid being transparent to the wavelength of light but need not be transparent in the visible region. This gives an advantage to the photoacoustic methods over optical methods.

Arguably, there are lesser assumptions to be made whilst inverting the function since a laser is almost a monochromatic point source whereas acoustic waves being generated would not be that precise. However it is the inversion of the same integral that makes this problem significantly difficult (Riefler and Wriedt, 2008). Photonic methods and acoustic methods require an inversion of the ill posed inversion of the Fredholm integral. Malvern has provided with an excellent GUI and offers a distinct advantage in terms of simplicity of use and requires very little training.

As stated earlier, Spraytec depends on two theories, Fraunhofer approximation and Mie theory.

One of the simplest theories used in particle sizing through laser diffraction is the Fraunhofer approximation. This model predicts the scattering pattern that is created when a solid, opaque disc of a known size is passed through a laser beam. This means that it is imperative that the transmission of light through the particle is assumed to be zero. For a bubble, that never happens. This model is satisfactory for large particles (over 50 μm diameter) but it does not describe the scattering exactly. The Fraunhofer approximation is no longer used a lot due

to the assumptions which do not necessarily hold true for particles. However, they do hold true for bubbles. Spraytec utilises both Fraunhofer approximation and Mie theory which makes it quite a comprehensive method.

The particle is much larger than the wavelength of light employed. ISO 13320:2009 defines this as being greater than 40 times the wavelength of incident light (i.e. 25µm when a He-Ne laser is used). The other approximation is that all sizes of particle scatter with equal efficiencies. That is not true since bubbles especially scatter more than particles. The particle is opaque and transmits no light is also not true for a bubble.

These assumptions do not hold true for all cases and makes this approximation valid over a few range of substances. This is why Mie theory was utilised which made an assumption that all the particles are spherical. For bubbles smaller than a 1mm, this approximation holds true and is also used for the resonant bubble approximation used in the ABS.

It is however required to know the refractive indices for the material and medium and the absorption part of the refractive index must be known or estimated. These can be estimated for most substances and for bubbles, it would be comparatively a simpler prospect.

Photonic methods along with optical methods have the problem that they cannot differentiate between particles and bubbles. MagIntyre *et al.* (Magintyre, 1986) has demonstrated that laser diffraction is not very effective for obtaining bubble size distributions and that the particles and bubbles are not differentiated and introduced errors in measurement. A time based study can be performed for the bubble size generated. This transient studied can be used for several things including work that requires. Particle and droplet sizing can be easily garnered as it has been specifically designed for these phases.

Spraytec is used for particle sizing and hence the results are in ppm. The concentration in ppm is found out by inference from the absorbance of a medium using the Beer Lambert law. This law expresses the ratio of transmitted intensity and incident intensity when a laser is passed through a surface of absorbance α and through a distance of b where the ratio of I_0 and I is known as the Transmittance, T .

$$\alpha = -\frac{1}{b}Ln\frac{I}{I_0} \quad - \text{(Equation 20)}$$

The concentration and size of the distribution can be determined from α via the Mie theory using

$$\alpha = Q_i \pi r_i^2 n_i \quad \text{-(Equation 21)}$$

Q_i is the efficiency of light extinction (by scattering and absorption) and is calculated from Mie theory for a bubble of radius r_i . It is dependent on the bubble and the dispersant medium i.e. specific for a bubble. The second term is the cross-sectional area of the bubble and the final term n_i is the number of bubbles of radius r_i .

The volume of a n bubbles is given by

$$V_i = \frac{4}{3} \pi r_i^3 n_i \quad \text{-(Equation 22)}$$

Resulting in the absorbance as

$$\alpha = \frac{3}{4} \sum \frac{Q_i V_i}{r_i} \quad \text{-(Equation 23)}$$

The size of the bubbles is expressed by the diameter d and the volume is divided into a relative volume distribution u and a total concentration C_V .

$$C_V = -\frac{2 \ln(T)}{3b \sum \frac{Q_i \theta_i}{r_i}} \quad \text{-(Equation 24)}$$

Concentration is measured in parts per million (ppm).

If d is measured in μm and b in mm, and u is the relative concentration of the size distribution (such that $\sum u_i = 1$) then:

$$C_V(\text{ppm}) = -\frac{2000 \ln(T)}{3b \sum \frac{Q_i \theta_i}{r_i}} \quad \text{-(Equation 25)}$$

The bubble size distribution u_i is the relative volume of element i with mean diameter d_i .

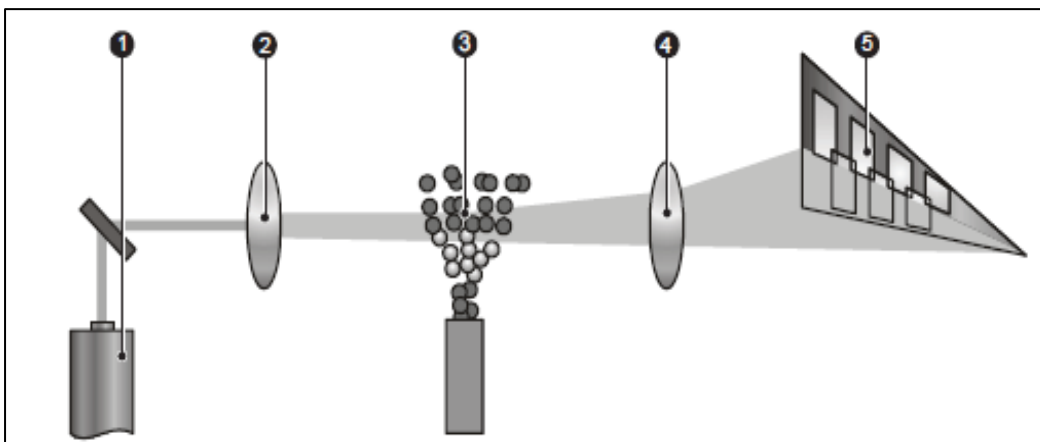


Figure 23 Fundamentals of Spraytec measurement (Spraytec, 2013)

Figure 23 represents the fundamentals of Spraytec measurement.

- Light from the laser 1 is scattered by the bubbles 3.
- The laser beam is expanded by the collimating optics 2 to provide a wide parallel beam.
- The scattered light is focused by a focusing lens 4 in a Fourier arrangement and picked up by the detector array 5.
- Unscattered light passes through the pinhole at the centre of the detector array. This is measured by the beam power detector.

Figure 24 demonstrates the principle of Spraytec and how the diffraction angle, being inversely proportional to the bubble size is responsible for obtaining the bubble size distribution.

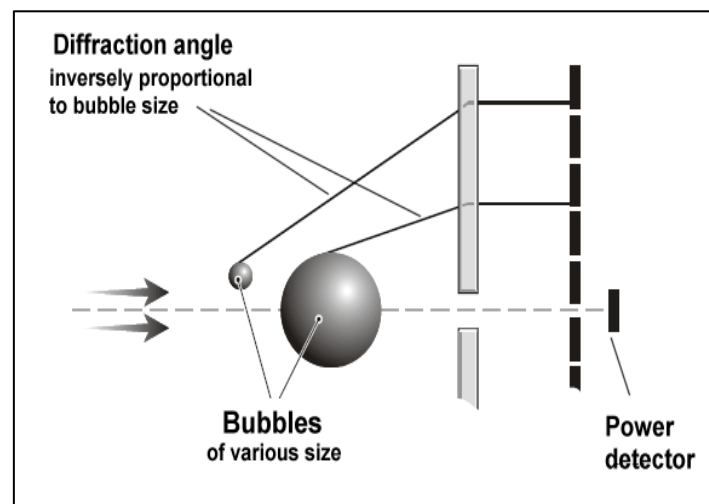


Figure 24 Measuring the angle of diffraction determines the size of the bubble (Spraytec, 2013).

Further to this, statistical methods need to be discussed since they are used in conjunction with any indirect forms of bubble size measurement.

Statistical analyses

Size distributions have been expressed in terms of number averages and void fraction averages. The number average is a simple average based on the number of bubbles. The concentration/ void fraction average is based on the volume occupied by the bubbles and

signifies transport phenomena associated with them. In particle sizing and bubble sizing by extension, there are several methods to look at a bubble size distribution. In this case it is seen that there are quite a few larger bubbles in the constant flow than the oscillatory flow. The number of bubbles for steady state flow seems to be less than the FO mediated bubbles for the smaller sizes. However, for the bigger bubbles, more are produced by the constant flow and contribute a very high amount to the bubble size distribution due to the effect of the volume on the average sizes. The volume of a larger bubble has a much higher effect than the smaller bubble on the bubble throughput. Therefore a bubble of 1 mm size has a 1000 times greater impact in terms of volume than a 100 μm bubble. This means that a thousand 100 μm bubbles would need to be produced to have the same volume as that of a single 1 mm bubble. Therefore, the bubble number and size distribution would be skewed due to this. Consider 1000 bubbles each of diameters 1 μm , 100 μm and 500 μm . Their number contribution is the same whereas their volume contribution is much higher and can be seen in Figure 25

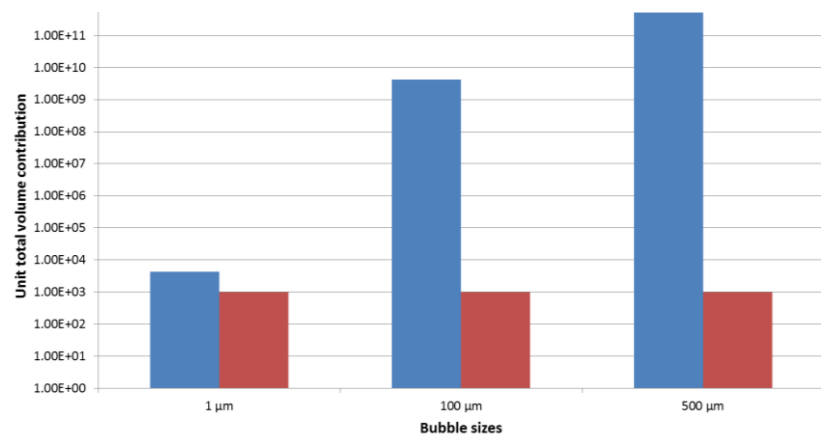


Figure 25 Effect of volume contribution and number contribution

Number mean is important when only the number of bubbles/particles is of interest. This is used when the number of bubbles is more important than obtaining the size.

Average bubble sizes vary with the particular data set being observed and are equally dependent on the analysis. However, this is amplified due to the change in the bubble dynamics. Single bubble generation would not be a problem since both the values are fairly close to each other since the variance is lower. However, for cloud bubble dynamics these effects become prominent.

Using these values would result in such a large difference in bubble sizes for just 1000 bubbles. When it comes to over 1,000-100,000 times that, even with a narrower size distribution, it would still result in large variances in bubble sizes depending on which method is used. For mass and heat transfer, it would generally be more appropriate to use void fraction for average bubble size for large sample sizes i.e. cloud bubble dynamics especially when dealing with transport phenomena.

Two factors are readily computable for the bubble size analysis obtained from the ABS- average bubble size in terms of number of bubbles and average bubble size in terms of void fraction contribution (volume contribution) of the bubble. Depending on the application, bubble sizing is usually reported using either of these two factors. Since volume contributions (due to their association with increased transport phenomena for microbubbles) are more relevant for a majority of industrial processes, this chapter discusses bubble sizes in terms of volume fraction contributions.

Error! Reference source not found. provides an exemplar for a case wherein there are 3 classes of bubbles – Class A- with a size of 1µm and 600 in number, Class B with size of 100 µm and 200 in number and Class C of size 500 and 200 in number. This would lead to a total of 1000 bubbles. The surface area and volume of the bubbles are computed. The bubble size can be computed by either using average bubble size in terms of numbers i.e. weighted bubble size divided by total numbers, or in terms of average bubble size in terms of volume contribution i.e. weighted bubble volume divided by total bubble volume.

Average bubble size in terms of number:

$$N_{av} = \sum_{i=1}^n \frac{n_i x_i}{n} \quad \text{(Equation 26)}$$

where n is the total number of bubbles, n_i is bubble contribution for each bubble of size x_i .

The average bubble size in terms of volume contribution is

$$N_{vc} = \sum_{i=1}^n \frac{n_i V_i}{nV} \quad \text{(Equation 27)}$$

with

$$V_i = \frac{4}{3} \pi x_i^3 \quad \text{(Equation 28)}$$

where n is the total number of bubbles and n_i is the bubble contribution for volume of each bubble of size x_i represented by V_i

Table 1 Exemplar

S.No.	Bubble	Size	Number	Volume of individual bubble	Total Volume Contribution	Surface Area	Total Surface Area	Surface Area/Volume
1	A	1	600	5.24E-01	3.14E+02	3.14E+00	1.88E+03	6.00E+00
2	B	100	200	5.24E+05	1.05E+08	3.14E+04	6.28E+06	6.00E-02
3	C	500	200	6.54E+07	1.31E+10	7.85E+05	1.57E+08	1.20E-02
			1000		1.32E+10			
N_{Av}	120.6	N_{Vc}	200	μm				

This also means that 1 million 1 μm bubbles would be required to occupy the same volume as a single 100 μm bubble. This brings about a massive disparity in bubble size in terms of volume contribution. However, the volume contribution would be a useful tool for estimating any transport phenomena exercise over number contribution.

Generally speaking, bubble size distributions obtained from membranes are narrow and the difference in the two averages is lower. A large difference in bubble sizes is observed for a highly dispersed distribution and it is beneficial to the system to have a narrower size distribution. This exemplar demonstrates how these two values need not be the same and their dispersity results in the width of the bubble size distribution.

The analysis utilises certain values used for calculating the different types of diameters and these values are known as moments.

The Volume mean diameter is known as $D[4,3]$ and is also known as the third moment whereas the surface area mean diameter is known as $D[3,2]$ and is called the Sauter Mean Diameter.

These are well known and used in particle sizing and can be found in Allen(Allen, 1996) , Xu (Xu, 2001)and Merkus(Merkus, 2009)

The Specific Surface Area is the total area of the particles divided by their total weight.

Percentiles have been commonly used in particle sizing that determine the portion of particles which lie below or above the said percentage.

Those used with particular emphasis are – Dx(10), Dx(50) and Dx(90).

These values are also used to calculate the span of a bubble size distribution which is actually the width of the size distribution. This is done using

$$\frac{Dx(90)-Dx(10)}{Dx(50)} \quad \text{– (Equation 29)}$$

Percentiles become important in order to characterise the histogram and size distributions.

All of these values can be found in the British Standard BS2955:1993 or the ISO 13320:2009.

Microbubble Stripping – Separation Phenomena

The Ammonia Problem

Ammonia is a unique problem when confronted with separations mediated by microbubbles. Whilst ethanol-water separations are easily separated based on a temperature gradient (Zimmerman *et al.*, 2014, Abdulrazzaq *et al.*,2016), such is not the case for ammonia-water separations.

Ethanol has a boiling point of 78°C and Water has a boiling point of 100 °C. Using microbubbles at 85 °C does not seem to be too unreasonable as temperature gradients can be used to preferentially vapourise ethanol over water. Ammonia has a boiling point of -34 °C. This would pose no problems at all for separation via a temperature gradient. However, the close affinity for ammonia to remain in solution with water forming a hydroxide is what causes a lot of problems for separation and the solubility for ammonia is very high. This chapter was designed to trial the hot microbubble injection in thin liquid layers in order to recover the ammonia. The concentration and temperature gradient would be the driving force here resulting in a competition between mass transfer of ammonia and dewatering, which is the hypothesis of the chapter.

Many parts of the world, now, feature a substantial surplus of ammonia. Following the invention of the Haber–Bosch (Haber, 1920) process it has been possible to produce ammonia in large quantities relatively cheaply and has transformed industrialised society and world population. The expansion of the global population from 1.6 billion people in 1900 to the current 6 billion would not have been possible without the synthesis of ammonia. (Smil, 2004) Growing world population has led to an increase in production of world municipal waste. Ammonia produced at 140MT per annum (Kelly, 2014) comprises 2% (Licht *et al.*, 2014) of the global energy consumption. This figure will only rise due to the multitude of uses and demand for ammonia. Ammonia is an essential precursor to fertilisers, pharmaceuticals and commercial cleaning products (Walton, 1973). Yet, its production via the Haber process requires a source of hydrogen, commonly from steam reformation of hydrocarbons which may or may not be renewable (Amin *et al.*, 2013). In particular, the widespread use of ammonia and its derivatives as agricultural nitrogen fertilizers has substantially increased emissions of ammonia to the atmosphere, leading to a wide range of different environmental problems (Sutton *et al.*, 2001, Erismann *et al.*, 2008, Erismann *et al.*, 2007). Half of industrial ammonia production is eventually lost to the global environment with significant effects (Erismann *et al.*, 2007). Sutton *et al.* (Sutton *et al.*, 2008b) provide a fascinating account of the history of ammonia.

The present nitrogen and ammonia surplus, especially in Europe, China and North America, contrasts strongly with a shortage in many parts of Africa and historically. Recovery and re-use are imperatives for these multiple uses including energy storage (Kitano *et al.*, 2012, Schüth *et al.*, 2012, Zhang *et al.*, 2015).

Ammoniacal nitrogen discharges from municipal, industrial and agricultural wastewater sites, which subsequently mixes into water resources (Sutton *et al.*, 2008a). For example, in China, about 80% of NH₃ emission is from agriculture (Ianniello *et al.*, 2010). In China, the biggest contributors are livestock (which contributes about 30%–60%) and the application of nitrogenous fertilizer (which contributes about 17%–47%), followed by 20% for energy, 1% for poultry and 2.5% for human beings (Ianniello *et al.*, 2010) and contributes to about 8.5Tg per annum (Huang *et al.*, 2012). Specifics for each faunal source are detailed in a study by Dianwu and Anpu carried out in 1994 (Dianwu and Anpu, 1994).

For NH₃ the estimated global emission for 1990 was about 54MT N year⁻¹. The major sources identified include excreta from domestic animals and wild animals, use of synthetic N fertilisers, oceans and biomass burning. About half of the global emission comes from Asia, and about 70% is related to food production (Olivier *et al.*, 1998, Murano *et al.*, 1995).

According to more recent studies (Paulot *et al.*, 2015, Liu *et al.*, 2014, Huang *et al.*, 2012), one of the consequences of greater anthropogenic nitrogen fixation is an increase of ammonia (NH₃) emissions to the atmosphere, with recent estimates suggesting that anthropogenic sources, primarily agriculture, account for over 70% of global ammonia emissions -65 Tg per annum. This agrees with growth from the estimated emission from EDGAR to be at 54 Gg per annum in 2010 and the rate of ammonia emission increase is equivalent to 621.6 Gg NH₃-N/year (Behera *et al.*, 2013).

A study conducted based on census data in 1993 in the UK determined that about 197kt per year of NH₃-N was emitted every year in wastewater due to UK agriculture with estimates increasing to 226kt per year based on the 1997 census data (Misselbrook *et al.*, 2000). Non-agricultural sources are detailed in a study performed by Sutton *et al.* (Sutton *et al.*, 2000).

Wastewater emissions of ammonia as per the EU Commission's EDGAR database, maps out the global ammonia emission for wastewater and biosolids.

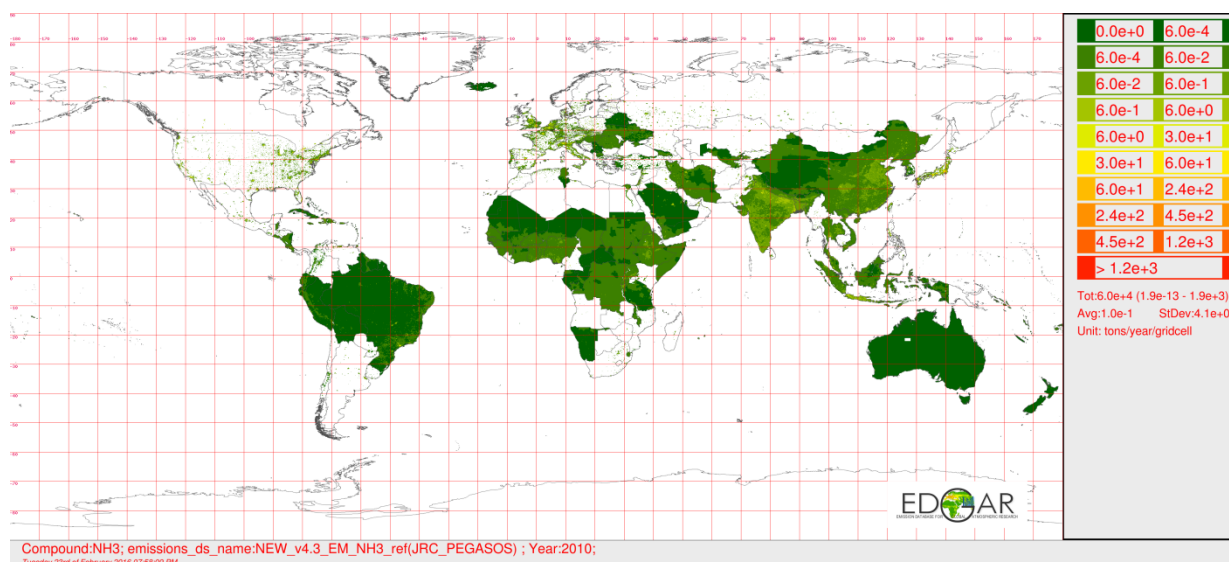


Figure 26 Global ammonia emissions from wastewater - courtesy EDGAR EU Commission

(http://edgar.jrc.ec.europa.eu/gallery.php?release=v431_v2andsubstance=NH3andsector=SWD)

Water, contaminated by ammonia and having a high concentration of ammonia must be treated prior to human consumption. Additionally, sewage water contaminated by ammonia needs to be remediated as it affects groundwater and seawater equally perniciously.

The most widely used methods for ammonia removal from wastewaters are adsorption, chemical precipitation, reverse osmosis, air stripping, ion exchange, breakpoint chlorination and biological nitrification and denitrification (Metcalf *et al.*, 2002).

Ramifications for ammonia release for source separated Municipal Solid Wastes (MSW) are quite acute, with ammonia being released 0.2-8.6 kg NH₃ per Mg of organic fraction of MSW. (Colón *et al.*, 2012) 60% of a typical MSW is composed of organic fraction (Lin *et al.*, 2013).

Advanced oxidation processes (AOPs) often used to destroy ammonia include direct photo oxidation (Capodaglio *et al.*, 2015), ozone oxidation (Hoigne and Bader, 1978), photocatalytic oxidation (Zhu *et al.*, 2005, Xiao and Liu, 2014) electrochemical oxidation (Wang *et al.*, 2012, Li and Liu, 2009, Zöllig *et al.*, 2017, Bunce and Bejan, 2011, Gotvajn *et al.*, 2009) and using ozone microbubbles (Khuntia *et al.*, 2012, Liu *et al.*, 2010). In the oxidation process, the end product is nitrate which is more toxic to aquatic life (Behera *et al.*, 2013, Akunna *et al.*, 1993, Liu *et al.*, 2010).

Even with so many treatment methods available, there is a large market gap due to the disadvantages posed by these methods. Since they require chemical addition, post-remediation clean up, further downstream processing, longer maintenance cycles and associated downtime, as well as high levels of secondary contaminants which make these processes arduous and expensive, they are not viable solutions. They also destroy the ammonia rather than recover it. They encounter further separation issues and suffer from fouling very readily. They can only handle certain ranges of ammonia in the system and cannot be controlled easily. Physico-chemical methods used for ammonia recovery also face severe limitations. One of the major methods used to recover ammonia is industrial air stripping, which is capital intensive but has been well characterised and understood. It is feasible to reduce the ammonia level to 15 mgL⁻¹ but special requirements of the process such as water temperature of over 15°C, requirement of non-freezing conditions and carbonate deposition are disadvantages of this system (Viotti and Gavasci, 2015). There is also the disadvantage that initial concentration for wastewater ought to be 100mgL⁻¹ for high

levels of separation, otherwise other carrier gases are required such as CO₂ and steam stripping or biological methods (Agency, 2000). Both physico-chemical and biological technologies have been applied for the ammonia recovery or remediation from ammonia rich liquors and wastewaters. Stripping with CO₂ as a carrier gas has resulted in stripping of ammonia at pH of 8, which is not possible by air stripping (Bonmatí and Flotats, 2003, Lei *et al.*, 2007).

Ammoniacal nitrogen, NH₄-N (a measure for the total amount of ammonia in both dissociated and undissociated forms) is produced by the decomposition of proteins (Lees, 2012). Most ammonia rich wastewaters are found in ranges of concentrations typically from 50 mg L⁻¹ - 2,200 mg L⁻¹ (Liao *et al.*, 1995, Vlyssides *et al.*, 2002, Uygur and Kargi, 2004, Mohibah Musa *et al.*, 2013, Yuan *et al.*, 2016a, Yuan *et al.*, 2016b). Some wastewater such as digestate can go as high as 5,000 mg L⁻¹ (Lin *et al.*, 2009).

Since there is no biological or innate mechanism by which the ammonia can be treated in the leachate, the ammonia levels keep increasing over time, and need to be specifically targeted and remediated in order to treat the liquor. Unlike sulphur containing compounds, there is no natural destruction of ammonia in a landfill site (Kabdasli *et al.*, 2000).

Ammonia toxicity takes place in any water source and even a small amount is harmful for flora and fauna (2 ppm). The ammonia turns the water alkaline and eutrophies lakes whilst providing a nitrogen source to algae which can lead to an algal bloom. Landfill sites contain valuable resource in the form of organic matter which can be decomposed by methanogenic bacteria in order to generate biogas. However, it is beneficial to have a higher solids loading in the system so that greater amounts of methane (a valorisable gas) can be generated. Ammonia being an inhibitor for bacterial action reduces the generation possibility and reduces the capability of SBR treatment for methane generation. The ammonia levels then need to be reduced by watering them down till they are no longer inhibitory and actually act as a nitrogen source (Monlau *et al.*, 2015). Using this approach, if correctly implemented, (Robinson, 2005) estimates a 0.9% of energy production supplemented from landfill sites and biogas/landfill gas collection and utilisation.

The Council Decision 2003/33/EC commits the UK to limits stated in SI 1998/389 and SI 1997/2560 and lists pollutants into 2 categories. List I includes the most dangerous pollutants

and list II includes controlled pollutants. $\text{NH}_4\text{-N}$ is listed as a list II pollutant, but thought of to be the most important component of wastewater in the long term (Burton and Watson-Craik, 1998, Marttinen *et al.*, 2002, Bernard *et al.*, 1997, Slack *et al.*, 2005). It is also highly likely, the reason behind the high toxicity of wastewater (Kjeldsen *et al.*, 2002, Robinson and Grantham, 1988, Robinson, 2005).

Physico-chemical processes were compiled to collate the best methods to be used for ammonia recovery and a literature map was generated as seen in Figure 27. Various physico-chemical methods for separation of ammonia (Table containing data points in the appendix). The green box delineates what would be an appropriate region to operate at – time of 24 hours and removal efficiencies from 50- 100%).

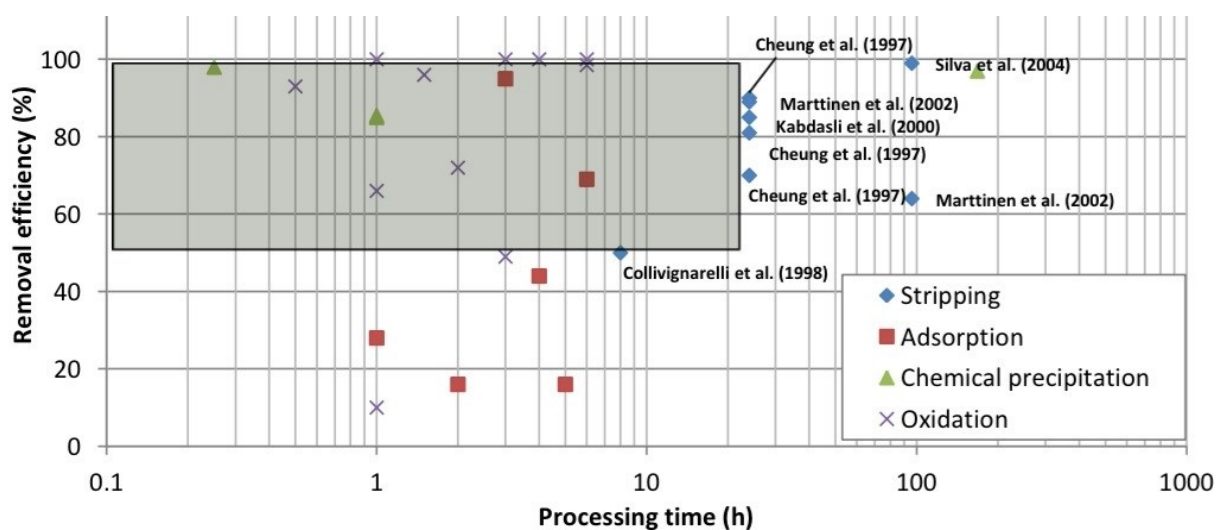


Figure 27 Mapping out the literature (Turley, 2015; Desai *et al.*, 2018)

Nitrogen removal from swine manure by ammonia stripping was also shown to be quite slow by Liao *et al.*, with 90% removal taking over 7 hours of processing time and 95% taking over 100hours (Liao *et al.*, 1995). One of the other disadvantages of using stripping columns is the rapid degradation in performance due to scaling problems on the wall (Viotti and Gavasci, 2015). Some other papers have discussed costing and design along with performance data for air stripping columns (Dzombak *et al.*, 1993, Little and Mariñas, 1997, Nirmalakhandan *et al.*, 1993, Onda *et al.*, 1968). This graph has ignored methods which involve considerably high

process economics such as (Xingjian Jiang 2015, Lin *et al.*, 2009, Ozturk and Bal, 2015, Luo *et al.*, 2015, El-Bourawi *et al.*, 2007, Ding *et al.*, 2006, Bohdziewicz *et al.*, 2001).

Microbubbles (bubbles sized between 1 μ m and 1000 μ m)(Parmar and Majumder, 2013) exhibit extremely high rates of transfer (heat and mass) with capabilities for phase separations with limited change in liquid temperature *i.e.* limited sensible heating(AlYaqoobi *et al.*, 2014, Zimmerman, 2014, Abdulrazzaq *et al.*, 2015, Al-Mashhadani *et al.*, 2015, Zimmerman *et al.*, 2013). These have been used for simple liquid separations such as Ethanol-Water with ethanol having boiling point 78°C and water with boiling point 100°C. This is a fairly simple separation in terms of temperature difference and volatility.

The seminal paper and subsequent patent by (Zimmerman *et al.*, 2013b, Zimmerman, 2014) associated with microbubble mediated transport phenomena demonstrated phase separations with limited sensible heat transfer.

The major problem associated with this process was the long processing time and the lack of appropriate heat transfer increase, and limited throughput possible for use with the system. This was a serious drawback as it would limit its usability.

Bubble mediated heat and mass transfer has been studied by (Sinnott and Towler, 2009, Coulson *et al.*, 1999, Green and Perry, 2007). Bubble columns have long been known and modelled previously and exist in classical textbooks in chemical engineering(Bird *et al.*, 2007, Incropera *et al.*, 2007, Joshi *et al.*, 2017, Amol A. Kulkarni 2005, Bhaskar N. Thorat, 2001).

(Campos and Lage, 2001, Campos and Lage, 2000b, Campos and Lage, 2000a) have finished some modelling work on bubble associated transport properties. Empirical studies on bubble associated transport properties, especially heat transfer have been recently conducted (Narayan *et al.*, 2013)

However, this work has been for larger bubbles and not microbubbles. (Hikita *et al.*, 1981, Saxena *et al.*, 1992, Heijnen and Van't Riet, 1984, Kantarci *et al.*, 2005, Deckwer, 1980, Gandhi and Joshi, 2010, Wu *et al.*, 2007).

Zimmerman *et al.* , performed the seminal theoretical study on microbubble associated transport phenomena leading to a novel understanding of the evaporation dynamics of

microbubbles (Zimmerman *et al.*, 2013b) and the existence of the trade-off between sensible heat transfer and evaporation (paying for the latent heat) at the phase interface. The approach of heating the gas instead of the liquid, which would lead to low energy density bubble generation, would lead to a significant change in separation phenomena associated with microbubbles. The modelling work had several assumptions.

The major assumptions of this model include a monodisperse microbubble population, equal throughput across the membrane, no effect of bubble wake on the bubble previously released, immediate heat transfer to the bubble such that the gas temperature is the same as the bubble temperature, no temperature change of the gas on volume expansion and for bubble transfer, and no heat transfer externally into the liquid. These assumptions cannot be made for an experimental process, and they were recorded as much as possible for the experimental work and the process design for microbubble stripping.

The findings from this paper suggested that the bubbles provided the latent heat to the liquid such that evaporation would be the dominant feature instead of sensible heating. This is counterintuitive but possible due to the uniquely high internal mixing rates for the microbubbles, and the subsequent low rise velocities (calculated by either Stokes rise velocity or by the Hadamard-Rybcynski equation ((Hermes, 2012, Hadamard, 1911) depending on the bubble size) would result in a very high mass and heat transfer rate within a short interval of a few bubble rises. This then follows, that 100% relative humidity is achieved, followed by sensible heating and vapour recondensation. The two stages comprise of an evaporation dominant step followed by the vapour recondensation step for which, the control parameter can be the liquid height above the bubble engendering surface (sparger/diffuser).

The height of the liquid over the bubble engendering surface is determined such that the bubble collapses at the surface when the concentration is maximal.

A performance parameter, α , was defined by (Zimmerman *et al.*, 2013a, Zimmerman *et al.*, 2013b) as follows:

$$\alpha = - \frac{c^*(T)}{N_{TOT}/V} \frac{\Delta H_v(T)}{\int_{T_\infty}^{T^0} c_{p,gas} dT'} \quad - \text{(Equation 30)}$$

Where: $c^*(T)$ = saturation concentration for the average temperature of the bubble, N_{TOT} = total number of moles of gas at a time, V = volume of the bubble, $\Delta H_v(T)$ = enthalpy of vaporisation for the average temperature of the bubble, c_p = specific heat capacity of the gas, T_0 = initial gas temperature, and T_∞ = bulk liquid temperature.

α helps calculate the fraction of excess enthalpy which is used for vaporisation, and an α value which is significantly larger than 0.5, represents mass transfer according to Henry's law, resulting in evaporative cooling.

An α value at 0.5 represents when both these processes are equal and this is usually the case for most systems that half the heat is distributed into each process. Using this, if the layer height, and corresponding inlet gas temperature can be chosen such that the process can achieve, preferentially, higher rates of latent heat being 'paid off' instead of sensible heating, the process can result in rapid mixing. One of the major findings of this paper was also the internal mixing observed in microbubbles and the much higher rates of internal mixing as opposed to coarse/larger bubbles. The coarse bubbles tend to have much lower mixedness than a microbubble. Controlling the layer height, gas temperature, liquid properties (temperature, volume, and composition), bubble size, will achieve the requisite isothermal conditions.

Fluidic oscillator generated microbubbles are injected at laminar flow (Zimmerman *et al.*, 2008a) unlike other conventional bubble production methods. The laminar flow decreases the rate of sensible heat transfer but instead favours vaporisation such that the excess enthalpy is split 19:1 between vaporisation and sensible heat transfer. Turbulent flow would lead to a dissipation of the heat very quickly and lead to high levels of sensible heating.

Experiments have been conducted for the evaporation of water and also the distillation of a methanol-water binary mixture using hot microbubbles as discussed previously. They do not compare well with the model unless it is highly idealised. The magnitude of the transfer rates remains the same.

However, it is observed how hot microbubbles have not yet been applied to a mixture where the gas (in this case ammonia), which is to be vaporised/separated, is highly soluble and readily dissociates in the liquid.

Ammonia with water is a different story. Ammonia has a boiling point of -34°C , so why then would it be that difficult to separate it out conventionally?

Ammonia exists in equilibrium with water(Clegg and Brimblecombe, 1989):

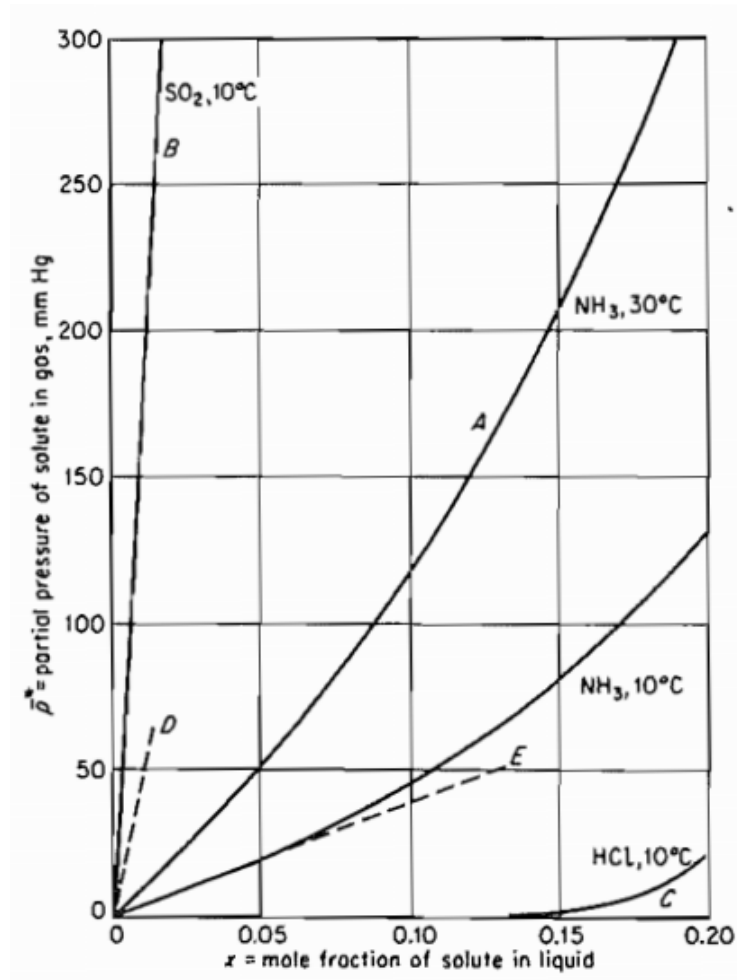


Figure 28 Gas solubility(Treybal, 1980) showing the high solubility of ammonia in water

Consequently an ammonia-water mixture is quite difficult to separate, as temperature differential cannot be used as the major driving force for separation.

Chapter 3 Experimental Section

3.1 Major Assumptions and Major Decisions – Hypotheses

3.1.1 Resonant pulsing frequency effect for much smaller bubble formation with fluidic oscillation

Fluidic oscillation driven microbubble generation has several advantages – it has a low energy cost and demand, no moving parts, low pressure drop, no electrical components, and can be easily retrofitted. Previous work has suggested that each pulse of air would be able to generate a bubble. This would imply that the frequency of the oscillation would determine the number of bubbles formed regardless of the momentum of the impinging jet. However, bubble formation theory depends on the bubble attachment forces and the bubble would detach if the forces were to be balanced. This is not a leap then to say that the amplitude of the jet needs to be higher. This is probably why the fluidic oscillator has been able to show a reduction in bubble size aside from the oscillatory flow dynamics in the system. The fluidic oscillator is a flow amplifier and this results in an increase in the momentum of the jet which aids in overcoming the bubble attachment forces and causes bubble detachment. So why then would the bubble still be larger than the size of the engendering orifice?

The frequency of oscillation that causes bubble generation could be too high which would result in bubble conjunction and coalescence or it could be too low and resemble steady flow or the amplitude could be low enough that the bubbles would conjugate too. Therefore the major hypothesis of this chapter is to artificially increase the amplitude and therefore separate the effects of amplitude and frequency and measure the bubble size thus generated. This should result in a condition wherein all the factors would be appropriately matched and the bubble size would be the smallest there due to no coalescence (or reduced coalescence) and appropriate bubble detachment. This shall be experimented in this chapter.

The usual method for bubble generation using fluidic oscillation is using two outlets connected to a set of bubble generating microporous membranes (aerators) placed under liquid of interest. The entire flow can be utilised for the generation for bubbles and this results in an unvented condition for the fluidic oscillator. Venting this jet, increases the momentum of the pulse post the fluidic oscillator as the oscillator is a flow amplifier. The flow

switches from each leg, and if the momentum of the jet and therefore the pulse strength associated with the jet can be increased whilst maintaining the appropriate flow into the sparger.

However, in order to prove the hypothesis, the flow will be vented in order to generate higher amplitude of the jet and only partially diverted into the diffusers used for bubble generation. This helps in two ways – increases the effect of the oscillatory flow (by virtue of an increase in amplitude by increasing momentum of the wave) in order to observe the difference between discrete oscillatory flow conditions (frequencies) for the lab scale and minimise the bubble coalescence due to the increased momentum imparted to the newly engendered microbubble. This FO mediated oscillation has an amplitude and frequency dependence on the inlet flow rate to the oscillator provided that conditions of *ceteris paribus* are maintained. This proposed addition to the experiment enhances the FO mediated microbubble size reduction. Increasing the amplitude by venting is a way to artificially increase the amplitude of the FO. Additionally, three conditions of feedback will be imposed on the FO by varying the volume of the feedback loop. Whilst the length of the feedback loop can be used to vary the frequency of the FO, the volume of the feedback imposed changes the flow dynamics in the loop and whilst intuitively delaying the onset of oscillation, will impose a greater oscillatory pulse for each switch. This is likely due to the fact that for a larger volume, there is a greater pressure differential generated in the control terminal which will result in an increased amount of jet diversion. This leads to a higher amplitude of pulse for each cycle and a greater 'negative' flow for the OFF pulse of the oscillatory cycle. For a lower feedback volume, the onset of oscillation is hastened as the requisite pressure differential is generated faster. However, upon increasing the flow, the frictional losses across the feedback loop increase and therefore whilst switching does take place, there is a limitation to the parasitic flow that can enter the feedback loop. The switching speed, i.e. the frequency will be higher in this case, but the amplitude of the pulse will be lower. The feedback conditions were chosen here based on the two extremes – the lowest condition that can be used would be – (I.D. 2.5mm, O.D.4mm) and the higher feedback condition would be – (I.D. 8mm ,O.D. 10mm). A medium condition was chosen which was based on matching the ducts for the FO in order to mitigate any effects of volume expansion or compression -

(I.D. 4mm, O.D. 6mm). Two different vent flowrates are used , coupled with these three feedback conditions, at various frequencies in order to test the hypothesis.

Several industrial applications can afford to have gas wastage for a significantly larger bubble throughput concomitant with reduced bubble size, since air, in particular, is not that expensive with respect to the decreased energetics, increase in reaction surface area and lack of maintenance requirements with the no-moving part FO input.

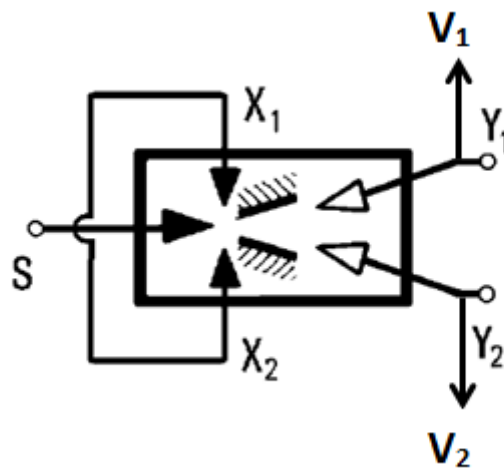


Figure 29 Vented Fluidic Oscillator (adapted from Tesař,2013a) V1 and V2 (vents).

Figure 29 shows the vented schematic of the FO with V1 and V2 acting as the vents to the system. Additional venting ensures that apropos flow can pass through the aerator whilst maintaining the appropriate flow into oscillator in order for it to switch. Additionally, this increases the momentum of the jet and the amplitude of the oscillatory flow.

Conventional bubble formation depends on a host of other factors such as surface energy of the bubble engendering surface and the liquid, liquid and gas viscosity, momentum of the gas, height of liquid, pressure exerted by the system and acting upon it, size of the bubble engendering orifice. These properties can be characterised by dimensionless quantities such as Strouhal number (Sh), Reynolds number (Re) and Weber number and (We). Fluidic devices such as the Tesař-Zimmerman Fluidic Oscillator generate a net positive hybrid synthetic oscillatory jet that results in a specific reduction in bubble size compared to conventional or steady flow as discussed previously.

3.1.2 Inventing the New Oscillator (Desai-Zimmerman Fluidic Oscillator)

The major hypothesis for efficient microbubble generation is that frequency and amplitude are important components and must be considered together. Frequency by itself is not a valid assumption. For a coalescent liquid (distilled deionised water), when the oscillatory pulse leads to bubble detachment, too high a frequency, results in bubble coalescence, too low a frequency results in similar bubble formation characteristics as observed for steady flow bubbling.

Whilst venting is a solution for the laboratory scale and for industrial purposes with high value added components or products, it is not a sustainable solution. This demonstrates that merely increasing the frequency would not result in a size reduction. The 'sweet spot' would be specific to the configuration and flow conditions. This means, for an industrial application, frequency manipulation (plasticity) would be desirable. The Tesař-Zimmerman Fluidic Oscillator (TZFO) has been used for microbubble generation. The TZFO exhibits frequency variation with flow –frequency increases with increase in flow rate and is quite a big change. This can be seen in the change in the sweet spot as well as the frequency response. This would not be an ideal property, especially for industrial applications as flow variation during routine operation is commonplace.

The lack of change of frequency with respect to flow would be a desirable property for an oscillator for microbubble generation.

From these two outcomes, the combination of the frequency elasticity with respect to a control handle and inelasticity with respect to flowrate variations would be ideal combinations for microbubble generation in an industrial application. These features are not present in the TZFO.

An additional requirement is the ability to make controllable waveforms as they would be highly desirable for microbubble generation mediated by oscillatory flow, as crisper waveforms, in fluidics, mean better momentum transfer and therefore lower friction losses. This would result in better bubble pinch-off without the additional energy losses due to the spread of the waveform.

Gap in the literature

There is a *gap in literature* about the use of an oscillator capable of achieving the requirements of the findings from Chapter 4 (Results and Discussions , section 4.1) maintain all the advantageous properties of the TZFO (no-moving parts, generate a hybrid synthetic jet, low pressure drop, ease of frequency control, and lower frictional losses), lower onset of oscillation, and have a higher amplitude of without associated venting. Whilst the previously described oscillators have been developed specifically for microbubble generation, they can achieve some of these points, but not all of them.

The TZFO has been the most extensively used device for microbubble generation and is considered to be extremely effective for the purpose. However, the microscaled TZFO can achieve some advantageous benefits (lower onset of oscillation, higher frequency, higher amplitude) but also present disadvantages such as smaller range of flowrates for oscillation, higher frictional losses, higher pressure drop). Likewise the Hartmann Resonator type oscillator and the Vortex based oscillator lose out on frequency control, gas losses, throughput, and the higher frictional losses and pressure drops associated with the systems.

The Desai-Zimmerman Fluidic Oscillator (DZFO) was invented to encompass all of these points and develop an oscillator capable of generating microbubbles effectively and not face the disadvantages posed by the previously mentioned systems.

The TZFO can be taken as the standard for microbubble generation since the literature deals almost exclusively with the TZFO for microbubble generation.

There were some drawbacks of the TZFO that needed to be addressed.

1. Lower onset of oscillation in order to reduce effective hydraulic losses. This has been discussed as an outcome of Chapter 2 and the motivation for this Chapter.
2. Higher momentum of pulse i.e. higher amplitude for smaller bubble formation. This can be achieved by the TZFO by increasing the flow or the amplification but there is a limit to which this can be done and also increasing the flow, whilst achieving the higher momentum, and results in the problem stated in 1.
3. Reducing friction losses due to the smaller relief features. Mass manufacturability is a significant advantage since most microbubble generating methods are not mass

manufacturable. As discussed previously, the TZFO (and amplified for the microscaled TZFOs) and other jet deflection type oscillators require a control nozzle along with the supply nozzle in order to oscillate. The control nozzle width has to be lower than the supply nozzle width in order to maintain the flow regime. For a standard TZFO, the smallest feature is 700 μm (control nozzle), for a supply nozzle of 1mm. To ensure that the flow switches and bistability is achieved, the flow needs to be switched by selectively flowing across the throat and using the amplification of the deflecting wave in the control nozzle to deflect the impinging wave. It also needs to be slightly stronger than the original wave in order to deflect it.

4. Inability to significantly change the shape of the waveform. The waveform can be changed slightly by extending the curve via geometric changes in order to provide greater inertance to the jet, changing it into a more rectangular waveform but not more than that. Superposition of waves would be possible due to controlled harmonics as seen in Tesař (Tesař, 2013a)

The Desai-Zimmerman Fluidic Oscillator (DZFO) – Major decisions regarding the design

The DZFO was invented based on a new principle as compared to the typical deflection mechanisms discussed earlier about load switching or jet deflection type oscillators.

A load switching oscillator is based on the 'loading' on the system. Therefore, higher the 'loading', lower is the frequency on the system. These typically have a higher backpressure due to the loading imposed on them and have very low deflection frequencies.

Conventional jet deflection type oscillators look like the ones described previously and like both variants - Warren type and Spyropolous type – oscillators including the TZFO.

For a flow to switch, the deflecting wave needs to be stronger than the impinging wave. Typically, this is done by reduction of the size of the control terminal (upto 70%reduction) - e.g. jet deflection type oscillator, inducing a higher pressurisation (load switching capacitive approaches such as Zalmanzon and TCFO), and using mechanical switching devices at the outlet (load switching type oscillators). However, if the deflecting wave is the returning wave from the outlet leg (like the Warren type oscillator but without the control nozzle or the TCFO type device but without the pressurisation), it will be able to switch the flow and cause

an onset of oscillation. The flow past the throat as described earlier will have a higher than unity in terms of flow, and if the deflecting wave has the sufficient momentum to deflect, jet diversion should occur. This has to be without the pressurisation or control nozzle as otherwise, there will be higher frictional losses for the system. However, for a system to be able to deflect in such a way there has to be a new mechanism for this deflection as well as a new mechanism of oscillation. The control parameters invented were based on acoustic resonators and the principle of acoustic resonance is used in order to create an oscillation which is different to both the mechanisms described previously (load switched or jet deflection). This new oscillator is based on the principle of an acoustic resonance mode. It resonates using this mode. This mode was designed to have an acoustic mode either antiparallel or parallel to the oscillator body and get deflected by the channels based on the length of the resonating channels. Load switching can also take place if there is a substantial loading but this is still a pseudo-Zalmanzon type oscillator since there is no pressurisation involved.

The hypothesis for the experiment to invent the DZFO was using the theory that jet deflections could be introduced in a controlled manner to create oscillations and that the flow that would be deflecting the impinging wave needed to be stronger than the impinging wave itself. This oscillation needed to be achieved at minimal expense in terms of energy. The other aspect was that in order to control the jet without having limitations pertaining to the original limitations of jet deflection, the author had previously discovered an oscillatory inducing mechanism that had previously not been published but had been attained by Tesař *et al.* (Tesař *et al.*, 2013). It was based on an acoustic mode for the oscillator which would enable high frequency pulsations which were not reliant on the flowrate but rather the resonator geometry. Figure 11 shows the Hartmann type quarter wave resonator. The key thing to note about this is the presence of the resonating chamber at the control port. There would not be a need for the control port to be present if the resonating chamber were to be placed on the legs of the oscillator post the throat nozzle. This could negate the need to have control terminals and also deflect the wave by the fact that the amplified wave (amplified due to the throat nozzle) would be used to deflect the impinging wave and the length of the resonating channel would be used to control the frequency of this deflection. Furthermore, the channel X1, in Figure 11, needed to be open in order to increase the amplitude in order

to create the jet deflection as it was accelerating at the nozzle. This would not be the case if the deflecting wave is the returning wave which has been amplified by the throat nozzle which in turn would then concomitantly reduce the hydraulic losses (no need to have an open channel in order to induce oscillation, therefore, no need to 'vent' it). A new mechanism was proposed for the DZFO.

Mechanism for switching as proposed by the hypothesis for the DZFO

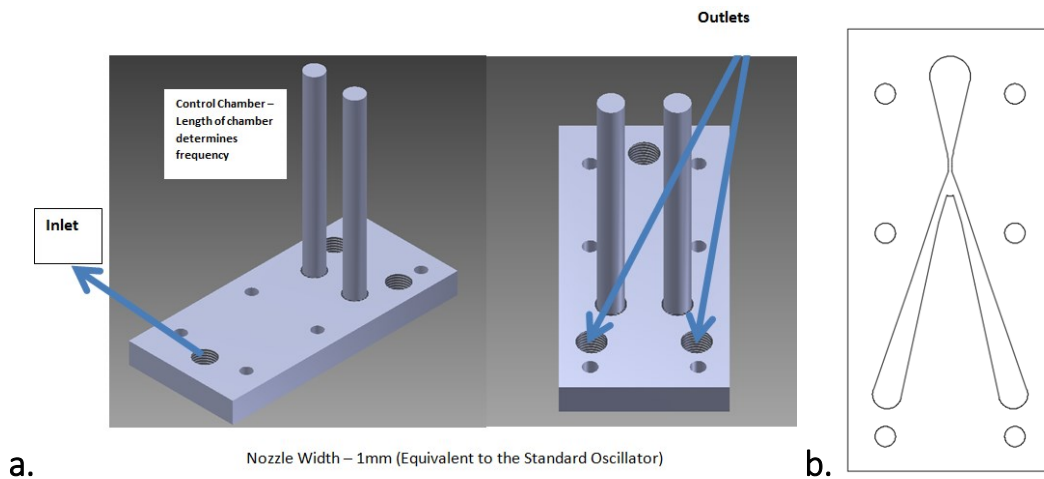


Figure 30 a. The external features of the DZFO. The Supply nozzle and the Outlets remain the same. b. Internal geometry of the DZFO plate. There are no control terminals.

Figure 30 a and b show the DZFO geometry in terms of the external and internal features. The supply nozzle (inlet) and the two outlets are located in the same position as the TZFO. The features that control the frequency here are two resonating chambers, placed midway (can be situated anywhere) on the outlet legs of the DZFO. The length of these chambers will determine the frequency of the oscillator. Figure 30b shows the internal geometry of the DZFO. The plate is similar to a standard TZFO but without the presence of the control terminals.

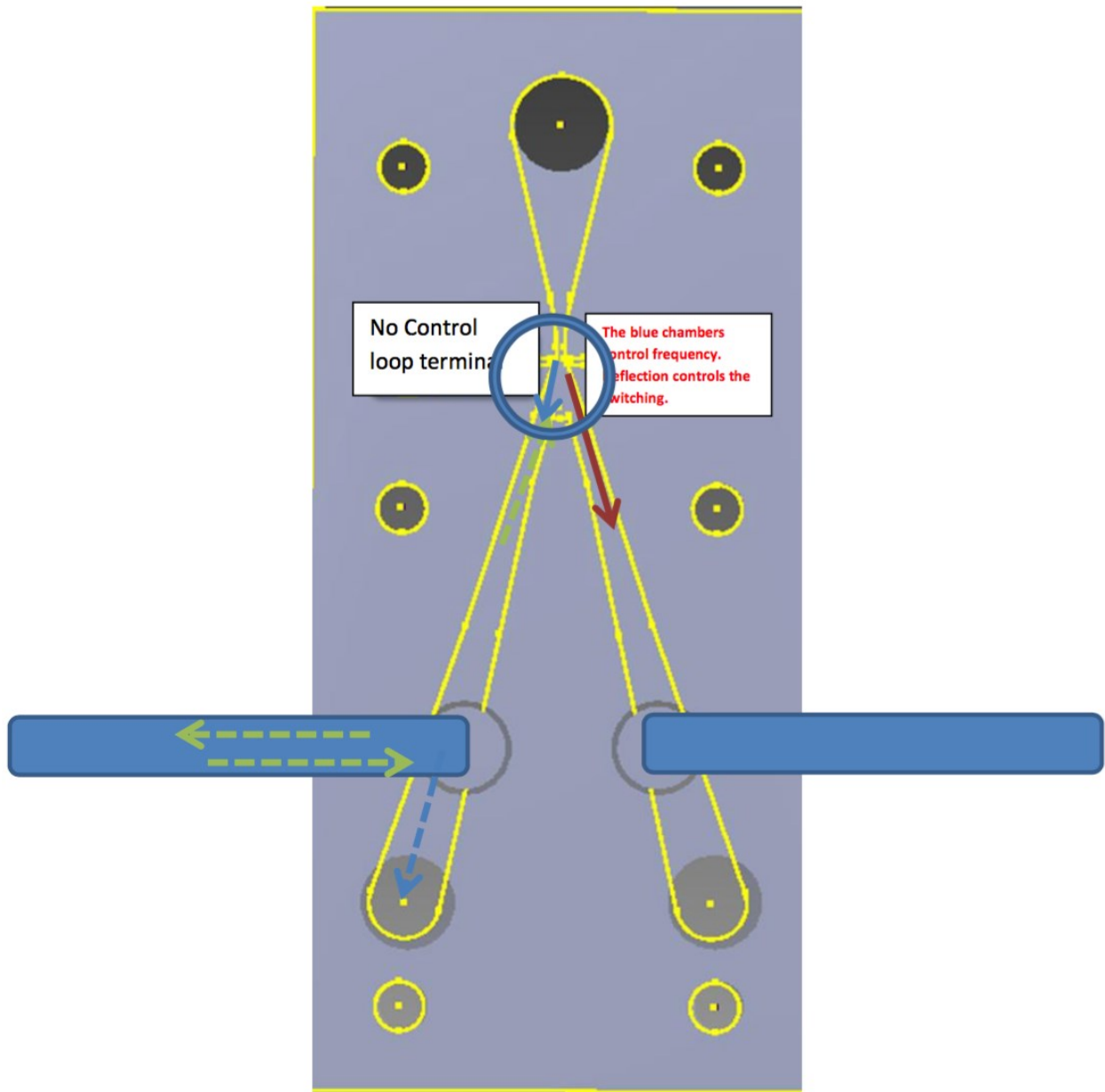


Figure 31 Mechanism of flow post throat nozzle amplification.

As can be observed in Figure 31, there is an amplified wave post the throat nozzle. The wave post the throat nozzle is represented by the blue arrow. There is a partial deflection into the resonating chamber (green arrow), partial deflection to the outlet, and the rest flows back depending on the ratios of the area for the different cavities designed. The partially deflected wave proceeds back to the throat nozzle and deflects the wave (blue arrow) to move across to the other leg (red arrow). This happens on both legs. There is no control port/terminal present as it is not required in this scenario.

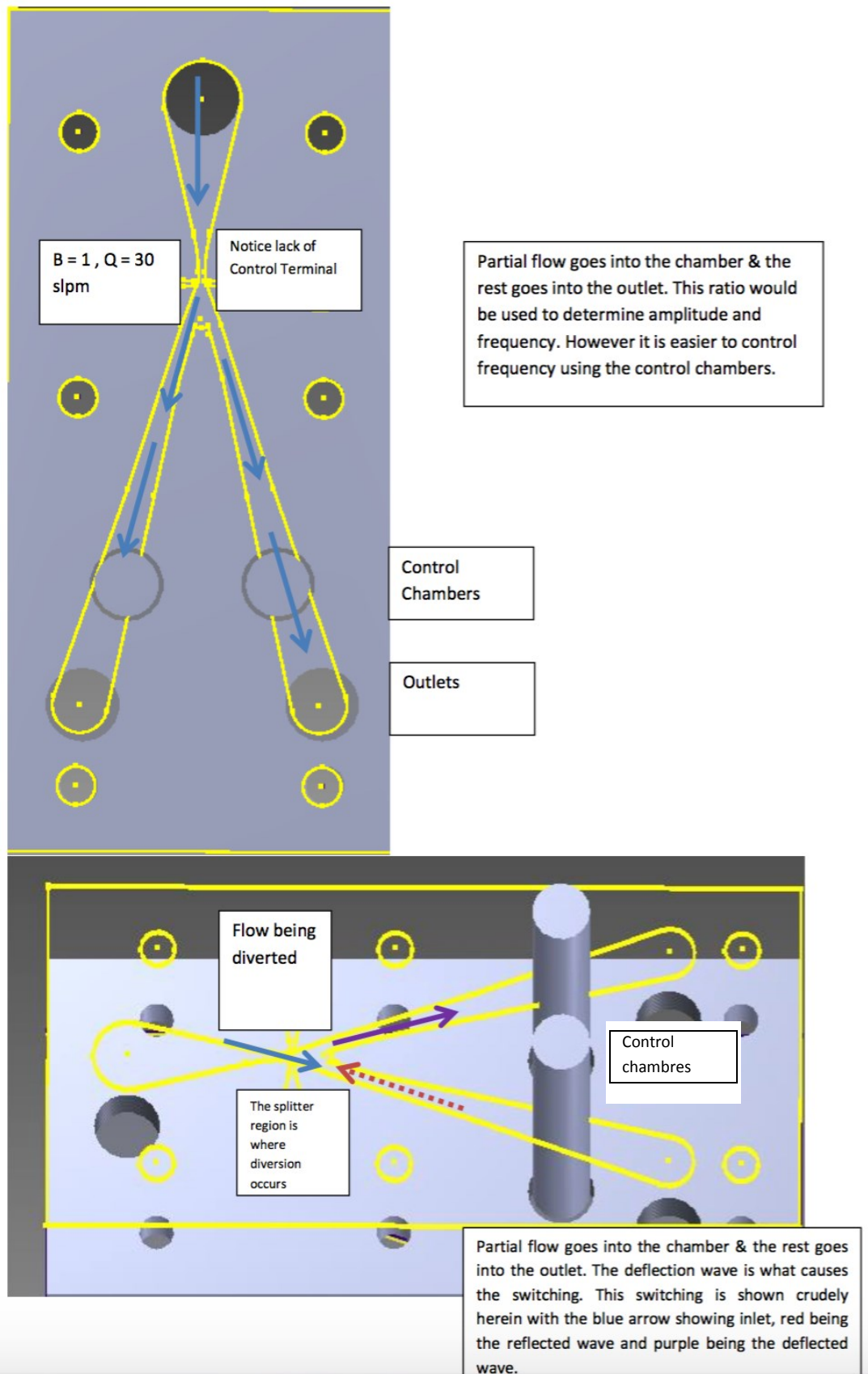
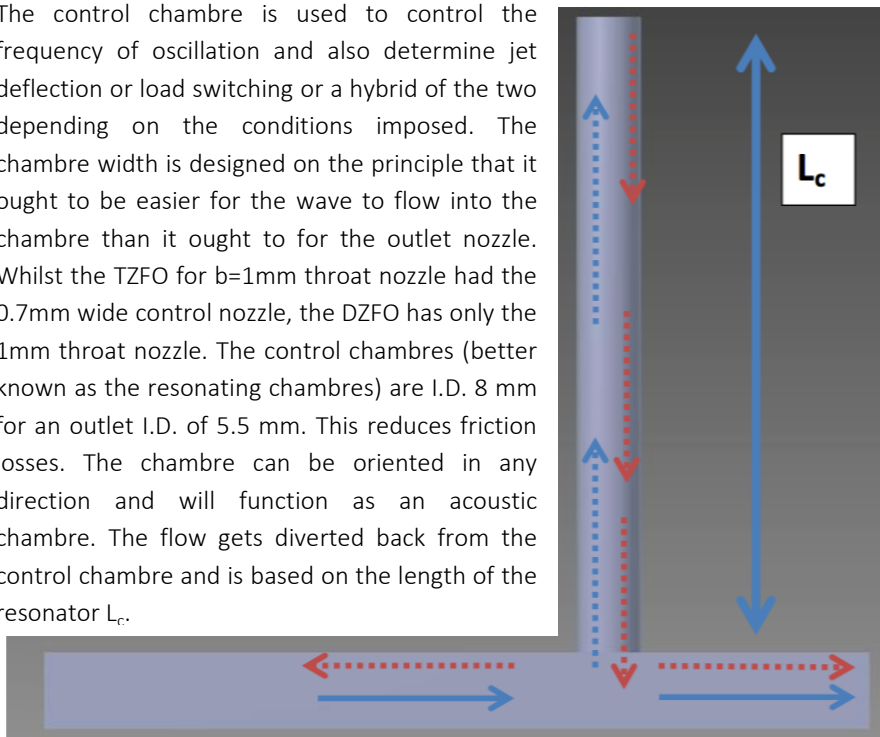


Figure 32 Flow diversion seen herein with the control chambers.

Figure 32 shows the flow diversion mechanism of the DZFO. The blue arrow denotes the wave post the throat nozzle. The purple arrow denotes the wave post deflection and the red arrow denotes the deflecting wave. The impinging wave travels past the throat nozzle, and is amplified. This then enters the resonating chamber and is partially gone through the outlet and partially into the chamber. The deflection frequency depends on the length of the chamber (Figure 33) and each leg can have a separate control for the frequency. Neglecting the flow that has gone on the output as discussed in Figure 31, the deflected wave now meets the impinging wave at the splitter region, and this flow is then diverted onto the other outlet leg. This follows a similar mirrored effect (unless the chambers are of unequal length, i.e. unequal frequencies which will lead to other effects discussed later) and is stably bistable.

There are other ways to control the resonance including changing the cavity geometry but the objective of this design and the inclusion of control chambers was that the feature of a resonator would be used in order to induce controllable oscillations. The length of the control chamber would determine the frequency of oscillation and the combination of the control chamber area and outlet nozzle would determine the amplitude coupled to the momentum of the impinging jet and the throat nozzle width.

The control chamber is used to control the frequency of oscillation and also determine jet deflection or load switching or a hybrid of the two depending on the conditions imposed. The chamber width is designed on the principle that it ought to be easier for the wave to flow into the chamber than it ought to be for the outlet nozzle. Whilst the TZFO for $b=1\text{mm}$ throat nozzle had the 0.7mm wide control nozzle, the DZFO has only the 1mm throat nozzle. The control chambers (better known as the resonating chambers) are I.D. 8 mm for an outlet I.D. of 5.5 mm . This reduces friction losses. The chamber can be oriented in any direction and will function as an acoustic chamber. The flow gets diverted back from the control chamber and is based on the length of the resonator L_c .



L_l - length of leg till the control chamber.

Frequency is dependent on $L_c + L_l$.

$$f \propto \frac{1}{L_c + L_l}$$

Figure 33 The frequency can also be changed by changing the L_l , length of the leg between the control chamber and throat nozzle.

Figure 33 shows the effect of the resonator and the frequency response for the same. The shorter the chamber or leg, the higher is the frequency. This is why, for a zero resonator cavity volume, there is still an oscillation possible due to the length of the leg. The control

chambre is used to control the frequency of oscillation and also determine jet deflection or load switching or a hybrid of the two depending on the conditions imposed. The chambre width is designed on the principle that it ought to be easier for the wave to flow into the chambre than it ought to for the outlet nozzle. Whilst the TZFO for $b=1\text{mm}$ throat nozzle had the 0.7mm wide control nozzle, the DZFO has only the 1mm throat nozzle. The control chambres (better known as the resonating chambres) are I.D. 8 mm for an outlet I.D. of 5.5 mm . This reduces friction losses. The chambre can be oriented in any direction and will function as an acoustic chambre. The flow gets diverted back from the control chambre and is based on the length of the resonator L_c . As can be seen, the dependency now is not the control nozzle to supply nozzle ratio (which results in the higher friction losses) but to the outlet and resonating chambre ratios which are much wider. This results in a substantial reduction in the frictional losses.

The hypotheses to be tested and prove a few properties about the DZFO are discussed below.

Hypotheses to be tested

- The DZFO switching was a hybrid oscillation flitting between an acoustic based switching wave and a load based switching with the control chambres acting as frequency modulators. Shorter the chambre, higher is the frequency obtained.
- The wave would be reflected and opposite in nature for both outlet legs and control chambres.
- The lack of control nozzles and smaller relief features as well as an intended design for efficient switching would result in better momentum transfer of pulse via lower frictional losses and a proxy used for measuring this would be crisper waveforms, lower backpressure, and higher pulse strength.
- Distance of the output would change the L_i slightly as compared to the L_f and therefore induce minor changes to the waveforms and make them clearer by reducing the interference of the waveform which is different to conventional oscillation which weakens over distance –higher dissipation rate.
- Due to this new mode of switching, a higher frequency would be possible than any other fluidic oscillator of comparable size and with no moving/ no electrical parts.

- The acoustic mode would mean that a variety of waveforms (shapes) would be achievable fairly easily mediated by the different combination of chambers used. Different acoustic phenomena can be exploited by using the DZFO if it is based on acoustic resonant mode of switching.
- The acoustic mode could also be used to induce the 'beats' phenomenon in order to generate larger pulses and introduce superposition principle (constructive interference) and destructive interference of the waveform.

3.1.3 Comparison of Bubble Size distributions inferred acoustic, visualisation, and laser diffraction

Various methods have been described herein. It is contended that there are certain features for these systems that are to be discussed. The hypothesis is that acoustic methods are most accurate for small microbubbles since they are specific to bubbles, they do not miss small bubbles (since they rely upon the resonant bubble theory) and can be used in particle based systems too due to this property (they neglect particles). They can also be used holistically rather than taking small sample sizes.

The hypothesis would ensure that acoustic methods are likely the best technique for obtaining bubble size distributions for microbubble clouds. Hearing the cloud is a much better way of garnering the bubble size distribution than direct visualisation or diffraction. The vignetting and small sampling of the photonic and optical system will result in erroneous distributions which increase due to extrapolation for a larger volume.

The major assumptions are:

Microbubbles are spherical (this is true for all microbubbles sized below 1mm)

The resonant bubble approximation holds true (bubbles resonate when insonated by specifically targeted frequencies)

There are no overlapping bubbles in the case of optical and photonic methods

The sparger produces bubbles equally, i.e. equal distribution of the bubbles across the sparger membrane.

Photonic method and optical method requires an assumption that the bubble population is similar throughout the region of interest, i.e. the bubble population remains the same across the membrane.

The other assumptions have been listed in Chapter 2 Literature review.

The major decision taken was selecting the three appropriate methods for garnering a size distribution for a high throughput microbubble cloud. Optical, photonic, and acoustic methods were chosen.

3.1.4 Separation Processes – Ammonia stripping in ammonia rich waste waters

The hypothesis posited in this paper is that one can use the concentration gradient in the bubble (the air bubble has zero ammonia concentration whilst the surrounding liquid has a higher ammonia concentration) and the associated temperature gradient (difference of the injected air bubble temperature and liquid temperature) to speed up the concentration gradient effect via the Soret effect (Bird *et al.*, 2007). The hot air microbubble is injected with zero ammonia concentration in the gas phase initially. Subsequent mass transfer occurs with limited sensible heating as described by Zimmerman *et al.* (Zimmerman *et al.*, 2013), until reaching equilibrium. This equilibrium occurrence, or rather rate of transfer, is determined by the contact time of the bubble with the substrate liquid, i.e. by liquid layer height (the simplest tuning parameter). Ideally, there would be a scenario where the bubbles would separate out the ammonia irrespective of the temperature of the system and the temperature of the gas would only enhance the rate of transfer for this process. Another hypothesis is that for ammonia rich liquor, which has a high organic loading, smaller bubbles ought to be generated. The hot air going through the oscillator would increase the frequency of the oscillator which would result in greater bubble flux (non-coalescent liquids result in bubble formation for every pulse as long as amplitude is high enough). The internal mixing increases greatly for smaller bubbles. The ammonia removal rates for these liquors ought to be significantly higher than ammonia-water systems. Additionally, volatile compounds ought to be removed as well.

Process design conditions are listed in the experimental section with some of the decisions for design listed in the materials section.

The following sections describe the experimental design and the methods and materials used for effective ammonia separation to test the hypothesis posited.

3.2 Data collection Procedures

3.2.1 Resonant pulsing frequency effect for much smaller bubble formation with fluidic oscillation

Methods and Materials

Fluidic Oscillator

The FO is oscillated at 86 standard litres per minute (slpm) and 92 slpm with most of the flow being vented and a frequency sweep is performed in order to confirm the hypothesis posited earlier. As discussed previously, vents have been introduced in order to increase the momentum of jet pulse and amplitude of oscillation whilst controlling apropos flow into the sparger (MBD 75).

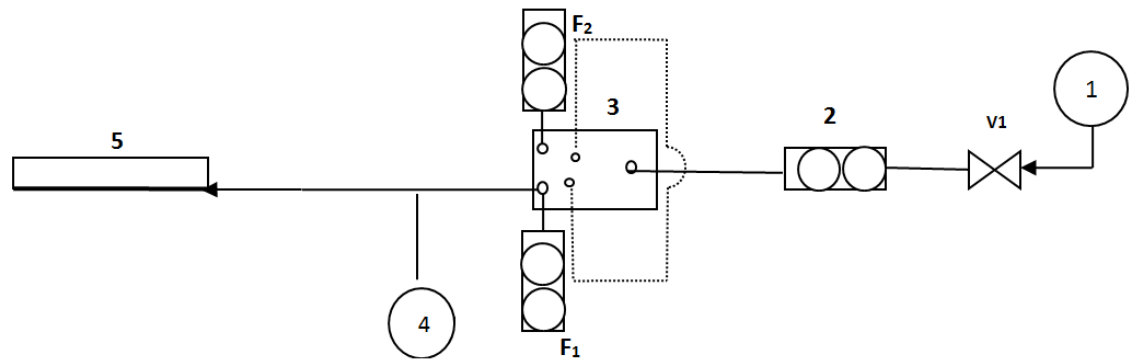
Rotameters have been utilised to act as metered valves. The frequency of oscillation and the amplitude of the oscillation are measured using an Impress G-1000 pressure transducer controlled and recorded using bespoke characterisation software developed using LabView and will be touched upon briefly. The pressure drop across the FO is 100 mbar. The total pressure drop depends on the combined pressure drop across the FO and sparger.

The Sparger

Point Four Systems has a proprietary product, a ceramic sparger, known as MBD 75 which produces a cloud of fine bubbles approximately 500 μm in size under steady flow and is used in aquaculture. MBD 75 has ultrafine ceramic pores and a flat surface, thereby retarding bubble coalescence as compared to other types of material such as sintered glass or steel membranes. Ceramic, being inert, hydrophilic, and robust, is a preferred surface for bubble generation in water.

System Set up

The system has been set up according to the schematic shown in Figure 34.



- 1. Pressure Gauge
 - 2. Flow meter
 - 3. Fluidic oscillator
 - 4. Pressure transducer
 - 5. MBD 75
- V₁. Shutdown Valve
 - F₁. Bleed Flow meter 1
 - F₂. Bleed Flow meter 2

Figure 34 Schematic of the Set up.

Figure 34 shows the system schematic. The gas enters via the pressure regulator at a fixed known pressure. A ball valve acts as an emergency safety valve, V1. Rotameter labelled 2 is used to control the flow appropriate to the FO in order to initiate oscillation. F1 and F2 acts as vents as seen in Figure 34 and are metered valves (rotameters). Pressure transducer labelled as 4 is used to measure the pressure and frequency of oscillation. 5 is the sparger used here, MBD75- proprietary ceramic made by PointFour systems.

Pneumatic set up:

The pressure regulator (Norgren) controls the systemic pressure which is set at 2 bar(g)- the required pressure for the particular sparger to bubble. A different sparger would require lesser pressure. The flow controller (FTI Instruments) has been corrected for the pressure being used in the system since the MBD 75 has been used at a different pressure. The air enters the system from the compressor via the pressure regulator and the flow controller regulates the global flow entering the FO. The FO is connected to two vent rotameters to act as metered valves and these are set up in order to vent appropriately and send apropos flow into the aerator. The aerator is placed in a tank wherein the bubble size is measured using acoustic bubble spectrometry.

The frequency and amplitude of pulse from FO is measured concomitantly using a combination of pressure transducers and an FFT code developed in LabView (*cf.* Frequency measurement and FFT).

The sparger is kept in the centre with the hydrophones set around it as shown in Figure 35 with the set operational conditions. Bubble sizing is performed continuously and the DDI water in the tank is replaced after each reading.

The frequency is changed whilst all other conditions are kept constant and two different vent flowrates are used, coupled with these three feedback conditions, at various frequencies in order to test the hypothesis.

Several configurations of the Spyropoulos type FO being used are also able to engender the same frequency which helps observe the effect of the frequency.

Bubble sizing using Acoustic Bubble Spectrometry

The hydrophones are placed over at a height 5 cm above the diffuser and equidistant at 15 cm. These data were repeated 7 times and performed at 2 different flow rates – 86 slpm² and 92 slpm. 22 frequencies were used in the study for each condition and flowrate performing a frequency sweep and 3 different configurations of feedback for FO as described earlier.

Bubble sizing was performed using Acoustic Bubble Spectrometry commercially available from Dynaflo Inc™. This has been found to be an extremely effective method for visualising cloud bubble dynamics. The Acoustic Bubble Spectrometer (ABS) with 4 pairs of hydrophones – 50,150,250, and 500 kHz were used in this study, with the capability to collate a size distribution from 3 μm to 600 μm in size (radius).

The ABS is then set up along with an octaphonic set up in the manner as shown in Figure 35. Two equi-responsive hydrophones are placed antipodal to each other with the sparger bubbling in the centre i.e. bubble cloud in the centre. The DAQ and computer (controlled using software) send out a frequency sweep via a signal generator with amplifier into the transmitting hydrophone. The signal passes through the bubble cloud (calibrated under no bubble condition) and into the receiving hydrophone which is demodulated using an

² Standard litres per minute, standard conditions – 293.15 K and 101 325 Pa

amplifier too. This is used in conjunction with the no bubble condition in order to generate a bubble size distribution.

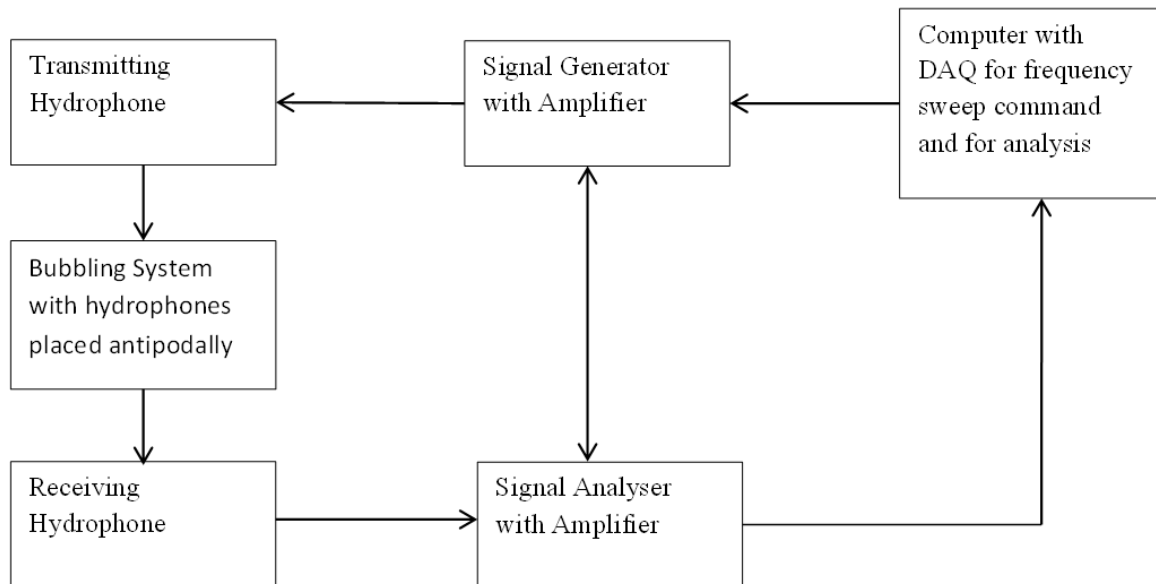


Figure 35 Information flow diagram of the ABS and the hydrophone set up

Hydrophone pairs are used, with one being a transmitter and the other acting as the receiver, and each hydrophone pair has a specific resonant frequency at which it works best and a range of frequencies that it can operate reasonably at. When a hydrophone insonates a bubble cloud with a specific frequency, the bubble corresponding to that size resonates and therefore oscillates, thereby attenuating the signal due to the pressure change caused by the oscillating bubble as compared to a clear/bubble-free solution. This attenuation is then measured by the receiving hydrophone and the signal is inverted in order to garner a bubble size distribution. A frequency sweep is performed at equally spaced frequencies between 5 kHz to 950 kHz, from which the bubble size distribution is compiled. Chahine *et al.* (Wu and Chahine, 2010, Chahine, 2008, X. Wu, 2008, Tanguay, 2008, Kalumuck, 2003, Georges L.Chahine 2003, G.L. Chahine, 2001, Chahine, 2000, Duraiswami *et al.*, 1998, Chahine *et al.*, 1998, Chahine, 1977) describe the methodology underpinning ABS and the algorithm for transformation of the raw data into a bubble size distribution.

Frequency measurement and Fast Fourier Transform

Impress G-1000 pressure transducers were used in this experiment. Fast Fourier Transforms are simple algorithms designed to convert a signal from one domain (time or space) and convert it to the frequency domain and *vice versa*. Figure 36 shows an exemplar waveform with an FFT. This provides a quick and easy way to determine the frequency of the oscillatory flow from an FO. LabView is used to acquire the signal and process it. The oscillatory pulse from an FO is composed of the amplitude and frequency of oscillation.

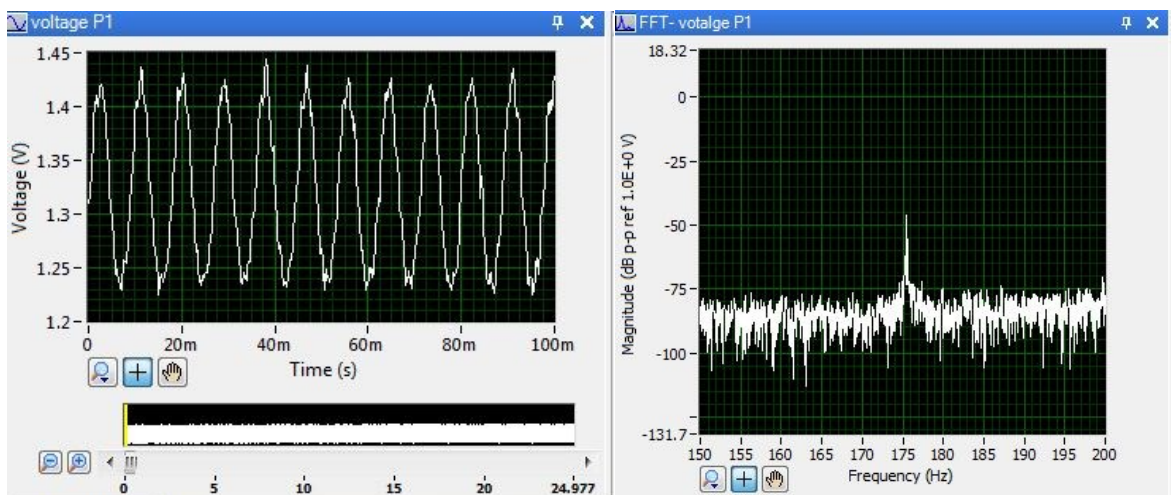


Figure 36 An exemplar of a raw waveform from FO and its translation in frequency domain post FFT. Aliasing effects of FFT are mitigated by having a high acquisition rate (512kHz with 512k samples acquisition window).

3.2.2 Inventing the New Oscillator (Desai-Zimmerman Fluidic Oscillator)

Materials and Methods

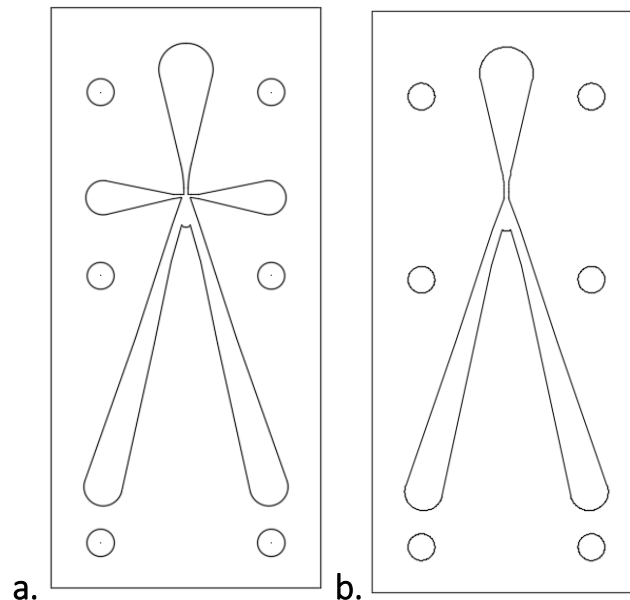


Figure 37 Left – (a)Original TZFO middle Plate with Control ports , Right(b) - New DZFO middle plate to be tested , without control nozzles

Figure 37 shows the internal plates and the difference between the TZFO (a) and DZFO(b) internal plate. The control terminal for the TZFO has been removed for the DZFO.

The resonating chambre for the DZFO would be placed in the middle of the output leg, with the centreline chosen to be midway between the output and the throat nozzle. This is not an arbitrary choice, as according to our hypothesis, the further away from the nozzle throat the chambre would be, the lower the amplitude achieved would be. This would be one of the control parameters for the amplification factor.

Figure 38 shows the placement of the pressure transducers (required to characterise the oscillators) The placement of the pressure transducers was maintained in order to measure the waveforms and frequency responses. F1 and F2 represent rotameters acting as control valves in order to simulate a 'load'. The Transducers were kept at right angles to each other in order to ensure phase variance existed.

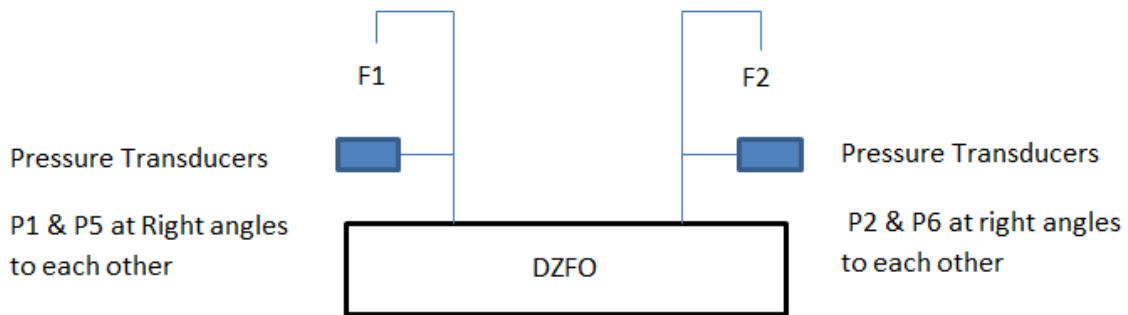
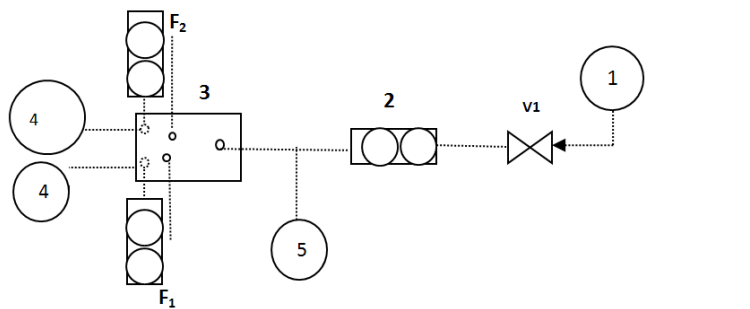


Figure 38 Pressure transducer placement and simulated loads (F_1 and F_2).

Pneumatic set up

Figure 39 shows the pneumatic set up for the system.



- | | |
|--|----------------------------|
| 1. Pressure Regulator | V_1 . Shutdown valve |
| 2. Mass flow controller | F_1 . Bleed flow meter 1 |
| 3. Fluidic oscillator (Different types) | F_2 . Bleed flow meter 2 |
| 4. Pressure transducers | |
| 5. Back pressure monitor | |

Pneumatic line
Pneumatic line

Figure 39 Pneumatic Set up

The set up for the system is similar to the ones used for conventional fluidic oscillation. The only difference is that there is no sparger attached to the system but rather a simulated load via metered valves or rotameters are used. This enables a more controlled experiment to be performed.

Air enters via the compressor with pressure regulation (1) and a mass flow controller(2) which controls the flowrate going into the fluidic oscillator. The fluidic oscillator is connected to pressure transducers (Impress G1000 and Impress GP100) (4) and metered valves (F_1 and

F₂) which simulate the loading and the pressure transducers record the Fast Fourier Transform (FFT) of the data. The backpressure regulator (5) enables the determination of the pulse strength and the amplitude of pulse for the system. The frequency measurement is achieved via bespoke code written using LabView and described in the next subsection.

Frequency Measurement

The frequency of the oscillator was determined by using a bespoke code in LabView. This could also be used to determine the magnitude of the pulse strength on the oscillatory wave. The code consisted of a Fast Fourier Transform (FFT) power spectrum for the raw data obtained from the pressure transducer at 128 kilo-samples per second. The FFT is a signal processing technique which, when observed with the Nyquist theorem and with sufficient sampling results in a sampling averaged frequency of a wave spectrum resulting in a peak formed for the various systems in use. The frequency of oscillation would help determine the amplitude of the wave jet engendering from the oscillator outlet into the sparger. Conventionally, an FFT suffers from averaging losses and can mistake peaks due to windowing errors. This is mitigated by using a high acquisition rate system capable of averaging several thousands of samples per second, i.e. NI Daq type system and taking the averaging window over a longer period of time. The author compared these readings with those obtained via using the Maximum Entropy Method (adapting from Numerical Recipes in C++(Press, 2002)) and a hybrid version of this method using Autocorrelation function in LabView. They compared very well and there was less than 1% discrepancy with the results in terms of frequency.

Method

The setup is seen and described in Figure 38 and Figure 39. The various hypotheses to be tested were now to be tested using the frequency set up and pneumatic setup with the only difference being that different oscillators were used. These oscillators were characterised maintaining *ceteris paribus* and depending on the experiment carried out, various properties such as the frequency, the waveforms, the amplitudes, the backpressures, and other items were measured.

3.2.3 Comparison of Bubble Size distributions inferred acoustic, visualisation, and laser diffraction

Methods and Materials

Materials

Point Four Systems has a proprietary product known as MBD aerator which produces a cloud of fine bubbles approximately 500 μm in size under steady flow and is used in aquaculture. These aerators have ultrafine ceramic pores and a flat surface, thereby retarding bubble coalescence as compared to other types of material such as sintered glass or steel membranes.

Multiporous ceramic membranes have been used -Commercially available - Point Four systems (P4)- (2 μm average pore size, 2 off - 50mm² area).

Fluidic Oscillator

The FO is oscillated at 30 standard litres per minute (slpm) with most of the flow being vented and a frequency sweep is performed in order to confirm the hypothesis posited earlier. As discussed previously, vents have been introduced in order to initiate oscillation and controlling apropos flow into the aerator.

Rotameters have been utilised to act as metered valves. The frequency of oscillation and the amplitude of the oscillation are measured using an Impress G-1000 pressure transducer controlled and recorded using bespoke characterisation software developed using LabView and has been described in Figure 36. The pressure drop across the FO is 100 mbar. The total pressure drop depends on the combined pressure drop across the FO and aerator.

Fluidic oscillator coupled with the accompanying pneumatic set up, Malvern Spraytec, Acoustic Bubble Spectrometer (ABS), High Speed Visualisation Set up, and Frequency analysis kit were used and set up as described below.

Optical Methods – High Speed Photography

The visualisation device is a high speed camera, (Photron FastCam S3) capable of 250 000 fps with a resolution of 1024x1024 and provided with a lens (Nikon Nikkor Lens, 1.8 D). The region of interest used was 1.764 cm³.

Systemic conditions were kept as constant as possible whilst comparing the different visualisation methods in order to introduce the least amount of error as possible. Since they each have their drawbacks and advantages, slight variations to the actual methods had to be used. For example, for photonic and optical (single camera systems) methods, they can only be used for a single plane to image accurately or in a small space and extrapolations have to be made. The acoustic method used was able to size the entire population but the hydrophones had to be used separately for two equiresponsive aerators and this was the major assumption made.

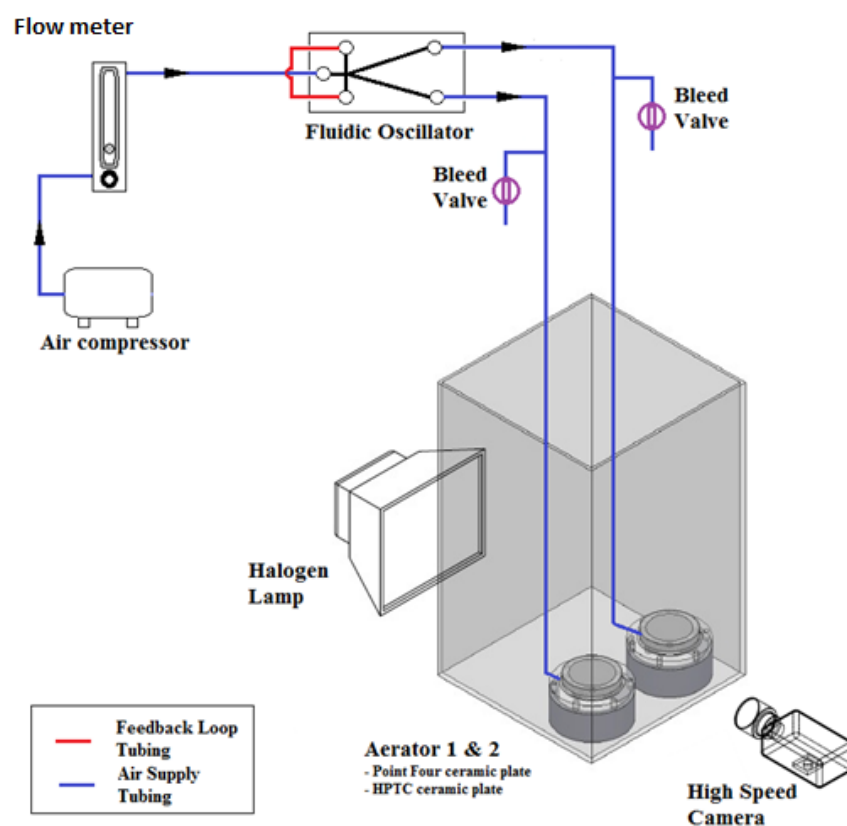


Figure 40Set up for optical methods comparison study

A single plane was used as the image analysis software is not designed for a cloud of bubbles. There has not been any significant work done on 3D cloud bubble dynamics and automated image analysis on a 3D bubble population has not been developed. It was assumed that it would be an equiresponsive surface and that a single plane could be used to garner an

overall idea about the system. This is one area where errors in measurement are going to be introduced.

The systemic conditions were kept constant. The bubbles were generated using the ceramic sparger – MBD aerator. Two different conditions of feedback i.e. frequency were used and 4 flow rates were used.

Air enters the system at a controlled pressure from the compressor into the rotameter. Pressure correction being applied, the appropriate flow was sent into the fluidic oscillator. The fluidic oscillator needs an appropriate amount of venting in order to initialise oscillation whilst maintaining appropriate flow into the sparger. Two rotameters were used as vents for the system. Optical set up was used as per Figure 40. Frequency was measured using an accelerometer using bespoke FFT code.

Bubbles were generated by using a systemic flow rate described in the bubble generating section.

Photonic Method – SprayTec

The pneumatic set up was similar to the one used for the optical method described. As mentioned the Spraytec looks at a small sampling section that is required to have the assumption in place that the bubbles are being produced equally at all regions of the aerators and that surface imperfections are negligible. This is the same problem observed in the optical methods and results in the different techniques. The gamut of the bubble population is possible only for a small test cell in case of bubble generation. Usually it is not required when compared to a spray. The Spraytec is able to infer bubble size distributions whilst automatically adjusting for the change in refractive index due to the addition of the test cell.

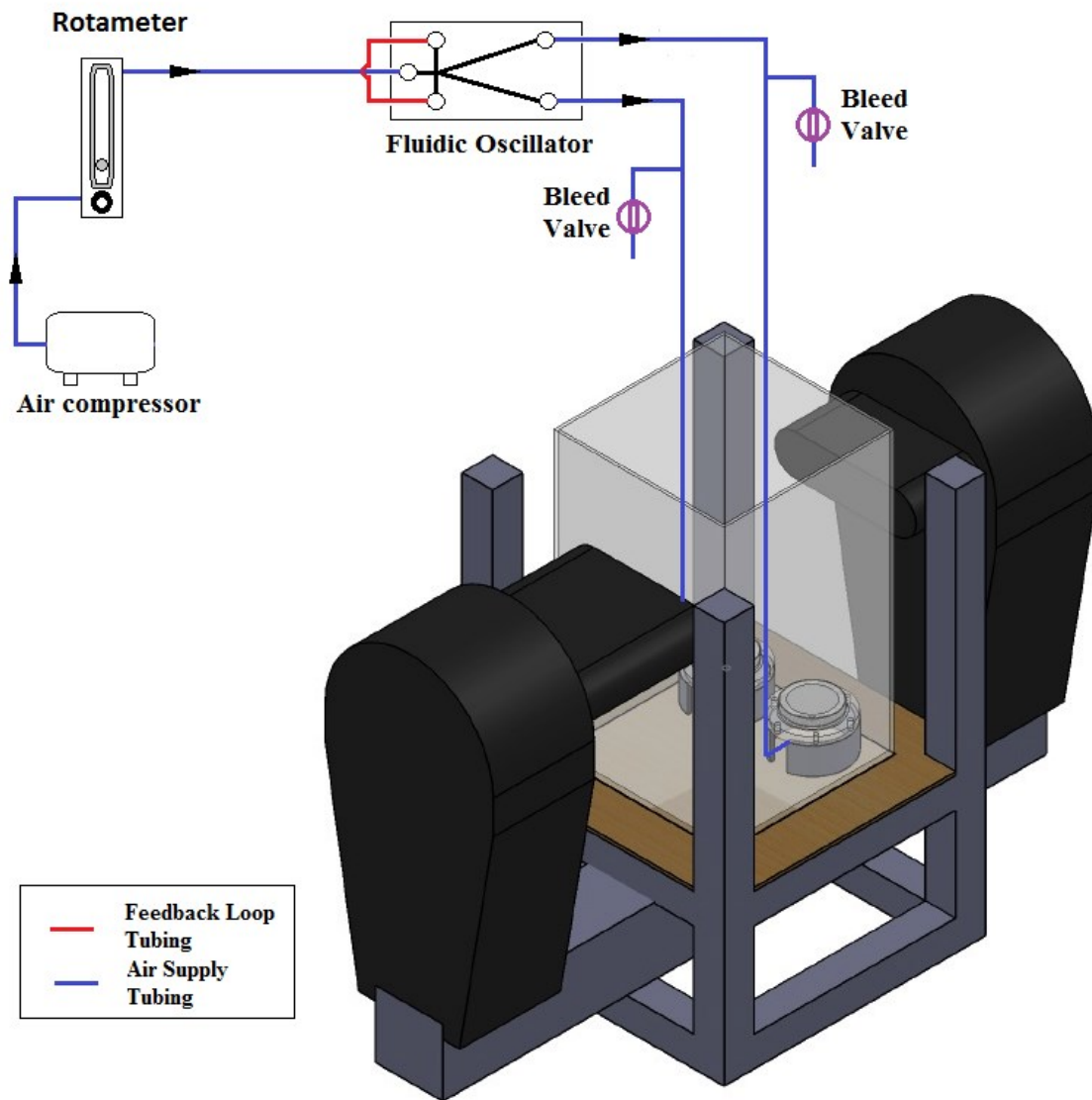


Figure 41 Spraytec Set up

The Spraytec was used for the sizing and the appropriate lenses were used.

Air entered the system at a controlled pressure from the compressor into the rotameter. Pressure correction being applied, the appropriate flow was sent into the fluidic oscillator. The fluidic oscillator needs an appropriate amount of venting in order to initialise oscillation

whilst maintaining appropriate flow into the sparger. Two rotameters were used as vents for the system. Photonic set up was used as per Figure 41. Frequency was measured using an accelerometer using bespoke FFT code.

The bubble size distribution was assumed to be equal at all points, i.e. it was assumed that the aerators would be equiresponsive and that taking a plane section would not be too much of an approximation. The 300 mm lens was used with particulate refractive index set at $1+0.01i$, dispersant refractive index set at 1.33. The particle density was 1.23 g/cc with residual set at 2.15% for the data.

The transmission measurement involves a spatial filtering of the collimated laser beam pre and post transmission through the bubble cloud. The spatial filter is the pinhole at the centre of the detector array which, as well as being used to ensure the detector array is centred on the laser beam, also rejects any scattered light. This is important as it removes backscatter for most cases. However, for high scatterers such as bubbles, due to concentration effects, multiple scattering inevitably causes some light to be re-scattered back to a near-zero scattering angle and it was set to on. This is a patented algorithm. The laser used in Spraytec is a 632.8nm, 2mW helium-neon laser. The transmitter contains the He:Ne laser source which produces a collimated beam of 10mm diameter with a wavelength of 632.8nm.

The detectors (over 30 of them), and the use of high-efficiency spatial filtering means the concentration calculation is reliable over a much wider concentration range than a method based on measuring total scattered energy as well as having the advantage of requiring no calibration. Water and air were the media set.

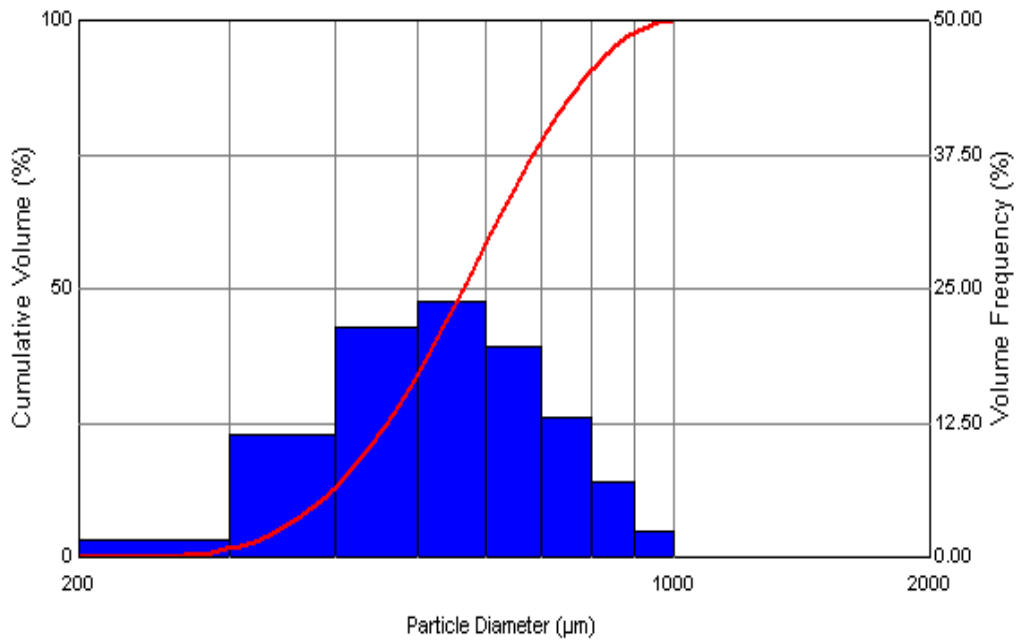


Figure 42 Example of spectrum for Spraytec

Acoustic Method – Acoustic Bubble Spectrometer (ABS)

The ABS had 4 pairs of transducers with resonant frequencies at 50 kHz, 150 kHz, 250 kHz and 500 kHz. This ensures that the entire gamut of the bubble size distribution can be observed. The working behind this system has been explained in the previous section. The hydrophones are placed opposite each other and the bubbles are insonated by the ultrasound. The frequency of insonation is what determines the bubble size. The attenuation provides the number of bubbles. The bubble sizes obtained were for the entire aerator and were near real time measurements. Spraytec is also able to measure the bubble sizing in real time.

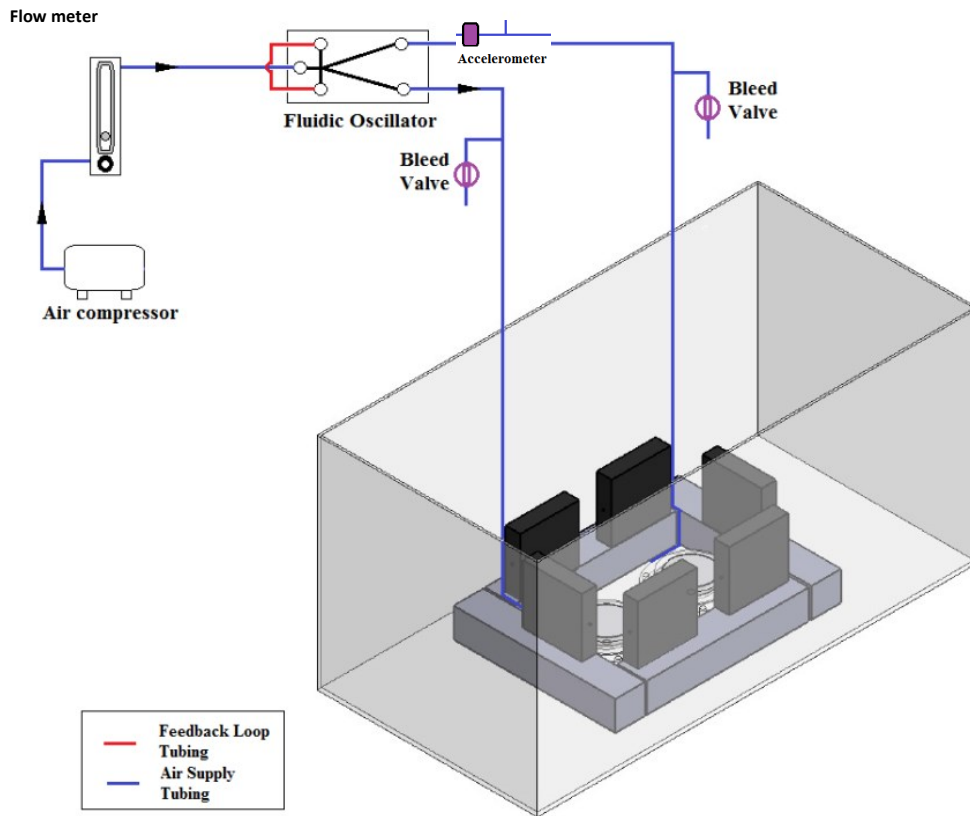


Figure 43 Set up for the ABS

Air enters the system at a controlled pressure from the compressor into the rotameter. Pressure correction being applied, the appropriate flow is sent into the fluidic oscillator. The fluidic oscillator needs an appropriate amount of venting in order to initialise oscillation whilst maintaining appropriate flow into the sparger. Two rotameters were used as vents for the system. The acoustic set up was used as per Figure 43. Frequency was measured using an accelerometer using bespoke FFT code.

Bubble Generation Set up

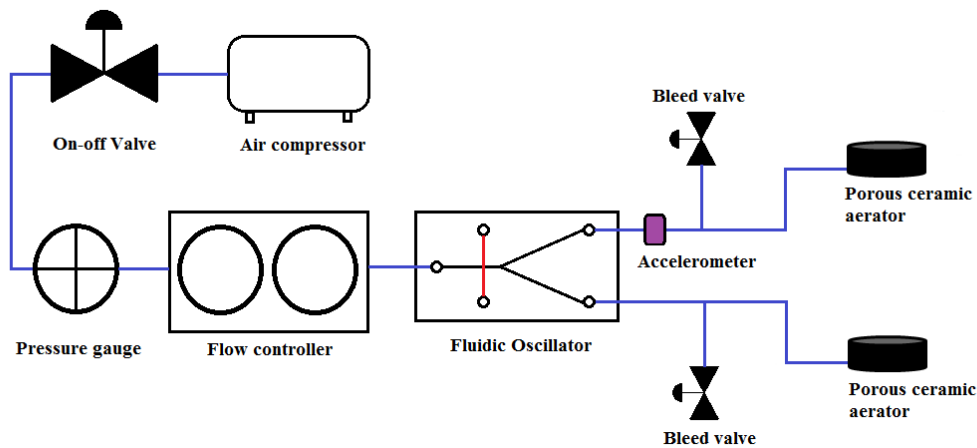


Figure 44 Pneumatic set up for bubble generation

The global flow rate is controlled by a flow meter with an accelerometer being placed at one of the legs in order to note the frequency of the FO in order to maintain similar conditions. The pressure regulator also helps maintain steady conditions in the rig and the FO is oscillated with the flow controlled to the aerators via bleed valves. The global flow rate is required in order for the FO to oscillate but the bleed valves help get the aerator get the appropriate flow rate. The frequency of the FO is dependent on the global flow rate, exit velocity as well as the length of the feedback tube. The exit velocity is dependent on the restriction imposed and this is dependent on the aerator (Zimmerman *et al.*, 2011a).

2 feedback tube lengths, each with 5 flow rates have been used in this study. 12 averages were taken for the ABS, 4 each for the optical and photonic method and there was less than 3% error in the readings estimated for the ABS and Spraytec and the optical method had 5% errors.

3.2. 4 Separation Processes – Ammonia stripping in ammonia rich waste waters

Method and Materials

Equipment

Prototype Reactor – HXRig

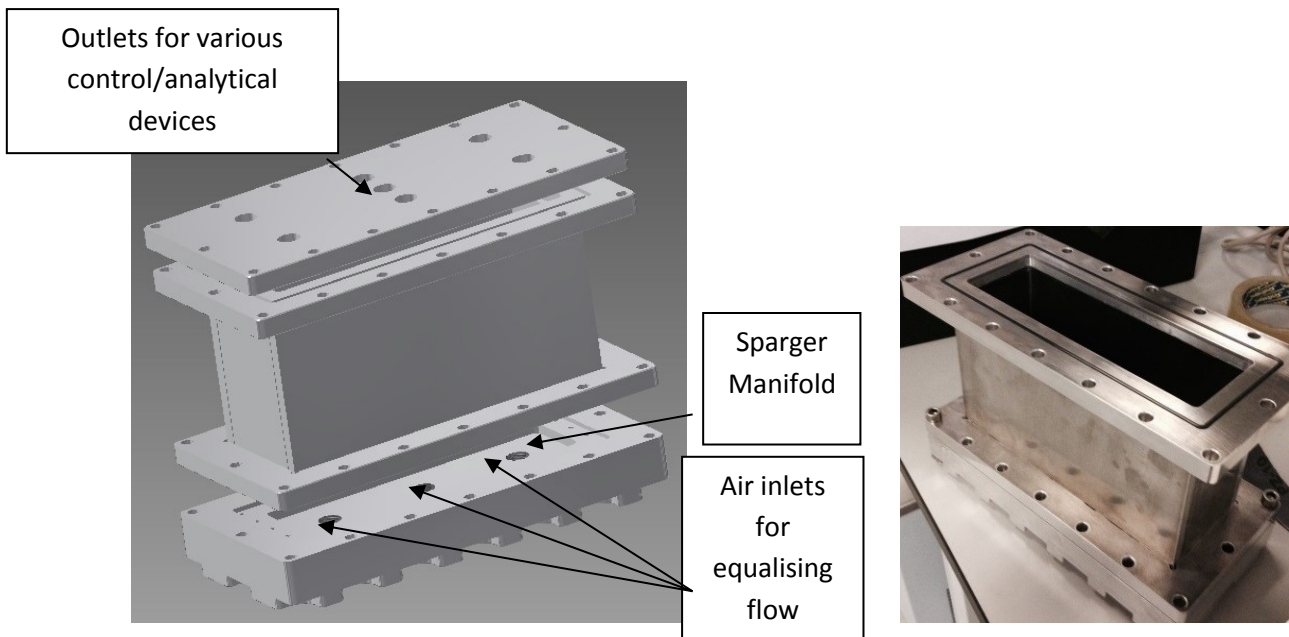


Figure 45 HXRig showing the air inlets, sparger manifold, control ports, and outlets.

A prototype rig was designed and used for hot microbubble injection into thin liquid layers. The rig has been designated as HXRig and has a few important features for use as a hot microbubble injection rig. Figure 45 shows HXRig.

The body was made out of stainless steel to ensure longevity. However, it was cladded using novel materials such as Kapton™ and Zircoflex Gold™ with sandwiched heat resistant wool in the middle. This would ensure almost negligible heat losses across the walls of the reactor. This ensured near isothermal behaviour.

The manifold has three inlets for better flow distribution. Between each pair of inlets there is a thermocouple which is used to check on the flow balance and a check on the temperature

controlling thermocouple. This rig is supported by using a sintered steel membrane of 100µm pore size.

Three inlets were present in order to equalise the flow across the membrane. The rig 'body' had extra height in order to place liquids of different volume as well as to check for foaming for mixtures that would foam.

Sensors are inserted within the top plate which includes measurement ports for thermocouples, pressure and flow indicators. The thermocouples measured liquid temperature, chambre temperature, gas temperature, inlet temperature, heater temperature, and ambient temperature. The active sparger/diffuser area is 150x30mm²

The height of the liquid above the membrane is correlated with the volume poured in over the active area. The fluidic oscillator is connected to the HXRig and known gas flow from the output of the oscillator is transferred into the rig. The outlet flow is temperature corrected.

The design will be elucidated as this was a redesign on the microbubble distillation process and from the published works by (AlYaqoobi *et al.*, 2014, Abdulrazzaq *et al.*, 2015).

It had 4 major components:

1. Part OPA20141001PD - "Diffuser/Sparger Manifold"
2. Part OPA20141002PD - "Diffuser/Sparger"
3. Part OPA20141003PD - "Vessel/Body"
4. Part OPA20141004PD - "Top"

Part OPA20141001PD - "Diffuser/Sparger Manifold"

The diffuser manifold was designed in order to best secure the bespoke stainless steel diffuser. There are 24 M2.5 screws threaded in order to maintain an even pressure across the membrane, which would minimise leaks. A gasket was made using aerospace grade silicone and following appropriate degassing protocols, a bubble free extremely high quality seal was made.

The manifold had a 1mm chambre and three inlets. The calculations required for the diffuser manifold and coupling to the sparger were determined by (Park *et al.*, 1976).

It was determined that for an oscillatory flow system, the best chambre volume would be approximately 1-4 cc.

The diffuser had been designed for minimal pressure drop which meant that the flow needed to be even. The design was to enable an equalised flow across the membrane and minimise maldistribution across the membrane.

This was performed by designing a trident flow distribution system and changes to the diffuser design. The trident flow inlet also helped with characterising the oscillation. In between the two extreme inlets were placed two thermocouples. These could be used in multiple ways –

1. To check distribution of flow and successful oscillation
2. To act as temperature control for the heater as the chambre would be the determining factor for air inlet temperature.

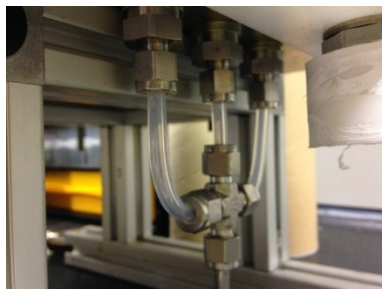


Figure 46 The trident air inlet distributor configuration

Part OPA20141003PD - "Vessel/Body"

The height was chosen to be approximately 20 cm to accommodate for any potential foam formation (since the liquids to be tested will have a greater ionic strength than water, they would also stabilise the bubbles formed, resulting in foam formation). A smaller height (10mm) flange was also designed in case the additional height was not required or if foaming would not pose to be a problem. The ethanol-water separations or other such separations would not require height for the chambre and therefore it was used for those trials. A viton gasket was on both sides of the vessel for the two connexions it would have.

Part OPA20141004PD - "Top"

Several ports were constructed on the top to allow *in situ* online continuous measurement and control -temperature probes, gas sensors, condenser, mass flow meters and liquid pumps.

Part OPA20141002PD - "Diffuser/Sparger"

A bespoke sintered stainless steel diffuser with a pore size range of 30 - 50 μm and an average pressure drop of 40-100mbar was designed and used to generate the bubbles

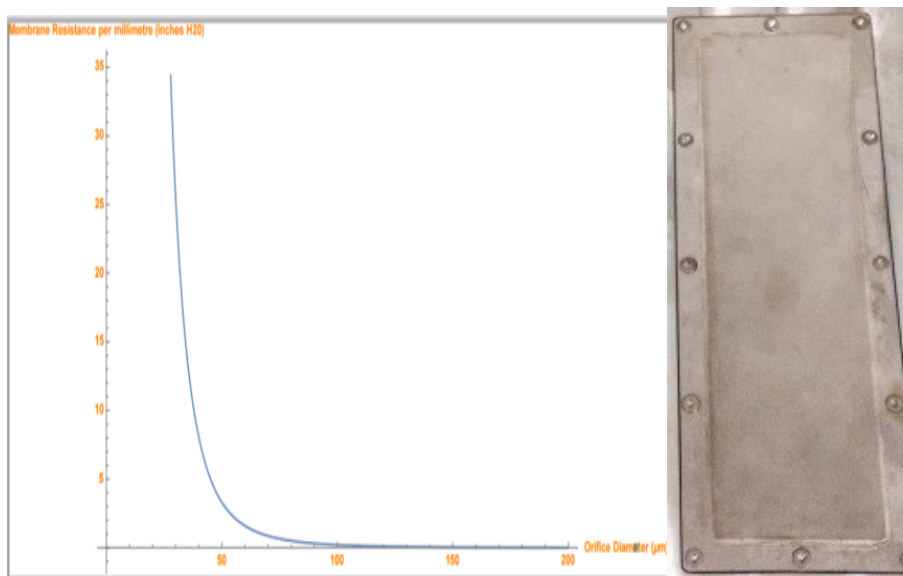


Figure 47 Diffuser and Diffuser calculations for pressure drop (Holdich *et al.*, 2006)

There were several reasons why a stainless steel sparger was selected.

1. Sintered stainless steel can be made into any shape and extremely thin (70-150 μm) which helps control pressure drop without compromising on mechanical integrity.
2. Has low thermal inertance, combined with the low pressure drop helps in transferring as much of heat as possible to the bubble.
3. Chemically inert (suitable for ammonia rich liquors)
4. Inexpensive material makes it extremely inexpensive once scaled up options are considered.

The calculations required for the sparger manifold and coupling to the sparger were determined by (Park *et al.*, 1976).

It was determined that for an oscillatory flow system, the best chambre volume would be approximately 1-4 cc.

The sparger was also designed to effect high heat transfer to the bubbles being formed without cooling it down. A sparger of any material will inevitably be heated by the hot air passing through it and so stainless steel was chosen as it has a low heat capacity, therefore, the steady state temperature of the diffuser during a run can be achieved faster. This results in a low thermal mass.

The sparger also required a lower pressure drop for the same reason. A higher pressure drop results in increased heat dissipation. Mesoporous (of the micro/nano scale) structures are really good for heat dissipation as has been observed for several hundreds of years and studied quite recently by (Fang, 2012).

The sparger was designed to have a proud centre *i.e.* is thicker in the centre by 1 mm to increase the pressure drop and force air flow hitting the centre to also use the sides thereby equalising the flow a bit. This is working concomitant with the trident inlet in order to equalise flow.

The bubble size was measured using acoustic bubble spectrometry, with distilled water as the liquid, and air as the gas, and resulted in a number average bubble size of 95 μm and a volume average bubble size of 240 μm .

Fluidic Oscillator

A jet diversion fluidic oscillator (FO) of the type described in (Brittle *et al.*, 2015, Fahad Rehman, 2015, Hanotu *et al.*, 2012, Desai *et al.*, 2018, Tesař, Tesař *et al.*, 2006, Zimmerman, 2008) has been used. The bubbles generated via the fluidic oscillator result in a hybrid synthetic jet as seen in Figure 17. A typical oscillator is used but made out of stainless steel in order to survive the hot temperatures.

Heater

Unlike Zimmerman *et al.* (2013a, 2013b), the heater was placed prior to the fluidic oscillator so as to minimise dampening of the oscillatory wave. This allows for a higher flowrate to go through the heater and at the allowable pressure drops associated with normal functioning of the heater. The change in the temperature would change the pressure drop associated

with the heater for the fluidic oscillator. This would result in an ascending frequency change and not be very controllable as it would then depend on the heating rate. Additionally, since the pressure drop across the heater would continuously be changing, the frequency as well as the flow through the oscillator would change (Strouhal number would change continuously). Therefore, it was decided to use the heater prior to the oscillator. An ON/OFF controller was used for this system instead of a PID system due to the slow response of the heater and minimising the minor changes to the temperature to minimise frequency changes in the system.

Pneumatic set up

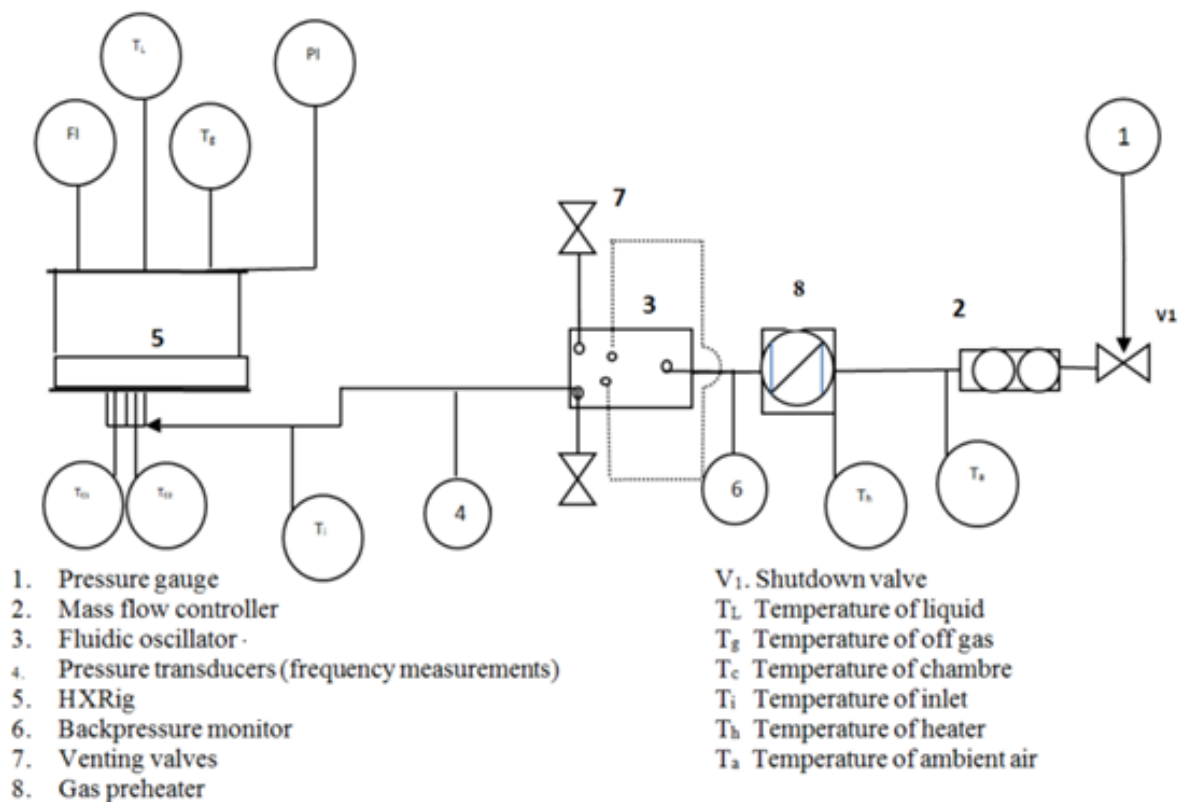


Figure 48 System Schematic

Figure 48 shows the schematic. The air supply is regulated via a pressure gauge and into an emergency shut down valve (V1 – standard ball valve). This is followed by a Mass Flow Controller which is used to control the air flowrate into the system. The temperature at this point is noted using a thermocouple. This is then fed into a process air heater (750W) which then heats the air to the required temperature (the heater temperature is measured and the

control thermocouple is placed in the chambre of HXRig). Process air heater is controlled using a PID controller with measurement for the control thermocouple being in the chambre right beneath the sparger.

The pressure of the system is measured (for room temperature (25°C) air, using Impress G1000 Pressure Transducers), and the controlled air flows into the fluidic oscillator following the heater. Appropriate amount of air is then siphoned off into HXRig as determined by the flow rate requirements of the oscillator. The oscillator requires a higher throughput into the system as it requires to be initialised. This therefore results in the use of vents in order to control apropos amount of air going into HXRig. The inlet is split into 3 and a pair of equi-responsive thermocouples assist in temperature control, allowing the monitoring for even flow distribution, and acting as redundancies for safety purposes. A flow indicator, pressure indicator and sets of thermocouples maintained at different liquid heights measure temperature for given liquid depth. An off gas thermocouple is also present.

Chemicals and Chemical Analysis

Ammonia Solution

Standard ammonia solution was prepared using dilution of ammonium hydroxide, Fischer Scientific, 7732-18-5 for analysis, 20% ammonium hydroxide solutions and they were diluted appropriately and checked with 1000 ppm (0.1M) standard – Cole Parmer (Item#WZ-27503-00)

Ammoniacal nitrogen concentration

The ammonium concentration in the solution was directly measured using the Cole-Parmer ammonium ion selective electrode (ISE) (#WZ-27504-00) as per the American Public Health Association (APHA (APHA, 2007)) Standard Method for the examination of water and wastewater (APHA, 2007) and literature (Marttinen *et al.*, 2002) (Silva *et al.*, 2004) (Collivignarelli *et al.*, 1998) (K. C. Cheung 1995, Cheung *et al.*, 1997). The probe can operate up to 18,000 ppm (~18,000 mg/L).

pH Measurement

The pH of the solution was directly measured using a Mettler Toledo LE 409 pH probe. These pH and ammonia concentrations were also confirmed by ALS Environmental Services

especially with the use of ammonia rich liquors as these liquids contain several different types of contaminants which result in cross sensitivities for these probes. (APHA, 2007)

Experimental Design (Turley, 2015 and Desai *et al.*, 2018)

Variable	-	+	Basis
Temperature (°C)	A 80	120	The initial test temperatures were taken from (Zimmerman <i>et al.</i> , 2013) to start the trial
Initial pH	B 10	11.5	Srinath and Loehr (Srinath and Loehr, 1974) suggested that, for a solution pH = 10.0 and T = 20°C (room temperature), the fraction of undissociated ammonia is 0.796 and for pH = 11.5 and T = 20°C, 0.975. Therefore, this experiment should show the effect, if any, of this difference and if evaporation of the water or removal of ammonia pushes equilibrium towards further production of ammonia without any alkali addition i.e. increasing the pH (Guštin and Marinšek-Logar, 2011)
Depth of liquid (mm)	C 5	15	The depth of liquid was chosen to be the minimum possible height that could be used in this system: 0.5 cm. The maximum height to be used is limited by the height of the experimental vessel.
Time (hrs)	D 0.5	1	The time was chosen to be 0.5 - 1 hours as this is well within the target operating envelope and provide the values required for calculating the mass transfer coefficients for this process
Initial concentration (mg L ⁻¹)	E 500	2000	Initial concentrations of 500 mgL ⁻¹ - 2,000 mgL ⁻¹ were chosen as wastewater which have been stripped in literature have typically had concentrations within this range
Air flowrate (LPM)	F 1	2	Rated flow across the designed diffuser/sparger.
Liquid Temperature (°C)	G 20	35	This was done due to noting that whilst room temperature is a nice standard to measure it with, generally speaking, the ammonia rich wastewater is at a higher temperature due to the methanogenic bacterial action.

Chapter 4 Results and Discussions

4.1 Resonant pulsing frequency effect for much smaller bubble formation with fluidic oscillation

Frequency sweep for different configurations

Steady flow

Bubble size for steady flow at the same conditions resulted in a volume averaged bubble size of approximately 350 μm and 450 μm at 86 slpm and 92 slpm conditions respectively.

Oscillatory flow

The frequency sweep performed over the gamut of frequencies for the different configurations and flowrates indicated the presence of the resonant condition or 'sweet spot' condition.

This confirmed previous work performed in literature that fluidic oscillation resulted in a significant decrease in bubble size when compared to conventional methods of microbubble generation. The sweep assisted in proving the hypothesis that there was a dip observed for all configurations at a singular frequency, with approximately 60% reduction in bubble size than the average bubble size estimated from oscillatory flow at other frequencies.

With the configuration that induced the higher negative feedback, there is a suggestion that two dips observed and this is probably due to the higher feedback introduced for oscillatory control thereby changing the effect of the system. The higher feedback in the system pushes a greater amount of flow back, which results in a greater amount of jet deflection. This results in a greater entrainment of the jet and increases the amount of jet that switches so that each oscillatory pulse is associated with increased pulse amplitude. The increase in the level of feedback has the advantage that the frictional losses are reduced but the onset of oscillation is delayed.

The varying the lengths of the tube were used to introduce a change in the feedback loop which would result in a frequency change. Frequency of the FO is dictated by the Strouhal number, which also means that if the flowrate is changed, the frequency changes. As an exemplar, for the condition of the lower feedback configuration (higher frictional losses), both feedback and frequency comparisons have been plotted.

Figure 49 and Figure 50 show that even though the feedback loop lengths were different, the frequency change observed due to the change in flow rate with respect to feedback loop length resulted in a minimum bubbles size at the same frequency. They are plots from a reading taken for single tubing, lower feedback configuration, at 2 different inlet global flow rates at 22 different frequencies. The bubble size distribution showed the dip in bubble size and the resonant condition or ‘sweet spot’ was obtained. Figure 49 shows that although the feedback loop lengths were different for the different dips in bubble size, the actual frequency remained the same and was approximately 150 Hz.

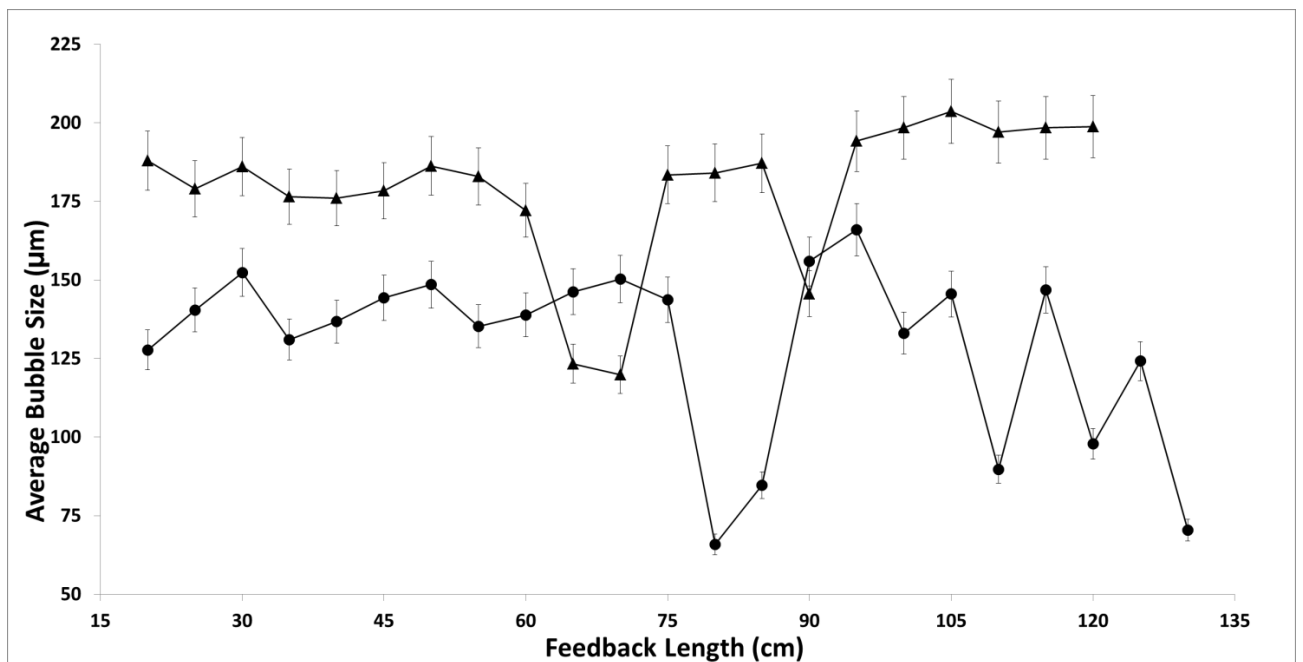


Figure 49 Feedback length vs Average Bubble Size. (● -92slpm OD4mm, ▲ - 86 slpm OD 4mm)

Figure 50 shows the FO frequency and bubble size domain for the lower feedback configuration and at two flowrates. At these two conditions, it is observed that the primary dip occurs *circa* 150Hz. The dip is large and observable and there is a suggestion of another dip prior to that. This is shifted slightly for different amplitudes. The frequency remains the

same for different configurations of feedback, resulting in a change in bubble size even for different conditions.

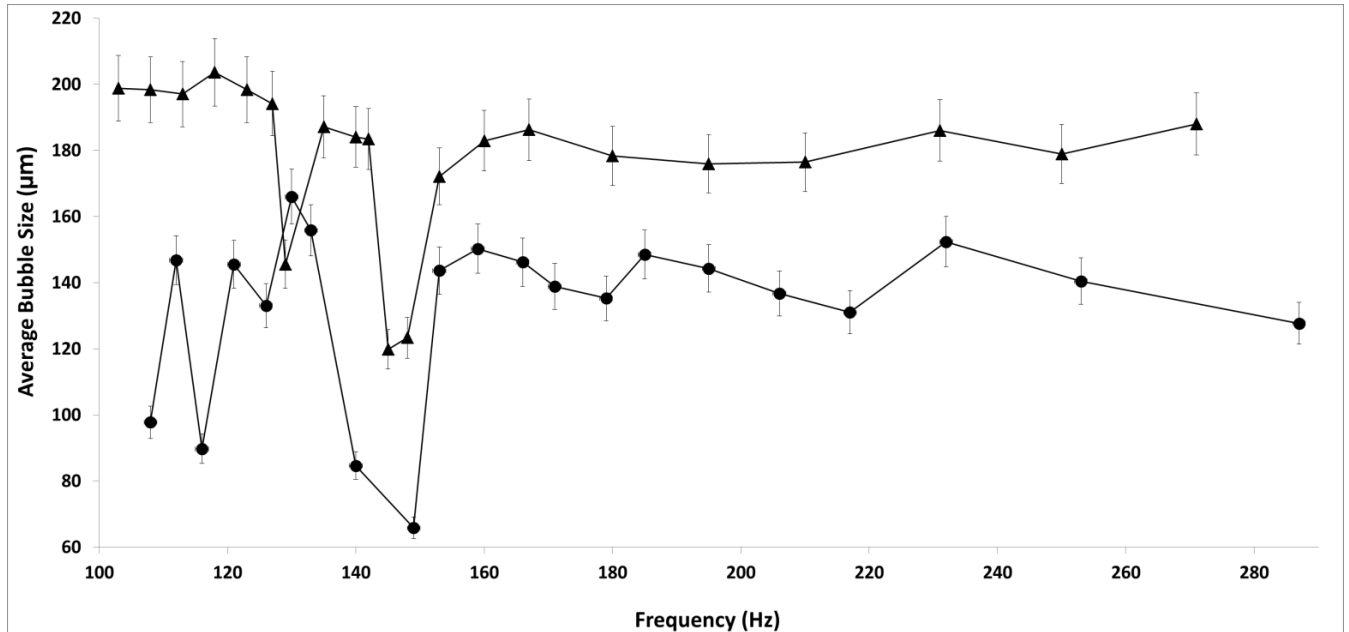


Figure 50 Frequency vs Average Bubble Size at different flow rates. (● -92slpm OD4mm, ▲ - 86 slpm OD 4mm).

In Figure 51, FO frequency and corresponding bubble size are plotted for the medium feedback condition at two flow rates. This condition is a good way to see the difference between the effect of the level of feedback condition or a proxy to frictional losses on the FO and this effect on the bubble size. The resonant dips are quite close to each other for this scenario. The frequency for the ‘sweet spot’ is similar to the low feedback condition and is at 150 Hz. There is a significant dip observed due to potential matching of the flow rate with the frequency of the system and bubble formation. As discussed, this is the medium feedback condition and is not as hampered by the frictional losses imposed on the low feedback condition, and so a sharp dip is observed. This condition was chosen such that the ducts would match the feedback tube and would result in minimal volume expansion or contraction for the flow, and it is seen in the bubble sizes obtained and the ‘sweet spot’ condition.

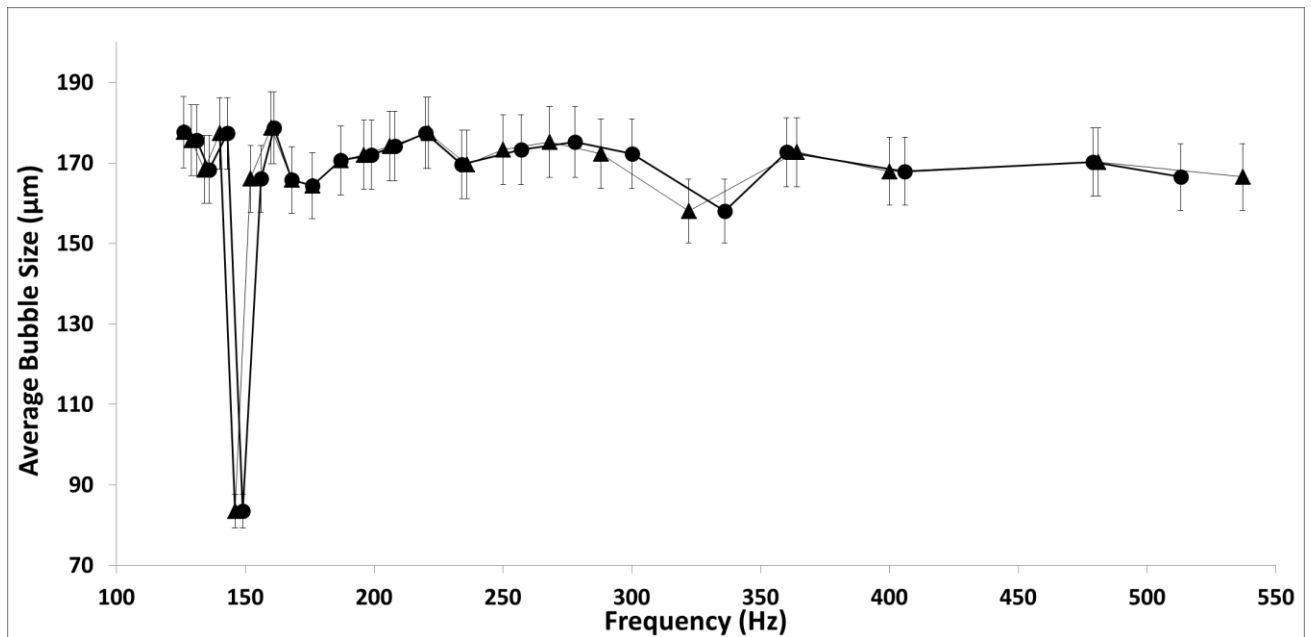


Figure 51 Frequency for bubble size - Sweet Spot – Medium feedback condition – (● -92slpm OD 6mm, ▲ - 86 slpm OD 6mm).

Figure 52 , shows that in the higher feedback condition (10mm O.D.), the frequency is higher for the dip aside from the initial dip. This is likely due to the higher amplitude observed for the higher feedback condition which results in lesser coalescence for the system. The dip observed is still consistent with the average bubble size formed at other ‘sweet spot’ conditions.

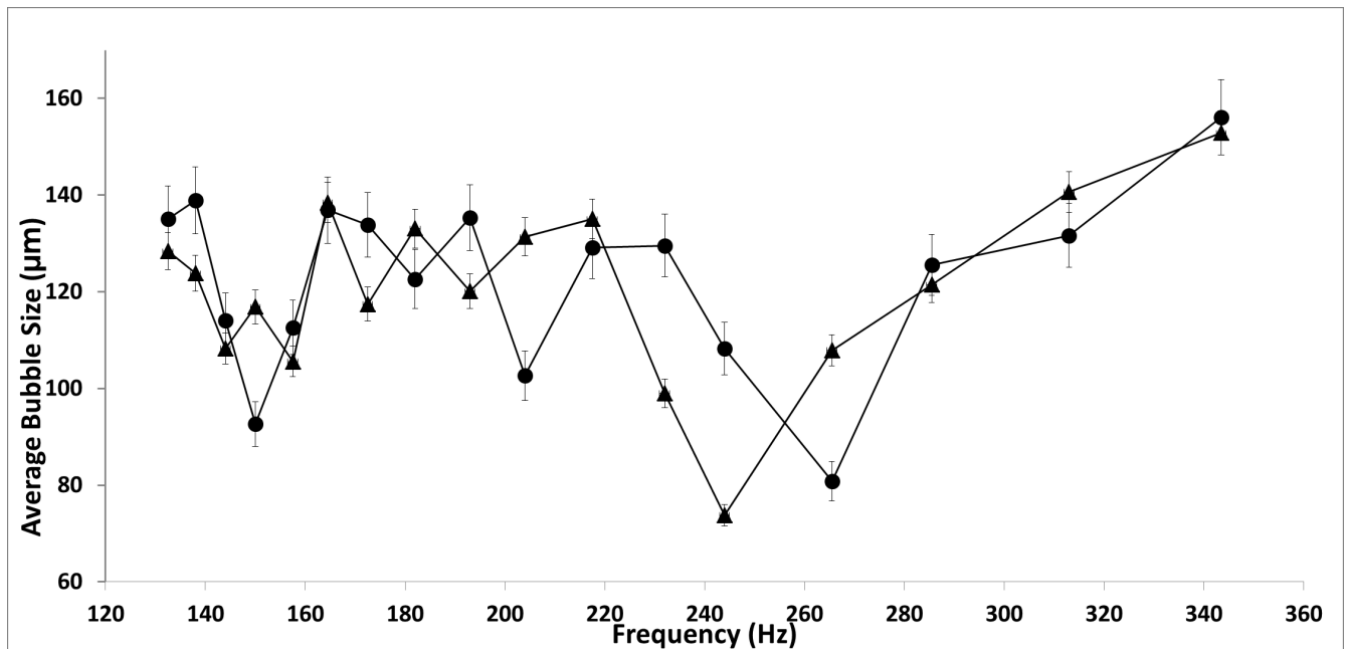


Figure 52 Bubble Size vs Frequency for two flow rates (higher feedback configuration). (● - 92slpm OD 10mm, ▲ - 86 slpm OD 10mm).

As discussed previously, there was a drawback to using the higher feedback condition, that the frequencies are limited. The frequency observed is typically lower than the other two conditions. The medium condition will have the highest range of operating frequencies, whereas the lower feedback condition will be limited due to the frictional losses, and the higher feedback condition needs to increase the flow across it but the pressure differential is not powerful enough to attain higher frequencies.

The presence of the sweet spot was observed for the higher feedback condition. However, the magnitude of the decrease in bubble size was not as significant as for the lower feedback condition (i.e. feedback loop length is constant but volume is lower) when considered in a relative manner. However, due to the greater amplitude, there is a higher frequency and several smaller bubbles being formed which results in the dampening of the sweet spot. There is another sweet spot formed at 250Hz

These figures also show a skew observed in terms of frequency and flow rate, with the skew being less for the larger feedback condition than for the lower feedback configuration indicating that even the shift observed in the frequency is due to the combination of the length of the feedback tube and the flow rate and this skews the bubble size and sweet spot.

These three conditions can therefore be taken as different conditions for which the sweet spot effect has been shown to be consistent. Of course, the flow rate is an additional variable influencing the frequency, (Tesař *et al.*, 2006) can be adjusted to achieve the same average bubble size. This is because the change in flow rate has a much larger impact on the frequency of the smaller feedback configuration than that of the larger one due to difference in the frictional losses for both conditions. The dip in bubble size is observed at different feedback conditions when the global flow rate is different. However, it is the same frequency at which bubble size reduction is observed, demonstrating that the change in global flow results in no significant shift in the frequency sweet spot, $\sim 150\text{Hz}$. A similar trend is observed at these different flow rates and there is a clear indication of the dip in bubble size at the specific flow rate and frequency. This is characteristic of the resonant condition or the 'sweet spot'. It is interesting to note that the extent of the dip in bubble size varies with the flow rate and therefore on the amplitude of FO. The sweet spot depends on the fluidic circuit i.e. sparger, liquid, FO, and gas aside from impinging flow rate. Amplitude is one of the major causes for a bubble size reduction which results in higher frequencies and bubble throughput.

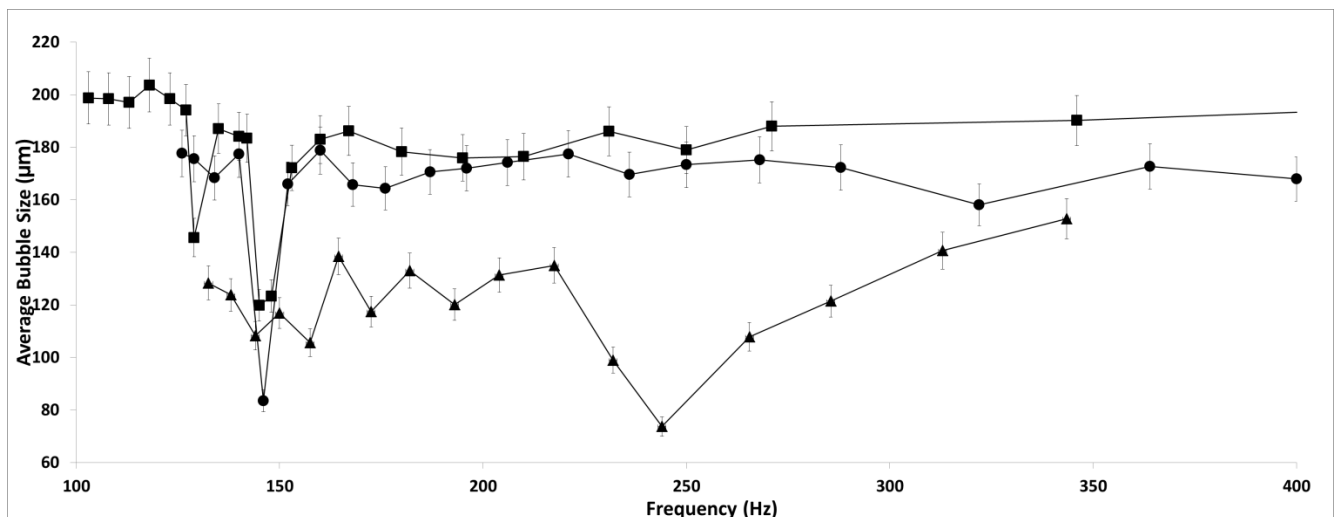


Figure 53 Comparison between amplitudes for the resonant or 'sweet spot' condition :.(\blacksquare - OD4mm , \bullet - OD 6mm , \blacktriangle - OD 10mm .)

It is seen in Figure 53, that there is a greater decrease in bubble size for the higher feedback condition (i.e higher amplitude), as also observed for higher FO impinging flow rate. This

happens at a higher frequency because of the change in the sweet spot condition. This means that the amplitude is higher for the same condition. This results in the lower feedback condition having the 'largest' bubble size for its sweet spot condition. There is a smaller difference between the lower feedback condition(OD 4mm) and the medium feedback condition (OD6 mm) due to smaller differences in the feedback introduced as compared to the higher feedback condition(OD 10 mm). This increases the condition substantially resulting in an increase in the effect observed

Mechanism for the 'Sweet Spot'

Bubble size is directly proportional to the rise velocity and inversely proportional to the bubble wake and liquid present in the system. There are two ways that can be used to increase the amplitude to test the hypothesis we have proposed – increase it by imposing a higher feedback (i.e. 10 mm OD) or by increasing the flow through the FO (86/92 slpm). Both conditions have been imposed in this study and this provides several conditions to observe for fluidic oscillation mediated bubble formation. The change between the lower feedback condition and the medium feedback condition is not as significant as between the two and the higher feedback condition. This is due to the large feedback introduced in the system in order to affect an improved performance regime in terms of momentum of the jet as well as amplitude of the oscillatory pulse.

This results in different systems being imposed whilst keeping the rest of the system as constant as possible. The reason why different diffusers/spargers were not used was because it would be difficult to compare two spargers (they can have several different properties – wettability, porosity, thickness, mesoporosity, polydispersity of orifice sizes, material of fabrication and pressure drop across the membrane).

The dynamics of bubbles generated in an oscillatory system can be defined by dimensionless quantities such as the Weber Number- We , Stokes Number - Sk , Strouhal Number - Sh and Reynolds Number – Re . (Kuneš, 2012a, Kuneš, 2012b)

The hypothesis comes from the fact that the bubble formation is most dependent on frequency of the system for oscillatory flow and the amplitude associated with it. If these two are appropriate, the bubble will cut off instantaneously and not coalesce. Balancing these forces together would result in pinch off. Compensation must be provided for the bubble rise and pinch off due to the oscillatory flow. The force balance turns out to be complicated due to the oscillatory waves and the hybrid synthetic jet engendered by the FO, resulting in a highly non-linear system.

It is seen in Tesař *et al.*, (Tesař, 2014, Tesař, 2013b) that the bubble rise is dominated by the conjunction and each individual conjunction leads to an increased probability for another

conjunction which leads to largeness in bubble size as compared to the orifice. Once two bubbles merge together, due to the increase in size and the change in the surface energy as well as the energy associated with the ascent, it is easier for the other bubble to catch up with it. This is better explained by the concept of bubble wake. Each bubble creates a wake (region of lower pressure) upon being created and this allows other bubbles to catch up, coalesce and result in larger bubbles.

Therefore, the smaller the bubble that is created will result in a smaller wake. However, it is easier for the small bubble to be affected by a wake of another bubble (especially a larger one – which is why a smaller bubble generated after a larger one usually results in conjugation.

Taking the size of the sparger to be the active diffusing area of the sparger:

$$0.15 \times 0.03 \text{ m}^2$$

The bubble flux recorded by the acoustic bubble spectrometry is based on the capture rate or acquisition rate that is set for the system at 200 ms.

The 200ms ensures that the flow in the system is captured at a fixed rate and this results in a delimiting information due to the resultant lower acquisition observed.

The capture results in a flow of 0.5 slpm.

Using these results, a size of 74µm approximately is observed. This is thus the minimum size achieved for this.

Taking this value and placing it in the equations (10-16) results in the bubble formation force, and taking a frequency of 150 Hz as the bubbling frequency, and the bubble flux from the ABS (120,000) it results in a pulse requirement of 0.007 bar to detach the bubble. This pulse requirement has been achieved by the oscillator as observed in Figure 36 and therefore explains the sweet spot possibility for these conditions of resonance.

Figure 36 shows that the amplitude of the FO pulse is approximately 0.2V, which is equivalent to 0.02 bar. This is roughly twice the required pulse strength for the bubble formation and this is

why the bubble is detached at the frequency. Judging by that, the frequency band is slightly wide due to the lack of conjugation at this point.

The amplitude of the pulse reduces as the frequency increases for the same flow and this results in intermittent pinch off (since the amplitude is important for imparting sufficient force for bubble detachment. Lower frequency has larger amplitude but the rate of generation is not fast enough. Additionally as can be seen in Tesař(Tesař, 2014, Tesař, 2013b), the conjunctions and conjugations result in coalescence which is perpetuated by the higher rise velocity of the larger bubble. This results in larger bubbles for the non-resonant conditions at lower frequencies. Therefore, the sweet spot is possibly the only condition where the amplitude, frequency and size is balanced so as not to have bubble coalescence.

There is higher amplitude for the higher feedback condition which results in the sweet spot occurs at a higher frequency (250Hz). This is what results in the larger increase in the number of bubbles throughput.

This chapter has placed a lot of emphasis on volume averaged bubble size which is suitable for transport phenomena but to compare the bubble sizes of the most widely reported values previously, such as Hanotu *et al.*, the size based on number of bubbles calculation - N_{Av} , provides a better idea for those applications concerned with size of the bubbles (flotation being one example)

Figure 54 shows the 'sweet spot' condition for a number average bubble size. This sweet spot is different as smaller number of bubbles can be generated at different conditions depending on the modality of the distribution, *i.e.* the dispersity of a bubble size distribution.

The 'sweet spot' changes slightly and shifts to 200Hz but there is still a dip observed at the higher frequencies.

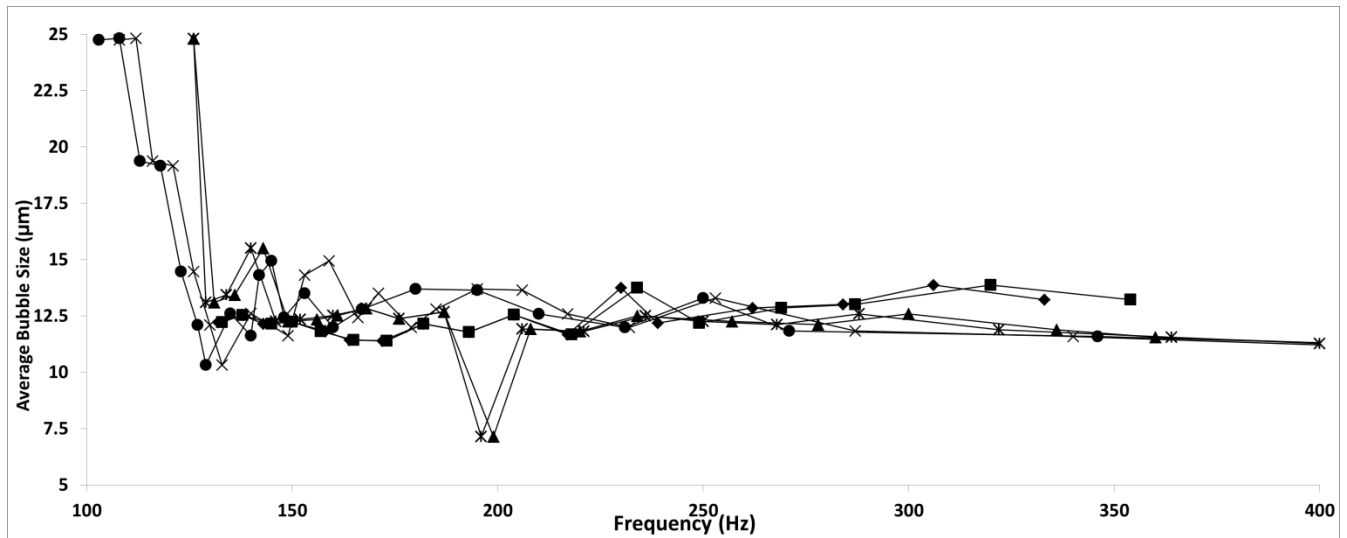


Figure 54 This is an exemplar of the sweet spot for the average bubble size when one considers number of bubbles as opposed to the volume fraction of bubbles. (◆ - OD 10 mm (92 slpm), ▲ - OD 6mm (92 slpm), ✕ - OD 4 mm (92 slpm), ■ - OD 10 mm (86 slpm), * - OD 6mm (86 slpm), ● - OD 4mm (86 slpm))

This brings down the average bubble size reduction producing about 7µm size bubbles in terms of average size distribution which makes it suitable for generating the bubbles for flotation studies. The sweet spot changes to 200Hz. This is because the size distribution changes due to the change in flow dynamics. The flow results in this size change as the effect of the number of bubbles cannot be discounted just as the volume average bubble size depends on the dispersity of the size distribution.

An exemplar is provided herewith.

The outlet flow of the diffuser was

0.1 lpm (1.67E-06 m³/s) for which, when corrected for the 200 ms acquisition rate of the ABS is

$$Q= 3.33E-07 \text{ m}^3/200\text{ms.}$$

N =Number of bubbles - Approximating total number of bubbles as 120,000 as an average, assuming that the distribution is narrow (for the purposes of a general understanding)

Assuming that since bubble pinch off force (by using equations 10-16) results in 0.007bar, and the pulse of the oscillator is an average of 0.02 bar, it exceeds the force required for bubble pinch off (*cf.* Figure 36). As seen from the FFT of the pulse for the oscillator, the pulse strength is at 0.02 bar per pulse which ensures that there is sufficient momentum and amplitude to generate the bubbles and ensure that the bubble detaches at each oscillatory pulse. So it is an accurate assumption providing no coalescence takes place. This is why the sweet spot is likely at 200 Hz as for the same momentum the force of the bubble pinch-off seems to be at the appropriate level.

This has been done in order to reduce the bubble size by matching the bubble formation characteristics to achieve the lowest possible bubble size and by increasing the amplitude of the oscillation in order to impart momentum to the jet and therefore the bubble so that it has a higher rise velocity. This reduces the bubble coalescence when the appropriate conditions are met. Too slow, and the bubble does not detach quickly enough and therefore coalesces, too fast, and the bubble cannot detach due to reduced amplitude and pinch-off. At the right frequency and amplitude, the resonant of 'sweet spot' condition, there is a possibility to detach the bubble at the smallest possible size for that system and it is significantly smaller than what was originally possible via conventional steady flow. This is achieved for the frequency at 200Hz.

Since $f = 200$ Hz means that it is per second, for 200ms, the equivalent frequency to be considered would be 40Hz.

Using the $A =$ diffusing area ($0.15 \times 0.03 \text{ m}^2$), and assuming that all the flow forms a bubble (there are no leaks and the bubble sizes are small enough to form bubbles rather than slugs,

$$V_{av} = \text{Average Volume of bubble formed} = \frac{Q}{A \times N \times f_{eq}}$$

$$= 3.33 \times \frac{10^{-7}}{0.0045 \times 120000 \times \left(\frac{200}{5}\right)}$$

$$V = \frac{4}{3} \pi r^3$$

Which results in D_B i.e. $(2r) = 6.8\mu\text{m}$ for 200 Hz.

This is in close agreement to the size obtained in the system. Of course, there will be several variations to this and this is due to the several other factors that interact with the system.

Figure 55 shows the calculations for a sweep for bubble formation via frequencies. Figure 56 shows the size for the bubbles that would be formed and when the graph is superimposed with the bubble size graph. There is an extension but this is likely due to the fact that at lower frequencies, steady bubble formation dominates as it results in faster bubble pinch-off.

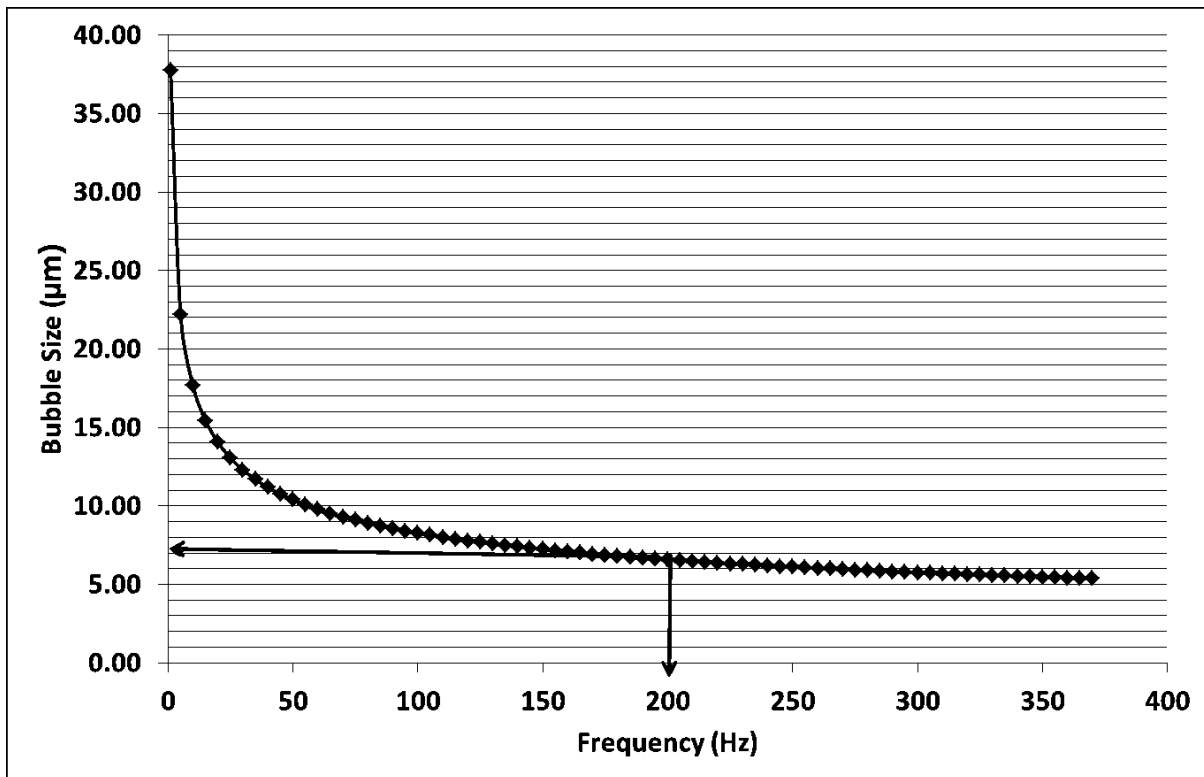


Figure 55 Bubble pinch-off and size generated using calculated values for various frequencies and the above calculations

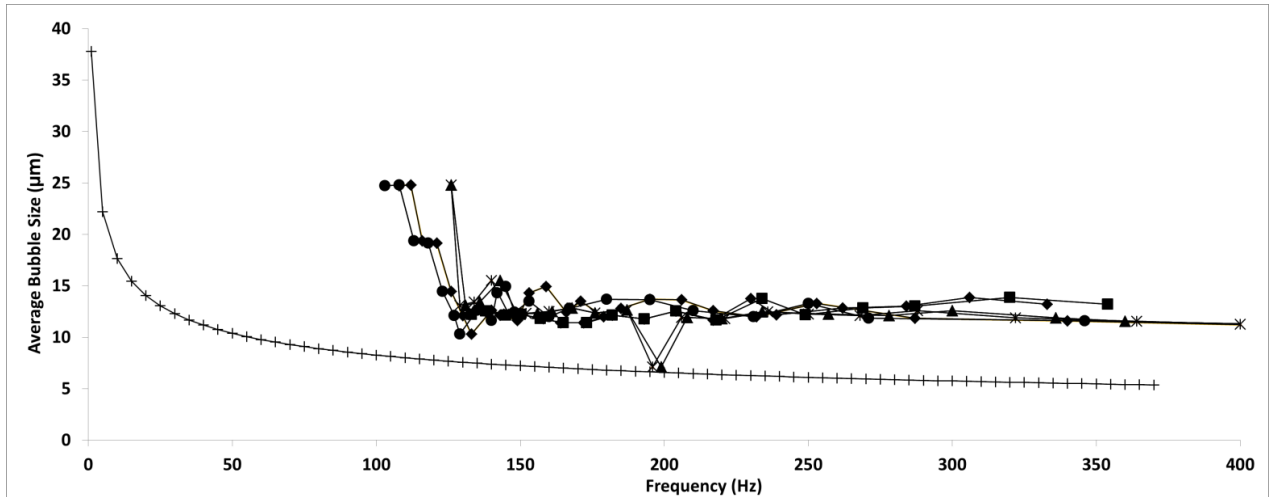


Figure 56 Calculated value as compared to the average bubble size garnered experimentally.

Deviation from the sweet spot is less than 0.0001%. + - Calculated ◆ - OD 10 mm (92 slpm),

▲ - OD 6mm (92 slpm), ✕ - OD 4 mm (92 slpm), ■ - OD 10 mm (86 slpm), * - OD 6mm (86

slpm), ● - OD 4mm (86 slpm)

4.2 Inventing the New Oscillator (Desai-Zimmerman Fluidic Oscillator)

Results and Discussions

Frequency tests are conducted and several of the hypotheses are tested. Comparisons are made (where possible) with the other oscillators – TZFO, microscaled TZFO, and TCFO.

The DZFO resonated at the various stated flows and there were several features to note when compared to the other oscillators. Each experiment conducted aims to demonstrate the hypotheses posed and compare the systems where they can. The experiments are also presented to showcase the various features of the different oscillators and what are the unique features arising from the DZFO.

Oscillator Comparison – Characterisation

The different oscillators were trialled for performance. Performance was measured using parameters such as frequency response, waveforms generated, amplitude/ magnitude of pulse, and backpressure (pressure drop across oscillator) for the same conditions imposed on each device.

The testing parameters were selected based on the aims of desirable characteristics in fluidic oscillators for microbubble production and according to our hypotheses.

The experiments were carried out at a standard global flowrate of 10 slpm, with the same length of the feedback introduced at 1.2m. There were 2 I.D. of feedback tubes used, in order to introduce different levels of feedback conditions as seen in the previous chapter. The Frequency, backpressure, and Magnitude of pulse were recorded. The waveforms were also recorded in order to see the variations. Configuration 1 was for a higher level of feedback (10mm O.D. and 8mm I.D.) whilst configuration 2 was for a lower level of feedback (6mm O.D. and 4mm I.D.). Figure 57 shows the waveforms corresponding to the conditions in Table 2. Table 2 delineates the results for this trial. TCFO configuration 2 did not oscillate. This is because, although it had been designed for these flowrates, it is the lower end of the flowrates that it would be possible to be designed for. This is due to the inability to initialise the pressurisation cycle in order to

initiate the oscillation. At the lower level of feedback, the TCFO would not work and a higher flowrate was used (15 slpm) and results were noted for that condition.

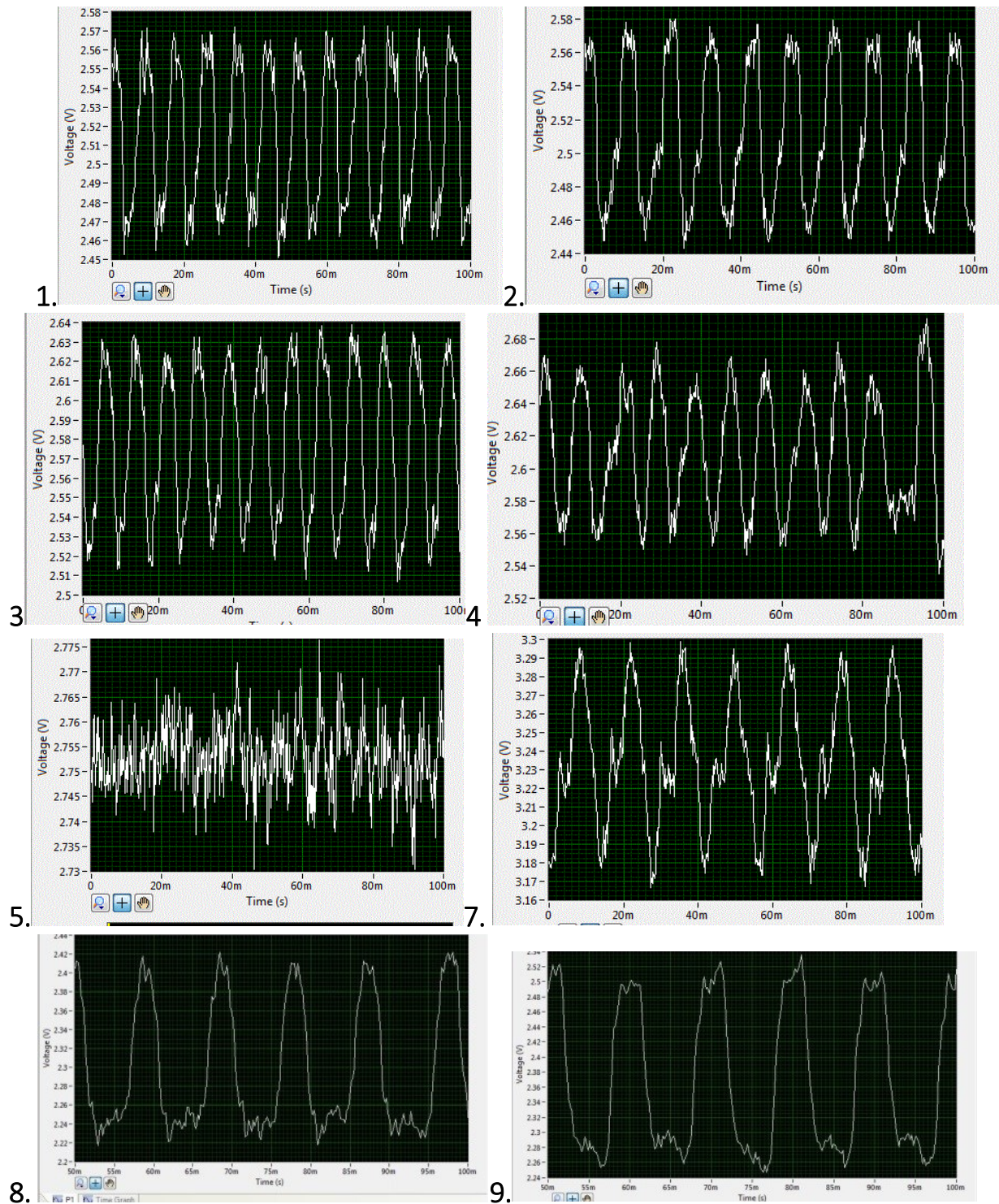


Figure 57 Waveforms corresponding to the Serial numbers in Table 2

Table 2 Results from the Oscillator Characterisation Study – Comparing Performances

S.No	Oscillator	I.D. of Feedback tube (mm)	Frequency (Hz)	Backpressure (bar(g))	Magnitude of pulse (bar(g))
1	TZFO 1	8	117	0.26	0.0158
2	TZFO 2	4	96	0.26	0.0132
3	Microscaled TZFO 1	8	121	0.28	0.0192
4	Microscaled TZFO 2	4	110	0.27	0.018
5	TCFO 1	8	72	0.29	0.0048
6	TCFO 2	4	NA	NA	NA
7	TCFO (15 slpm)	4	96	0.35	0.0125
8	DZFO 1	8	112	0.27	0.06
9	DZFO 2	4	101	0.28	0.05

A set of exemplar data is used as a comparison as several trials have been carried out with the same trend. This is a comparison study to benchmark the performance in terms of the parameters mentioned previously which helps characterise the oscillator and determine the best one for microbubble generation.

Figure 57 shows the waveforms corresponding to the conditions in Table 2 with the numbers in the SNo column corresponding to the numbers next to the waveforms in the Figure.

From Table 2 it is quite evident that the DZFO has the strongest pulse strength (highest magnitude) at 0.06 and 0.5 bar(g) for the two conditions. This is approximately 3-4 times higher in magnitude than the TZFO and microscaled TZFO configurations. The magnitude of pulse for the DZFO is 10 times higher than the TCFO. This is likely due to the low flowrate and higher friction losses for the TZFO, microscaled TZFO, and TCFO.

The TCFO has additional requirements in terms of pressurisation as described in the earlier section, which further reduces the pulse strength at the output and results in a dispersion of the wave. This is due to the compression effects observed for the capacitance or cavity filling.

Microscaled TZFO has a higher pulse strength as compared to the TZFO as the flow is amplified due to the smaller channels. So the amplification ratio, i.e. the velocity of the exit jet is higher, which leads to a higher magnitude of pulse but also concomitantly higher backpressure.

This means that the TCFO would not be effective for microbubble generation. Also, the performance of the TCFO, a load switch based, Zalmanzon type oscillator is extremely different from the performances of the jet deflection based (TZFO and microscaled TZFO) and the new type of oscillation mechanism (DZFO).

The backpressure reflects the loading on the oscillators. Whilst the flowrate is not high enough to cause significant frictional losses, there is still a difference that can be observed for the various systems. The DZFO has a throat of 1mm, the TZFO has throat of 1mm and 0.7mm control nozzle width, the microscaled TZFO has a throat of 0.5mm and control nozzle width of 0.35mm and the TCFO has 1 mm and 4mm channels. The mechanism of load switching results in higher backpressures, the jet deflection results in similar levels of backpressures whereas the new mode of oscillation results in a similar level of backpressure but much higher magnitude of pulse.

When the flowrates are increased to 20slpm, the TZFO has a backpressure of 0.57bar(g), the microscaled TZFO has a backpressure of 0.89 bar(g), the DZFO has a backpressure of 0.47 bar(g), and the TCFO has a backpressure of 0.81 bar(g). This indicates that the mechanism of switching is different for the different groups and also demonstrates how quickly the TCFO and the microscaled TZFO incur the friction penalties due to these losses and pressure drops. This then results in a dispersal of the waveform and a weaker bubble pinch-off pulse.

The frequency responses are comparable for each other. The crispness of the waveforms for the different oscillators is seen in Figure 57. The TZFO and the microscaled TZFO have similar waveforms and show dispersion to other modes. The DZFO has a crisp and clear waveform and

this is seen in subsequent studies as well. There is little or no dispersion of the wave. The TCFO also shows dispersion in other modes and not a crisp waveform. Also, it suffers from interference from the previous cycle, i.e. the compression effects that result in a secondart peak formed which is smaller in amplitude but very close in frequency. However, when the flowrate is increased, the waveform gets crisper although the reverberating/returning wave also correspondingly gets stronger as seen in Figure 58.

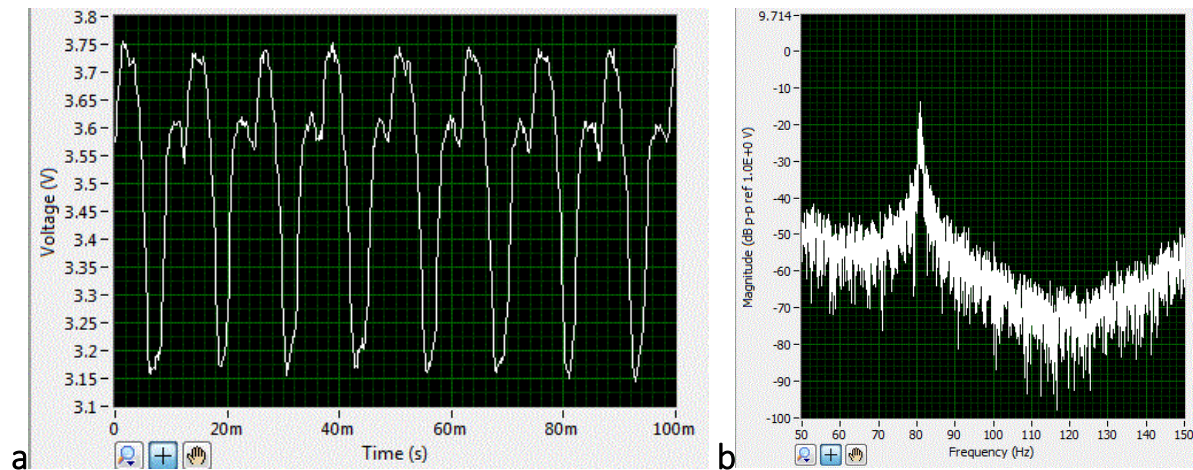


Figure 58 (left) a. TCFO Waveform (right) b.FFT for TCFO.

Figure 58a shows a TCFO waveform and Figure 58b shows the FFT for this waveform to obtain the frequency. As this oscillator has not been characterised by the high speed frequency acquisition system developed by Desai, the waveform seems different to that obtained and reported by (Tippetts, 2014). There are two peaks or waves that are joining into a coupled wave, and this is likely due to the compression/capacitive cycle associated with the load switched oscillator. The returning wave interferes with the compression wave and this causes the double peak. The FFT looks uneven as it is an averaging method and when the two frequencies are extremely close to each other, it will tend to produce the average of the two frequencies.

However, the next section tests the maximum frequency that can be attained in the system and prove the next hypotheses about the higher frequency modes possible.

High Frequency and presence of the third harmonic

Tesař (Tesař *et al.*, 2013a) using the excitation of the third harmonic for the Hartmann Resonator Oscillator attained a frequency response of 1800Hz.

The highest achievable frequency for the TZFO has been 300 Hz (in published literature) and 670 Hz by Desai via minor channel modifications.

The TCFO has been able to achieve 270-300 Hz as a frequency response.

The microscaled TZFO had been able to achieve 870Hz – 990Hz for the different types of configurations used but the $b=0.5$ mm (the one used in these trials) has been able to achieve a maximum of 860 Hz as can be seen in the FFT , in Figure 59.

Scaling it down further gets the frequency up at 1800Hz for $b=0.1$ mm but the channels are small and prone to clogging that it shall not be possible to use that device for any practicable purposes.

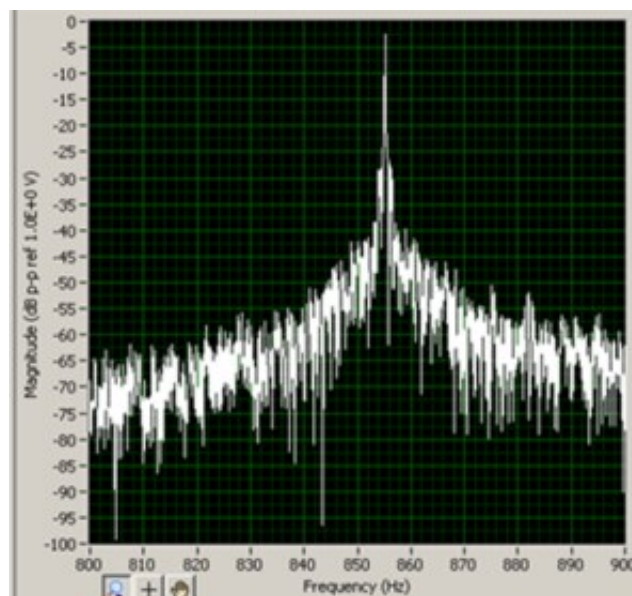


Figure 59 FFT for $b=0.5$ mm microscaled TZFO.

The ability to excite the third harmonic such that the third harmonic has a higher amplitude than the primary harmonic, and therefore is responsible for the generated pulse is performed for the Hartmann Resonator Oscillator and the hypothesis is to test whether the DZFO can also be able

to excite this mode since the underpinning mechanism of switching for the DZFO is based on acoustic resonance.

The experiment was carried out to find out the highest frequency that could be attained by the individual oscillators. The TZFO, microscaled TZFO , and TCFO attained the frequencies well below 1000Hz.

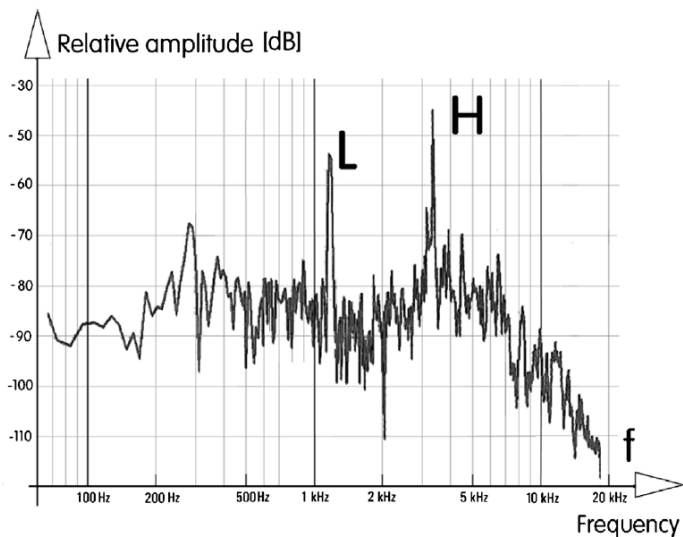
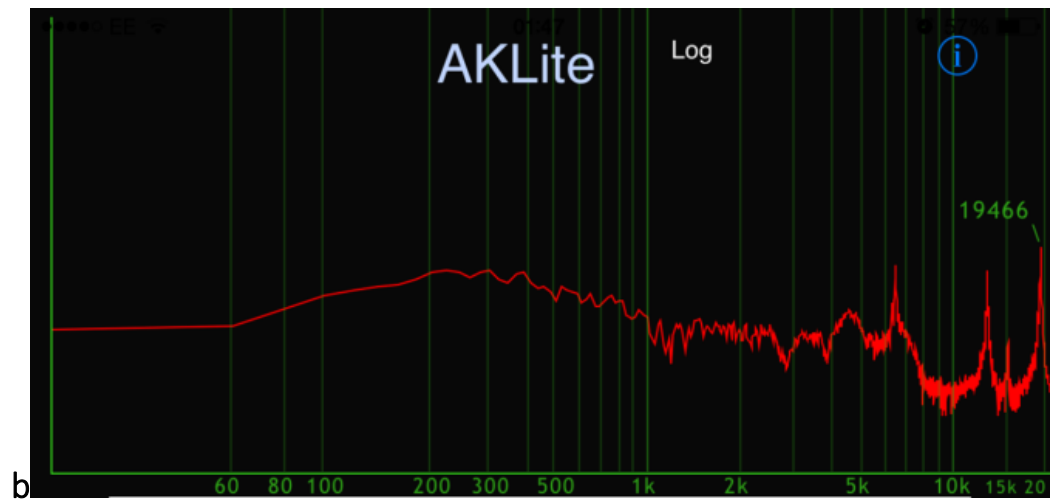
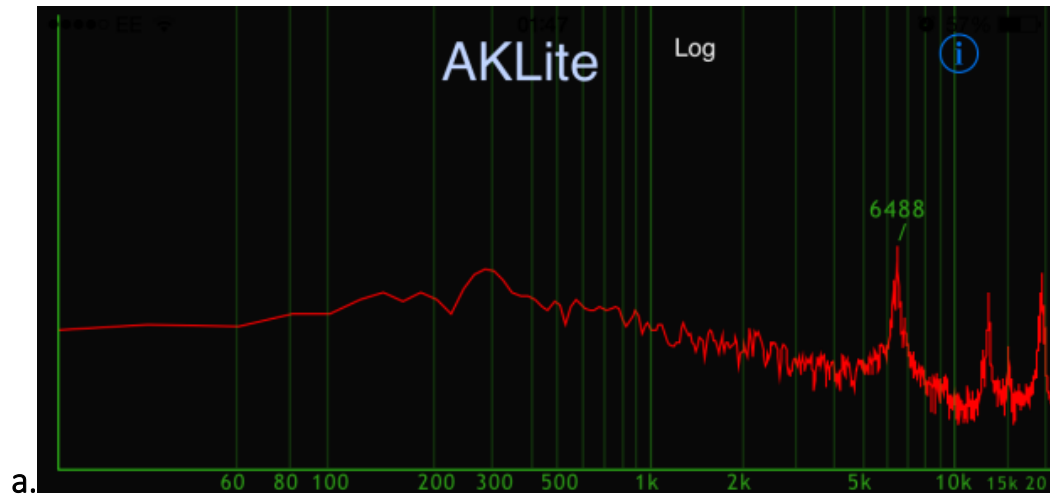
Figure 60 shows the primary frequency attained and the third harmonic excitation achieved for the DZFO as well as the third harmonic excitation by Tesař(Tesař *et al.*, 2013c) for the Hartmann Resonator fluidic oscillator. Figure 60c, shows the third harmonic excitation by Tesař. The primary frequency is approximately 1200 Hz, and the third harmonic is 3,600Hz. The figure has been taken from the paper and used to match the performance for the third harmonic achieved by the DZFO. A piezoelectric speaker/microphone had to be used to measure the frequency instead of the frequency measuring set up as the pressure sensors were not sensitive enough due to the pulse strength being very low. The flowrate for the DZFO was 1 slpm.

A frequency of 6,488 Hz is the primary frequency and 19,466 Hz as a third harmonic excitation (having a higher amplitude than the prime harmonic) is observed for the DZFO. This can be seen in Figure 60a (primary frequency) and Figure 60b(excitation of the third harmonic). This is significantly higher than any other oscillator observed especially with a channel width of 1 mm for the throat nozzle. The primary frequency is attained is significantly higher than the other oscillators. The third harmonic excitation then increases it to almost 20kHz. Higher frequencies for the third harmonic are also possible but are limited by measurement limitations. This provides more evidence that the acoustic mode is guiding the oscillation as physical switching of waves at such low flows (1 slpm) and low back pressure of 39 mbar is very unlikely. The other oscillators have not been able to oscillate at such low flowrates.

This mode also allows substantially higher frequencies attainable as compared to the other oscillators including the jet deflection based Hartmann Resonator fluidic oscillator which can attain a maximum of 3.6kHz based on the excitation of the third harmonic, whereas the prime frequency attained by the DZFO is 6.8kHz, which when excited , can attain approximately 20kHz. Additionally, whilst it was required to severely increase the flow rate of the Hartmann Resonator

oscillator (Tesar, 2013a) in order to attain that frequency and the flow rate was not measurable anymore, the DZFO was able to achieve that frequency at 1 slpm.

Additionally, the Hartmann Resonator fluidic oscillator requires 0.27g/s of mass air flow (>200slpm) as a minimum in order to start oscillating and a much higher rate in order to achieve the third harmonic excitation as opposed to the DZFO which attains it at 1 slpm, which is 0.02 g/s. This is 3 orders of magnitude different which differentiates it from the other oscillator.



c

Figure 60 a. Primary Frequency for the DZFO at 6,488Hz, b. Third Harmonic excited for the DZFO-Frequency 19,466 Hz, c. Shows the 1200 Hz (prime frequency) and 3,600Hz achieved as the third harmonic by Tesař in (Tesař, 2013a). (courtesy AKLite for a and b for audio spectrum analysis)

Better bubble generation due to lesser friction losses

An indicator for friction loss and the hypothesis for better bubble pinch off is the presence of a crisper waveform and no dispersion to the other harmonics.

This can be seen in Figure 61 which shows the FFT and raw magnitude waveforms obtained for microscaled TZFO (a and b) at 4 slpm , and the FFT and raw magnitude waveform for the DZFO (c and d) at 4 slpm. The other oscillators did not work at these flowrate. 4slpm is the lowest flowrate that the microscaled TZFO can oscillate. Whilst the waveforms obtained for the microscaled TZFO Figure 61(a and b) show wide FFT peaks and fairly broad magnitude waveforms (which indicate friction loss and dispersion into other resonant modes), the waveforms obtained for the DZFO, Figure 61(c and d) have a higher magnitude and pulse strength as well as are crisp with the FFT showing sharp peaks and the raw magnitude waveform is crisp and clear. This indicates a much lower friction loss and almost no dispersal into the other resonant/harmonic modes.

In the previous study, the peak obtained at 1slpm , still looked well preserved with sharp peaks and low dispersals whereas none of the oscillators would oscillate at such a flowrate. The frequency of approximately 20kHz confirms an acoustic mode of switching since load switching at such frequencies is impossible. There is a phase shift observed which links well with the theory and hypothesis about mode of oscillation and the FFT is also clearly delineated.

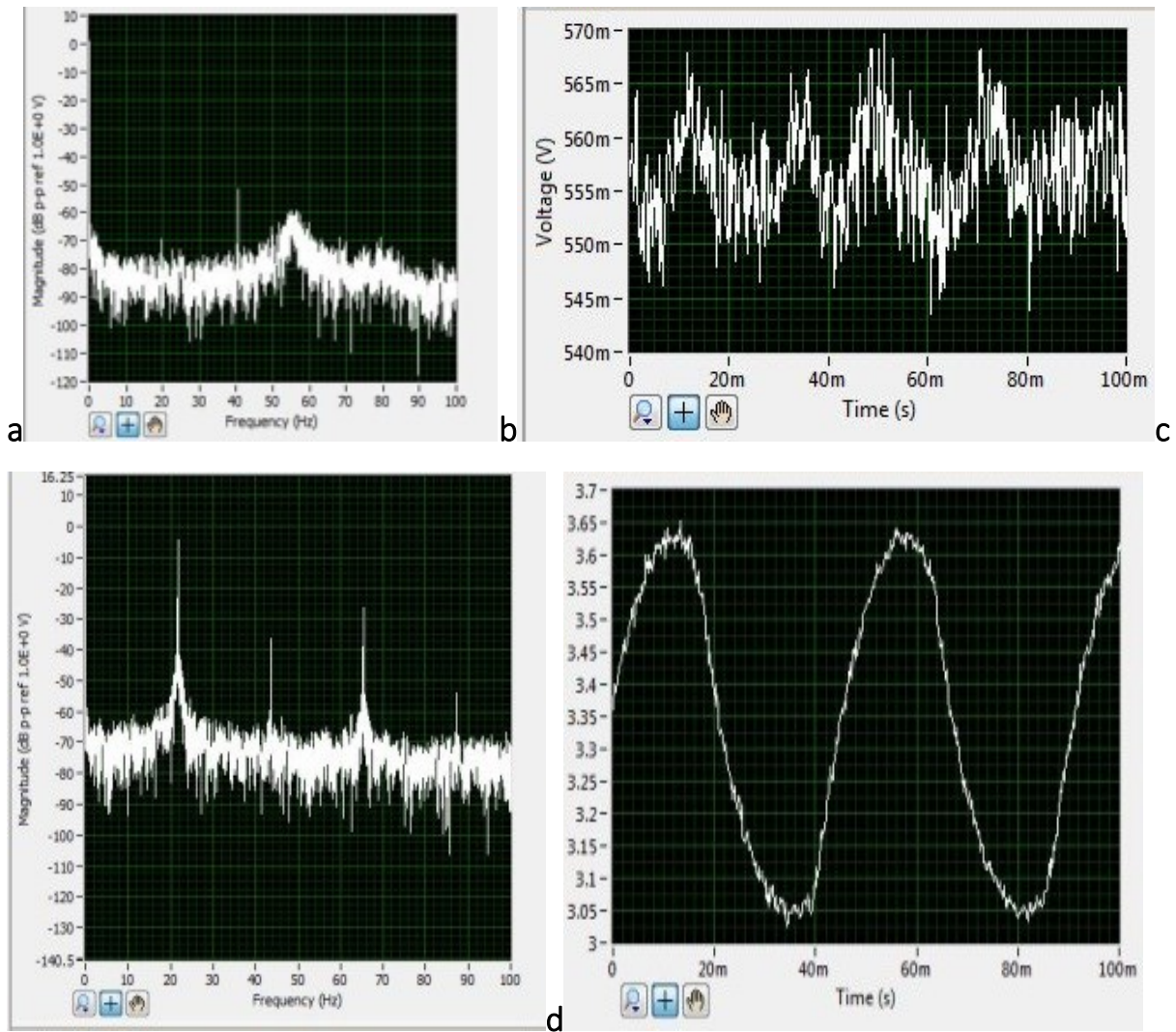


Figure 61 Microscaled TZFO (a- FFT , b-raw magnitude waveform) and DZFO (c- FFT, d- raw magnitude waveform)

This demonstrates the acoustic nature of the wavefront as well as the crispness of the momentum pulse and the lower friction losses for the DZFO.

These trials complete the comparison of the oscillators and the next set of experiments deal with proving the hypotheses for the mechanism of the DZFO and demonstrating the nature of the oscillation as well as test bubble formation characteristics for the DZFO.

Comparisons in terms of waveforms and outlet leg lengths

This section aims to compare the proposed mechanism of the DZFO to experimental observations carried out to prove the hypotheses and the proposed mechanism.

The motivation for the hypothesis on pressure drop reduction, crisper pulse and lower frictional losses is that there would be a reduction in the pressure drop of the system in order to generate the bubbles more efficiently.

It is done in order to prove the argument posed that reduction in friction losses and using a new mechanism for oscillation should translate into better bubble production by increasing amplitude of pulse, higher frequencies achieved and reduce the bubble size thereby increasing bubble throughput.

A comparison was made in order to determine the pressure drop across the DZFO i.e. backpressure, the amplitude of the pulse generated by the oscillator, the frequency of the oscillator and the magnitude of the pulse previously.

This part of the study is to determine whether the distance from the chambre of the oscillator to the outlet would have any impact on the pulse strength of the system which is a proxy for bubble formation when coupled with frequency as discussed in Chapter 2.

Changing the chambre surface area to volume ratio, i.e. smaller I.D. tubes as resonating chambres, would induce an artificial increase in the frictional losses of the system (increasing level of feedback) which has been previously investigated in Chapter 2 for the TZFO feedback loop. This is analogous to the resonating chambre for the DZFO.

The conditions that were kept constant were the standard flow rate of 10 slpm, the length of the resonating chambre – 120cm, and the distance of the distance of the outlet leg where the pressures were also measured. The waveforms were recorded at the outlet and the end of the tube depending on the distance – The 100 cm, 300cm, and 600cm.

The configurations tested were for i. 6mm OD resonator (4mm ID) and ii. 10 mm OD resonator (8mm ID)

The backpressure for (0.28 bar(g)) and the frequency (101Hz) for (i) and (0.27 bar(g)) and frequency of 112Hz for (ii) remained the same as per the previous experiment and see in Table 2.

Figure 62 shows the different waveforms which have been numbered from 1-6. Configuration(i) is listed first with 1 corresponding to 100cm distance, 2 corresponding to 300cm distance, and 3 corresponding to 600cm distance. Configuration(ii) is listed next with 4 corresponding to 100cm distance, 5 corresponding to 300cm distance, and 6 corresponding to 600cm distance. For each image, i.e. Figure 62.1, the waveforms on the top, which are extremely crisp correspond to those for the pressure transducer placed at the outlet leg of the oscillator, and the one on the bottom corresponds to the tube post the distance correspondingly.

Although the shape of the waveform changed slightly showing that attachment of the jet was changing with less interference from harmonic waves by increasing the distance between impinging wave, amplified wave and reflected wave, the frequency stayed the same and was controlled by the resonator rather than the distance.

For configuration (i) there was a slight change (less than 3Hz) which can be attributed to the L_1 fraction changing. Magnitude of pulse is equal to 0.025-0.05 bar.

For configuration (ii) there was a slight change (less than 2Hz) which can be attributed to the L_1 fraction changing. Magnitude of pulse is equal to 0.05-0.06 bar.

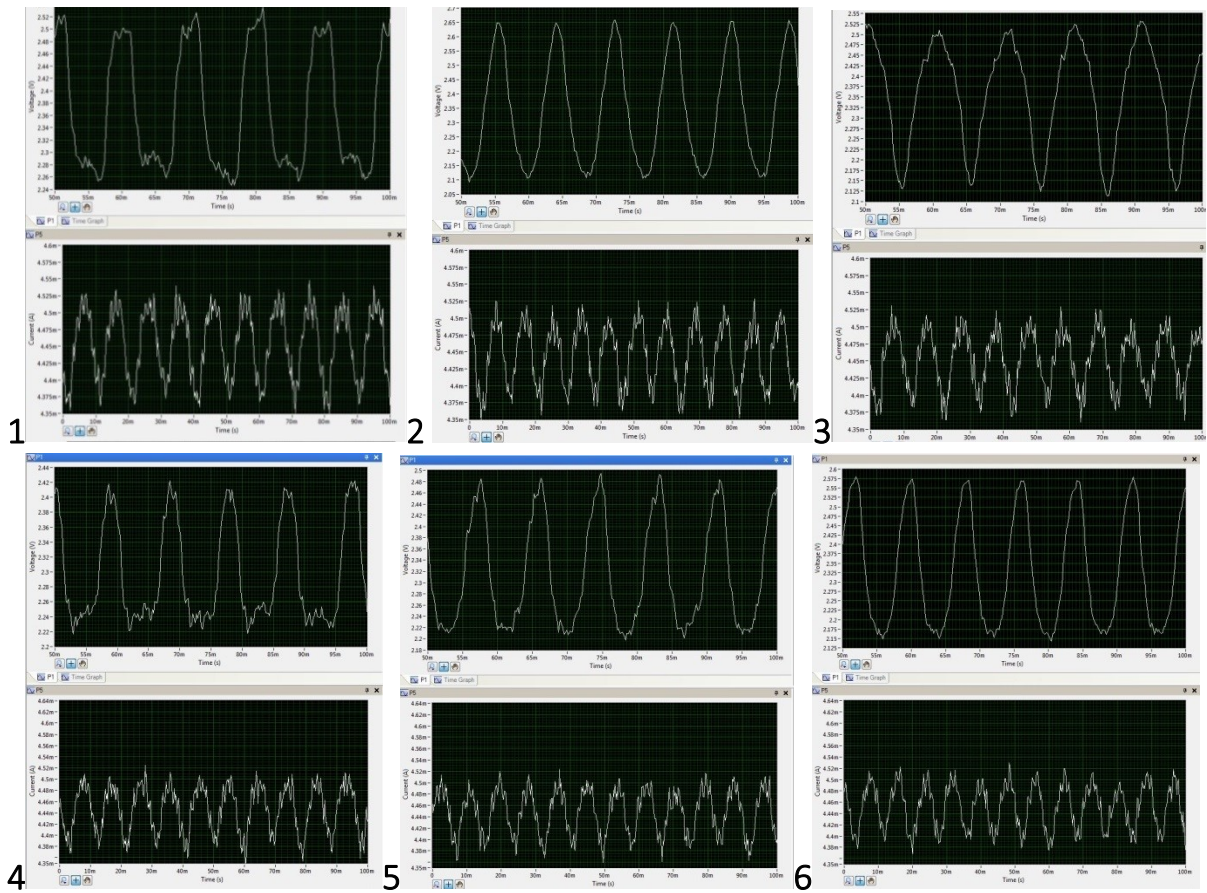


Figure 62 Waveforms at various distances with pressures noted at the outlet and corresponding distance (100cm, 300cm, and 600cm) for configuration(i)- 1,2,and 3, and configuration(ii)-4,5,and 6.

The waveforms are crisp and get ‘cleaner’ with increase in length of outlet shows that the interference is reduced from the backscatter and reflections which improves the switching mechanism. The reduction in interference results in a much cleaner raw waveform. This supports the acoustic basis of the mechanism.

The bubble size is reduced with lower friction and increased pulse strength which corresponds to the findings in Chapter 2 which results in the following:

The bubble size for configuration (i) average bubble size – 60 μm - average number, and 210 μm - average volume

The bubble size for configuration (ii) average bubble size – 30 μm - average number, and 160 μm -average volume

The change in the average bubble size is not distance dependent for these distances. This shows that for a reduced friction loss, there is smaller bubble generation. The possibility for a larger difference in the bubble size generated between the two configurations can be likely attributed to the low overall friction losses across the DZFO, which then result in a larger difference between the two configurations as opposed to that for the TZFO.

The bubble size for the comparable oscillators is seen in Table 3 and follows conditions from Table 2. However, the TCFO has only one condition since it does not oscillate for Condition 6, and Condition 7 has a higher flowrate which is not a fair comparison for bubble size studies as they will be larger than the other oscillators. These points are single values and have been placed here as indicative bubble sizes.

Table 3 shows that the TCFO is not ideal for bubble size reduction and this is likely due to the returning wave, seen in Figure 58, which interferes with bubble generation. It also has only a single output, which increases the frictional losses associated with it for bubbling. The TCFO, TZFO, and microscaled TZFO show a similar trend to the DZFO in terms of the bubble size in terms of the feedback level on them and the impact of frictional losses on the system. However, this is not as prominent on the TZFO and the microscaled TZFO as compared to the DZFO. The DZFO has a smaller bubble size as compared to the others for this test. A frequency sweep has not been performed which means it is likely not the resonant frequency ('sweet spot') that is operating currently. The higher amplitude of the DZFO is likely impacting the bubble size and this can be seen here. The microscaled TZFO, which has a higher amplitude as compared to the TZFO, has smaller bubbles generated. The TCFO has larger bubbles due to the lower amplitude generated by the oscillator.

The bubble size distribution obtained by the DZFO is narrower than the bubble size obtained for the other oscillators. This is also likely due to the higher amplitude of the DZFO, as it prevents conjunctions and coalescence of the bubbles leaving the orifice.

The waveform of the DZFO, as seen in Figure 62 and the other oscillators seen in Figure 57, show that the crisp and clear waveform generated by the DZFO, is likely impacting the bubble size. The TZFO and microscaled TZFO have similar waveforms and generate bubbles of a similar size. The TCFO has a waveform that has a lot of losses due to dispersion into the other modes, (the TZFO and microscaled TZFO also face that problem but less so), and this can be seen in the waveform and the bubble size.

Table 3 Oscillator- Comparing bubble sizes

S.No	Oscillator	I.D. of Feedback tube (mm)	Frequency (Hz)	Number Average Bubble Size (μm)	Volume Average Bubble Size (μm)
1	TZFO 1	8	117	93	227
2	TZFO 2	4	96	115	420
3	Microscaled TZFO 1	8	121	51	175
4	Microscaled TZFO 2	4	110	72	310
5	TCFO 1	8	72	168	495
8	DZFO 1	8	112	30	160
9	DZFO 2	4	101	60	210

The following results demonstrate the acoustic nature of the DZFO, and the potential possibility to further improve the bubble generation capabilities.

Different Possible Waveforms Generated and 'Beats' dynamics

This different possible waveforms being generated by the DZFO indicate that it is extremely likely that the mechanism proposed for the DZFO is accurate. Several different types of waveforms are possible to be generated, with different shapes and features including 'beats' dynamics. Saw type, shark tooth, square waves, and others are possible using the DZFO.

This is a feature as yet not available or possible in other fluidic devices. There has been some work on coupling fluidic devices to get waveforms and there is an attachment principle involved but bubble detachment via this process may be even more efficient than previously obtained due to the sharp peaks obtained which look ideal for bubble formation. This needs further testing in terms of bubble formation ability but the likelihood is high considering the waveform and the proposed mechanism for oscillator driven microbubble generation in (Tesař, 2015, Dančová *et al.*, 2013, Jilek, 2013, Tesař, 2012, Zimmerman *et al.*, 2009c, Zimmerman *et al.*, 2009d, Tesař, Tesař)

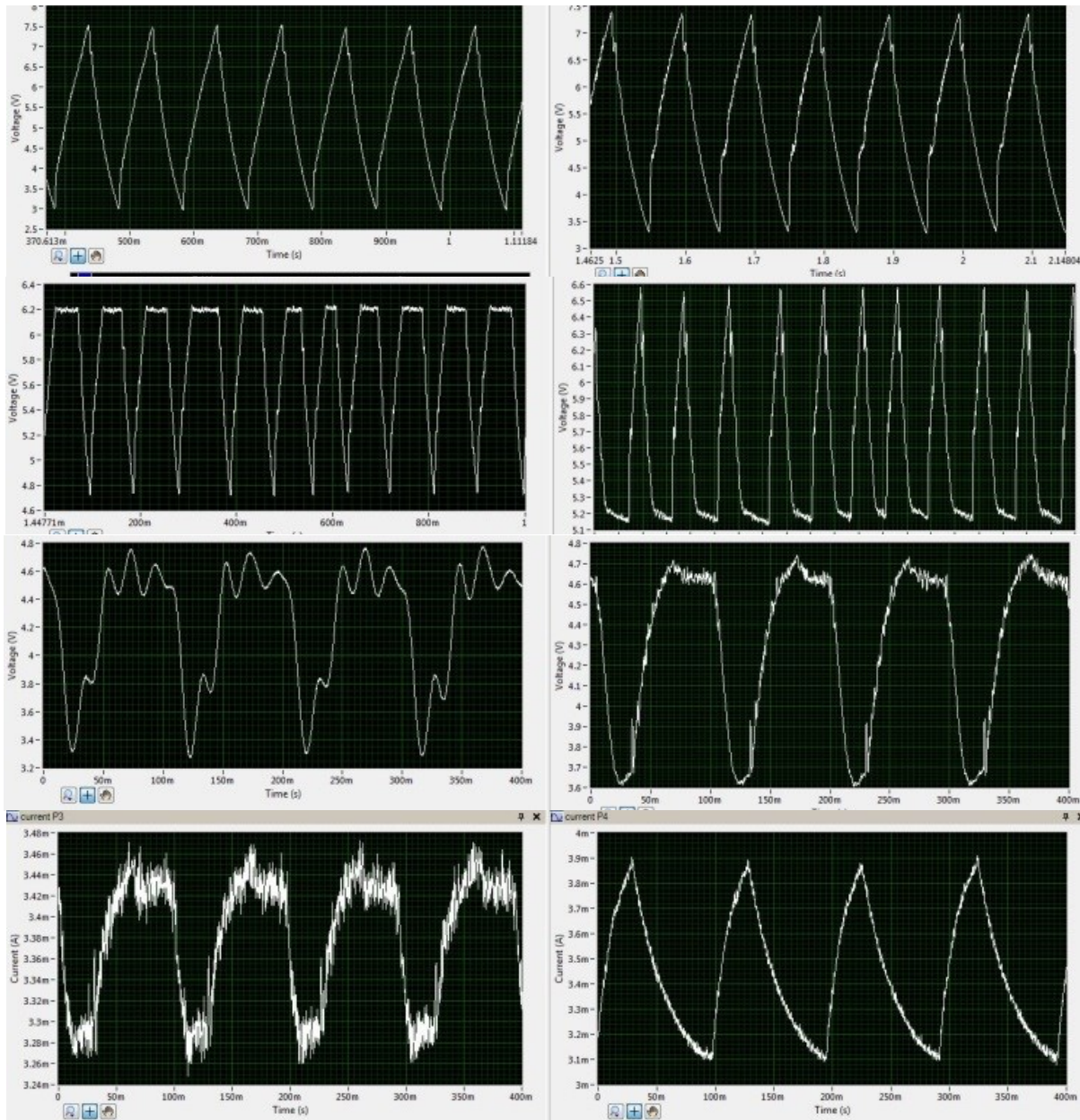


Figure 63 Different waveforms possible using different combinations of resonators

Another feature observed from the waveforms in Figure 63 and Figure 64 is the negative pulse and positive pulse for each leg of the oscillator. Since the pressure transducers are measuring in real time, the pulse demonstrates the positive and negative nature of the oscillatory output for each outlet leg simultaneously, demonstrating that the wave is part of the same but inverted i.e. showing negative pulse and not just 2 separate mechanisms taking place.

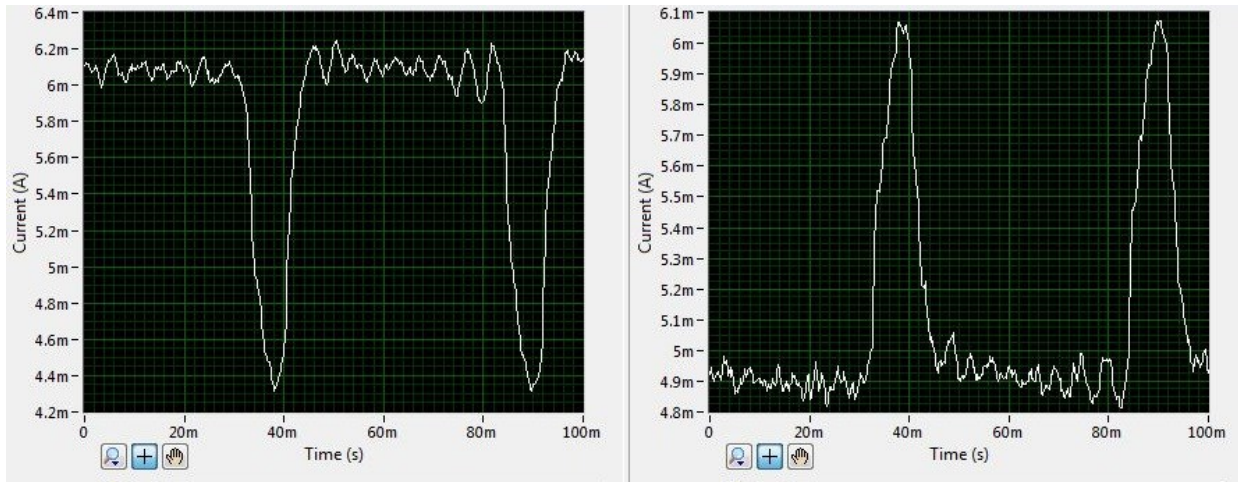


Figure 64 Principle of superposition (constructive interference) and destructive interference (left) and Amplitude data for various conditions similar to (left) for both outlet legs (right).

Figure 64 shows the principle of superposition with respect to constructive interference and destructive interference. The major observation here is the behaviour of the wave dynamics where the interference behaves precisely like an acoustic wave with constructive and destructive interference. The switching takes place but there is an interesting effect. Whilst acoustically, it can be easily reconciled that the wavefront is based on the modulus of the frequency difference, *i.e.* the average frequency is $f_1 + f_2$ and the beat frequency is $Abs. (f_1 - f_2)$.

However, the gas flow pulsating/transmitting or bubble formation is as if there were two frequencies operating for the generation imposed at the same time as observed by Tesař in the third harmonic excitation of the Hartmann Resonator fluidic oscillator (Tesař, 2014).

This is seen in Figure 66 which has been taken from (Tesař,2014) as it explains the case where there are two waves, the primary harmonic (600Hz) and the third harmonic (1800Hz) which acoustically add together and the waveform observed or noted by a pressure transducer resembles a rectangular wavetrain and is a summation of the two components. However, for the pulsating gas and the associated bubble generation, there are two different frequencies that are being used to generate the bubbles and cause the gas to oscillate.

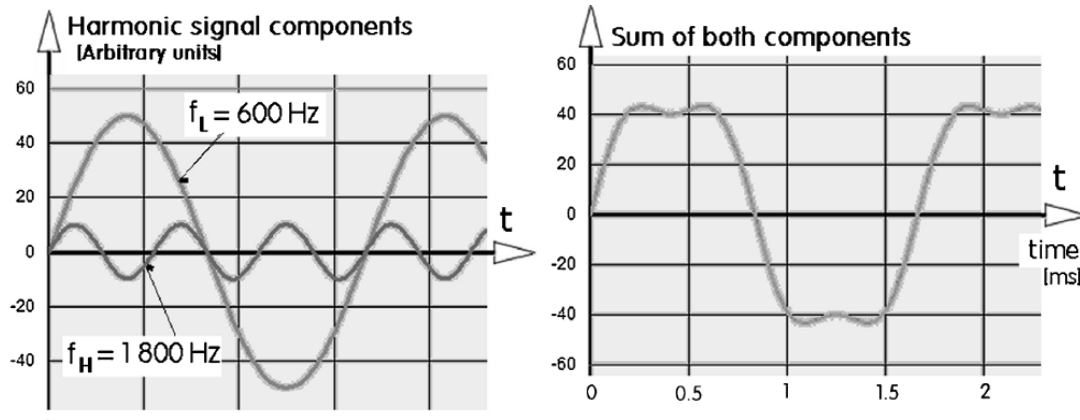


Figure 65 Third Harmonic Excitation and implications for other acoustic effects (Tesař, 2014)

Whilst the third harmonic excitation is a singular effect for the Hartmann Resonator Fluidic Oscillator by Tesař and the DZFO, the DZFO is based on an acoustic mode for switching and therefore there are several acoustic effects that can be exploited with this device. This can be used to adapt the DZFO for a variety of applications where this is required or subharmonic frequencies are required – gas mixing operations and use as a valve. The delay added here makes for an extremely simplified circuit making it highly manoeuvrable.

The output signal is higher than what would normally be obtained for a symmetric configuration of resonant chambers and this can be tuned further for specific applications.

An example is present in Figure 66. Amplitude waveforms for the system for (a) standard DZFO with equal resonating chambers – maximum amplitude at 6.2mA and minimum amplitude of 4.6mA as a non-dimensionalised parametric response, (b) showing principle of constructive interference due to asymmetric chambre lengths with maximum amplitude at 6.2mA and minimum amplitude at 4.1 mA (c) showing asymmetric chambers but the principle of destructive interference (not entirely destructive as that would convert it to steady flow) with a maximum amplitude of 5.8mA and minimum amplitude of 4.9mA.

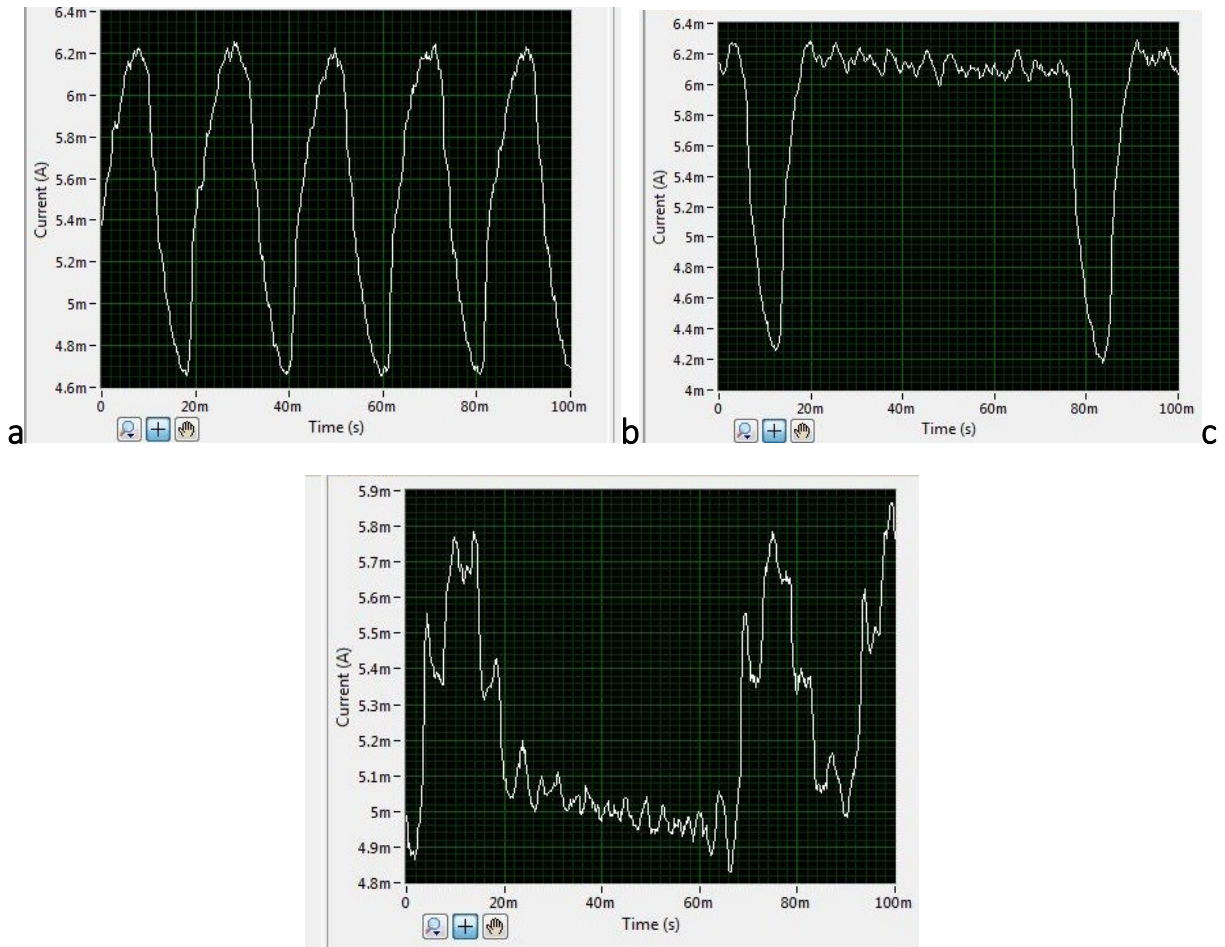


Figure 66 Amplitude waveforms for the system for (left) a. standard DZFO with equal resonating chambers (middle) b. demonstrating principle of constructive interference due to unequal chamber lengths (right) c. showing unequal chamber lengths

The phenomenon of beats can then be translated into microbubble generation in viscous liquids as this has not been achieved in an energy efficient manner. The rise velocity of a bubble in a highly viscous liquid is low, and this is a problem unless the impinging jet has a high amplitude that imparts momentum to the bubble. The higher pulse strength would ensure bubble detachment overcoming conventional bubble forces and forcing the bubble to detach for highly wetting or highly viscous liquids easily (*cf.* Appendix for work on DZFO application in ionic liquids).

Low oscillation frequencies such as those achieved by the Vortex fluidic oscillator (2-10Hz) or high frequencies as achieved by the Hartmann Resonant fluidic oscillator (350-400Hz) are easily achieved by the DZFO but this brings about the possibility of even partial/fractional frequencies.

The asymmetry introduced to the bistable device also creates another interesting phenomenon. Unequal pulsations on each output leg can be used for other purposes such as ratio controlled operations or ratio based mixing or disproportionate gas mixing (i.e. inexpensive way of mixing gases to achieve 75%/25% mixtures and 25%/75% mixtures). Figure 67 shows the unequal pulsation wherein the pressure transducers measure, simultaneously, the frequency and waveform response on each leg.

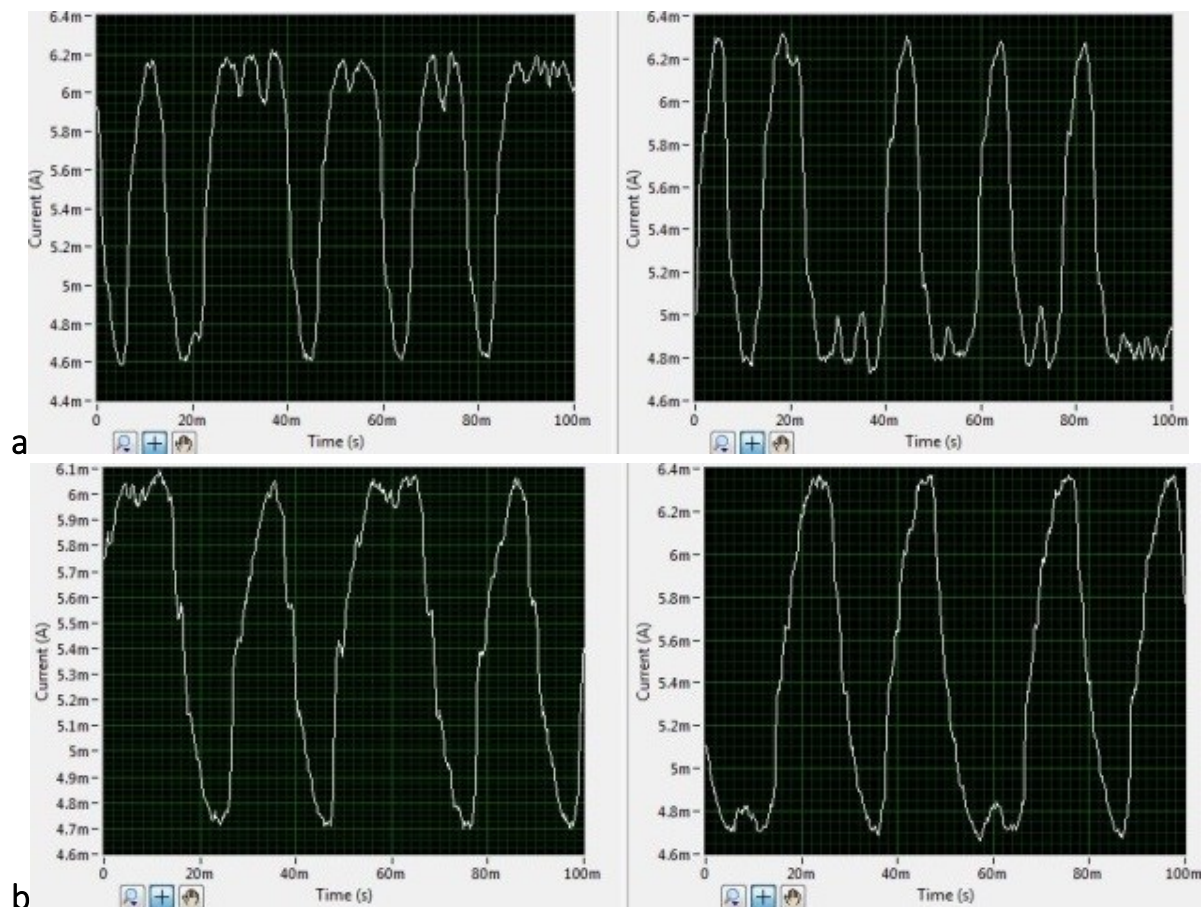


Figure 67 Two unequal waveforms (a and b) demonstrating the ability to generate two separate gas mixtures or have ratio controlled operations in place

These two unequal waveforms in Figure 67 (a and b) demonstrating the ability to generate two separate gas mixtures or have ratio controlled operations in place which has not been easily performed for other devices unless a combination of devices are added which increase the probability of failure and decrease energy efficiency(Tesař, 2007c). Each leg will have positive output and a negative cycle but the asymmetric nature of the pulse ensures unequal mixing but controlled mixing. This can also be used for flow diversion, controlled vapour release, heat transfer and recovery applications as well as for energy harvesting.

Figure 67a, the wave train can be seen as it is just merging into a larger rectangular waveform. The asymmetry of the oscillation shows how the wavetrain is made from the combination of the different waves. Similarly, Figure 67b, the combination of the waves merging into the wavetrain and not for the other set.

4.3 Comparison of Bubble Size distributions inferred acoustic, visualisation, and laser diffraction

A comparison was made on the bubble sizing with the three methods and to ensure repeatability, the frequencies for the system were measured. Different frequencies were obtained for the FO using feedback loops and flow rates as described in previously published papers (Brittle *et al.*, 2015, Desai *et al.*, 2018, Tesař *et al.*, 2006) . Figure 68 and Figure 69 show the bubble size distributions estimated for P4 aerators at different flow rates and for 2 feedback loops using the 3 methods.

For Figure 68, the acoustic method shows an average bubble size with smaller bubbles than the other methods. However, when the bubble size distribution is checked for each data point, then it turns out that even for conditions with the same bubble size, the bubble size distribution is different. It is co-incidental that the bubble sizes are comparable for the optical and photonic method as that is due to the averaging of the larger and smaller bubbles which leads to the size differential.

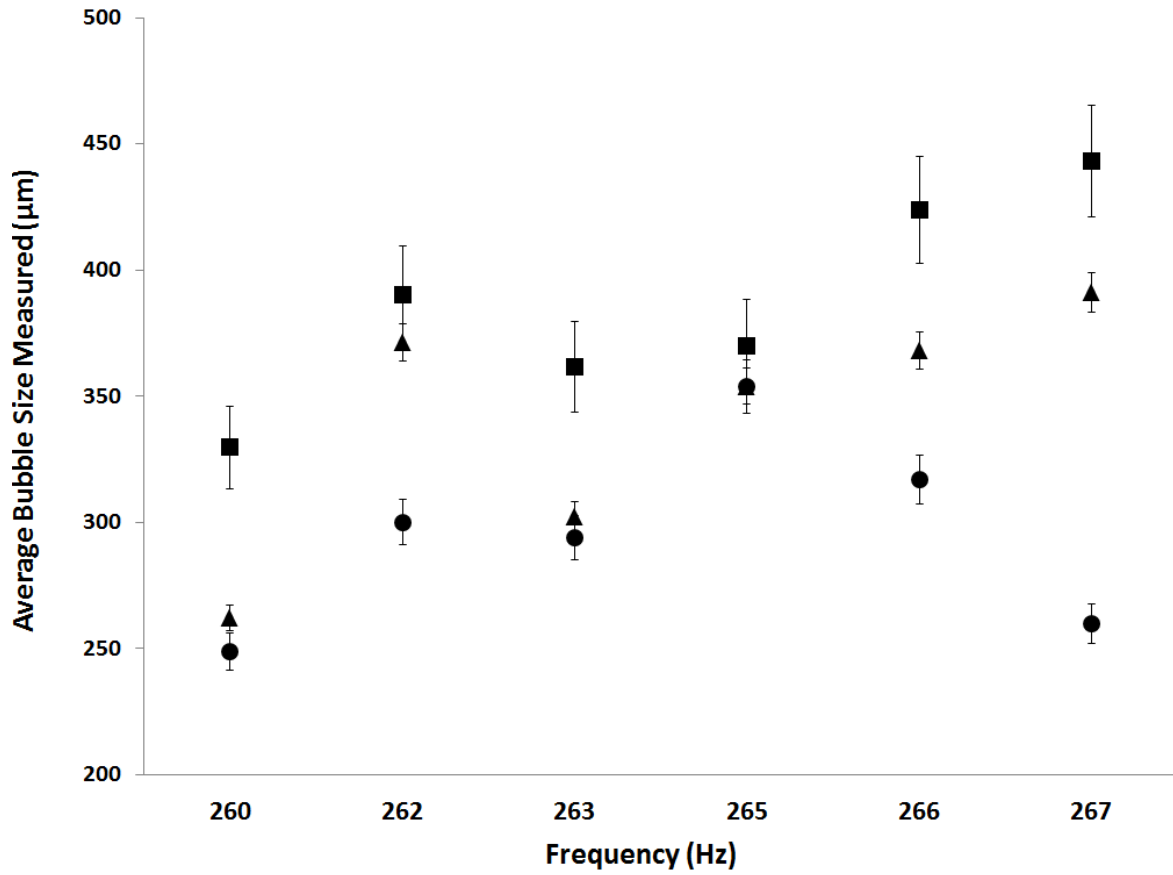


Figure 68 Bubble Size Distributions for feedback loop length of 300 mm for different methods

(● - ABS, ▲ - Spraytec, ■ - optical methods) at various flow rates.

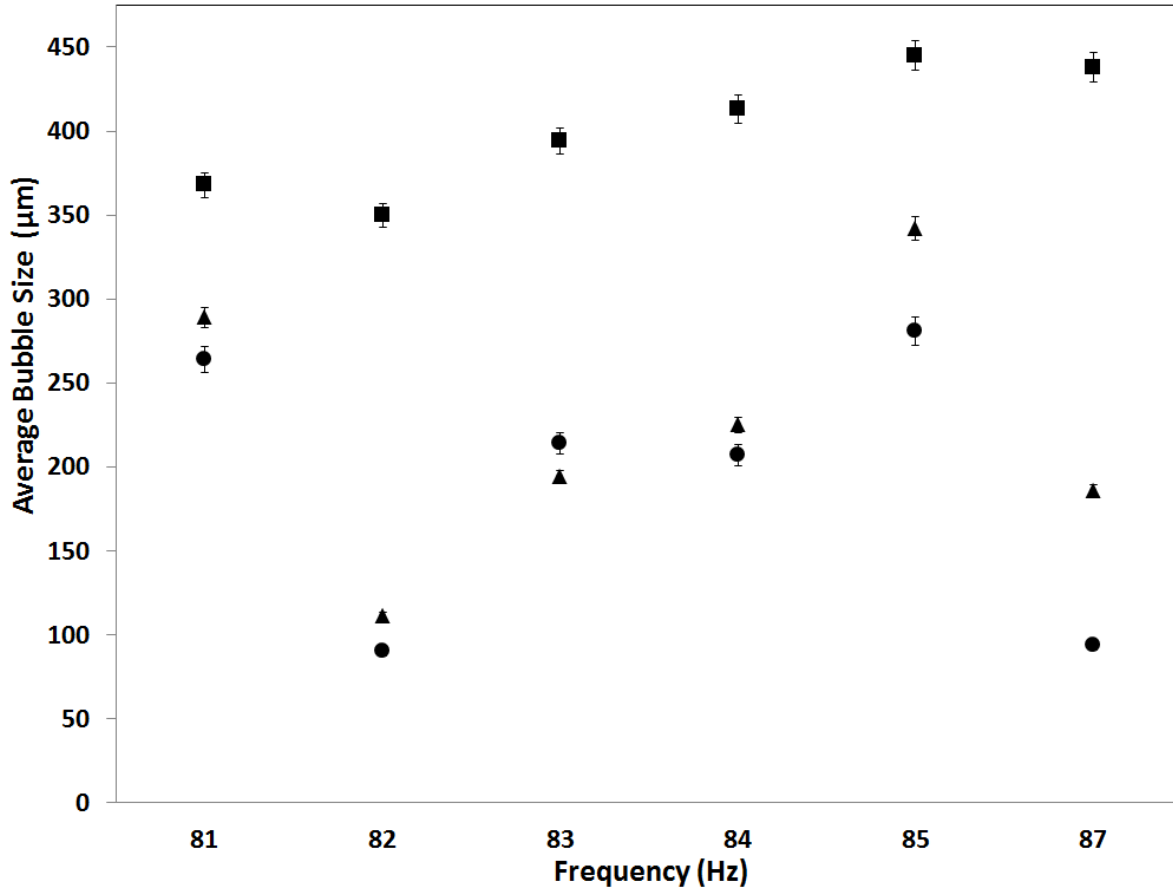


Figure 69 Bubble Size Distributions for feedback loop length of 1950 mm for different methods

(● - ABS , ▲ - Spraytec, ■ - optical methods) at various flow rates

Figure 69 also presents similar findings to that of the Figure 68, and in order to better understand the system, the bubble size distributions have to be looked into. The major problem observed for these methods is that aside from the fact that they are all based on different underlying principles, they also have different capabilities which offer an insight into how the bubble size is collated. Bubble sizes can be observed at the measured frequencies and although the Spraytec seems to correlate well with the high speed camera, the average bubble size obtained by the ABS seems to be lower. This is one of the major drawbacks of using a simple average bubble size (which is widely reported in literature) as a lot of data is condensed into a single point to garner the results observed herein resulting in a loss of fidelity and

understanding. The window used for bubble sizing also helps determine the bubble size. For the acoustic bubble spectrometry, the sizes obtained can be smaller if using a shorter acquisition window which would result in smaller bubbles being measured. These have not been noted herein as due to the number average calculations, the bubble sizes become much smaller as can be seen from the exemplar calculation.

The major thing to note is the region of interest recorded for these systems. Each system has a different sizing performed and this has to be normalised as the optical method to be used would have a single plane of interest which would depend on the *focus*. The photonic method depends on the 'width' of the laser and the depth of the spray. Since the light diffracts and the sensors record it, it is the beam of light for which the spread is measured. This means that the accuracy is reduced for a polydisperse distribution but increased in accuracy for a narrower size distribution. The averaging performed reduces the errors induced herein. The ABS records a much larger sample size and this is due to the volume of interest being much larger for the hydrophones. This results in a much more comprehensive size distribution obtained.

Discussion

The results in Figure 68 and Figure 69 demonstrate that there is a certain size difference obtained for the various conditions. This is due to the loss in fidelity due to the reduction of an extremely large dataset into a singular point. Since bubble sizing normally deals with the number average, we have used it herein.

Figure 70 shows the bubble size distribution for the 257 Hz frequency condition in Figure 68. The bubbles formed have been recorded over several averages for an acquisition time of 200ms in order to collate the maximum breadth of information without taxing the systems. This is for a volume of 1 cm^3 and the axis is a logarithmic scale. As can be seen that the bubbles smaller than $150\mu\text{m}$ are recorded for both Spraytec and the ABS. The ABS records more of them since it does not suffer from some of the drawbacks that Spraytec does, which will be discussed in the section.

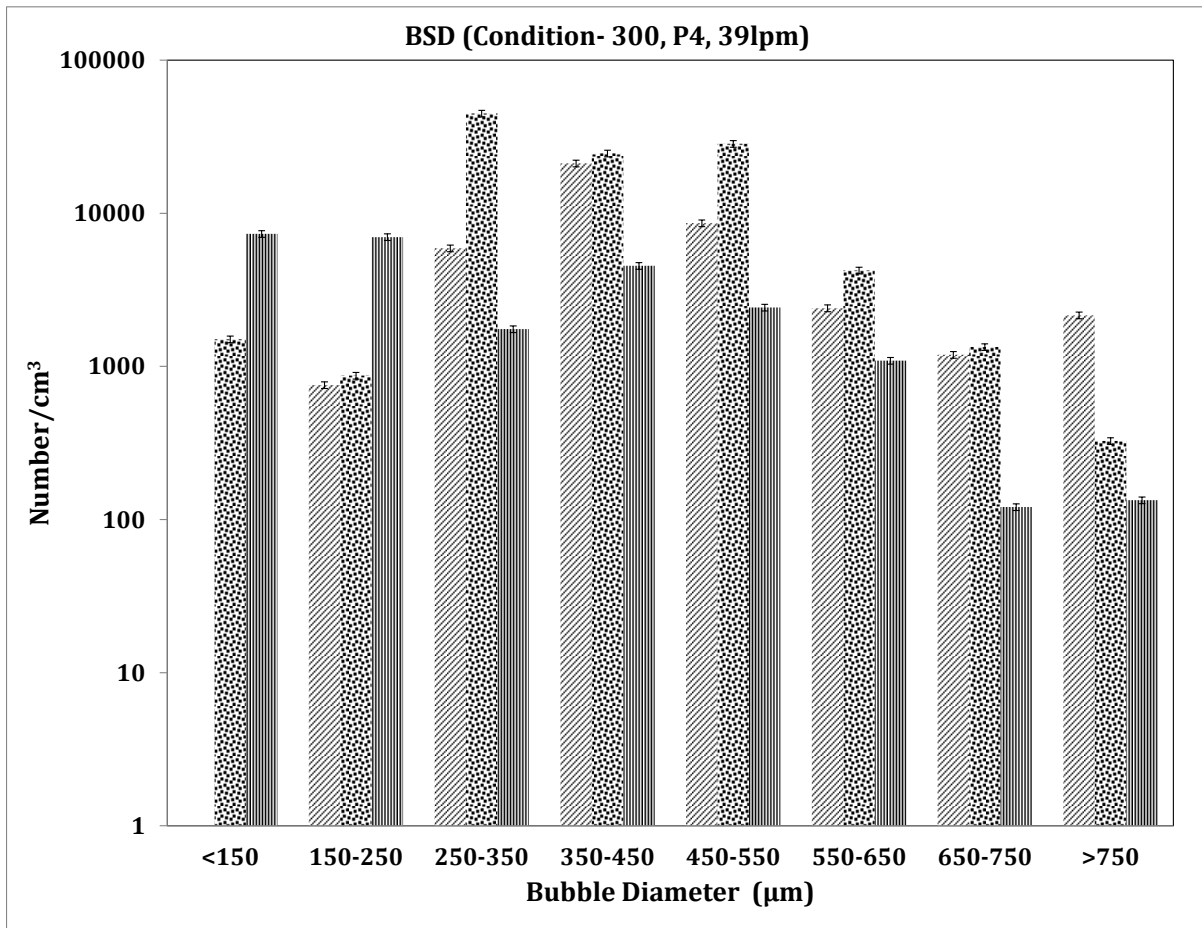


Figure 70 Bubble Size Distribution for condition at 257Hz i.e. 39lpm FO condition in Figure 68

- Optical method ,  - Spraytec,  - Acoustic bubble spectrometry

A general trend has been observed with the average bubble size being shown to be smaller than the Spraytec or the high speed camera. The Spraytec measures the bubbles in a plane, which is the method adopted for the high speed photography. However several averages are taken for the Spraytec automatically which ensures accuracy especially for narrow size distributions. The high speed photography as well as the Spraytec cannot differentiate between bubbles and particles whereas the ABS measures only bubble size and neglects particles due to the resonant bubble approximation. The ABS also obtains the gamut of the bubble size within the volume of liquid between the two hydrophones. However, this also means that one has to use larger bins,

shorter acquisition times and high speed acquisition i.e. a powerful computing package. Figure 70 shows a point where there is some difference observed in the sizes for all the three methods. There is a distinct difference observed. However, this is not the case for other systems.

Figure 71 showcases the scenario where the averaging performed for bubble size calculations results in the same size observed and this is due to the balancing of the smaller bubbles and larger bubbles recorded. Spraytec and the Optical method face the problem that overlapping bubbles will provide faulty data or skewed larger bubbles sizes. The acoustic method depends on the innate property of the bubble and therefore does not face this problem.

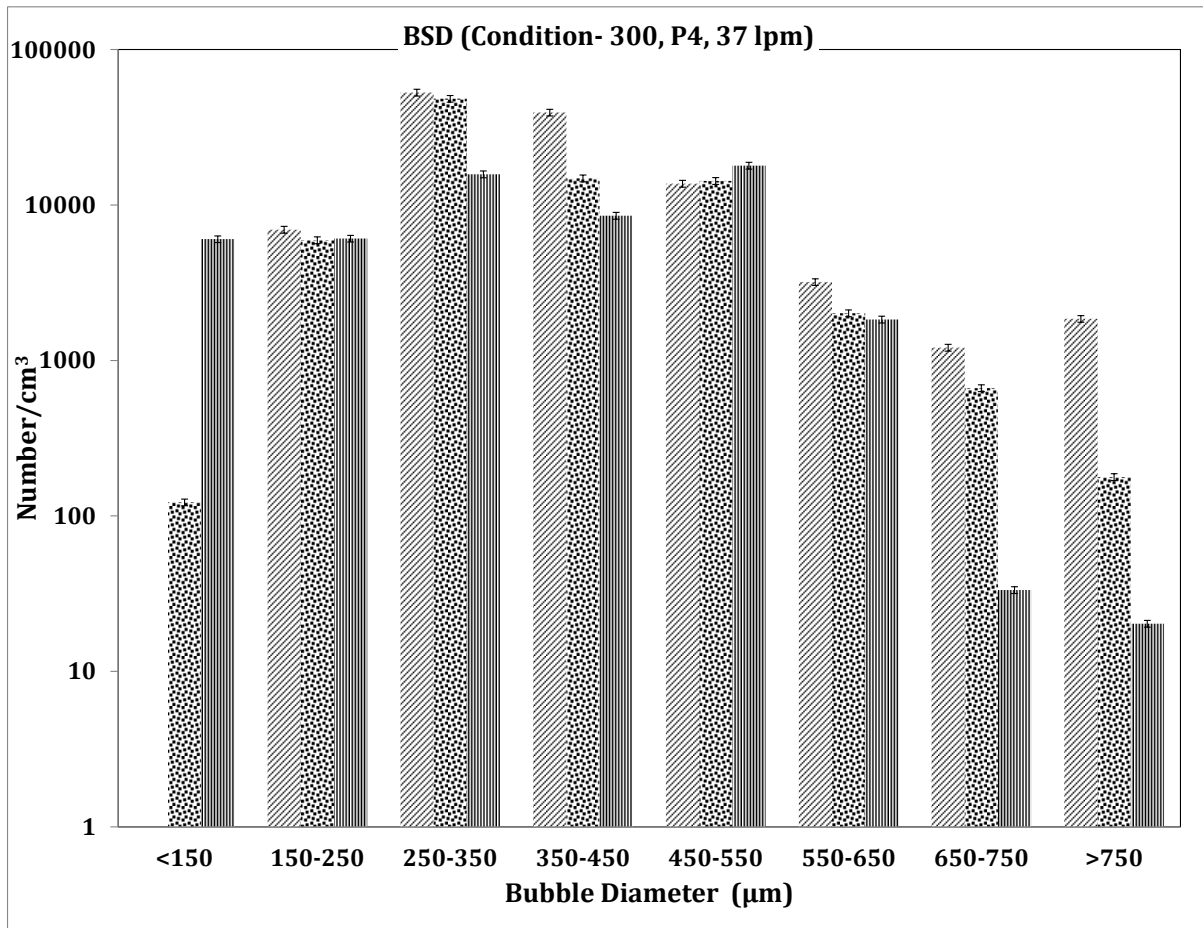





Figure 71 Bubble size distributions for the data point – 265Hz in Figure 68.  - Optical method ,  - Spraytec,  - Acoustic bubble spectrometry

This point is almost similar for the singular point when taken with Figure 70. However, it can be clearly seen that the size distributions are fairly different and just merely balanced out even with the averaging performed. The ABS and Spraytec measure the smaller bubbles and the bubbles are not accounted for by the optical methods. There are also larger bubbles observed but the per cm³ figure is a construct in some sense for the Spraytec and the Optical method. This is because optical methods measure a plane and not a significant depth. The depth has to be introduced artificially and expanded. Likewise, for the Spraytec the volume has to be modified appropriately in order to get values per cm³. The ABS on the other hand, has to be reduced by

calculations as the gamut and volume captured is larger than 1cm^3 . This brings about a more statistically significant value but has the drawback that salient features can sometimes be missed due to lack in computing powers. However, computers and acquisition cards are getting better and better which will improve performance significantly.

The size distribution would be better for the Spraytec if the sampling chamber was designed accordingly so as to be able to engender a comprehensive size distribution. The ABS needs to have the sampling chamber big enough for the hydrophones to fit in, in order to obtain a bubble size distribution. With this in place, the ABS can also be used outside the liquid and in another liquid if the acoustic impedance is matched. This means that the ABS can be used in optically opaque media. Liquids usually have a higher acoustically transparency over optical transparency. There is also the case where if the acoustic impedance of the liquid is known and the resonant frequency of the hydrophone can be obtained, they can be used for the bubble sizing in a variety of liquids. This is not true for optical methods and not for photonic methods.

Photonic methods depend on diffraction and therefore are not specific to bubbles. The ABS is bubble specific and optical methods tend to miss this distinction and also have problems with non-circular or overlapping bubbles. Bubbles and particles in the vicinity affect the bubble size distribution obtained with Spraytec and the Image analysis is made difficult for overlapping or coalescing bubbles. Scattering of laser light is very sensitive to changes and this, results in errors in measurement. It also neglects smaller bubbles as they 'hide' behind the larger bubbles. Both Spraytec and the ABS depend on inversions as well as statistical techniques in order to engender a bubble size distribution and therefore this leads to some errors in the measurement. These methods are indirect methods as compared to the images obtained with the high speed camera.

The aerators are commercially available microbubble generators and are supposed to be equiresponsive. This is also an assumption that introduces errors in the system as not only shall this create an error for the three methods but can also introduce errors with the ABS since it was measuring two aerators at the same time. Smaller bubble sizes might be observed using acoustics since liquids are more transparent to sound than light. The bubbles are multiphasic emboli having distinct boundaries and possibly able to scatter light in such a way that the entire

population is not measured. As demonstrated previously, acoustic methods are more consistent for bubble sizing with the ability to provide a wider range bubble size distribution.

In case of optical and photonic techniques, vignetting might affect the results due to the incorrect measurement of light scattering angles which results from incorrect focussing. This is easier to correct for optical methods but a little difficult to do so with photonic methods. Optical methods would also suffer from the fact that the lenses and focussing possible is very limited. The bubble size can be either magnified and a small ROI (region of interest) can be used otherwise a broader region but a larger ROI is used. This means that sub150 μm measurements would result in a substantial reduction for bubbles being measured.

Figure 72 shows the bubble size distribution for the 87 Hz condition in Figure 69. The bubble size difference is not as high in the points but there is a substantial bubble size distribution observed for bubbles smaller than 150 μm . The bubbles recorded are two orders of magnitude larger than the ones observed by Spraytec and over 9 orders of magnitude as compared to optical methods

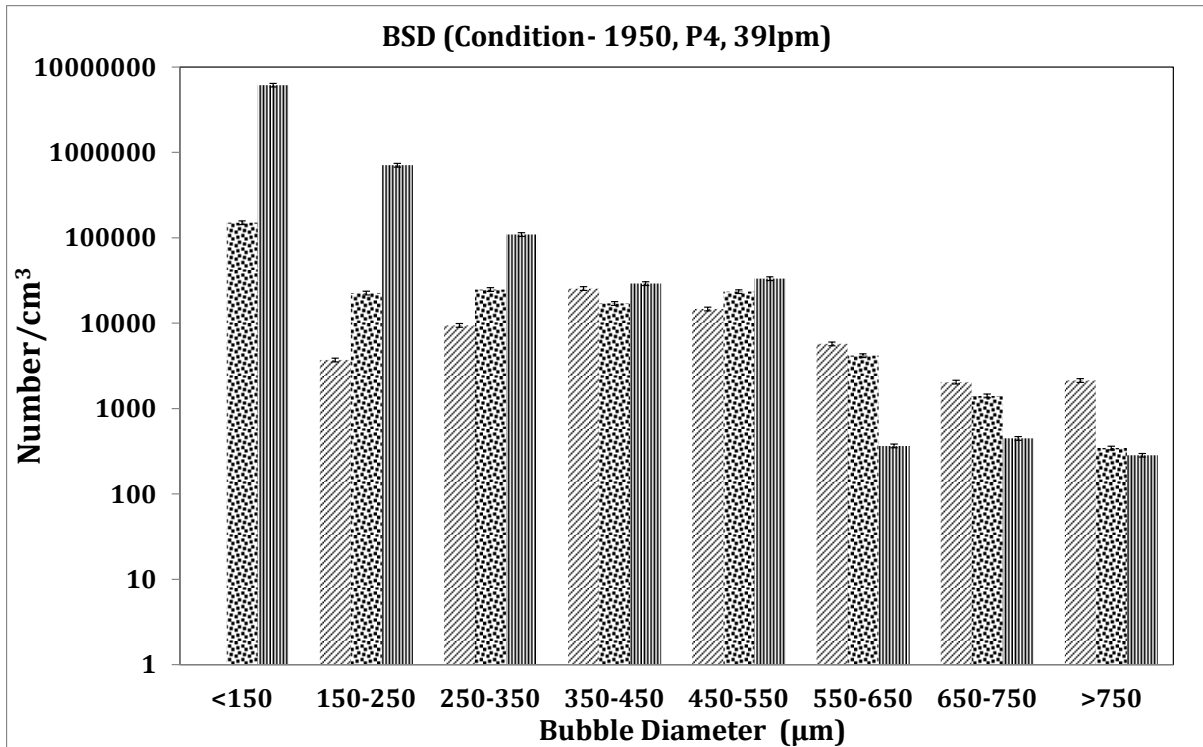





Figure 72 shows a bubble size distribution for 87Hz condition in Figure 69  - Optical method ,  - Spraytec,  - Acoustic bubble spectrometry

The bubbles being measured result in a smaller bubble size distribution and much larger number of bubbles which would be severely skewed for the other two methods due to the problems of 'hidden' bubbles and overlapping bubbles. This however is not missed by the ABS. Bubble size distributions thus obtained, vary considerably. When volume averages are taken, smaller bubbles do not contribute as much as the larger bubbles. However; the problem with this measurement is that whilst it will reconcile the data obtained for the acoustic method and Spraytec better, it shows much larger average bubble size for the optical method, since, then the volume contributions become much larger. Just as a billion 1µm bubbles occupy the same volume as a single 1 mm bubble, the bubbles >750 µm will have a larger contribution. This will result in a much larger bubble size for the optical method. The D50 and D[4,3] are also therefore not that useful for this exchange. This also removes the effect that the small bubbles have on the bubble size distribution. However, as can be seen in Zimmerman *et al.* (Zimmerman *et al.*,

2013b), the smaller bubbles have a much higher impact due to their high internal convection/mixing as well as the rate of transfer. This means that with singular values in bubble sizes, one can have similar values for the system but highly varied performances which are not effectively described. Since the transport phenomena associated is highly proportional to the size of the bubbles in question, the composition of the bubble cloud can make a large difference.

4.4 Separation Processes – Ammonia stripping in ammonia rich waste waters

Results and Discussions

Table 4 Results table with the variations with liquid temperature varied

Run number	Temperature (°C), <i>A</i>	Initial pH (±0.1), <i>B</i>	Height of liquid (mm), <i>C</i>	Time (hours), <i>D</i>	Initial concentration (mg L ⁻¹), <i>E</i>	Air flow rate (LPM) (±0.2), <i>F</i>	Liq. Temp. (°C)	mV reading (±0.1)	Final NH ₄ -N concentration (mg L ⁻¹)	$\% \Delta$
										NH ₄ -N concentration reduction (%)
1	80	10.02	5	0.5	500	1	20	23	32.66	93.47
2	120	10.02	5	0.5	2000	2	35	-32	1.58	99.92
3	80	11.49	5	0.5	2000	2	20	-71	0.18	99.99
4	120	11.5	5	0.5	500	1	35	-71	0.18	99.96
5	80	9.9	15	0.5	2000	1	35	56	201.22	89.94
6	120	10.02	15	0.5	500	2	20	-32	1.58	99.68
7	80	11.49	15	0.5	500	2	35	-20	3.06	99.39
8	120	11.46	15	0.5	2000	1	20	47	122.55	93.87
9	80	9.96	5	1	500	2	35	-26	2.20	99.56
10	120	10.02	5	1	2000	1	20	29	45.45	97.73
11	80	11.48	5	1	2000	1	35	6	12.80	99.36
12	120	11.49	5	1	500	2	20	-60	0.34	99.93
13	80	10.03	15	1	2000	2	20	63	295.92	85.20
14	120	10.06	15	1	500	1	35	35	63.26	87.35
15	80	11.49	15	1	500	1	20	8	14.29	97.14
16	120	11.48	15	1	2000	2	35	-4	7.38	99.63

Table 4 shows the different initial scoping studies which were subsequently repeated 8 times with very high reproducibility (discrepancies within 3%). The liquid temperature was extremely important for inducing a high rate of mass transfer taking place in the system.

The scoping trials showed occurrence of successful separation. The separation efficiencies were extremely high and temperature dependence on separation was noted as well as layer height dependence. This demonstrated high separation efficiencies and provided useful data for understanding the process behind it.

A parametric study was conducted immediately after that in order to better understand the underlying mechanism for the system and quantify the mass transfer information.

Parametric trials

Parametric trials were conducted in order to obtain better performance information with the window parameters obtained from the original scoping trial. The parameters used for this trial were Temperature of the inlet air, pH, and temporal study i.e. processing time.

Temperature Trials

Temperature studies for air inlet temperature were conducted from 22°C onwards to 140°C. The air temperature could be high with the liquid temperature remaining lower at about 50°C -60°C due to very little sensible heating taking place. Figure 73 shows the efficiency of the process with a variety of inlet air temperatures.

The non-linear regression line of best fit is plotted across the data and extrapolated. The error bars created using the data from the averaged runs of each inlet air temperature. The run time was fixed at 30 minutes.

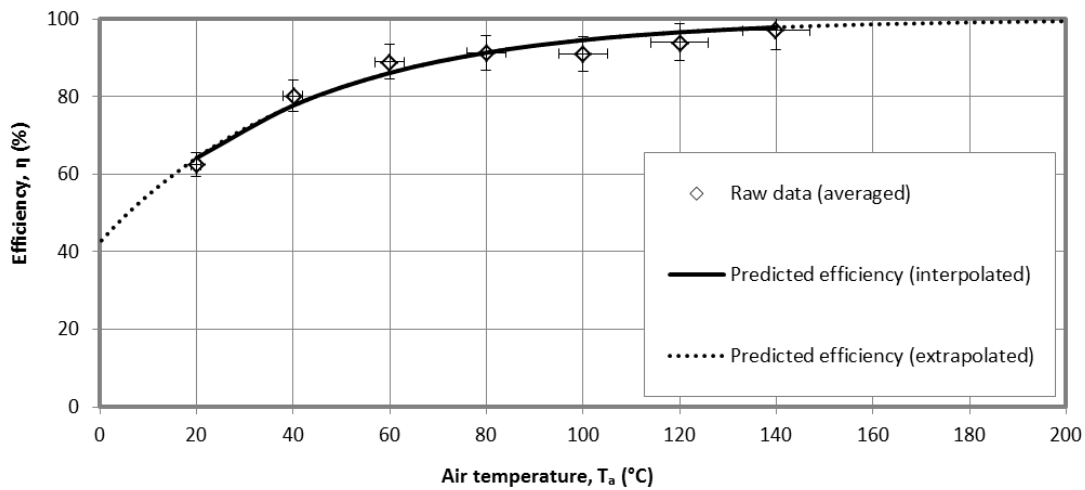


Figure 73 Efficiencies for a range of inlet air temperatures.

(Taking it from Turley, 2015 and Desai *et al.*, 2018)

Conducting an ammonia mass balance:

$$\text{Accumulation} = \text{In} - \text{Out} + \text{Generated} - \text{Reacted}$$

Equation 1

$$\frac{dC}{dt} = -kA_iCF$$

Where: C = concentration of ammoniacal nitrogen (mol)

k = mass transfer coefficient ($\text{m}^{-2} \text{h}^{-1}$)

F = fraction of undissociated ammonia

A_i = interfacial area (m^2)

F is given by:

Equation 2

$$F = \frac{10^{pH}}{\frac{k_b}{k_w} + 10^{pH}}$$

Substituting Equation 2 into Equation 1 yields:

Equation 3

$$\frac{1}{C} dC = -K_D \left[\frac{10^{pH}}{\frac{k_b}{k_w} + 10^{pH}} \right] dt$$

Where K_D = overall mass transfer coefficient, kA_i (h^{-1})

In this experiment, pH is uncontrolled and so decreases linearly with time such that:

Equation 4

$$pH = pH_0 - zt$$

Where: $z = (pH_0 - pH_1) / (t_1 - t_2)$

Substituting Equation 4 into Equation 3 and integrating:

Equation 5

$$\ln \left[\frac{C_2}{C_1} \right] = \frac{K_D}{z \ln[10]} \left(\ln \left[\frac{k_b}{k_w} + 10^{pH_2} \right] - \ln \left[\frac{k_b}{k_w} + 10^{pH_1} \right] \right)$$

Denoting $\frac{k_b}{k_w} + 10^{pH_n}$ as L_n :

Equation 6

$$\ln \left[\frac{C_2}{C_1} \right] = \frac{K_D}{\ln[10]} \frac{(t_2 - t_1)(L_2 - L_1)}{(pH_1 - pH_2)}$$

Equation 6 is derived by Srinath and Loehr(Srinath and Loehr, 1974), however, it is noted that they carried an error forward by integrating Equation 3 to give an equation which defines pH as rising with time. Defining efficiency, η , as:

$$\eta = \frac{C_1 - C_2}{C_1} \times 100\%$$

Equation 6 can be rearranged to give:

Equation 7

$$\eta = 100 \left(1 - e^{\left(\frac{K_D}{\ln[10]} \frac{(t_2 - t_1)(L_2 - L_1)}{(pH_1 - pH_2)} \right)} \right)$$

Srinath and Loehr (1974) define k_b / k_w as:

Equation 8

$$\frac{k_b}{k_w} = (-3.398 \ln[0.0241 \times \theta(^{\circ}\text{C})]) \times 10^9$$

Therefore, the non-linear regression curve takes the form:

Equation 9

$$\eta = 100(1 - Ae^{(BT_{air,inlet})})$$

Where A and B are constants which are fitted by nonlinear least squares regression to be -57.53 and 0.02374 respectively. The resulting curve closely follows the data, justifying crediting the inlet air temperature for the efficiency, rather than the liquid temperature which is transient and therefore more complicated to correlate with efficiency.

Using the constants, the overall mass transfer coefficient, K_D , can be determined. The resulting values are reported across the range of temperatures in Figure 74. The figure shows an excellent correlation ($R^2 = 0.9993$) between the inlet air temperature (rather than transient) and the coefficient thereby justifying the use of the average liquid temperature to determine L_n . The stark feature is that they agree on K_D with $\sim 10^1$ magnitude. Srinath and Loehr (1974) (Srinath and Loehr, 1974) reported $K_D \sim 10^{-3}$ magnitude whilst Smith and Arab (Smith and Arab, 1988) as between 10^{-3} and 10^{-2} . This can be explained by noting that the size of the bubbles typically used in literature are of a millimetre size and this increase and further improvements are due to the substantially increased surface area wrt volume. There is also the thin layer effect for the boundary and the high internal mixing within the microbubble as shown in (Zimmerman *et al.*, 2013).

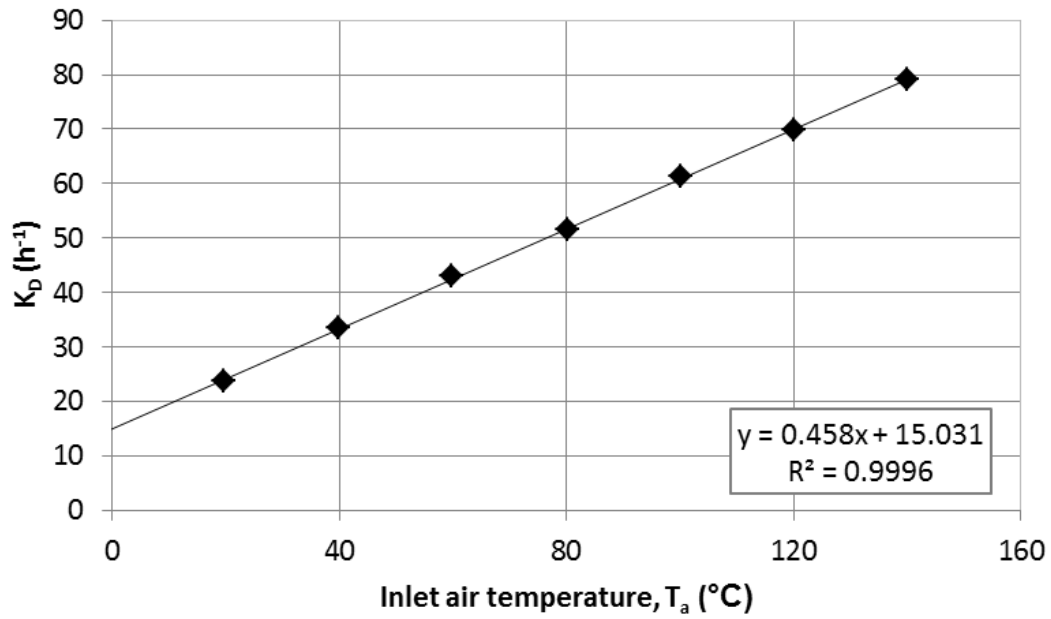


Figure 74. Overall mass transfer coefficient vs. inlet air temperature with a linear regression and the corresponding correlation and equation for the 30 minute run.

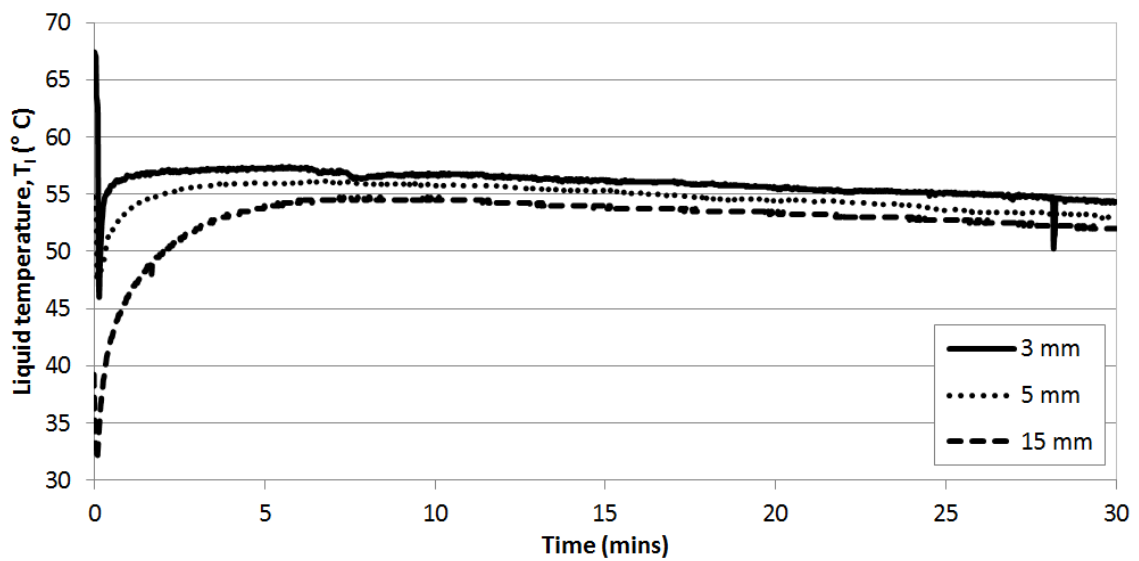


Figure 75 shows the average liquid temperature curve for various temporal runs. This shows that the liquid temperature does not rise significantly even at an inlet air temperature of 180°C. Different layer heights are shown as although layer height reduction results in an increase in efficiency, there is a decrease in the throughput observed.

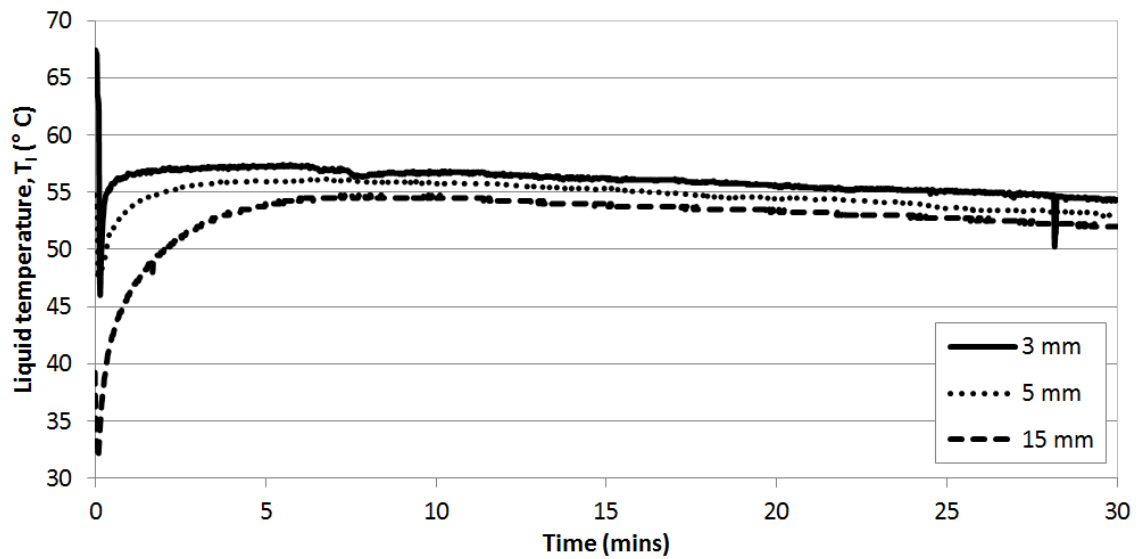


Figure 75 Liquid temperature over time and an average of the 3 runs for each liquid height using thermocouples placed at different locations. The initial immediate drop has been included to show the sharp decrease in temperature when the liquid enters the vessel. This is for air temperature at 180°C and for a 30 minute run.

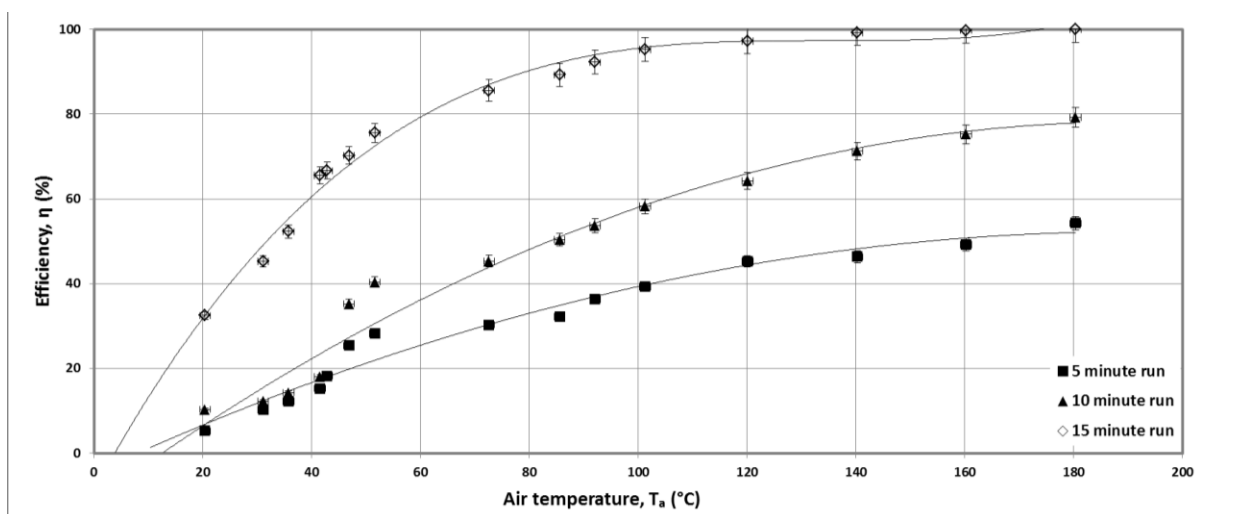


Figure 76 Temporal run carried out in order to see the efficiency for various temperatures.

Figure 76 compares various inlet air temperatures with a temporal run in order to demonstrate that whilst 30 minute runs seen in Table 4 and Figure 73 show high stripping efficiency, there is an advantage to run the system at the 15 minute run as similar stripping efficiencies are achieved with the same processing time.

There is an observable decrease in performance when concentration basis is used instead of total mass for the ammonia. This is simply because there is a competing process – dewatering – over ammonia stripping which is exacerbated for lower liquid heights across the membrane. According to experiments with a selected condition fixing all other parameters allowing just variation of the liquid layer height, one can see the difference in performance. For a lower layer height, there is volume reduction in total liquid observed. The dewatering step is also hastened due to this and we have observed a dramatic increase in mass transfer when using lower liquid heights such as (Abdulrazzaq *et al.*, 2015, AlYaqoobi *et al.*, 2014, Zimmerman *et al.*, 2014, Abdulrazzaq *et al.*, 2016). This results in a significant reduction in the total liquid volume which then results in a ‘lower’ efficiency of ammonia removal and an increase in concentration of ammonia. This is easily rectified by adding a partial condenser for the evolving vapours which will ensure that the water re-enters the system whilst ammonia remains as a gas and escapes the system. However, Figure 77 demonstrates the effect for two points in the trial. The total ammonia removed is still high (which is seen in the mass basis) and the volume reduction decreases (as the bubble gets wetter with therefore the concentration difference reduces) with increased layer height.

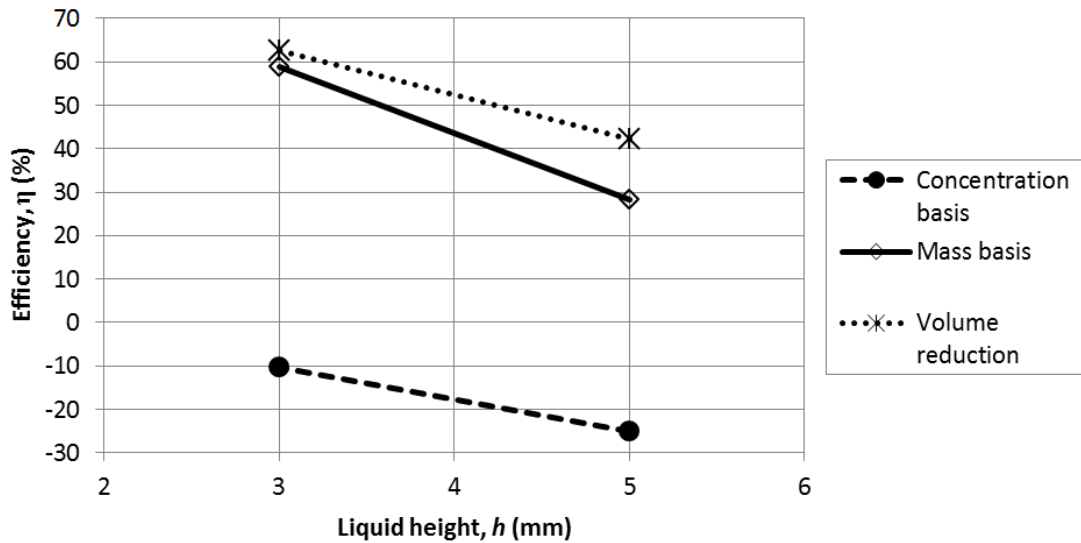


Figure 77 Ammoniacal nitrogen removal on both mass and concentration bases with percentage volume reduction plotted.

Figure 77 shows the ammonia removal on the basis of concentration (ammonia relative to water in the solution) and mass (absolute amount of ammonia). It is observed that the liquid layer height increase results in higher efficiencies as compared to what has been observed previously in literature. The mass basis demonstrates the performance better. The negative percentage simply means that the dewatering process is taking place at a higher rate and this can be negated by placing a condenser to condense the liquid back into the solution.

pH variation was also explored in Figure 78. Concentration and mass basis were used to calculate removal efficiencies. Figure 78 and Figure 79 show the pH study.

The microbubble stripping efficiency can be increased to 95% without changing the pH by extending the processing time to 1 hour.

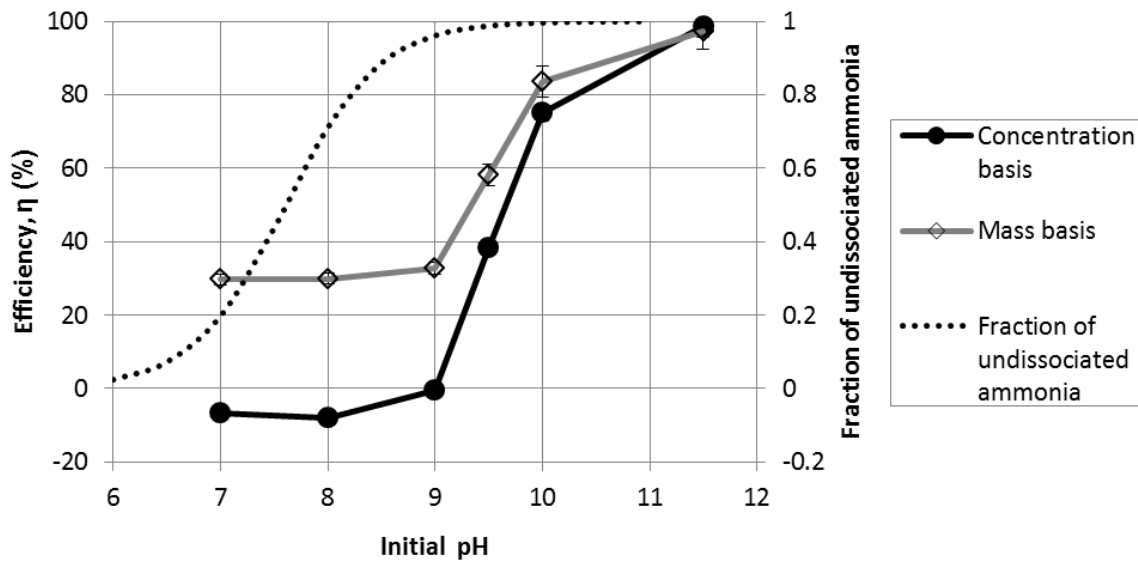


Figure 78 Average efficiencies on both mass and concentration bases with the theoretical fraction of undissociated ammonia also plotted (Behera *et al.*, 2013). 30 minute run with 140°C air temperature. Error bars cannot be prominently seen in the figure, but are approximately 3%.

Higher pH will increase the stripping efficiency significantly and agrees well with literature. However, the ability to strip ammonia even at a pH lower than 9 has not been observed in literature while it has been achieved here. This is due to the dewatering step which forces the ammonia out of the solution and the rate of reaction mitigates recombination that forms the ammonium hydroxide. This is the entropic pull which dissociates the ammonia due to the hot microbubble and the ammonia then leaves the system via the bubble.

Increasing the pH creates a strong concentration gradient. According to Le Chatelier's principle, the presence of the OH^- favours re-association of ammonia, thereby increasing the ability to strip ammonia out. Increasing the pH for the same experiment between 8 to 10 increases stripping performance significantly from 30% removal efficiency to 87% in terms of concentration and from 60% in terms of mass to 92%. This is observed in Figure 79 Alternatively, the microbubble stripping efficiency can be increased to 95% without pH change by extending processing time to 1 hour.

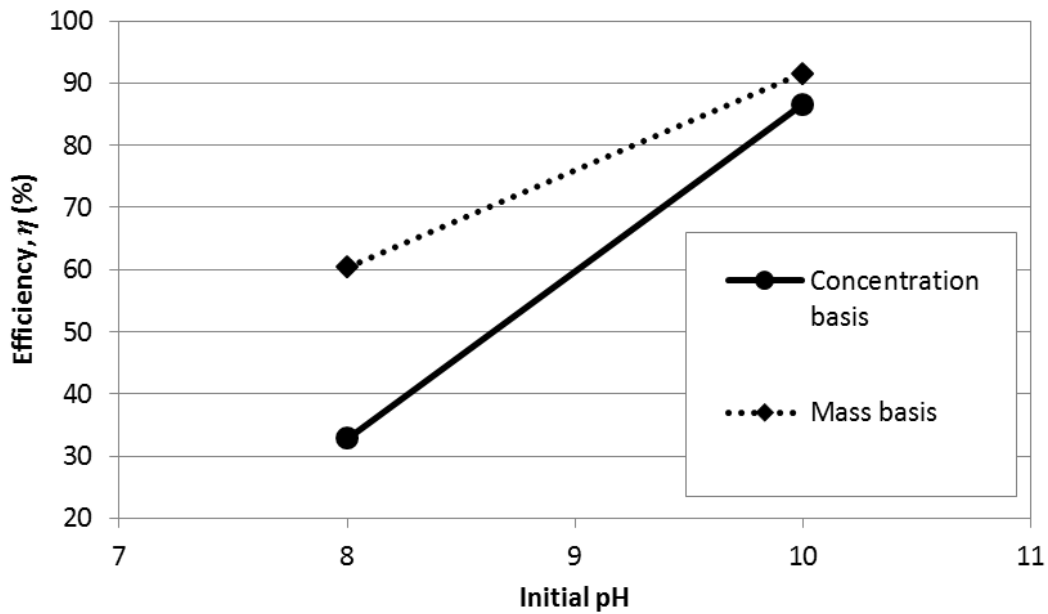


Figure 79 Removal efficiencies for ammonia when compared to mass and concentration basis.

The difference in separation efficiencies can be seen for the mass and concentration basis. However, the difference is greater for lower pH as compared to the higher pH. This is due to the fact that the processes of dewatering and stripping are competitive and the increase in pH results in an increased gradient thereby improving the ability for the ammonia stripping to take place.

Figure 80 shows the performance of the system with the superimposed charts and how the mass transfer improvement with the hot microbubble injection and microbubble stripping has led to a performance far exceeding the original operating envelope as well as previously published studies.

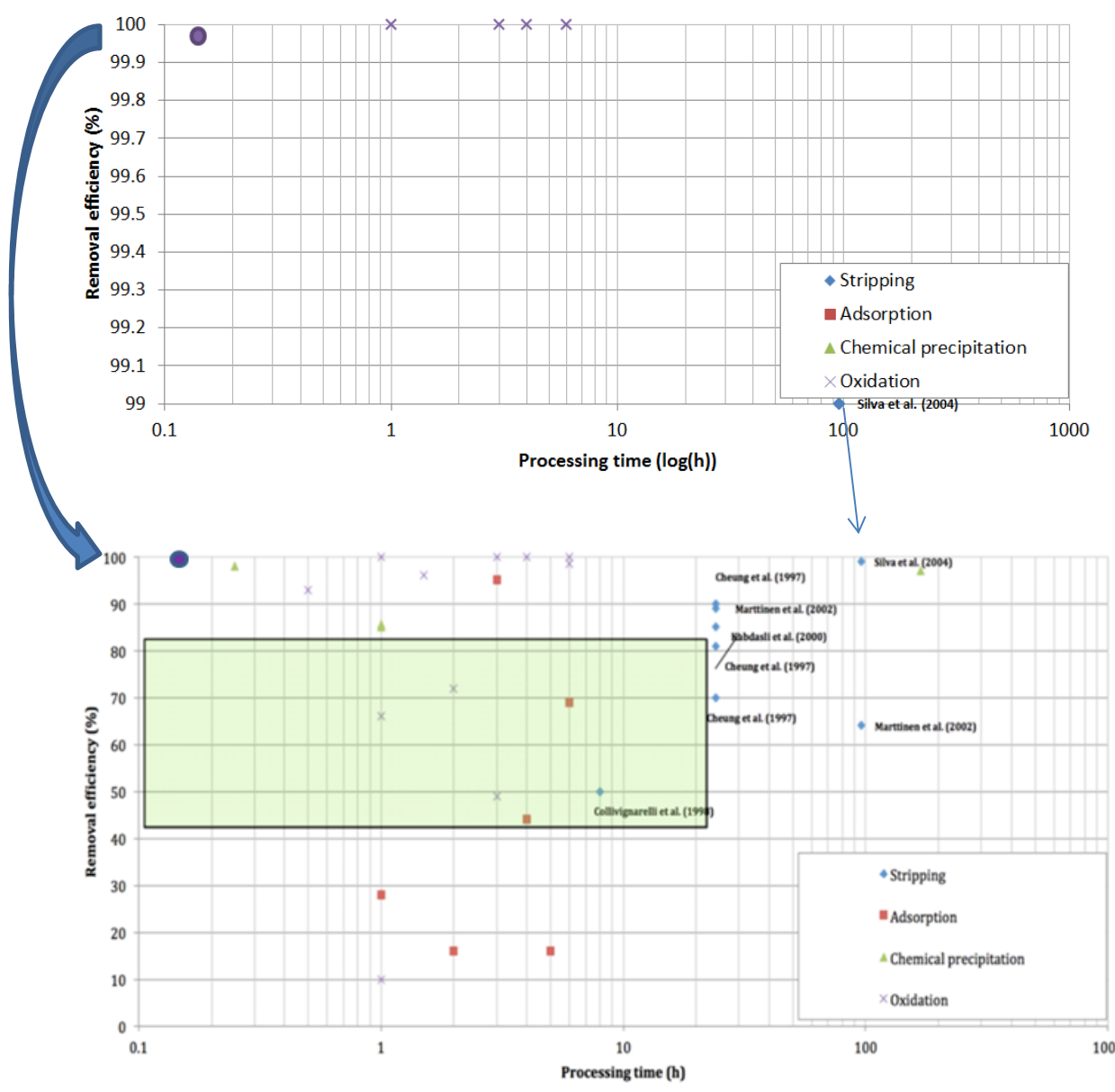


Figure 80 Superimposing performance of one of the points observed into Figure 27 and is the purple circle.

The versatility of the designed process ensures that several routes can be used in order to get similar performances based on availability and requirements and driving forces- sustainability, energetics, availability of process heat being some examples.

The major scientific finding was that the concentration driving force of the bubble was able to extract the ammonia from a system despite the fact that it existed in a dissociated state in

the water. This resulted in the additional ability to strip ammonia at pH of and lower than 9 when the vaporisation became the chief driving force and not concentration gradient. This is a first as reported in literature.

The two driving forces, dewatering/evaporation and ammonia removal are opposite in nature, and can be tuned by tuning the liquid layer height. According to Le Chatelier's principle, adding the OH⁻ ion to the system (increasing the pH) would increase the

1000-3000 times increase in mass transfer coefficient for ammonia stripping has been observed. The presence of the temperature gradient which increases the effect of the concentration gradient is recorded and this follows from the Ludvig-Soret effect.

The next section deals with using this approach for ammonia rich liquor such as leachate and digestate. Additionally, for the exemplar liquid, it will have a lot more ionic strength due to the large amounts of contaminants and surfactants. These result in smaller bubble size and non-coalescence due to a charge formed on the surface (Browne *et al.*, 2011, Yaminsky *et al.*, 2010, Vincent S.J. Craig, 1993, Zieminski, 1971). This should result in smaller bubbles and therefore faster removal efficiencies.

Additionally, the presence of high levels of volatile organic compounds results in a more opaque liquid. Since there are thousands of volatile components in the liquor, they cannot be quantitated easily. The opacity of the liquid acts as a proxy to the removal efficiency of these components. The greater the removal of these components, the higher is the reduction of opacity of the liquor. Since the process design cannot compensate for the tens of thousands of volatile compounds present, the process conditions previously developed will be used and studied in the next section. Using these findings, the next set of experiments were carried out and the work was expanded to include real world ammonia rich liquors such as leachate and centrate/digestate

Ammonia Rich Liquors – Leachate and Centrate/Digestate

Ammonia rich waste liquors comprise of amongst other liquors, landfill leachate and anaerobic digester digestate/centrate. These liquors have typical ammonia concentrations

between 500mgL^{-1} – 5000mgL^{-1} . The Waste Framework Directive, Waste Water Directive, and the FoodWaste Framework Directive delineate what needs to be done to these liquors and the appropriate treatment for these liquors. In order to ensure that the product of this study would be compatible to be emitted, governmental sampling and testing agencies (ALS Environmental) were used to correlate and compare the results.

Two approaches were taken in this study.

Three conditions have been used in this study for single liquor in order to understand whether the versatility of the method survives a real scenario.

They have been mapped out in terms of performance. Multiple liquors have then been used in order to apply this technique and check its effectiveness.

Two experimental campaigns were conducted –

1. A single liquor was used in order to test three conditions derived from ammonia-water stripping, in order to strip off the ammonia from the liquor– Trial 1.
2. Multiple liquors were used in order to apply a single performance condition to see if the method was holistically effective – Trial 2.

The leachate (taken from Erin, a Viridor owned and operated site) did not contain sufficient concentration of pollutants which could interfere with either of the analytical probes. The composition was tested for $\text{NH}_4\text{-N}$ and found to contain $2,450\text{ mg L}^{-1}$ (91 mV).

A hypothesis proposed is that operational time could be extended and the conditions relaxed sufficiently which would yield similar results. Whilst the rate of removal would be reduced due to the reduced temperature gradient, the concentration gradient, upon which this process is derived from as garnered from the previous findings, would result that, if the hypothesis is proven true, the removal efficiency could be matched by just depending on the concentration gradient as opposed to the temperature gradient. The reduction in bubble size due to the high levels of ionic strength of the liquid, would result in faster rates to compensate for the lower temperature gradient.

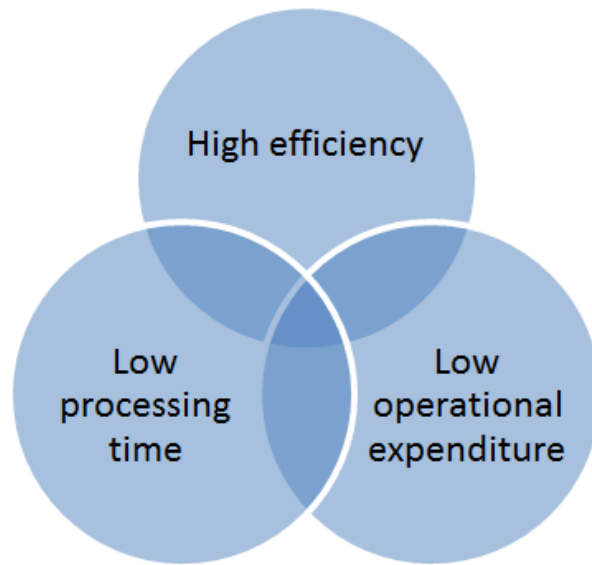


Figure 81. Three distinct features where only 2 can be achieved within 3 distinct operating modes.

Figure 81 discusses the three features which have been used to devise the three operating modes. One can only achieve two out of the three features for successful process implementation.

Table 5 Operational Modalities and conditions

Mode	1	2	3
Temperature (°C)	145	20	20
Initial pH	11.5	11.5	11.5
Liquid height (mm)	3	3	3
Processing time (min)	30	30	120
Air flowrate (LPM)	1.5	1.5	1.5
Partial Condenser	Y	N	N

Table 5 discusses the different experimental conditions and modalities that have been devised based on the understanding in the previous study. This was done in order to better understand the system dynamics. The maximum temperature used was 145 °C as experiment 2 showed that any additional increase in temperature cause negligible increase of efficiency.

Mode 1 had a partial condenser to recover the vaporised water. Operationally, this could be leachate circulating in a coil in order to recondense the vapour. The pH was set to 11.5 for all of the experiments including modes 2 and 3 so as to ensure the equilibrium driving force. The height was set to 3 mm to achieve maximum vaporisation for mode 1 and for modes 2 and 3 to ensure a fair comparison. The processing time for modes 1 and 2 was set at 30 minutes as removals of up to 95% were achieved in this time. 2 hours was used for mode 3 which still ensured that it is still operating well within the target of 24 hours.

6 runs of each mode were made so as to increase the certainty of the results and it was anticipated that the leachate may cause high standard deviations due to other contaminants present.

Results for Trial 1

Table 6. Raw data with calculated NH₄-N concentrations.

Run	Mode											
	1				2				3			
	pH _{final}	mV	V _{final}	C _{NH4-N, final}	pH _{final}	mV	V _{final}	C _{NH4-N, final}	pH _{final}	mV	V _{final}	C _{NH4-N, final}
1	10.2	19	21	77	10.4	78	30	1311	10	26	25	108
2	10.3	16	30	67	10.6	54	26	413	10	23	22	93
3	10.3	19	25	77	10.5	65	24	702	10.2	19	19	77
4	10.3	18	24	73	10.5	62	24	607	10.1	6	21	41
5	10.3	14	29	60	10.4	65	25	702	10	20	21	81
6	10.4	17	29	70	10.5	59	25	526	10.1	21	22	85

Table 7. Calculated efficiencies (/ 100 %) on a concentration basis (blue) and on a mass basis (red)

Run	Mode			Run	Mode		
	1	2	3		1	2	3
1	0.97	0.46	0.96	1	0.98	0.53	0.97
2	0.97	0.83	0.96	2	0.98	0.87	0.98
3	0.97	0.71	0.97	3	0.98	0.80	0.98
4	0.97	0.75	0.98	4	0.98	0.82	0.99
5	0.98	0.71	0.97	5	0.98	0.79	0.98
6	0.97	0.79	0.97	6	0.98	0.84	0.98
Av.	0.97	0.71	0.97	Av.	0.98	0.78	0.98

Table 6 and Table 7 discuss the results with respect to the experiments conducted for trial 1. The removal of ammonia was achieved and there were improvements that could be made for the system based on the results herein which could be inculcated in the study.

One of the main conditions to note was that temperature had a very high effect on the system. There were some discrepancies in performance. This and the decolouring observed due to the higher temperature of gas used, seen in Figure 82, seems to agree with the hypothesis that the volatile compounds which cause the opacity in the liquor are also removed with the ammonia leading to a shotgun approach.



Figure 82. Stripped leachate (left) compared to untreated leachate (right). The stripped leachate was processed in mode 1 and there is a noticeable colour change.

Analysis

ANOVA was conducted on the result with deviations and residuals seen in Figure 83 and Figure 84 . Table 8 shows the calculated results of the ANOVA.

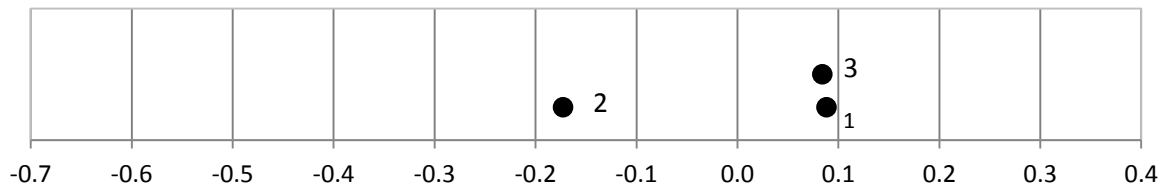


Figure 83. Dot plot of the treatments for each mode.

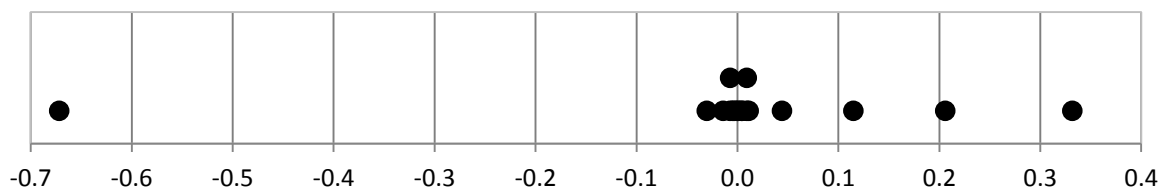


Figure 84. Dot plot of the residuals.

This is a simple concept but the reactor design and sparger design helped with this significantly. The residual plot shows that most of the data is clustered together and therefore not a result of random noise (there is an outlier - -0.67 - and is likely due to foaming in the system which might have been caused due to operator error). Results from 1 and 3 are similar signifying that temperature and processing time, and by extension, most of the other parameters, can be substituted in order to achieve similar results. This improves the ability for process control.

Table 8. Calculated results from the ANOVA test.

Groups (mode)	Average	Variance			
1	0.97	0.0000			
2	0.71	0.0165			
3	0.97	0.0001			
Source of Variation	SS	df	MS	F	P-value
Between Groups	0.269	2	0.134	24.35	2.E-05
Within Groups	0.083	15	0.006		
Total	0.351	17			

This shows a large consistency with regards to the rate of ammonia removal for modes 1 and 3 but less so with mode 2. Also, the P -value was calculated to be 2×10^{-5} which rejects the possibility that these results are due to noise and random error.

The P -value was calculated from the F -value (the ratio of the two mean square (MS) values: $0.134 / 0.006$) of 24.35 which is $\gg 1$ also indicating that the variation between the group means is not due to chance.

Comparing the concentration and mass efficiencies, there is a small difference between those of modes 1 and 3 and a 7% difference for 2. However, no vaporisation of water is occurring for either modes 2 or 3 (minus humidification of the dry air) and so the loss of volume is likely due to the foam formation and the stability imposed by the highly ionic components of the leachate. (Turley, 2015)

Processing time is a good test parameter and intuitively, a longer processing time would improve performance due to the longer residence time for the microbubble. As discussed previously, there are two competing processes – Ammonia stripping and Dewatering. The ammonia stripping follows the Le Chatelier's principle, wherein the bubbles are working on the principle of concentration gradient and with the pH increased, the OH^- ions increase the rate of ammonia removal. The dewatering, due to the temperature gradient (and slight humidification gradient) increases in rate due to hot microbubble injection. This follows non-equilibrium thermodynamics, since the air temperature injected into the liquid, the liquid temperature, and the gas temperature leaving the system are never the same. There is always a gradient and entropic pull applies wherein the ammonia is pulled into the bubble. The dissociation followed by the bubble burst leads to the ammonia removal from the system. The process is always in thermodynamic non-equilibrium because of this temperature gradient. The ammonia (with the water) escapes the system. The process works best when both dewatering and ammonia stripping compete. When this effect is reduced, there is variation due to the conditions in the reactor and the air supply. For a longer period of processing time, these effects and variations are averaged out. The additional advantage is that each microbubble acts as an ammonia puller/carrier and therefore increasing the bubble flux also increases the ammonia removal rates. For an ammonia-rich liquor such as leachate, that has a high concentration of ions and organic compounds, smaller bubbles are produced

due to the non-coalescence. The hot air also results in a higher frequency for the oscillator as can be determined from We_{osc} and Sk . Additionally, a smaller bubble will have a higher internal mixing rate and this increases substantially, the smaller the bubble. In a non-coalescent liquid, a higher oscillator frequency results in a greater bubble flux. This is why the ammonia stripping has greatly increased for this system as opposed to the ammonia-water system. Therefore, using liquor with even more organic content would result in a much quicker removal rate. This has been tested in the next section using a digestate from Walpole.

The operating envelope had been previously identified in Figure 27 which now includes the points where the three operational modes like and where the performance is achieved.

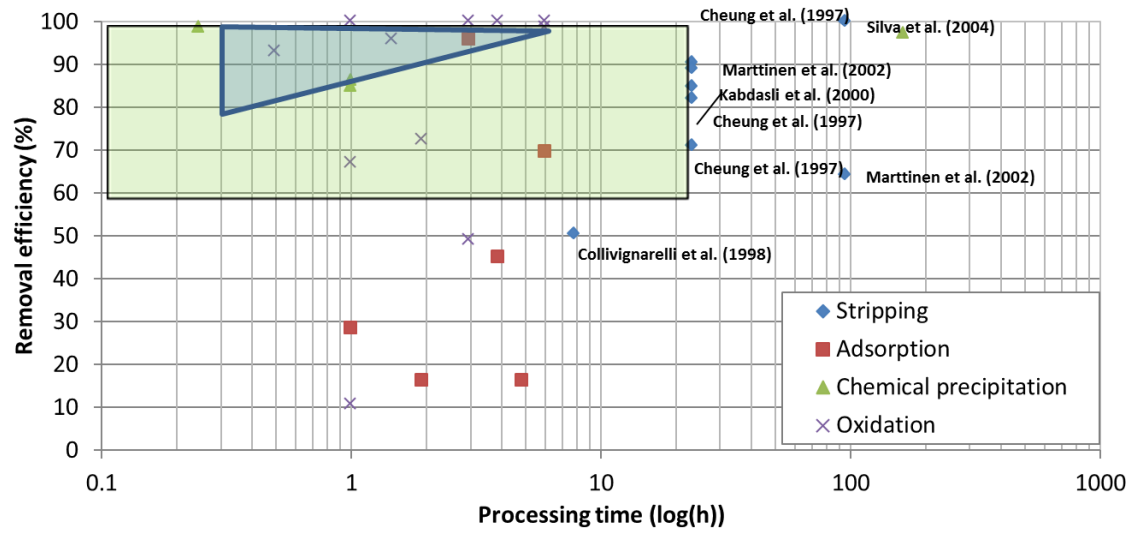


Figure 85. Operating envelope using microbubbles identified in blue.

The next section deals with experiments performed with various liquors and different trials performed on them.

Trial 2 – Experiments with different liquors

Optical transparency

The leachate experiments were performed at various conditions in order to better understand performance specific to the leachate being used. The leachate used initially was that from the Erin site again. The decolourisation has been labelled optical transparency or

percentage decolourisation from original sample. A percentage lower than 100% indicates increase in the transparency and therefore an increase in transmittance for the liquid sample. This means, more light can penetrate in the system and vice versa, a value greater than 100% indicates that less light is penetrating through the media and this implies that the liquor is now darker. This expands upon the hypothesis stated previously, with reduced opacity, there is a possibility of remediating the system via further biological processing but also, the removal of the volatile components of the leachate even at reduced temperature results in a faster separation process.

A set of 6 experiments at a variety of operational conditions was run in order to better understand operationally how it would work for use with leachate.

All of these experiments include a partial condenser. The effect of liquid temperature coupled with various conditions was studied in order to understand whether there were other effects that would result from the variations and quantitatively determine how important are the interactions between the different controllable parameters for leachate.

Table 9 Operating conditions for trial

Run	Liquid temperature (°C)	Depth of liquid (mm)	Air temperature (°C)	pH	Flow (slpm)	Time (h)
1	70	5	140	7	1.5	0.5
2	70	5	140	7	1.5	1
3	20	5	140	11	1.5	0.5
4	35	5	140	11	1.5	0.5
5	40	5	140	11	1.5	0.5
6	35	5	140	11	1.5	1

Table 10 Responses table

% Volume of reduction	Final pH	Final concentration (ppm)	Removal Efficiency (%)
60	9.08	143	94.14
70	9.87	115	95.29
31	10.39	63	97.42
27	10.43	87	96.43
39	10.28	63	97.42
44	11.01	78	96.80

Table 9 and Table 10 show the operating conditions and the responses observed for the trial. As can be seen that the initial pH is quite instrumental in ammonia removal and that high removal rates can be achieved when different conditions are matched. This shows that the concentration gradient is used as the primary driving force at a fixed temperature.

An important point to note herein is the ability to increase the optical transparency of the leachate by using temperature or processing time to release other volatiles in the system concomitant to the oxidation. An exemplar of this is seen in Table 11 .

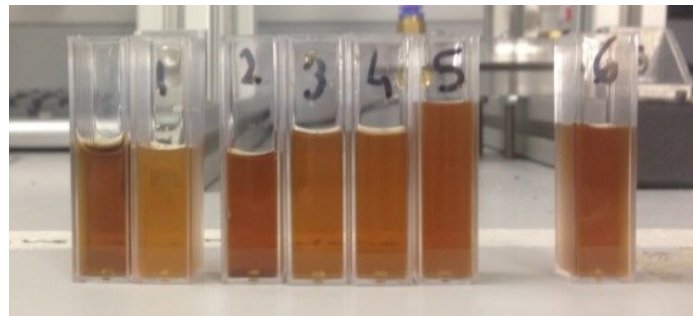
In order for ammonia removal efficiencies to be coupled with increased optical transparencies, UV-Vis spectroscopy was used for two wavelengths, 600 and 660 nm (optimal wavelength for light absorption for the microbial communities) ,and to show that hot microbubble injection could actually provide an additional benefit to the process by increasing microbial/algal growth and thereby improving the process. This process can be expanded into an entire cycle – DZ MMARP , *cf.* Appendix.

The idea for the reduction in transparency and using microbial consortia would either be targeted or selected for targeted heavy metal ion uptake. This would further improve the process remediation and provide a circular approach to this problem. Ammonia is one of the major inhibitors for growth of a microbial algal community and so is the optical transparency of the waste liquor. Conventionally, process water and pre-treatment is required before considering using biological treatment methods and even then, the dilution results in a larger, per volume, liability, further increasing costs.

The fact that the ammonia was removed and the microbial algal communities could be grown in the system was a major benefit observed. This was primarily dependent on the temperature of the liquid/inlet air and the processing time.

Table 11 Optical transparency at two wavelengths

Runs	660 nm	600 nm
Blank	100%	100%
Run 1	61.7%	64.7%
Run 2	65.30%	45.8%
Run 3	86.70%	88.3%
Run 4	87.20%	94.5%
Run 5	41.90%	39.2%
Run 6	56.70%	55.1%



As can be seen, aside from the increased ammonia removal efficiencies, there is also an increased transparency. This means that these processes (with liquid temperature and air temperature being particularly useful) can be used for ammonia removal concomitant with likely better growth in the system for the microbial consortia. The runs where the transparency has reduced is due to the dewatering process competing with the ammonia and volatile stripping process and the volatiles not being stripped enough.

Dewatering

To demonstrate the hypothesis that dewatering was competing with this process, the partial condenser was removed and the next set of experiments were conducted to study that effect. This was also done in order to test the dewatering and therefore the volume reduction possibility of the process. This is important in order to determine whether the dewatering process and the ammonia removal process, although opposite in nature as seen in the previous section, might be able to be exploited and controlled, thereby effectively proving the hypothesis set out by Zimmerman *et al.* (Zimmerman *et al.*, 2014) about these two opposing forces but for a concentration gradient dependent process rather than a temperature dependent process.

Optical transparency would be an easy indicator of dewatering taking place or not as the volatiles will behave like ammonia in the system and therefore the opacity will be related to the presence of the ammonia and volatiles in the system.

Table 12 Experimental conditions

Run	Condenser	Liquid temperature (°C)	Initial pH	Flowrate (slpm)	Time (h)	Air temperature (°C)
1	No	40	11	1.5	1	140
2	Yes	40	11	1.5	0.5	140
3	No	40	7	1.5	1	140
4	Yes	40	7	1.5	0.5	140

Table 13 Optical Transparency

	660 nm	600 nm	% reduction	Volume
Blank	100%	100%		
Run 1	195.7%	199.9%	95.83	
Run 2	61.5%	69.1%	45.14	
Run 3	176%	180.3%	77.23	
Run 4	76%	80.3%	24.02	

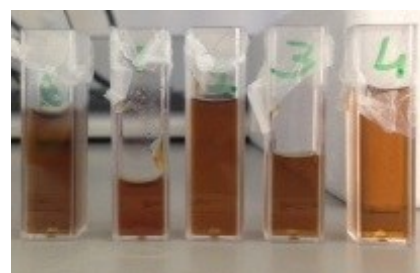


Table 12 and

Table 13 shows the conditions of the run and shows the results of the run. It was observed that the dewatering could be achieved with a significant amount and increase the optical transparency dramatically. This could be used as a process to reclaim process water on sites where just process water was required whilst concomitantly reducing the volume of the liquid. This is important as it reduces liabilities although it is not as elegant a solution as the ammonia removal is. This study was just performed in order to study the dewatering potential of the process and this was shown to be significantly high.

Process Relaxation

The next set of experiments were run in order to test the effect of a decrease in air temperature on the system. This helps prove the hypothesis of whether the temperature gradient can be relaxed, and still maintain the process rates by the smaller bubble size and concentration gradient with increased processing time.

Table 14 shows the process conditions. The effect of pH and temperature needed to be studied as well as the interactions with the ammonia removal and optical transparency. As has been previously observed, ammonia levels might reduce but transparency need not decrease. The corollary, however, is not true so far.

Table 14 Experimental conditions

Run	Depth of liquid (mm)	Liquid temperature (°C)	pH	Flowrate (slpm)	Time (h)	Air temperature (°C)
1	3	40	11	1	1	70
2	3	40	11	1	0.5	70
3	3	40	7	1	1	70
4	3	40	7	1	0.5	70

Table 15 Optical Transparency

	660 nm	600 nm	% Removal of Ammonia
Blank	100%	100%	
Run 1	104.2%	106%	98.25
Run 2	104%	110%	95.92
Run 3	126.2%	120.3%	94.15
Run 4	90.8%	88.1%	91.48

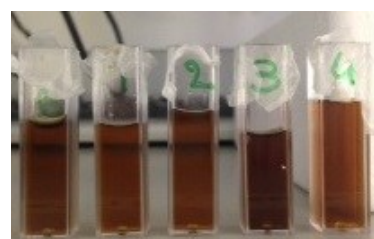


Table 15 shows the results of the study. This study proved several points. Firstly, over 90% removal of ammonia was achieved at the conditions used. This also explains why the results herein are significantly higher than the ones by (AlYaqoubi *et al.*, 2014, Zimmerman *et al.* 2014, and Abdulrazzaq *et al.* 2016). The new process and reactor design enables higher mass transfer coefficients but the smaller bubbles likely produced in the complex media, and the concentration gradient synergistically coupled with the temperature gradient drives this process forward.

Secondly, it was observed that there could be a removal of ammonia but not necessarily an increase in optical transparency. Additionally, 70°C is a fairly relaxed operational temperature and ammonia removal could be achieved easily. This agrees with the hypothesis that the driving forces that control the removal of the volatiles, ammonia, and water can be controlled as long as the component is known. The problem arises due to the complexity of the liquid mixture.

Thirdly, it was also observed that pH could be reduced and operational time could be increased in order to effect a reduction in ammonia levels and an increase in optical transparency.

These findings helped in formulating the optimum process for a high level of optical transparency in order to ensure removal of the volatiles without significant dewatering as seen in Table 16 and Table 17.

Table 16 Experimental Conditions for optimised conditions

Run	Depth of liquid (mm)	Liquid temperature (°C)	pH	Flowrate (slpm)	Time (h)	Air temperature (°C)
1	5	30	11	1	0.5	120
2	5	30	11	1	1	120

Table 17 Optical Transparency

	660 nm	600 nm	% Ammonia removal
Blank	100%	100%	
1	64.4%	69.1%	99.2
2	47.6%	47.9%	99.985



These sets of experiments showed that a concomitant reduction in ammonia and an increase in optical transparency could be achieved in an economically and environmentally sustainable manner.

The next set of experiments were performed for additional liquors being used in order to see the variability of the process (as the liquors are extremely complex) with an aim to see if a trend can be observed for a system with varying amounts of volatile compounds.

These are trials with several liquors and will be used to simply mark performance with the operational conditions remaining constant. The operational conditions used were the same as the optimised conditions seen in Table 16 .

Table 18 contains the results. Each sample in the table contains the name of the sampling site in the run name with the results. A % reduction in optical transparency, i.e. decolourisation due to less than 100% value, implies that the liquid is significantly lighter than before the trial. There are variations for different liquors (some are leachate and others are diluted digestate³) due to different compositions and properties for each of these liquors.

³ Undiluted samples were not being provided during the trial for the digestate due to safety concerns

Table 18 Final tests conducted on various ammonia rich liquors

Run	Final pH	Initial concentration (ppm)	Final Concentration (ppm)	Removal Efficiency (%)	Optical Transparency (660nm)	Optical Transparency (600nm)
Shelford 1	9.1	2800	57	97.96	32.4	49.9
Shelford 2	8.6	2800	1.9	99.932	27.9	44.3
Erin 1	8.9	1950	13	99.33	64.4	69.1
Erin 2	8.5	1950	0.26	99.985	47.6	47.9
Ardley 1	8.1	1210	45	96.28	21.5	28.4
Ardley 2	7.8	1210	18	98.51	18.4	19.9
Bredbury 1	9.7	1270	39	96.90	19.1	21.5
Bredbury2	9.1	1270	25	98.03	15.7	14.2
Walpole	NA	3400	NA	NA	NA	NA

The results can be seen in Table 18 but Walpole, being an example of a digestate, was not measurable. This was because the run time was deemed too high for this liquor and all of the liquor evaporated for both scenarios. Upon investigating this situation, it was seen that Walpole foamed extensively and this resulted in an unexpected improvement in performance. The bubbles were much smaller for this liquor as opposed to the other liquors due to the additional presence of organics which added stability to the bubbles and non-coalescence. The study was interesting as the foam had enhanced stability due to the high levels of organics present in the system. This resulted in a dramatic reduction in processing time and an increase in ammonia removal efficiencies increasing the mass transfer coefficient to 15,000 times that observed in (Srinath and Loehr, 1974).

Temporal runs were carried out for Walpole in order to estimate the mass transfer coefficients in the system and the results for Walpole are observed in Figure 86, with over 99.98% of the ammonia removed in 7 minutes and 93% was removed in 2 minutes.

Chapter 5 Conclusions

5.1 Resonant pulsing frequency effect for much smaller bubble formation with fluidic oscillation

The conclusions of this chapter have a very important finding as they contradict established literature where efforts have been made to develop new methods for oscillatory flow mediated bubble generation with increased or decreased frequencies.

Zimmerman *et al.* (Zimmerman *et al.*,2011) postulated that higher frequency oscillations would result in smaller bubble formation. A lot of work has been performed using the highest attainable frequency possible for the FO as a default, such as ((Hanotu *et al.*,2012), (Hanotu *et al.* ,2013), (Rehman *et al.*, 2015), and Tesař attempted to achieve the higher frequencies required for smaller bubble formation either by the third harmonic excitation of the FO (Tesař, 2013a), or by developing a new high frequency FO, Hartmann Resonator FO (Tesař *et al.*, 2013).

Based on high speed photographic evidence (Tesař *et al.*, 2014), it was concluded that the liquid impingement into the bubble engendering pore would result in reduced coalescence and conjunctions. This would imply that a low frequency (2-10Hz) would be beneficial for reducing the bubble size. A low frequency FO, Vortex based FO, was invented for this purpose (Tesař *et al.*, 2016) and whilst 2-10Hz would generate smaller bubbles, the throughput is similar to steady flow bubble formation.

The new understanding in this chapter negates the need to develop a low frequency or a high frequency oscillator without the accompanying amplitude of pulse. This changes the bubble formation understanding mediated by oscillatory flow. There is a presence of a resonant pulsing frequency, a 'sweet spot' condition which generates the bubbles with the right spacing and sizing such that they are formed significantly faster than steady flow but do not coalesce. This reduces bubble size concomitantly increasing associated bubble throughput.

The condition occurs at a particular frequency and is specific to a particular set up. At this condition, a substantial reduction in bubble size ($\approx 60\%$) is observed. This size reduction can be achieved by change in configuration without substantial change and without any

additional energy input. It has been hypothesised that tuning of all the different parameters controlling bubble formation will result in a smaller overall bubbles size, presumably by the combined effect of more efficient pinch off and reduced conjunction/ coalescence.

Changing the amount of feedback by changing the feedback loop volume also results in interesting dynamics and simulates frictional losses and amplitude increase. This is an important finding as it helps understand the dynamics in the feedback tube and the mechanism of bubble generation related to the amount of feedback imposed on the system. Since the amplitude of the pulse is strengthened by the higher feedback condition, which results in a greater net positive jet deflection, the bubble size is smaller and higher throughput is obtained. The frictional losses are lower for this condition in the feedback loop as opposed to the lower feedback configuration which results in the 'largest' bubble size when compared with the other feedback configurations but also therefore a high impact due to the resonant frequency/ 'sweet spot' effect. The medium condition is matched with the ducts in the FO, which then reduces losses due to volume expansion or contraction. This is an important effect as it reduces the bubble size without significant attenuation. At the resonant frequency, a 'sweet spot' dip is observed and is a very sharp dip as opposed to the higher feedback condition. The higher feedback condition, due to the higher amplitude and lower frictional losses, has a consistently smaller bubble size especially at the higher flowrate. The dip however is not as sharp as that observed for the lower and medium feedback condition. The medium condition has the sharpest peak. The throughput increases with the increasing feedback and the higher feedback condition results in a magnitude increase in bubble throughput.

Changing the flow rate, shifts the resonant frequency is observed as well as modulating the magnitude of the reduction. This will also be observed if the liquid height, liquid properties, and other changes are made to the system. However, there will be a condition present in the system where these properties match and the bubble detachment matches the rise velocity in such a way that there is not a significant amount of coalescence but is fast enough to substantially improve over steady flow. Tesař, (Tesař *et al.*, 2017) discussed the use of lower frequency oscillatory flow mediated microbubble generation in order to generate smaller bubbles but this inhibits the formation properties as it will be similar to the throughput obtained by steady flow.

For purposes where average bubble size obtained by number average is required such as biomedical applications and flotation, the FO mediated bubbles with the flow amplification has been able to generate 7 μ m bubbles.

Aside from the dependence on the frequency-amplitude combination, the venting observed would need to be offset in order to make this industrially applicable and reduce the operating expenditure for this process. The generation, even with the venting, is a significant improvement over conventional methods of generation but the gas wastage mitigates the benefits by vitiating some of the environmental benefits accrued.

The major requirement for an oscillator for microbubble generation would be, based on these findings, a higher amplitude of pulse (by extension, lower pressure drops and frictional losses), frequency modulation across broader range of frequencies (if amplitude is increased, a higher throughput can be achieved at higher frequencies and with smaller bubble formation as seen in the higher feedback condition), and flow inelasticity (changes in flowrates would change the frequency, and since the 'sweet spot' range is narrow and specific, the condition would no longer hold true).

Chapter 3 discusses the invention of a new oscillator invented specifically for microbubble generation and assessing it compared to the other oscillators. It also discusses the mechanism of the new oscillation mode and experiments carried out to test the hypotheses that support the new theory developed by Desai and Zimmerman.

5.2 Inventing the New Oscillator (Desai-Zimmerman Fluidic Oscillator)

This work has discussed several features and the underpinning mechanism of the new invention, the DZFO. The DZFO is based on a novel principle and is neither a jet deflection based nor is it a load switched oscillator. It can exhibit features of both these systems but is based on an acoustic resonant mode of switching. The DZFO is an enabling device capable of several applications and when compared with the other oscillators retains all of their advantages and betters their performance for each condition tested.

A new mode of oscillation was discovered upon which the DZFO is based on, which is an acoustic resonant mode, and it does not fall into jet deflection or load switched oscillators.

This is a major finding as both jet deflection and load switching oscillators were invented in the 1960's and no new modes have been found since then. They have been actuated in different ways, such as using plasma or magnetic fields, mechanical actuators and switches, vortices, and electrical fields but still adhere to the two original categorisations.

The acoustic mode presents a much cleaner mode of oscillation and the waveforms are 'crisp' and there is very little dispersion into the other modes as compared to other oscillators. This also results in a reduced pressure drop, reduced frictional losses, and lower onset of oscillation as compared to other oscillators. This also makes them distinct from load switched oscillators which require a higher pressurisation step in order to switch which has been observed the TCFO as the capacitive pressurisation step.

The new mechanism has resulted in several properties that were intended for the DZFO and are beneficial for microbubble generation. The combination of the properties has resulted in achieving smaller bubble size as compared to all the other oscillators tested.

This mode also allows substantially higher frequencies attainable as compared to the other oscillators including the jet deflection based Hartmann Resonator fluidic oscillator which can attain a maximum of 3.6kHz based on the excitation of the third harmonic, whereas the prime frequency attained by the DZFO is 6.8kHz, which when excited, can attain approximately 20kHz. Additionally, whilst it was required to severely increase the flow rate of the Hartmann Resonator oscillator (Tesar, 2013a) in order to attain that frequency (the flow rate was not measurable anymore by the measurement device as described in the paper), the DZFO was able to achieve that frequency at 1 slpm. The Hartmann Resonator fluidic oscillator requires 0.27g/s of mass air flow (>200slpm) as a minimum in order to start oscillating and a much higher rate in order to achieve the third harmonic excitation as opposed to the DZFO which attains it at 1 slpm, which is 0.02 g/s. This is 3 orders of magnitude different which differentiates it from the other oscillator.

The ability of the acoustic mode to achieve various types of waveforms presents a unique ability to generate bubbles of specific sizes. The mechanism of the oscillator flow mediated bubble generation requires that the peak of the wave is sharp since a flatter peak indicates a longer detachment period. If the amplitude can be high enough to detach the bubble (which is one of the major features of the DZFO), and if the waveform can be made to resemble a

triangular or shark tooth type waveform (Figure 63) , then there is a high possibility for much smaller bubble formation and when combined with the 'sweet spot' condition might generate smaller bubbles. Aside from being useful, it also presents a new scientific understanding of the new mechanism , that instead of acting like two separate resonators with two individual outlets, the DZFO acts as a singular system with a resonant mode, i.e. it is not one or the other , but an amalgam of the two modes. This is then further exploited in order to understand 'beats' characteristics.

The 'beats' characteristics help potentially attain fractional frequencies , which in pulsed air flow means, a steady flow plugged with a gas reversal. The 'beats' can also significantly increase the pulse strength and amplitude , which when combined with the low frequencies , can result in a much better bubble generating device than the one designed for low frequency bubble generation (Tesar, 2016) based on vortices. The flow reversal can be utilised for multiporous/mesoporous spargers to introduce a lubrication effect as observed for the ionic liquids (*cf.* Appendix for work on DZFO application in ionic liquids) and result in smaller bubble sizes. The higher amplitude can be used in combination with higher frequencies using the superposition principle and then generate much smaller bubbles at higher frequencies for membranes with slits such as those in (Zimmerman *et al.* , 2011) and (Zimmerman *et al.* , 2009c) .

The asymmetric oscillations, another unique feature, provide another positive proof that the acoustic mode is active and the DZFO behaves as a single system as opposed to two independent resonators. This can be used to generate several types of control valves and gas mixing possibilities with simple fluidic control (different resonant chambers) to generate the bubbles. The waveforms start to merge into a larger rectangular wavetrain, which is observed only for the Hartmann Resonator fluidic oscillator in published literature. This, coupled with the similarity of the pulse strength also signifies a lower frictional loss as opposed to the wave merging and reverberation seen in the TCFO waveform (Figure 58). In the TCFO, the waveforms are unequal due to the frictional losses accompanying the capacitive step, whereas for the DZFO (Figure 67) , the waveforms are equal, but with different frequencies, which show a combinatorial step as opposed to a reverberation and signify a single system.

In summary, the following features were identified and hypotheses confirmed for the underpinning mechanism of the DZFO-

The pulse strength –amplitude (4-10 times that of comparable oscillators), low pressure drop switching i.e. efficient oscillation, larger relief features (1mm instead of 0.2-0.7mm) for mass manufacturability, lower onset of oscillation (oscillates at 1 slpm), high downturn ratio, smaller bubbles generated due to a combination of these features, various possibilities and modalities with waveforms including beats, asymmetric oscillations, higher momentum transfer for pulse, lower dispersion into other modes (crisper and cleaner waveforms generated) , higher frequencies attainable(20 kHz), and lower friction losses results in the emergence of a disruptive enabling technology capable of a multitude of applications. These features are present whilst retaining all the advantageous features of the TZFO which has been published previously.

The next chapter discusses the development and use of visualisation and inferential techniques for visualisation of microbubble clouds. Visualisation of a single microbubble or low throughput microbubbles is very simple but polydisperse cloud of microbubbles create several complications.

5.3 Comparison of Bubble Size distributions inferred acoustic, visualisation, and laser diffraction

This chapter discusses the different methods that can be used for bubble size visualisation and the ability for these methods to be used for cloud microbubble visualisation. It provides useful criteria for judging the best method for a specific situation. It also helps understand the cloud microbubble dynamics and helps reconcile discrepancies in bubble sizes obtained and the transfer rates observed.

Each of these methods offers distinct drawbacks and advantages.

Spraytec and the ABS are indirect methods used for garnering bubble size distribution but offer near real time results and have high throughput acquisition capabilities. High speed

photography/videography is a direct method but not as effective for high throughput bubble/microbubble cloud dynamics and needs post processing and image analysis.

The Spraytec needs an appropriately sized sampling chamber to engender the bubble size distribution and works better for a smaller sample (ml) whereas the ABS is better for a larger system (litres and m^3). The ABS needs to have the hydrophones placed in the liquid medium whereas the lasers need to have a clear path to traverse through. Therefore depending on the application, a relevant system ought to be used. The ABS does not require the need for the sampling chamber to be transparent whereas Spraytec and high speed photography have this prerequisite. An acoustically transparent substance need not be an optically transparent one. There are a lot of construction and design materials that are acoustically transparent but not optically transparent. Optically transparent materials are limited. Whilst laser diffraction can still be used (not Spraytec but designed on the same principle), by placing the laser and the lens in an operationally controlled environment, the lenses are delicate and the region of interest measured will be too low and prone to errors in a larger vessel due to internal reflections which will lead to errors in measurement.

This is due to the region of interest and whilst a larger region of interest is easily possible for a piezoelectric based hydrophone, lasers are harder to enlarge. Measurements using optical methods had to use a plane due to complications relating to the overlapping bubbles and automated image analysis.

Depending on the uses, availability, expertise, and the application, different methods can be used to compute the bubble size distribution and upon significant inference, accurate bubble size distributions can be estimated. However, the findings here present an indication of the likely errors to be encountered or things to account for whilst undertaking these measurements.

The major scientific finding for this work is that hearing bubbles is much more effective than direct visualisation or using diffractive properties for the system. High throughput cloud microbubble dynamics are difficult to visualise or infer but acoustic methods are useful determinants. This method is to be used in most high throughput scenarios.

In case of optical and photonic techniques, vignetting might affect the results due to the incorrect measurement of light scattering angles which results from incorrect focussing. This is easier to correct for optical methods but a little difficult to do so with photonic methods. Optical methods would also suffer from the fact that the lenses and focussing possible is very limited. The bubble size can be either magnified and a small ROI (region of interest) can be used otherwise a broader region but a larger ROI is used. This means that sub150 μm measurements would result in a substantial reduction for bubbles being measured. Acoustic methods would also suffer from this problem but sound speed is easier to measure, calculate, and account for.

Using small sample sizes and extrapolating the results requires major assumptions which do not hold true in any practicable setting. This is why sizes obtained by laser diffraction (maximum possible region of interest = 1 cm^3 at most) and optical measurements (lens dependent but 1 cm^3 is likely based on magnification) are not accurate and can represent a very small fraction of the bubble population. Slight errors in measurement can lead to much larger errors due to this exponential extrapolation. This is avoided by the ABS, as there is no theoretical higher limit to the size of the hydrophone and they are inexpensive materials. The size distribution obtained is based on averaging across the region of measurement which is a better assumption than extrapolation.

Whilst the average bubble size can be the same, and comparable, the bubble size distribution need not be the same as observed in Figure 68, Figure 70, Figure 71, and Figure 72. This is why there has been discrepancy observed in terms of size measured and the properties observed such as (Al-Mashhadani *et al.*, 2011) where the effect of the microbubbles indicate a smaller size than what has been measured.

Another finding is that whilst published literature relies on the average bubble size based on the number of bubbles, for most purposes, the transport properties of microbubbles are required and these are dependent on their surface area to volume ratio. This means that the volume average bubble size is more important and relevant.

The next chapter deals with the transport properties of the microbubbles and the development of a novel unit operation – Microbubble Stripping and its use for separation phenomena.

5.4 Separation Processes – Ammonia stripping in ammonia rich waste waters

The major scientific finding was that the concentration driving force of the bubble was able to extract the ammonia from a system despite the fact that the ammonia exists in a dissociated state in the water.

This resulted in the additional ability to strip ammonia at pH of and lower than 9 when the vaporisation became the chief driving force and not concentration gradient. This is a first as reported in literature. The Le Chatelier's principle dictates that adding the OH^- ion, i.e. increase the pH drives the ammonia removal. However, the hot microbubble injection is also providing the increased entropy which pulls the ammonia into the bubble. This is why removal at a pH lower than 9 is also possible.

The presence of the temperature gradient which increases the effect of the concentration gradient is recorded and this follows from the Ludwig-Soret effect.

The two driving forces, dewatering/evaporation and ammonia/volatile removal are opposite in nature, and can be tuned by tuning the liquid layer height.

The temperature gradient controls the dewatering and removal of volatiles whereas the concentration gradient governs ammonia removal.

The reduction in bubble size due to the presence of the complex mixtures, and increased non-coalescence as observed in the Walpole liquor, results in a substantial increase in the transfer rates mediated by microbubbles. This follows from the theoretical model in Zimmerman *et al.* (Zimmerman *et al.*, 2014). Additionally, in this liquid, aside from smaller bubble formation, there is an increase in the bubble throughput due to the increased frequency of the oscillator. The frequency of the oscillator increases with the increase in the temperature of the air. Since each bubble acts as either the concentration push due to the OH^- ions, or the entropic pull due to the hot microbubble (temperature gradient) , it follows that increasing the throughput concomitant with the increased internal mixing of the smaller bubble would result in a much greater removal efficiency. This is why, 1000-3000 times increase in mass transfer coefficient for ammonia stripping has been observed for ammonia

water systems, whilst up to 15,000 times the increase in mass transfer coefficient is seen in the complex liquors such as Walpole.

This process is non-thermodynamic in nature due to the temperature gradient. The hot bubble enters the liquid at a set temperature, the liquid temperature is different to the impinging bubble temperature, and the bubble bursts. The temperature of the air from the bubble is at a different temperature than the temperature of the liquid and the temperature of the bubble. Therefore, this process is at constant non-equilibrium which keeps the driving force. The removal of the organic volatiles from the ammonia rich liquors, results in the decolouration due to the oxidation and removal of the volatiles along with the ammonia. This process can be controlled and is temperature dependent and therefore based more on the entropic pull. However, the concentration gradient will likely come into play once the component is volatilised. The removal of the components depends on a variety of factors and whilst a shotgun method can be used to target remediation, specific removal is also possible when the right balance between the temperature gradient and concentration gradient is used.

Chapter 6 Future Work

The future work follows from the findings from the thesis.

The presence of a resonant frequency - 'sweet spot' has been determined for all systems that generate bubbles mediated by oscillatory flow. Since most industrial processes involve cross flow, an additional advantage would be to include crossflow of liquid across the membrane. The crossflow of liquid across the membrane results in an additional force that causes the bubble pinch off. This can be matched with the 'sweet spot' i.e. frequency of generation of the microbubble which would result in a further reduction in bubble size. This is particularly useful for the hot microbubble approach as it improves its continuous processing ability.

An industrial scale application of the 'sweet spot' approach would be a useful determinant of whether this new understanding can be translated into something practicable.

The new oscillator, DZFO, was developed in order to use it for microbubble generation. The crisper peaks and higher amplitude of pulse enables the DZFO to inject the engendered microbubble with momentum. This provides an advantage for microbubble unit operations – distillation and stripping.

Microbubble distillation has had a limitation posed by (Abdulrazzaq *et al.*, 2015) and (AlYaqoobi *et al.*, 2014) with respect to the liquid height above the membrane that the injection of the microbubble can take place. The layer height controls the separation process and has to be thin (>5mm) in order to work effectively. The DZFO removes the limitations imposed on the microbubble distillation approach as posed by (Abdulrazzaq *et al.*, 2015) and (AlYaqoobi *et al.*, 2014) with the increased momentum of jet.

This hypothesis was tested for ethanol-water and methanol –water separations using the DZFO, and over 2-4 orders of magnitude change in performance was observed and the liquid height that can be used for the system is 5cm instead of 5mm. A layer, 5 cm thick, is no longer a thin layer but rather a plug. A continuous flowing system is a plug flow system of 5 cm thickness.

The ammonia-water separations, along with the ancillary cycles, need to be tested next, on a larger scale, as described in Appendix entitled DZ MMARP / DZ Waste Factory. For the scaled version, applying the DZFO in combination with the liquid crossflow enhanced 'sweet spot'

frequency would be a highly effective combination for achieving higher throughputs and separation rates.

Generating the shark tooth wave from the different waveforms possible to be generated by the DZFO might lead to a better bubble pinch-off. This might further reduce the bubble size.

Using the 'beats' phenomena, accompanied by the higher amplitude, will likely improve bubble formation for both membrane slit diffusers and multiporous ceramic membranes. Asymmetric oscillations need to be tested if they can be used for unequal gas mixing and reactions at the interface or apply them with plasma micro-reactors and solid oxide fuel cells in order to study the changing boundary layer.

References

- ABDULRAZZAQ, N., AL-SABBAGH, B. H., REES, J. M. & ZIMMERMAN, W. B. 2016. Purification of Bioethanol Using Microbubbles Generated by Fluidic Oscillation: A Dynamical Evaporation Model. *Industrial & Engineering Chemistry Research*, 55, 12909-12918.
- ABDULRAZZAQ, N., AL-SABBAGH, B., REES, J. M. & ZIMMERMAN, W. B. 2015. Separation of azeotropic mixtures using air microbubbles generated by fluidic oscillation. *AIChE Journal*, 62, 1192-1199.
- AGARWAL, A., NG, W. J. & LIU, Y. 2011a. Principle and applications of microbubble and nanobubble technology for water treatment. *Chemosphere*, 84, 1175-80.
- AGENCY, C. I. 2013. *Insectothopter: The Bug-Carrying Bug* [Online]. Langley, Virginia CIA. Available: <https://www.cia.gov/library/video-center/video-transcripts/insectothopter-the-bug-carrying-bug.html> [Accessed 06.06.2017 2017].
- AGENCY, E. P. 2000. Wastewater technology fact sheet / Ammonia stripping.: United States Environmental Protection Agency, Office of Water,.
- AGHAMOHAMMADI, N., AZIZ, H. B. A., ISA, M. H. & ZINATIZADEH, A. A. 2007. Powdered activated carbon augmented activated sludge process for treatment of semi-aerobic landfill leachate using response surface methodology. *Bioresource Technology*, 98, 3570-3578.
- AKUNNA, J. C., BIZEAU, C. & MOLETTA, R. 1993. Nitrate and nitrite reductions with anaerobic sludge using various carbon sources: Glucose, glycerol, acetic acid, lactic acid and methanol. *Water Research*, 27, 1303-1312.
- ALLEN, T. 1996. *Particle Size Measurement: Volume 1: Powder sampling and particle size measurement*, Springer.
- AL-MASHHADANI, M. K. H., BANDULASENA, H. C. H. & ZIMMERMAN, W. B. 2011. CO₂ Mass Transfer Induced through an Airlift Loop by a Microbubble Cloud Generated by Fluidic Oscillation. *Industrial & Engineering Chemistry Research*, 51, 1864-1877.
- AL-MASHHADANI, M. K. H., WILKINSON, S. J. & ZIMMERMAN, W. B. 2015. Airlift bioreactor for biological applications with microbubble mediated transport processes. *Chemical Engineering Science*, 137, 243-253.
- AL-MASHHADANI, M. K. H., WILKINSON, S. J. & ZIMMERMAN, W. B. 2016. Carbon dioxide rich microbubble acceleration of biogas production in anaerobic digestion. *Chemical Engineering Science*, 156, 24-35.

- ALWAN, A.A., GARIM, M. M, & HAMEED, F.S., 2012. Measuring of bubble rise velocity by using image processing technique. *Journal of Petroleum and Gas Exploration Research*, 2, 12.
- ALYAQOOBI, A. , ZIMMERMAN, W.B. 2014. Microbubble distillation studies of a binary mixture. In: PRATIK DESAI, Z. L., DR. RACHAEL ELDER, DR. DMITRIY KUVSHINOV (ed.) *USES - University of Sheffield Engineering Symposium 2014*. Sheffield: WhiteRose Consortia.
- AMIN, M. R., SHAREAR, S., SIDDIQUE, N. & ISLAM, S. 2013. Simulation of ammonia synthesis. *American Journal of Chemical Engineering*, 1, 59-64.
- ANDERSON, L. J. E., HANSEN, E., LUKIANOVA-HLEB, E. Y., HAFNER, J. H. & LAPOTKO, D. O. 2010. Optically guided controlled release from liposomes with tunable plasmonic nanobubbles. *Journal of Controlled Release*, 144, 151-158.
- APHA, 2007. Standard Methods for the Examination of Water and Wastewater - Part 4000 (Inorganic nonmetallic constituents), Section 4500-NH3. In: ANIMAL AND PLANT HEALTH AGENCY, G. U. (ed.). GOV.UK: APHA.
- AREBI, B. & DEMPSTER, W.M. 2008. Bubble formation at two adjacent submerged orifices in inviscid fluids. *Journal of Engineering Research*, 10.
- BAE, J., KIM, S. & CHANG, H. 1997. Treatment of landfill leachates: ammonia removal via nitrification and denitrification and further COD reduction via Fenton's treatment followed by activated sludge. *Water Science and Technology*, 36, 341-348.
- BEHERA, S. N., SHARMA, M., ANEJA, V. P. & BALASUBRAMANIAN, R. 2013. Ammonia in the atmosphere: a review on emission sources, atmospheric chemistry and deposition on terrestrial bodies. *Environ Sci Pollut Res Int*, 20, 8092-131.
- BERNARD, C., COLLIN, J. R. & ANNE, L. D.-D. 1997. Estimation of the hazard of landfills through toxicity testing of leachates. *Chemosphere*, 35, 2783-2796.
- BIRD, R. B., STEWART, W. E. & LIGHTFOOT, E. N. 2007. *Transport Phenomena*, Wiley.
- BOHDZIEWICZ, J., BODZEK, M. & GÓRSKA, J. 2001. Application of pressure-driven membrane techniques to biological treatment of landfill leachate. *Process Biochemistry*, 36, 641-646.
- BONMATÍ, A. & FLOTATS, X. 2003. Air stripping of ammonia from pig slurry: characterisation and feasibility as a pre- or post-treatment to mesophilic anaerobic digestion. *Waste Management*, 23, 261-272.
- BOZZANO, G. & DENTE, M. 2001. Shape and terminal velocity of single bubble motion: a novel approach. *Computers & Chemical Engineering*, 25, 571-576.
- BREITZ, N. & MEDWIN, H. 1989. Instrumentation for in situ acoustical measurements of bubble spectra under breaking waves. *The Journal of the Acoustical Society of America*, 86, 739-743.
- BRITTLE, S., DESAI, P., NG, W. C., DUNBAR, A., HOWELL, R., TESAŘ, V. & ZIMMERMAN, W. B. 2015. Minimising microbubble size through oscillation frequency control. *Chemical Engineering Research and Design*, 104, 357-366.
- BRITTLE, S., SAMUEL, A.R., & ZIMMERMAN, W.B., 2014. Atmospheric Moisture Content Effects on Ionic Liquid Wettability of Alumina. In: PRATIK DESAI , Z. Y. L., DR. RACHAEL ELDER, DR. DMITRIY KUVSHINOV (ed.) *University of Sheffield Engineering Symposium, 2014*. Sheffield: WhiteRose Press.
- BROWNE, C., TABOR, R. F., CHAN, D. Y., DAGASTINE, R. R., ASHOKKUMAR, M. & GRIESER, F. 2011. Bubble coalescence during acoustic cavitation in aqueous electrolyte solutions. *Langmuir*, 27, 12025-32.
- BRUUS, H. 2008. *Theoretical Microfluidics*, OUP Oxford.
- BUNCE, N. J. & BEJAN, D. 2011. Mechanism of electrochemical oxidation of ammonia. *Electrochimica Acta*, 56, 8085-8093.
- BURTON, S. A. Q. & WATSON-CRAIK, I. A. 1998. Ammonia and nitrogen fluxes in landfill sites: applicability to sustainable landfilling. *Waste Management & Research*, 16, 41-53.
- BYAKOVA, A. V., GNYLOSKURENKO, S. V., NAKAMURA, T. & RAYCHENKO, O. I. 2003. Influence of wetting conditions on bubble formation at orifice in an inviscid liquid: Mechanism of bubble evolution. *Colloids and Surfaces A: Physicochemical and Engineering Aspects*, 229, 19-32.

- CABEZA, A., URTIAGA, A., RIVERO, M.-J. & ORTIZ, I. 2007. Ammonium removal from landfill leachate by anodic oxidation. *Journal of Hazardous Materials*, 144, 715-719.
- CAI, X. 2012. Applications of Magnetic Microbubbles for Theranostics. *Theranostics*, 103.
- CAMPOS, F. B. & LAGE, P. L. C. 2000a. Heat and mass transfer modeling during the formation and ascension of superheated bubbles. *International Journal of Heat and Mass Transfer*, 43, 2883-2894.
- CAMPOS, F. B. & LAGE, P. L. C. 2000b. Simultaneous heat and mass transfer during the ascension of superheated bubbles. *International Journal of Heat and Mass Transfer*, 43, 179-189.
- CAMPOS, F. B. & LAGE, P. L. C. 2001. Modelling and simulation of direct contact evaporators. *Brazilian Journal of Chemical Engineering*, 18, 277-286.
- CAPODAGLIO, A. G., HLAVÍNEK, P. & RABONI, M. 2015. Physico-chemical technologies for nitrogen removal from wastewaters: a review. *Revista Ambiente & Água*, 10, 481-498.
- CERRETELLI, C., WUERZ, W. & GHARAIBAH, E. 2010. Unsteady Separation Control on Wind Turbine Blades using Fluidic Oscillators. *AIAA Journal*, 48, 1302-1311.
- CHAHINE, G.L., & KALUMUCK, M. K. 2003. Development of a Near Real-Time Instrument for Nuclei Measurement - The ABS. *International Symposium on Cavitation Inception, 4th ASME_JSME Joint Fluids Engineering Conference*. Honolulu, Hawaii, USA.
- CHAHINE, G. L. 1977. Interaction Between an Oscillating Bubble and a Free Surface. *Journal of Fluids Engineering*, 99, 709-716.
- CHAHINE, G. L. 2008. Numerical Simulation of Bubble Flow Interactions. *Cavitation: Turbo-machinery & Medical Applications-WIMRC FORUM 2008*. Warwick University, UK.
- CHAHINE, G. L., DURAISWAMI, R. & FREDERICK, G. 1998. DETECTION OF AIR BUBBLES IN HP INK USING DYNAFLOW'S ACOUSTIC BUBBLE SPECTROMETER (ABS) TECHNOLOGY. Hewlett Packard.
- CHAHINE, G.L., & GUMEROV, N. A. 2000. An inverse method for the acoustic detection, localization and determination of the shape evolution of a bubble. *Inverse Problems*, 16, 1-20.
- CHAHINE, G.L., KALUMUCK M. K., J-Y CHENG AND G. S. FREDERICK 2001. Validation of Bubble Distribution Measurements of the ABS with High Speed Video Photography. *CAV2001: sessionA7.004*.
- CHEUNG, K. C., CHU, L. M. & WONG, M. H. 1997. Ammonia stripping as a pretreatment for landfill leachate. *Water, Air, and Soil Pollution*, 94, 209-221.
- CHIANG, L.-C., CHANG, J.-E. & WEN, T.-C. 1995. Indirect oxidation effect in electrochemical oxidation treatment of landfill leachate. *Water Research*, 29, 671-678.
- CHIAPPE, C. & PIERACCINI, D. 2005. Ionic liquids: solvent properties and organic reactivity. *Journal of Physical Organic Chemistry*, 18, 275-297.
- CHOI, B. K., B.-C. K., B.-N. K. & S. W. Y. 2006. Assessment of Acoustic Iterative Inverse Method for Bubble Sizing to experimental data. *Ocean Science Journal* 41, 4.
- CHRISTIANSEN, C., KRYVI, H., SONTUM, P. C. & SKOTLAND, T. 1994. Physical and biochemical characterization of Albnex, a new ultrasound contrast agent consisting of air-filled albumin microspheres suspended in a solution of human albumin. *Biotechnology and applied biochemistry*, 19 (Pt 3), 307-20.
- CLEGG, S. L. & BRIMBLECOMBE, P. 1989. Solubility of ammonia in pure aqueous and multicomponent solutions. *The Journal of Physical Chemistry*, 93, 7237-7248.
- CLEVELAND, R. O., COHEN, A. L., ROY, R. A., SINGH, H. & SZABO, T. L. 2004. Imaging Coral II: Using Ultrasound to Image Coral Skeleton. *Subsurface Sensing Technologies and Applications*, 5, 43-61.
- COANDA, H. 1936. Device for deflecting a stream of elastic fluid projected into an elastic fluid. Google Patents.
- COLELLA, D., VINCI, D., BAGATIN, R., MASI, M. & ABU BAKR, E. 1999. A study on coalescence and breakage mechanisms in three different bubble columns. *Chemical Engineering Science*, 54, 4767-4777.

- COLLIVIGNARELLI, C., BERTANZA, G., BALDI, M. & AVEZZÙ, F. 1998. Ammonia stripping from MSW landfill leachate in bubble reactors: process modeling and optimization. *Waste Management & Research*, 16, 455-466.
- COLÓN, J., CADENA, E., POGNANI, M., BARRENA, R., SÁNCHEZ, A., FONT, X. & ARTOLA, A. 2012. Determination of the energy and environmental burdens associated with the biological treatment of source-separated Municipal Solid Wastes. *Energy Environ. Sci.*, 5, 5731-5741.
- COMMANDER, K. W. & PROSPERETTI, A. 1989. Linear pressure waves in bubbly liquids: Comparison between theory and experiments. *The Journal of the Acoustical Society of America*, 85, 732-746.
- COULSON, J. M., SINNOTT, R. K., RICHARDSON, J. F., BACKHURST, J. R. & HARKER, J. H. 1999. *Coulson & Richardson's Chemical Engineering: Chemical Engineering Design. 3rd ed*, Butterworth-Heinemann.
- CROSSLEY, I. A. & VALADE, M. T. 2006. A review of the technological developments of dissolved air flotation. *Journal of Water Supply: Research and Technology - Aqua*, 55, 479-491.
- CZERSKI, H. 2012. An Inversion of Acoustical Attenuation Measurements to Deduce Bubble Populations. *Journal of Atmospheric and Oceanic Technology*, 29, 1139-1148.
- DANČOVÁ, P. & TESAŘ, V. 2017. Taxonomic trees of fluidic oscillators. *EPJ Web of Conferences*, 143, 02128.
- DANČOVÁ, P., TESAŘ, V., PESZYNSKI, K. & NOVONTÝ, P. 2013. Strangely behaving fluidic oscillator. *EPJ Web of Conferences*, 45, 01074.
- DANČOVÁ, P., TESAŘ, V., PESZYNSKI, K., SMYK, E. & VESELÝ, M. 2016. Fluidic low-frequency oscillator consisting of load-switched diverter and a pair of vortex chambers. *EPJ Web of Conferences*, 114, 02121.
- DECKWER, W. D. 1980. On the mechanism of heat transfer in bubble column reactors. *Chemical Engineering Science*, 35, 1341-1346.
- DEJONG, N., KOOIMAN, K., HARTEVELD, M. & VANDERSTEEN, T. 2010. Drug uptake by endothelial cells through targeted microbubble sonoporation. *The Journal of the Acoustical Society of America*, 128, 2442.
- DESAI, P. D. , & ZIMMERMAN, W.B. 2015. Hot microbubble injection in thin liquid layers for ammonia-water separations. In: JOSE GORDILLO, U. D. S. (ed.) *The 68th Annual Meeting of the American Physical Society - Division of Fluid Dynamics*. MIT, Boston, Massachusetts USA: APS.
- DESAI, P.D., HINES, M.J., RIAZ, Y., & ZIMMERMAN, W.B., 2017. Determining the optimum oscillation frequency for generating the minimum microbubbles for a system: Enhanced microbubble generation mediated by optimised fluidic oscillation. [Submitted]
- DIANWU, Z. & ANPU, W. 1994. Estimation of anthropogenic ammonia emissions in asia. *Atmospheric Environment*, 28, 689-694.
- DING, Z., LIU, L., LI, Z., MA, R. & YANG, Z. 2006. Experimental study of ammonia removal from water by membrane distillation (MD): The comparison of three configurations. *Journal of Membrane Science*, 286, 93-103.
- DURAIWAMI, R., PRABHUKUMAR, S. & CHAHINE, G. L. 1998. Bubble counting using an inverse acoustic scattering method. *The Journal of the Acoustical Society of America*, 104, 2699-2717.
- DZOMBAK, D. A., ROY, S. B. & FANG, H.-J. 1993. Air-stripper design and costing computer program. *J. AWWA*, 85, 63.
- EARLE, M. J., ESPERANCA, J. M., GILEA, M. A., LOPES, J. N., REBELO, L. P., MAGEE, J. W., SEDDON, K. R. & WIDEGREN, J. A. 2006. The distillation and volatility of ionic liquids. *Nature*, 439, 831-4.
- EFREMOV, G. I. & VAKHRUSHEV, I. A. 1968. Formation of bubbles of gas in different liquids from cylindrical nozzles. *Chemistry and Technology of Fuels and Oils*, 4, 441-447.
- EL-BOURAWI, M. S., KHAYET, M., MA, R., DING, Z., LI, Z. & ZHANG, X. 2007. Application of vacuum membrane distillation for ammonia removal. *Journal of Membrane Science*, 301, 200-209.

- ELMORE, P. A. & CARUTHERS, J. W. 2003. Higher order corrections to an iterative approach for approximating bubble distributions from attenuation measurements. *Oceanic Engineering, IEEE Journal of*, 28, 117-120.
- ERISMAN, J. W., BLEEKER, A., GALLOWAY, J. & SUTTON, M. S. 2007. Reduced nitrogen in ecology and the environment. *Environ Pollut*, 150, 140-9.
- ERISMAN, J. W., SUTTON, M. A., GALLOWAY, J., KLIMONT, Z. & WINIWARTER, W. 2008. How a century of ammonia synthesis changed the world. *Nature Geosci*, 1, 636-639.
- FANG, J. 2012. Thermal Transport in Nanoporous Materials for Energy Applications.
- FARAG, H. I., MEJDELL, T., HJARBO, K., EGE, P., LYSBERG, M., GRISLINGÅS, A. & DE LASA, H. 1997. FIBRE OPTIC AND CAPACITANCE PROBES IN TURBULENT FLUIDIZED BEDS. *Chemical Engineering Communications*, 157, 73-107.
- FARMER, S. V. A. D. M. 1998. A Comparison of Four Methods for Bubble Size & Void Fraction Measurements. *IEEE Journal of Oceanic Engineering*, 23, 12.
- FARMER, S. V. D. 1991. Measurement of Bubble Size Distributions by Acoustical Backscatter. *Journal of Atmospheric and Oceanic Technology*, 9, 15.
- FIABANE, J., PRENTICE, P. & PANCHOLI, K. 2016. High Yielding Microbubble Production Method. *BioMed Research International*, 2016, 3572827.
- FRASCARI, D., BRONZINI, F., GIORDANO, G., TEDIOLI, G. & NOCENTINI, M. 2004. Long-term characterization, lagoon treatment and migration potential of landfill leachate: a case study in an active Italian landfill. *Chemosphere*, 54, 335-343.
- GAIL P. BOX, K. M. S., MICHAEL A. BOX 1992. Inversion of Mie Extinction measurements using analytic eigenfunction theory. *Journal of Atmospheric Sciences*, 49, 7.
- GANDHI, A. B. & JOSHI, J. B. 2010. Estimation of heat transfer coefficient in bubble column reactors using support vector regression. *Chemical Engineering Journal*, 160, 302-310.
- GOTTFRIED, B. S., LEE, C. J. & BELL, K. J. 1966. The leidenfrost phenomenon: film boiling of liquid droplets on a flat plate. *International Journal of Heat and Mass Transfer*, 9, 1167-1188.
- GOTVAJN, A. Ž., TIŠLER, T. & ZAGORC-KONČAN, J. 2009. Comparison of different treatment strategies for industrial landfill leachate. *Journal of Hazardous Materials*, 162, 1446-1456.
- GRAY, N. B., & LIOW, J.-L. 1988. A Model Of Bubble Growth In Wetting And Non-Wetting Liquids. *Chemical Engineering Science*, 43, 12.
- GREEN, D. & PERRY, R. 2007. *Perry's Chemical Engineers' Handbook, Eighth Edition*, McGraw-Hill Education.
- GREGORY, J. W., SULLIVAN, J. P. & RAGHU, S. 2005. Visualization of Jet Mixing in a Fluidic Oscillator. *J. Vis.*, 8, 169-176.
- GUET, S., FORTUNATI, R. V., MUDDE, R. F. & OOMS, G. 2003. Bubble Velocity and Size Measurement with a Four-Point Optical Fiber Probe. *Particle & Particle Systems Characterization*, 20, 219-230.
- GUŠTIN, S. & MARINŠEK-LOGAR, R. 2011. Effect of pH, temperature and air flow rate on the continuous ammonia stripping of the anaerobic digestion effluent. *Process Safety and Environmental Protection*, 89, 61-66.
- H. CZERSKI, M. T., X. ZHANG, AND S. VAGLE 2011. Resolving size distributions of bubbles with radii less than 30 μm with optical and acoustical methods. *Journal of Geophysical Research*, 116, 13.
- HABER, F. 1920. The synthesis of ammonia from its elements. *Nobel Lecture*.
- HADAMARD, J. S. 1911. Mouvement permanent lent d'une sphere liquide et visqueuse dans un liquide visqueux. *Cr. Acad. Sci*, 152, 1735-1738.
- HALLIDAY, D., RESNICK, R. & WALKER, J. 2010. *Fundamentals of Physics*, John Wiley & Sons.
- HANOTU, J., BANDULASENA, H. C. & ZIMMERMAN, W. B. 2012. Microflotation performance for algal separation. *Biotechnol Bioeng*, 109, 1663-73.
- HANOTU, J., BANDULASENA, H. C. H., CHIU, T. Y. & ZIMMERMAN, W. B. 2013. Oil emulsion separation with fluidic oscillator generated microbubbles. *International Journal of Multiphase Flow*, 56, 119-125.

- HANOTU, J., KONG, D. & ZIMMERMAN, W. B. 2016. Intensification of yeast production with microbubbles. *Food and Bioproducts Processing*, 100, Part A, 424-431.
- HASHIMOTO, M. & WHITESIDES, G. M. 2010. Formation of Bubbles in a Multisection Flow-Focusing Junction. *Small*, 6, 1051-1059.
- HASHIMOTO, M., SHEVKOPLYAS, S. S., ZASONSKA, B., SZYMBORSKI, T., GARSTECKI, P. & WHITESIDES, G. M. 2008. Formation of bubbles and droplets in parallel, coupled flow-focusing geometries. *Small*, 4, 1795-805.
- HEIJNEN, J. J. & VAN'T RIET, K. 1984. Mass transfer, mixing and heat transfer phenomena in low viscosity bubble column reactors. *The Chemical Engineering Journal*, 28, B21-B42.
- HERMES, O. 2012. *Hadamard-Rybczynski Equation*, Bellum Publishing.
- HIBINO, H. T. A. S.-I. 1978. Bubble Formation from a Submerged Single Orifice Accompanied by Pressure Fluctuations in Gas Chamber. *Journal of Chemical Engineering of Japan*, 11, 6.
- HIKITA, H., ASAI, S., KIKUKAWA, H., ZAIKE, T. & OHUE, M. 1981. Heat transfer coefficient in bubble columns. *Industrial & Engineering Chemistry Process Design and Development*, 20, 540-545.
- HOIGNE, J. & BADER, H. 1978. Ozonation of water: kinetics of oxidation of ammonia by ozone and hydroxyl radicals. *Environmental Science & Technology*, 12, 79-84.
- HOLDICH, R., KOSVINTSEV, S., CUMMING, I. & ZHDANOV, S. 2006. Pore Design and Engineering for Filters and Membranes. *Philosophical Transactions: Mathematical, Physical and Engineering Sciences*, 364, 161-174.
- HUANG, X., SONG, Y., LI, M., LI, J., HUO, Q., CAI, X., ZHU, T., HU, M. & ZHANG, H. 2012. A high-resolution ammonia emission inventory in China. *Global Biogeochemical Cycles*, 26, n/a-n/a.
- IANNIELLO, A., SPATARO, F., ESPOSITO, G., ALLEGRINI, I., RANTICA, E., ANCORA, M. P., HU, M. & ZHU, T. 2010. Occurrence of gas phase ammonia in the area of Beijing (China). *Atmospheric Chemistry and Physics*, 10, 9487-9503.
- INCROPERA, F. P., LAVINE, A. S., BERGMAN, T. L. & DEWITT, D. P. 2007. Fundamentals of heat and mass transfer.
- JANSSEN, A. J. H., LETTINGA, G. & DE KEIZER, A. 1999. Removal of hydrogen sulphide from wastewater and waste gases by biological conversion to elemental sulphur: Colloidal and interfacial aspects of biologically produced sulphur particles. *Colloids and Surfaces A: Physicochemical and Engineering Aspects*, 151, 389-397.
- JIA-LING RUAN, P.-W. C., SUZ-CHIA CHEN, YUEH-HSUN CHUANG, PAI-CHI L. In vitro Evaluation of Ultrasound-Assisted Thrombolysis Using Targeted Ultrasound Contrast Agents 2008 IEEE International Ultrasonics Symposium Proceeding, 2008.
- JILEK, V. T. M. 2013. INTEGRAL FLUIDIC GENERATOR OF MICROBUBBLES. *Colloquium Fluid Dynamics 2013*. Prague: Institute of Thermomechanics AS CR.
- JOKELA, J. P. Y., KETTUNEN, R. H., SORMUNEN, K. M. & RINTALA, J. A. 2002. Biological nitrogen removal from municipal landfill leachate: low-cost nitrification in biofilters and laboratory scale in-situ denitrification. *Water Research*, 36, 4079-4087.
- JOSHI, J. B., NANDAKUMAR, K., EVANS, G. M., PAREEK, V. K., GUMULYA, M. M., SATHE, M. J. & KHANWALE, M. A. 2017. Bubble generated turbulence and direct numerical simulations. *Chemical Engineering Science*, 157, 26-75.
- K. C. CHEUNG, L. M. C. A. M. H. W. 1995. Ammonia stripping as a pretreatment for landfill Leachate. *Water, Air, and Soil Pollution*, 94, 209-221.
- KABDASLI, I., ÖZTÜRK, İ., TÜNAY, O., YILMAZ, S. & ARIKAN, O. 2000. Ammonia removal from young landfill leachate by magnesium ammonium phosphate precipitation and air stripping. *Water Science and Technology*, 41, 237-240.
- KALUMUCK, G. L. C. K. M. Development of a Near Real time Instrument for Nuclei measurement : The ABS. International Symposium on Cavitation Inception, 4th ASME_JSME Joint Fluids Engineering Conference, 2003 Honolulu, Hawaii.
- KANTARCI, N., BORAK, F. & ULGEN, K. O. 2005. Bubble column reactors. *Process Biochemistry*, 40, 2263-2283.

- KARGI, F. & PAMUKOGLU, M. Y. 2004. Adsorbent supplemented biological treatment of pre-treated landfill leachate by fed-batch operation. *Bioresource Technology*, 94, 285-291.
- KARGI, F. & YUNUS PAMUKOGLU, M. 2003. Simultaneous adsorption and biological treatment of pre-treated landfill leachate by fed-batch operation. *Process Biochemistry*, 38, 1413-1420.
- KAWAHARA, A., SADATOMI, M., MATSUYAMA, F., MATSUURA, H., TOMINAGA, M. & NOGUCHI, M. 2009. Prediction of micro-bubble dissolution characteristics in water and seawater. *Experimental Thermal and Fluid Science*, 33, 883-894.
- KELLY, T. D., AND MATOS, G.R., COMPS 2014. U.S. Geological Survey, 2014, Nitrogen (fixed)—ammonia statistics. In: SURVEY, U. S. G. (ed.). U.S. Geological Survey.
- KHUNTIA, S., MAJUMDER, S. K. & GHOSH, P. 2012. Removal of Ammonia from Water by Ozone Microbubbles. *Industrial & Engineering Chemistry Research*, 121227123644009.
- KHURANA, A. K. & KUMAR, R. 1969. Studies in bubble formation — III. *Chemical Engineering Science*, 24, 1711-1723.
- KIM, G.-H. 2011. *A STUDY OF FLUIDIC OSCILLATORS AS AN ALTERNATIVE PULSED VORTEX GENERATING JET ACTUATOR FOR FLOW SEPARATION CONTROL*. Doctor of Philosophy, University of Manchester.
- KITANO, M., INOUE, Y., YAMAZAKI, Y., HAYASHI, F., KANBARA, S., MATSUSHI, S., YOKOYAMA, T., KIM, S.-W., HARA, M. & HOSONO, H. 2012. Ammonia synthesis using a stable electride as an electron donor and reversible hydrogen store. *Nat Chem*, 4, 934-940.
- KJELSDEN, P., BARLAZ, M. A., ROOKER, A. P., BAUN, A., LEDIN, A. & CHRISTENSEN, T. H. 2002. Present and Long-Term Composition of MSW Landfill Leachate: A Review. *Critical Reviews in Environmental Science and Technology*, 32, 297-336.
- KOOIMAN, K., FOPPEN-HARTEVELD, M., DER STEEN, A. F. W. V. & DE JONG, N. 2011. Sonoporation of endothelial cells by vibrating targeted microbubbles. *Journal of Controlled Release*, 154, 35-41.
- KULKARNI, A. & JOSHI J.B., 2005. Bubble Formation and Bubble Rise Velocity in Gas-Liquid Systems: A Review. *Industrial & Engineering Chemistry Research*, 44, 59.
- KUNEŠ, J. 2012a. 8 - Technology and Mechanical Engineering. *Dimensionless Physical Quantities in Science and Engineering*. Oxford: Elsevier.
- KUNEŠ, J. 2012b. Technology and Mechanical Engineering. 353-390.
- KUZNETSOV, I. A. 2010. *Microfluidics: Theory and Applications*, Nova Science Publishers, Incorporated.
- LA NAUZE, R. D. & HARRIS, I. J. 1972. On a model for the formation of gas bubbles at a single submerged orifice under constant pressure conditions. *Chemical Engineering Science*, 27, 2102-2105.
- LANAUZE, R. D. & HARRIS, I. J. 1974. A note on gas bubble formation models. *Chemical Engineering Science*, 29, 1663-1668.
- LASKOWSKI, Y. S. C. A. J. S. 2002. Bubble Coalescence and Its Effect on Dynamic Foam Stability. *The Canadian Journal of Chemical Engineering*, 80, 7.
- LEE, J.-W. K., HYEON-WOO; SOHN, JONG-IN; YOON, GIL-SANG 2013. A Study on Micro Bubbles Influence on Human Skin Cleaning. *Advanced Science Letters*, 19, 5.
- LEE, M., COLLINS, J. W., AUBRECHT, D. M., SPERLING, R. A., SOLOMON, L., HA, J.-W., YI, G.-R., WEITZ, D. A. & MANOHARAN, V. N. 2014. Synchronized reinjection and coalescence of droplets in microfluidics. *Lab on a Chip*, 14, 509-513.
- LEES, F. 2012. Appendix 11 - Safety, Health, and the Environment. In: MANNAN, S. (ed.) *Lees' Loss Prevention in the Process Industries (Fourth Edition)*. Oxford: Butterworth-Heinemann.
- LEI, X., SUGIURA, N., FENG, C. & MAEKAWA, T. 2007. Pretreatment of anaerobic digestion effluent with ammonia stripping and biogas purification. *J Hazard Mater*, 145, 391-7.
- LEIBACHER, I., SCHATZER, S. & DUAL, J. 2013. Impedance matched channel walls in acoustofluidic systems. *Lab Chip*, 14, 463-70.

- LEIBSON, I., HOLCOMB, E. G., CACOSO, A. G. & JACMIC, J. J. 1956. Rate of flow and mechanics of bubble formation from single submerged orifices. II. Mechanics of bubble formation. *AIChE Journal*, 2, 300-306.
- LEIGHTON, T. G. 1994. *The Acoustic Bubble*, Academic Press.
- LI CHEN, Y. L. A. R. M. 1998. THE COALESCENCE OF BUBBLES - A NUMERICAL STUDY. *Third International Conference on Multiphase Flow, ICMF'98*. Lyon.
- LI, L. & LIU, Y. 2009. Ammonia removal in electrochemical oxidation: mechanism and pseudo-kinetics. *J Hazard Mater*, 161, 1010-6.
- LI, X. Z., ZHAO, Q. L. & HAO, X. D. 1999. Ammonium removal from landfill leachate by chemical precipitation. *Waste Management*, 19, 409-415.
- LIAO, P. H., CHEN, A. & LO, K. V. 1995. Removal of nitrogen from swine manure wastewaters by ammonia stripping. *Bioresource Technology*, 54, 17-20.
- LICHT, S., CUI, B., WANG, B., LI, F.-F., LAU, J. & LIU, S. 2014. Ammonia synthesis by N_2 and steam electrolysis in molten hydroxide suspensions of nanoscale Fe_2O_3 . *Science*, 345, 637-640.
- LIN, C. S. K., PFALTZGRAFF, L. A., HERRERO-DAVILA, L., MUBOFU, E. B., ABDERRAHIM, S., CLARK, J. H., KOUTINAS, A. A., KOPSAHELIS, N., STAMATELATOU, K., DICKSON, F., THANKAPPAN, S., MOHAMED, Z., BROCKLESBY, R. & LUQUE, R. 2013. Food waste as a valuable resource for the production of chemicals, materials and fuels. Current situation and global perspective. *Energy & Environmental Science*, 6, 426-464.
- LIN, L., YUAN, S., CHEN, J., XU, Z. & LU, X. 2009. Removal of ammonia nitrogen in wastewater by microwave radiation. *J Hazard Mater*, 161, 1063-8.
- LINDNER, J. R. 2004. Microbubbles in medical imaging: current applications and future directions. *Nat Rev Drug Discov*, 3, 527-533.
- LINSEY C. PHILLIPS (PHD STUDENT), A. L. K., PHD, BRIAN R. WAMHOFF PHD, JOHN A. HOSSACK, PHD 2011. Ultrasound Mediated Targeted Drug Delivery. In: HEALTH, B. A. & SCHOOL OF ENGINEERING AND APPLIED SCIENCE, S. O. M. (eds.).
- LINSEY C. PHILLIPS, A. L. K., BRIAN R. WAMHOFF AND JOHN A. HOSSACK Intravascular Ultrasound Detection and Delivery of Molecularly Targeted Microbubbles for Gene Delivery. IEEE International Ultrasonics Symposium Proceedings, 2009.
- LITTLE, J. C. & MARIÑAS, B. J. 1997. Cross-Flow versus Counterflow Air-Stripping Towers. *Journal of Environmental Engineering*, 123, 668-674.
- LIU, B., PENG, X. Y., TIAN, Q. & ZHAO, H. 2014a. Removal of Ammonia Nitrogen from Landfill Leachate by Ultrasound/Ultraviolet Process. *Applied Mechanics and Materials*, 448-453, 536-539.
- LIU, S., WANG, Q., ZHAI, X., HUANG, Q. & HUANG, P. 2010. Improved Pretreatment (Coagulation‐Floatation and Ozonation) of Younger Landfill Leachate by Microbubbles. *Water Environment Research*, 82, 657-665.
- LIU, T., WANG, X., WANG, B., DING, X., DENG, W., LÜ, S. & ZHANG, Y. 2014b. Emission factor of ammonia (NH₃) from on-road vehicles in China: tunnel tests in urban Guangzhou. *Environmental Research Letters*, 9, 064027.
- LIU, Y., MIYOSHI, H. & NAKAMURA, M. 2006. Encapsulated ultrasound microbubbles: Therapeutic application in drug/gene delivery. *Journal of Controlled Release*, 114, 89-99.
- LO, I. M. C. 1996. Characteristics and treatment of leachates from domestic landfills. *Environment International*, 22, 433-442.
- LOUBIÈRE, K. & HÉBRARD, G. 2003. Bubble formation from a flexible hole submerged in an inviscid liquid. *Chemical Engineering Science*, 58, 135-148.
- LOUKIDOU, M. X. & ZOUBOULIS, A. I. 2001. Comparison of two biological treatment processes using attached-growth biomass for sanitary landfill leachate treatment. *Environmental Pollution*, 111, 273-281.
- LUKIANOVA-HLEB, E. Y., HANNA, E. Y., HAFNER, J. H. & LAPOTKO, D. O. 2010. Tunable plasmonic nanobubbles for cell theranostics. *Nanotechnology*, 21, 085102.

- LUO, X., MCCREARY, E. I., ATENCIO, J. H., MCCOWN, A. W. & SANDER, R. K. 1998. Bubble chamber as a trace chemical detector. *Applied Optics*, 37, 5640-5646.
- LUO, X., YAN, Q., WANG, C., LUO, C., ZHOU, N. & JIAN, C. 2015. Treatment of Ammonia Nitrogen Wastewater in Low Concentration by Two-Stage Ozonization. *Int J Environ Res Public Health*, 12, 11975-87.
- MACHADO, A. 1912. *Proverbs and Songs 29- Selected Poems of Antonio Machado*, Louisiana State University Press.
- MAEHLUM, T. 1995. Treatment of landfill leachate in on-site lagoons and constructed wetlands. *Wat. Sci. Tech.*, 32, 129-135.
- MAGINTYRE, F. 1986. On Reconciling Optical and Acoustical Bubble Spectra in the Mixed Layer. In: MONAHAN, E. & NIOCAILL, G. (eds.) *Oceanic Whitecaps*. Springer Netherlands.
- MARTIN, C. D. & JOHNSON, K. D. 1995. The use of extended aeration and in-series surface-flow wetlands for landfill leachate treatment. *Water Science and Technology*, 32, 119-128.
- MARTINEZ, C. J. 2009. Bubble generation in microfluidic devices. *Bubble Science, Engineering & Technology*, 1, 40-52.
- MARTINEN, S. K., KETTUNEN, R. H., SORMUNEN, K. M., SOIMASUO, R. M. & RINTALA, J. A. 2002. Screening of physical-chemical methods for removal of organic material, nitrogen and toxicity from low strength landfill leachates. *Chemosphere*, 46, 851-858.
- MEAIRS, S. & ALONSO, A. 2007. Ultrasound, microbubbles and the blood-brain barrier. *Progress in Biophysics and Molecular Biology*, 93, 354-362.
- MEDWIN, H. 1977. Counting bubbles acoustically: a review. *Ultrasonics*, 15, 7-13.
- MEIJERING, B. D. M., HENNING, R. H., VAN GILST, W. H., GAVRILOVIĆ, I., VAN WAMEL, A. & DEELMAN, L. E. 2007. Optimization of ultrasound and microbubbles targeted gene delivery to cultured primary endothelial cells. *Journal of Drug Targeting*, 15, 664-671.
- MERKUS, H. G. 2009. *Particle Size Measurements: Fundamentals, Practice, Quality*, Springer.
- METCALF, EDDY, I., TCHOBANOGLOUS, G., BURTON, F. & STENSEL, H. D. 2002. *Wastewater Engineering: Treatment and Reuse*, McGraw-Hill Education.
- MING YANG SU, D. T. A. J. C. 1994. Laboratory Comparisons of Acoustic and Optical Sensors for Microbubble Measurement. *Journal of Atmospheric and Oceanic Technology*, 11, 12.
- MIRCA BOSCIANU, V. P., IONICA CIRCUI 2010. Applications and Computational Aspects regarding the Coanda Effect. *Science and Military*, 1, 5.
- MISSELBROOK, T. H., VAN DER WEERDEN, T. J., PAIN, B. F., JARVIS, S. C., CHAMBERS, B. J., SMITH, K. A., PHILLIPS, V. R. & DEMMERS, T. G. M. 2000. Ammonia emission factors for UK agriculture. *Atmospheric Environment*, 34, 871-880.
- MOHIBAH MUSA, K. H. K. H., MIRADATUL NAJWA, RODHI, M. & FAKULTI KEJURUTERAAN KIMIA, J. I. 2013. Removal of Ammoniacal Nitrogen Ion in Old Landfill Leachate by Using Biological Stripping Column. *Business Engineering and Industrial Applications Colloquium (BEIAC)*. Langkawi, Malaysia: IEEE.
- MONLAU, F., SAMBUSITI, C., FICARA, E., ABOULKAS, A., BARAKAT, A. & CARRÈRE, H. 2015. New opportunities for agricultural digestate valorization: current situation and perspectives. *Energy Environ. Sci.*, 8, 2600-2621.
- MORAES, P. B. & BERTAZZOLI, R. 2005. Electrodegradation of landfill leachate in a flow electrochemical reactor. *Chemosphere*, 58, 41-46.
- MULVANA, H., ECKERSLEY, R. J., TANG, M. X., PANKHURST, Q. & STRIDE, E. 2012. Theoretical and experimental characterisation of magnetic microbubbles. *Ultrasound Med Biol*, 38, 864-75.
- MURANO, K., HATAKEYAMA, S., MIZOGUCHI, T. & KUBA, N. 1995. Gridded ammonia emission fluxes in Japan. *Water, Air, and Soil Pollution*, 85, 1915-1920.
- MURATA, S. 1984. MEASUREMENT OF MICRO AIR BUBBLES IN THE EXTRACORPOREAL CIRCULATION BY LASER BUBBLE DETECTOR. *Journal of the Japanese Association for Thoracic Surgery*, 32, 19-29.

- NARAYAN, G. P., SHARQAWY, M. H., LAM, S., DAS, S. K. & LIENHARD, J. H. 2013. Bubble columns for condensation at high concentrations of noncondensable gas: Heat-transfer model and experiments. *AIChE Journal*, 59, 1780-1790.
- NGUYEN, N. T. & WERELEY, S. T. 2002. *Fundamentals and Applications of Microfluidics*, Artech House.
- NIRMALAKHANDAN, N., SPEECE, R. E., PEACE, J. L. & JANG, W. 1993. Operation of counter-current air-stripping towers at higher loading rates. *Water Res.*, 27, 807.
- OLIVIER, J. G. J., BOUWMAN, A. F., VAN DER HOEK, K. W. & BERDOWSKI, J. J. M. 1998. Global air emission inventories for anthropogenic sources of NO_x, NH₃ and N₂O in 1990. *Environmental Pollution*, 102, 135-148.
- ONDA, K., TAKEUCHI, H. & OKUMOTO, Y. 1968. Mass transfer coefficients between gas and liquid phases in packed columns. *J. Chem. Engrg. of Japan*, 1, 56.
- OZTURK, E. & BAL, N. 2015. Evaluation of ammonia-nitrogen removal efficiency from aqueous solutions by ultrasonic irradiation in short sonication periods. *Ultrasonics Sonochemistry*, 26, 5.
- OZTURK, I., ALTINBAS, M., KOYUNCU, I., ARIKAN, O. & GOMEZ-YANGIN, C. 2003. Advanced physico-chemical treatment experiences on young municipal landfill leachates. *Waste Management*, 23, 441-446.
- PAMME, N. 2006. Magnetism and microfluidics. *Lab Chip*, 6, 24-38.
- PANCHOLI, K., STRIDE, E. & EDIRISINGHE, M. 2008. Dynamics of Bubble Formation in Highly Viscous Liquids. *Langmuir*, 24, 4388-4393.
- PARK, Y., TYLER, A. L., & NEVERS, N.D, 1976. The Chamber Orifice Interactions in the Formations of Bubbles. *Chemical Engineering Science*, Vol 32, pp 907-916.
- PARMAR, R. & MAJUMDER, S. K. 2013. Microbubble generation and microbubble-aided transport process intensification—A state-of-the-art report. *Chemical Engineering and Processing: Process Intensification*, 64, 79-97.
- PAULOT, F., JACOB, D. J., JOHNSON, M. T., BELL, T. G., BAKER, A. R., KEENE, W. C., LIMA, I. D., DONEY, S. C. & STOCK, C. A. 2015. Global oceanic emission of ammonia: Constraints from seawater and atmospheric observations. *Global Biogeochemical Cycles*, 29, 1165-1178.
- PHILLIPS, L. C., KLIBANOV, A. L., WAMHOFF, B. R. & HOSSACK, J. A. 2010. Targeted Gene Transfection from Microbubbles into Vascular Smooth Muscle Cells Using Focused, Ultrasound-Mediated Delivery. *Ultrasound in Medicine & Biology*, 36, 1470-1480.
- PHILLIPS, L. C., KLIBANOV, A. L., WAMHOFF, B. R. & HOSSACK, J. A. 2011. Localized ultrasound enhances delivery of rapamycin from microbubbles to prevent smooth muscle proliferation. *Journal of Controlled Release*, 154, 42-49.
- PINCZEWSKI, W. V. 1981. The formation and growth of bubbles at a submerged orifice. *Chemical Engineering Science*, 36, 405-411.
- PLECHKOVA, N. V. & SEDDON, K. R. 2008. Applications of ionic liquids in the chemical industry. *Chem Soc Rev*, 37, 123-50.
- PRESS, W. H. 2002. *Numerical Recipes in C++: The Art of Scientific Computing*, Cambridge University Press.
- RAGHU, S. 2013. Fluidic oscillators for flow control. *Experiments in Fluids*, 54.
- RAMAKRISHNAN, S., KUMAR, R. & KULLOOR, N. R. 1969. Studies in bubble formation-I bubble formation under constant flow conditions. *Chemical Engineering Science*, 24, 731-747.
- REHMAN, F., MEDLEY, G., BANDALUSENA, H.C.H., ZIMMERMAN, W.B., 2015. Fluidic oscillator-mediated microbubble generation to provide cost effective mass transfer and mixing efficiency to the wastewater treatment plants. *Environmental Research*, 137, 32-39.
- RIEFLER, N. & WRIEDT, T. 2008. Intercomparison of Inversion Algorithms for Particle-Sizing Using Mie Scattering. *Particle & Particle Systems Characterization*, 25, 216-230.
- ROBINSON, A. H. 2005. Landfill leachate treatment. *Membrane Technology*, 2005, 6-12.
- ROBINSON, H. D. & GRANTHAM, G. 1988. The treatment of landfill leachates in on-site aerated lagoon plants: Experience in Britain and Ireland. *Water Research*, 22, 733-747.

- ROGERS, R. D. & SEDDON, K. R. 2003. Chemistry. Ionic liquids--solvents of the future? *Science*, 302, 792-3.
- SADATOMI, M., KAWAHARA, A., KANO, K. & OHTOMO, A. 2005. Performance of a new micro-bubble generator with a spherical body in a flowing water tube. *Experimental Thermal and Fluid Science*, 29, 615-623.
- SANADA, T., SATO, A., SHIROTA, M. & WATANABE, M. 2009. Motion and coalescence of a pair of bubbles rising side by side. *Chemical Engineering Science*, 64, 2659-2671.
- SATYANARAYAN, A., KUMAR, R. & KULLOOR, N. R. 1969. Studies in bubble formation—II bubble formation under constant pressure conditions. *Chemical Engineering Science*, 24, 749-761.
- SAXENA, S. C., RAO, N. S. & SAXENA, A. C. 1992. Heat transfer and gas holdup studies in a bubble column: Air-water-sand system. *The Canadian Journal of Chemical Engineering*, 70, 33-41.
- SCHROEDER, A., KOST, J. & BARENHOLZ, Y. 2009. Ultrasound, liposomes, and drug delivery: principles for using ultrasound to control the release of drugs from liposomes. *Chemistry and Physics of Lipids*, 162, 1-16.
- SCHÜTH, F., PALKOVITS, R., SCHLÖGL, R. & SU, D. S. 2012. Ammonia as a possible element in an energy infrastructure: catalysts for ammonia decomposition. *Energy Environ. Sci.*, 5, 6278-6289.
- SHIROTA, M., SANADA, T., SATO, A. & WATANABE, M. 2008a. Formation of a submillimeter bubble from an orifice using pulsed acoustic pressure waves in gas phase. *Physics of Fluids*, 20, 043301-11.
- SILVA, A. C., DEZOTTI, M. & SANT'ANNA JR, G. L. 2004. Treatment and detoxification of a sanitary landfill leachate. *Chemosphere*, 55, 207-214.
- SINNOTT, R. & TOWLER, G. 2009. *Chemical Engineering Design*, Oxford, Butterworth-Heinemann.
- SLACK, R. J., GRONOW, J. R. & VOULVOULIS, N. 2005. Household hazardous waste in municipal landfills: contaminants in leachate. *Science of the Total Environment*, 337, 119-137.
- SMIL, V. 2004. *Enriching the Earth: Fritz Haber, Carl Bosch, and the Transformation of World Food Production*, MIT Press.
- SMITH, P. G. & ARAB, F. K. 1988. The role of air bubbles in the desorption of ammonia from landfill leachates in high pH aerated lagoon. *Water, Air, and Soil Pollution*, 38, 333-343.
- SPICKA, P., MARTINS, A. A., M. DIAS, M. & LOPES, J. C. B. 1999. Hydrodynamics of gas-liquid flow in 2D packed/unpacked rectangular reactor. *Chemical Engineering Science*, 54, 5127-5137.
- SPRAYTEC, M. 2013. Malvern Spraytec Manual. Malvern Spraytec.
- SRINATH, E. G. & LOEHR, R. C. 1974. Ammonia Desorption by Diffused Aeration. *Journal (Water Pollution Control Federation)*, 46, 1939-1957.
- STEINEMANN, J. & BUCHHOLZ, R. 1984. Application of an Electrical Conductivity Microprobe for the Characterization of bubble behavior in gas-liquid bubble flow. *Particle & Particle Systems Characterization*, 1, 102-107.
- STRIDE, E. & EDIRISINGHE, M. 2008. Novel microbubble preparation technologies. *Soft Matter*, 4, 2350-2359.
- STRIDE, E. 2008. The influence of surface adsorption on microbubble dynamics. *Philosophical Transactions of the Royal Society A: Mathematical, Physical and Engineering Sciences*, 366, 2103-2115.
- STROUHAL, V. 1878. Ueber eine besondere Art der Tonerregung. *Annalen der Physik*, 241, 216-251.
- SUTTON, M. A., DRAGOSITS, U., TANG, Y. S. & FOWLER, D. 2000. Ammonia emissions from non-agricultural sources in the UK. *Atmospheric Environment*, 34, 855-869.
- SUTTON, M. A., ERISMAN, J. W., DENTENER, F. & MOLLER, D. 2008b. Ammonia in the environment: from ancient times to the present. *Environ Pollut*, 156, 583-604.
- SUTTON, M. A., TANG, Y. S., DRAGOSITS, U., FOURNIER, N., DORE, A. J., SMITH, R. I., WESTON, K. J. & FOWLER, D. 2001. A spatial analysis of atmospheric ammonia and ammonium in the U.K. *ScientificWorldJournal*, 1 Suppl 2, 275-86.

- SUTTON, M., REIS, S. & BAKER, S. 2008a. *Atmospheric Ammonia: Detecting emission changes and environmental impacts. Results of an Expert Workshop under the Convention on Long-range Transboundary Air Pollution*, Springer Netherlands.
- SZCZUCZYSKI, J. M. D. 2009. Inverse Problems Formulated in Terms Of First-Kind Fredholm Integral Equations in Indirect Measurements. *Metrology and Measurement Systems*, 16, 333-357.
- TANGUAY, G. L. C. M. 2008. Acoustic Measurements of Bubbles in Biological Tissue. *Cavitation: Turbomachinery & Medical Applications*. Warwick University.
- TAYLOR, S. F. R., BRITTLE, S. A., DESAI, P., JACQUEMIN, J., HARDACRE, C. & ZIMMERMAN, W. A. 2017a. Factors affecting bubble size in ionic liquids. *Physical Chemistry Chemical Physics*, 19, 14306-14318.
- TESAŘ, V. & BANDALUSENA, H. 2011. Bistable diverter valve in microfluidics. *Experiments in Fluids*, 50, 1225-1233.
- TESAŘ, V. & BANDULASENA, H. C. H. 2011. Bistable diverter valve in microfluidics. *Experiments in Fluids*, 50, 1225-1233.
- TESAŘ, V. & TRÁVNÍČEK, Z. 2008. Excitational metamorphosis of surface flowfield under an impinging annular jet. *Chemical Engineering Journal*, 144, 312-316.
- TESAŘ, V. & ZIMMERMAN, W. B. Fluidic aerator: A new concept for aerobic water treatment. The University of Sheffield.
- TESAŘ, V. 2001. Microfluidic Valves for Flow Control at low Re. *The Visualisation Society of Japan and Ohmsha Ltd.*, 4, 9.
- TESAŘ, V. 2004. Fluidic Valve for Reactor Regeneration Flow Switching. *Chemical Engineering Research and Design*, 82, 398-408.
- TESAŘ, V. 2005. Fluidic Valves for Variable-Configuration Gas Treatment. *Chemical Engineering Research and Design*, 83, 1111-1121.
- TESAŘ, V. 2007a. Configurations of fluidic actuators for generating hybrid-synthetic jets. *Sensors and Actuators A: Physical*, 138, 394-403.
- TESAŘ, V. 2007b. "Paradox" of flow reversal caused by protective wall-jet in a pipe. *Chemical Engineering Journal*, 128, 141-154.
- TESAŘ, V. 2007c. *Pressure-Driven Microfluidics*, Artech House.
- TESAŘ, V. 2008. Characterisation of subsonic axisymmetric nozzles. *Chemical Engineering Research and Design*, 86, 1253-1262.
- TESAŘ, V. 2008. *Fluidic Oscillator Devices Based On The "Aerodynamic Paradoxon"*, Prague 8, Acad Sci Czech Republic, Inst Thermomechanics.
- TESAŘ, V. 2009a. Enhancing impinging jet heat or mass transfer by fluidically generated flow pulsation. *Chemical Engineering Research and Design*, 87, 181-192.
- TESAŘ, V. 2009b. Fluidic control of reactor flow—Pressure drop matching. *Chemical Engineering Research and Design*, 87, 817-832.
- TESAŘ, V. 2009c. Mechanism of pressure recovery in jet-type actuators. *Sensors and Actuators A: Physical*, 152, 182-191.
- TESAŘ, V. 2009d. Oscillator micromixer. *Chemical Engineering Journal*, 155, 789-799.
- TESAŘ, V. 2010. Development of fluidic weft insertion sensors. *Sensors and Actuators A: Physical*, 163, 101-110.
- TESAŘ, V. 2012. Microbubble generation by fluidics. part i: Development of the oscillator. *Colloquium FLUID DYNAMICS 2012*. Prague, Czech Republic.
- TESAŘ, V. 2013a. Microbubble Generator, Excited by Fluidic Oscillator's, Third Harmonic Frequency. *Chemical Engineering Research and Design*.
- TESAŘ, V. 2013b. Microbubble smallness limited by conjunctions. *Chemical Engineering Journal*, 231, 526-536.
- TESAŘ, V. 2013c. Shape Oscillation of Microbubbles. *Chemical Engineering Journal*.
- TESAŘ, V. 2014. Mechanisms of fluidic microbubble generation part ii: Suppressing the conjunctions. *Chemical Engineering Science*.

- TESAŘ, V. 2015. Fluidic Generator Of Microbubbles – Oscillator With Gas Flow Reversal For A Part Of Period. *Acta Mechanica et Automatica*, 9.
- TESAŘ, V. 2016. Stochastic regimes in very-low-frequency fluidic oscillator. *EPJ Web of Conferences*, 114, 02123.
- TESAŘ, V. 2017. What can be done with microbubbles generated by a fluidic oscillator? (survey). *EPJ Web Conf.*, 143, 02129.
- TESAŘ, V. Mechanisms of fluidic microbubble generation Part I: Growth by multiple conjunctions. *Chemical Engineering Science*.
- TESAŘ, V. Mechanisms of fluidic microbubble generation part II: Suppressing the conjunctions. *Chemical Engineering Science*.
- TESAR, V., HUNG, C. H. & ZIMMERMAN, W. B. 2006. No-moving-part hybrid-synthetic jet actuator. *Sensors and Actuators a-Physical*, 125, 159-169.
- TESAŘ, V., HUNG, C.-H. & ZIMMERMAN, W. B. 2006. No-moving-part hybrid-synthetic jet actuator. *Sensors and Actuators A: Physical*, 125, 159-169.
- TESAŘ, V., PESZYNSKI, K. & SMYK, E. 2016. Fluidic low-frequency oscillator consisting of load-switched diverter and a pair of vortex chambers. *EPJ Web of Conferences*, 114, 02121.
- TESAŘ, V., TIPPETTS, J. R., LOW, Y. Y. & ALLEN, R. W. K. 2004. Development of a Microfluidic Unit for Sequencing Fluid Samples for Composition Analysis. *Chemical Engineering Research and Design*, 82, 708-718.
- TESAŘ, V., TRÁVNÍČEK, Z., KORDÍK, J. & RANDA, Z. 2007. Experimental investigation of a fluidic actuator generating hybrid-synthetic jets. *Sensors and Actuators A: Physical*, 138, 213-220.
- TESAŘ, V., ZHONG, S. & RASHEED, F. 2013. New Fluidic-Oscillator Concept for Flow-Separation Control. *AIAA Journal*, 51, 397-405.
- THORAT, B.N. , KATARIA, K., KULKARNI A.V., & JOSHI, J.B., 2001. Pressure Drop Studies in Bubble Columns. *Ind. Eng. Chem. Res.*, 40, 3675-3688.
- TING, C.-Y., FAN, C.-H., LIU, H.-L., HUANG, C.-Y., HSIEH, H.-Y., YEN, T.-C., WEI, K.-C. & YEH, C.-K. 2012. Concurrent blood–brain barrier opening and local drug delivery using drug-carrying microbubbles and focused ultrasound for brain glioma treatment. *Biomaterials*, 33, 704-712.
- TIPPETTS, J. R. 2014. Tippetts' Fluidic Oscillator - Low flow oscillator for use with highly viscous ionic liquids - 4CU Project Internal Report - Consultancy
- TRÁVNÍČEK, Z. & TESAŘ, V. 2003. Annular synthetic jet used for impinging flow mass-transfer. *International Journal of Heat and Mass Transfer*, 46, 3291-3297.
- TRÁVNÍČEK, Z. & TESAŘ, V. 2004. Annular impinging jet with recirculation zone expanded by acoustic excitation. *International Journal of Heat and Mass Transfer*, 47, 2329-2341.
- TRÁVNÍČEK, Z., TESAŘ, V. & WANG, A.-B. 2005. Enhancement of synthetic jets by means of an integrated valve-less pump. *Sensors and Actuators A: Physical*, 125, 50-58.
- TREBOUET, D., SCHLUMPF, J. P., JAOUEN, P. & QUEMENEUR, F. 2001. Stabilized landfill leachate treatment by combined physicochemical–nanofiltration processes. *Water Research*, 35, 2935-2942.
- TREBOUET, D., SCHLUMPF, J. P., JAOUEN, P., MALERIAT, J. P. & QUEMENEUR, F. 1999. Effect of Operating Conditions on the Nanofiltration of Landfill Leachates: Pilot-Scale Studies. *Environmental Technology*, 20, 587-596.
- TREVENA, D. H. 1987. *Cavitation and Tension in Liquids*, Published under the Adam Hilger imprint by IOP Publishing.
- TREYBAL, R. E. 1980. *Mass-transfer Operations*, McGraw-Hill.
- TSUGE, H. & HIBINO, S. I. 1983. BUBBLE FORMATION FROM AN ORIFICE SUBMERGED IN LIQUIDS. *Chemical Engineering Communications*, 22, 63-79.
- TSUGE, H., TERASAKA, K., TOZAWA, K. & HIBINO, S.-I. 1987. Bubble Formation from an Orifice Submerged in Highly Viscous Liquids. *KAGAKU KOGAKU RONBUNSHU*, 13, 857-860.

- TSUGE, H., TEZUKA, Y. & MITSUDANI, M. 2006. Bubble formation mechanism from downward nozzle—Effect of nozzle shape and operating parameters. *Chemical Engineering Science*, 61, 3290-3298.
- U GEBHARDY, H. H. A. U. S. 1996. Numerical investigation of fluidic micro-oscillators. *J. Micromech. Microeng*, 6, 2.
- UYGUR, A. & KARGI, F. 2004. Biological nutrient removal from pre-treated landfill leachate in a sequencing batch reactor. *Journal of Environmental Management*, 71, 9-14.
- VILAR, V. J. P., ROCHA, E. M. R., MOTA, F. S., FONSECA, A., SARAIVA, I. & BOAVENTURA, R. A. R. 2011. Treatment of a sanitary landfill leachate using combined solar photo-Fenton and biological immobilized biomass reactor at a pilot scale. *Water Research*, 45, 2647-2658.
- VINCENT S.J. CRAIG, B. W. N., RICHARD M. PASHLEY 1993. The Effect of Electrolytes on Bubble Coalescence in Water. *Journal of Physical Chemistry*, 97, 5.
- VIOTTI, P. & GAVASCI, R. 2015. Scaling of ammonia stripping towers in the treatment of groundwater polluted by municipal solid waste landfill leachate: study of the causes of scaling and its effects on stripping performance. *Revista Ambiente & Água*, 10, 240-252.
- VÍT, T., TESAŘ, V., PESZYNSKI, K., DANČOVÁ, P. & NOVOTNÝ, P. 2014. Water oxygenation by fluidic microbubble generator. *EPJ Web of Conferences*, 67, 02116.
- VLYSSIDES, A. G., KARLIS, P. K., RORI, N. & ZORPAS, A. A. 2002. Electrochemical treatment in relation to pH of domestic wastewater using Ti/Pt electrodes. *Journal of Hazardous Materials*, 95, 215-226.
- VLYSSIDES, A., KARLIS, P., LOIZIDOU, M., ZORPAS, A. & ARAPOGLOU, D. 2001. Treatment of Leachate from a Domestic Solid Waste Sanitary Landfill by an Electrolysis System. *Environmental Technology*, 22, 1467-1476.
- VOS, H. J., DOLLET, B., BOSCH, J. G., VERSLUIS, M. & DE JONG, N. 2008. Nonspherical Vibrations of Microbubbles in Contact with a Wall—A Pilot Study at Low Mechanical Index. *Ultrasound in Medicine & Biology*, 34, 685-688.
- Wafa GHOZLANI, L. B., AZEDDINE KOURTA, HENRI-CLAUDE BOISSON, STÉPHANE COLIN. DESIGN AND EXPERIMENTAL ANALYSIS OF A MICROFLUIDIC OSCILLATOR FOR ACTIVE FLOW CONTROL. Proceedings of the 2nd European Conference on Microfluidics - Microfluidics 2010, December 8-10, 2010 Toulouse.
- WALTON, M. 1973. Industrial ammonia gassing. *British Journal of Industrial Medicine*, 30, 78-86.
- WANG, S., WU, X., WANG, Y., LI, Q. & TAO, M. 2008. Removal of organic matter and ammonia nitrogen from landfill leachate by ultrasound. *Ultrasonics Sonochemistry*, 15, 933-937.
- WANG, Y., GUO, X., LI, J., YANG, Y., LEI, Z. & ZHANG, Z. 2012. Efficient Electrochemical Removal of Ammonia with Various Cathodes and Ti/RuO₂-Pt Anode. *Open Journal of Applied Sciences*, 02, 241-247.
- WARREN, R. W. 1962. *Negative Feedback Oscillator*. United States patent application.
- WEBER, D. B. A. M. E. 1981. Bubbles in viscous liquids: shapes, wakes and velocities. *Journal of Fluid Mechanics*, 105, 24.
- WEIGL, B., DOMINGO, G., LABARRE, P. & GERLACH, J. 2008. Towards non- and minimally instrumented, microfluidics-based diagnostic devices. *Lab on a Chip*, 8, 1999-2014.
- WESLEY, D. J., BRITTLE, S. A. & TOOLAN, D. T. 2016a. Development of an optical microscopy system for automated bubble cloud analysis. *Appl Opt*, 55, 6102-7.
- WESLEY, D. J., SMITH, R. M., ZIMMERMAN, W. B. & HOWSE, J. R. 2016b. Influence of Surface Wettability on Microbubble Formation. *Langmuir*, 32, 1269-1278.
- WU, C., AL-DAHMAN, M. H. & PRAKASH, A. 2007. Heat transfer coefficients in a high-pressure bubble column. *Chemical Engineering Science*, 62, 140-147.
- WU, X.-J. & CHAHINE, G. L. 2010. Development of an acoustic instrument for bubble size distribution measurement. *Journal of Hydrodynamics, Ser. B*, 22, 330-336.
- X. WU, C.-T. H., G. L. CHAHINE 2008. ABS Acoustic Bubble Spectrometer User Manual. Dynaflo inc.

- XIAO, B. & LIU, S.-Q. 2014. Photocatalytic Oxidation of Ammonia via an Activated Carbon-Nickel Ferrite Hybrid Catalyst under Visible Light Irradiation. *Acta Physico-Chimica Sinica*, 30, 1697-1705.
- XINGJIAN JIANG , Z. C., WEI MA*, ZHANXIAN GAO, XUEHU MA, REN WANG Removal of Ammonia from Wastewater by Natural Freezing Method *In: GAO, Y., ed. International Conference on Chemical, Material and Food Engineering (CMFE-2015) 25-26 July 2015 2015 Kunming, Yunan, China Atlantis Press, 920.*
- XU, R. 2001. *Particle Characterization: Light Scattering Methods*, Springer.
- XUE, J., AL-DAHMAN, M., DUDUKOVIC, M. P. & MUDDE, R. F. 2003. Bubble Dynamics Measurements Using Four-Point Optical Probe. *The Canadian Journal of Chemical Engineering*, 81, 375-381.
- XUE, J., AL-DAHMAN, M., DUDUKOVIC, M. P. & MUDDE, R. F. 2008. Four-point optical probe for measurement of bubble dynamics: Validation of the technique. *Flow Measurement and Instrumentation*, 19, 293-300.
- YAMINSKY, V. V., OHNISHI, S., VOGLER, E. A. & HORN, R. G. 2010. Stability of aqueous films between bubbles. Part 1. The effect of speed on bubble coalescence in purified water and simple electrolyte solutions. *Langmuir*, 26, 8061-74.
- YING, K., GILMOUR, D. J., SHI, Y. , ZIMMERMAN W.B., 2013a. Growth Enhancement of Dunaliella salina by Microbubble Induced Airlift Loop Bioreactor (ALB)—The Relation between Mass Transfer and Growth Rate *Journal of Biomaterials and Nanobiotechnology*, 4, 1-9.
- YING,K., AL MASHHADANI M. K. H., HANOTU, J.O., GILMOUR, D.J., & ZIMMERMAN W. B. 2013b. Enhanced Mass Transfer in Microbubble Driven Airlift Bioreactor for Microalgal Culture. *Engineering*, 5, 735-743.
- YUAN, M.-H., CHEN, Y.-H., TSAI, J.-Y. & CHANG, C.-Y. 2016a. Ammonia removal from ammonia-rich wastewater by air stripping using a rotating packed bed. *Process Safety and Environmental Protection*, 102, 777-785.
- YUAN, M.-H., CHEN, Y.-H., TSAI, J.-Y. & CHANG, C.-Y. 2016b. Removal of ammonia from wastewater by air stripping process in laboratory and pilot scales using a rotating packed bed at ambient temperature. *Journal of the Taiwan Institute of Chemical Engineers*, 60, 488-495.
- ZALMANZON, L. A. 1967. Method of automatically controlling pneumatic or hydraulic elements of instruments and other devices. Google Patents.
- ZHANG, F., LIU, J., YANG, W. & LOGAN, B. E. 2015. A thermally regenerative ammonia-based battery for efficient harvesting of low-grade thermal energy as electrical power. *Energy Environ. Sci.*, 8, 343-349.
- ZHANG, T., DING, L. & REN, H. 2009. Pretreatment of ammonium removal from landfill leachate by chemical precipitation. *J Hazard Mater*, 166, 911-5.
- ZHEN XU , M. R., TIMOTHY L. HALL, CHING-WEI CHANG, MARY-ANN MYCEK, J. BRIAN FOWLKES AND CHARLES A. CAIN 2007. High Speed Imaging of Bubble Clouds Generated in Pulsed Ultrasound Cavitational Therapy—Histotripsy. *IEEE Trans Ultrason Ferroelectr Freq Control.*, 54, 10.
- ZHU, X., CASTLEBERRY, S. R., NANNY, M. A. & BUTLER, E. C. 2005. Effects of pH and catalyst concentration on photocatalytic oxidation of aqueous ammonia and nitrite in titanium dioxide suspensions. *Environ Sci Technol*, 39, 3784-91.
- ZIEMINSKI, R. R. L. S. A. 1971. Bubble Coalescence and Gas Transfer in Aqueous Electrolytic Solutions. *Industrial & Engineering Chemistry Fundamental*, 10, 10.
- ZIMMERMAN, W. B. J. 2014. Mass transfer processes with limited sensible heat exchange. Google Patents.
- ZIMMERMAN, W. B., AL-MASHHADANI, K. H. & IGENEGBAI, V. O. 2013a. Cold boiling: fine and microbubble mediated binary distillation of methanol and water liquid solution. (*Internal report*).
- ZIMMERMAN, W. B., AL-MASHHADANI, M. K. H. & BANDULASENA, H. C. H. 2013b. Evaporation dynamics of microbubbles. *Chemical Engineering Science*, 101, 865-877.

- ZIMMERMAN, W. B., HEWAKANDAMBY, B. N., TESAŘ, V., BANDULASENA, H. C. H. & OMOTOWA, O. A. 2009a. On the design and simulation of an airlift loop bioreactor with microbubble generation by fluidic oscillation. *Food and Bioproducts Processing*, 87, 215-227.
- ZIMMERMAN, W. B., TESAŘ, V., BUTLER, S. & BANDULASENA, H. H. 2008. Microbubble Generation. *Recent Patents on Engineering*, 2.
- ZIMMERMAN, W. B., TESAŘ, V. & BANDULASENA, H. C. H. 2009c. Part I: Laboratory bench scale studies. *Efficiency of an aerator driven by fluidic oscillation*. The University of Sheffield.
- ZIMMERMAN, W. B., TESAŘ, V. & BANDULASENA, H. C. H. 2011a. Towards energy efficient nanobubble generation with fluidic oscillation. *Current Opinion in Colloid & Interface Science*, 16, 350-356.
- ZIMMERMAN, W. B., TESAŘ, V. & BANDULASENA, H. RE: *Efficiency of an aerator driven by fluidic oscillation. Part I: Laboratory bench scale studies*.
- ZIMMERMAN, W. B., TESAŘ, V., BANDULASENA, H. C. H. & OMOTOWA, O. A. 2009d. Part II: Pilot scale trials with flexible membrane diffusers. *Efficiency of an aerator driven by fluidic oscillation*. The University of Sheffield.
- ZIMMERMAN, W. B., ZANDI, M., HEMAKA BANDULASENA, H. C., TESAŘ, V., GILMOUR, D.J., & YING, K. 2011b. Design of an airlift loop bioreactor and pilot scales studies with fluidic oscillator induced microbubbles for growth of a microalgae *Dunaliella salina*. *Applied Energy*, 88, 3357-3369.
- ZIMMERMAN, W.B. , TESAŘ ,V., BUTLER, S., & BANDULASENA H.C.H., 2008. Microbubble Generation. *Recent Patents on Engineering*, 2, 1-8.
- ZÖLLIG, H., REMMELE, A., MORGENROTH, E. & UDERT, K. M. 2017. Removal rates and energy demand of the electrochemical oxidation of ammonia and organic substances in real stored urine. *Environ. Sci.: Water Res. Technol.*, 3, 480-491.

Appendices

Appendix A- Ionic Liquids – Formation Dynamics and Effect of Staging

The effect of oscillatory injected flow on microbubble formation dynamics in viscous ionic liquids

Pratik Desai^{1, 4}, Sarah FR Taylor², Stuart Brittle¹, Johan Jacquemin³, Christopher Hardacre², William B Zimmerman^{1*}

1 – Department of Chemical and Biological Engineering, Mappin Street, University of Sheffield, Sheffield, S1 3JD, United Kingdom

2 – School of Chemical Engineering & Analytical Science, The Mill, University of Manchester Manchester, M13 9PL, United Kingdom

3 – School of Chemistry and Chemical Engineering, Queen's University Belfast, David Keir Building, 39 Stranmillis Road, Belfast, BT9 5AG, United Kingdom

4- Perlemax Ltd., 40 Leavygreave Road, S3 7RD, Sheffield, United Kingdom

*Corresponding Author – William Zimmerman – w.zimmerman@sheffield.ac.uk

Abstract (225 words)

Oscillatory flow, under tailored conditions, has dramatically decreased the bubble size compared with steady flow into a range of complex, but low viscosity, largely aqueous liquids. In this paper, oscillatory flow is injected into novel room temperature ionic liquids(ILs) as exemplar liquids, due to higher viscosity and their potential to play a substantial role in carbon capture and catalysis. The microbubble formation dynamics are explored. Five ILs were selected, namely [C₂mim][DCA], [C₂mim][EtSO₄], [C₂mim][NTf₂], [C₄mim][NTf₂] and [C₄mim][TFA]. An overall bubble size reduction, up to a factor of four, is observed for the ILs tested with fluidic oscillation([C₂mim][DCA], 900 μm- 250 μm) and an increase in throughput (≈8 times for [C₂mim][NTf₂] from 500 to 3,900). Furthermore, bubble formation dynamics change with fluidic oscillation. Wetting properties strongly influence bubble size. The minimum bubble size is found at an intermediate contact angle between liquid wetting and non-wetting. Different formation dynamics are observed compared to conventional viscous liquids due to the surface interactions of the chemical moieties present. This physical chemistry of bubble formation study suggests possibilities for a low cost carbon capture and

release system mediated by microbubbles which are explored sequel studies of CO₂ adsorption/desorption dynamics soon to be reported. The resulting increase in surface area and throughput for the same volume greatly enhances possibilities for low cost use of ILs for catalysis and carbon capture and release.

Introduction

Microbubbles have been the focus of much research of late, due to their greatly enhanced transport phenomena. Their usage has not been widespread in industrial applications due to their inherently high generation energetics via conventional means [1], except for specific applications where the end-products are of high value or are resultant of the unique features exhibited by microbubbles in the field of medical theranostics and as gene vectors [2-7]. As such, the high-energy consumption associated with their production is substantially offset by these enhanced transport dynamics or advantageous imaging features. However, most chemical processes would benefit from the increased mass and heat transfer phenomena associated with microbubbles if they could be produced in an economical fashion. Zimmerman *et al.* [8, 9] demonstrated the low energy and, crucially, low capital and operating cost, generation of microbubbles via fluidic oscillation resulting in a paradigm shift in existing technology.

A fluidic oscillator is a no-moving-part bistable diverter valve capable of engendering bubbles in an energy efficient and economical manner by generating oscillatory flow [10-12]. The oscillatory flow thus generated is a hybrid synthetic jet as described by Tesar *et al.* [13] and shown in Figure 88.

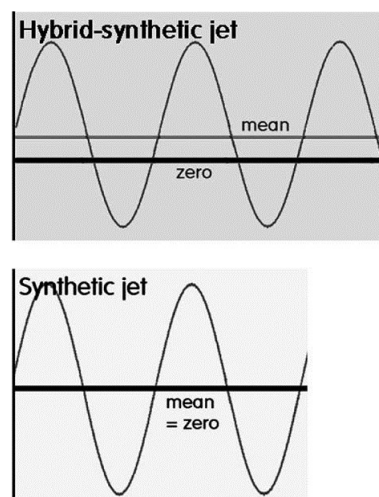


Figure 88 Hybrid synthetic jet (reproduced with permission Tesar *et al.* [13]).

A hybrid synthetic jet generates a flow field with overall positive throughput, that cannot easily be replicated using a simple sinusoid and a speaker, for instance. This results in a net positive displacement rather than a null sum jet as seen in the synthetic jet in Figure 88. A typical example of a null sum jet is an acoustic sinusoid produced by a speaker. The hybrid synthetic jet is a net positive displacement jet which causes a switching with positive and negative pulses in nozzles with a net positive output. This signal is different to a simple sinusoid or speaker set up and cannot be easily artificially reproduced with conventional actuators.

The fluidic oscillator is composed of typical parts as described by Figure 89.

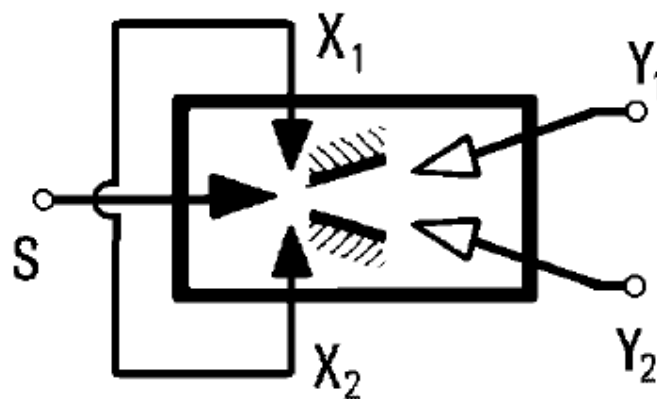


Figure 89 Fluidic oscillator for microbubble generation taken from Tesar *et al.* [11] Spyropolous type fluidic oscillator. Where S is the supply nozzle), X1 and X2 are the control terminals and Y1 and Y2 the outlets.

The gas enters the inlet of the fluidic oscillator via the supply nozzle (S). The gas is then accelerated due to the throat (nozzle) which acts as an amplifier. X1 and X2 are the control terminals attached to each other in the third dimension and the length of this 'feedback' loop determines the frequency of switching for the system. Y1 and Y2 are the diffuser legs that are attached to the aerators (spargers) which generate the bubbles of the same order of magnitude as the engendering orifice. Additional information is provided in Zimmerman *et al.* [9] regarding the bubble formation mechanism via fluidic oscillation. The oscillator generates an ON/OFF pulse on each leg as part of the oscillatory cycle. Each

oscillation/ pulse typically generates a bubble when the force balance is satisfied. In such case, the bubble is released from the engendering surface when the wetting force is overcome by the buoyant force of the bubble and the acceleration inertia due to the oscillator. Widespread industrial utilisation for microbubbles was a difficult prospect not envisaged to be practical prior to the invention of fluidic oscillator driven microbubble formation.

However, when the energetics associated with microbubble generation is significantly reduced, the possibility to implement microbubbles in several industrial applications [14-23] becomes a possibility. A major point to note for the purpose of this paper is that the microbubbles formed so far have been either in aqueous based systems or in liquids with a viscosity comparable with water. Highly viscous liquids have usually been avoided for bubbling due to the difficulty in generating microbubbles in viscous liquids. The viscosity of the system is an extremely important determinant of the engendered bubble size due to forces responsible for bubble detachment. Although bubble detachment is affected by several factors, the two primary forces responsible for determining detachment are buoyancy and viscous forces [24]. The higher the viscosity, the more difficult it is to detach the bubble and therefore balance the forces on the bubble. As a result, there is a larger bubble size generated from the orifice if other conditions remain the same for an aqueous system. The rise velocity of the bubble, given by the Stokes' law approximation,

$$F = 6 \pi \mu R V \quad - \quad (1)$$

where F is the Stokes' drag force acting on the interface between the fluid and the bubble [Pa], μ is the dynamic viscosity [Pa.s], R is the radius of the bubble [m], and V is the terminal rise velocity [m/s]. An increase in friction forces would therefore result in a reduction in rise velocity for highly viscous liquids and a consequent increase in bubble size due to coalescence and conjunction. The literature provides varying views on the effect of viscosity on bubble formation dynamics. These range from a) viscosity has no effect on bubble size, [25,26, 27], b) an increase in viscosity results in a monotonic increase in bubble size [25, 28] and c) viscosity results in a decrease in bubble size [29]. Based on water-glycerol mixtures (unpublished scoping study) and work published by Taylor *et al.* [30] for steady flow, it has been seen that the strongest correlation was an increase in bubble size with an increase in viscosity with contact angle and viscosity being the two factors having the highest correlation to the bubble size. Previous work that discusses larger bubble sizes in viscous liquids (although some manage to generate microbubbles) displays severe practical limitations due to limited bubble throughput, high pressure drops, or higher energy consumed for bubble generation [31-37].

For example, in [30], microbubbles were generated but not in an industrially applicable scenario since the bubbling pressure required for this was 2.4bar(g) which would be highly expensive to achieve in an industrial setting. Additionally, the scalability problems linked with the material in question would pose problems. The formation characteristics are also indeterminate since it is only a correlation but not a trend. The large chemical moieties on the surface of the IL and the interactions between the anion and cation are responsible for the trend observed in the bubble size. The sigma moments alone better describe the system as opposed to the physico-chemical properties involved [30]. This is a novel finding not observed elsewhere in literature and one of the major reasons for this finding was the 'suppression' of the physico-chemical parameters by the reduction in pore size to such an extreme that there was a 2.4bar(g) pressure drop across the system. The ceramic used in that paper is a mesoporous structure with an average pore size of 2.5 μ m, with 10mm thickness, which results in the large pressure drop across the system. This means that the pressure beneath the sparger(chambre pressure) has equalised and the bubbles formed are suppressed enough for the effect of the chemical moieties and sigma moments for the ILs to take place. However, with a pressure drop this high, it cannot be used for an industrial application as an energy efficient process.

Bubbling in a viscous liquid in an energy efficient manner has been highly sought after in several fields such as polymeric and catalytic chemistry, manufacturing metallic foams or for degassing purposes in molten metals, the food and beverage industry (*e.g.* bubbling in chocolate), paper and pulp industry, fine chemicals and distillation (for example bubbles can separate phases concomitant with little or no sensible heating [16, 38, 39]) to name a few. Another major application is for the use with novel room temperature ionic liquids (RTILs – ILs for purposes of this paper). ILs are a relatively new class of designer liquids capable of competing against conventional carbon capture solutions such as monoethanolamine (MEA) due to their relatively low vapour pressure and solvent degradation rates[40,41]. To increase the sorption kinetics, *i.e.* rate of sorption, the key design parameter is the available surface area, which can be provided by microbubbles. Consequently, improving the kinetics of sorption improves the associated transport phenomena. However, this enhancement must be balanced with formation cost to best obtain sufficient information for the same since mole solvent/mole CO₂ ILs are better performing than MEA solutions with the additional advantage of negligible solvent degradation during the desorption cycle. ILs are generally highly viscous with viscosities ranging from several times that of water to thousands to even a million times that of water. Additionally, ILs are made of complex anionic and cationic moieties with charge distribution dependent on the moieties present. As discussed above, one of the major findings for bubbling in ILs [30] dealt with a higher pressure system in order to simulate bubbling with sufficient backpressure to

overcome the viscous and wetting forces and amplify the effect of the sigma moments, *i.e.* a probe of interactions between the anions and cations, which resulted in a strong effect on bubble formation.

Our hypothesis is that the successful generation of smaller microbubbles via fluidic oscillation is achieved by fluidic circuit matching. Furthermore, this will result in a size ordering related to the viscosity and wettability of the IL in the system and thereby revert to conventional bubbling in viscous liquids. The oscillatory pulse generated by the oscillator comprises of both a positive and negative cycle. The positive cycle of the pulse results in the bubble formation as discussed in [9]. The negative cycle results in an increased wetting by virtue of backflow/ seepage into the pores. This creates a lubricating effect and has been labelled as the lubrication effect in this paper and the phenomenon has been experimentally demonstrated by Tesar *et al* [42]. This mechanism has been described in more detail in the discussions section of the paper. This should result in a change in bubble formation dynamics, with bubble size reduction for these highly viscous liquids with fluidic oscillator implementation as per the hypothesis. The reduction depends on the liquid and wetting properties which is different to what has been observed in Taylor *et al.* [30] where bubble size is dependent on the chemical moieties present on the system and there was only a strong correlation of viscosity / molecular weight if physico-chemical properties were taken into account. The chemical moieties here would have an effect but the reduction in the backpressure of the sparger (to 40 mbar from 2.4 bar(g) in Taylor *et al.* [30]), coupled with larger pore size (20 μ m instead of 2.5 μ m), would likely result in a reduced contribution to the effect on bubble size. Taylor *et al.* [30] had a higher simulated backpressure in order to investigate the effects of the moieties and bubbling dynamics in ILs without necessarily being dominated by physico-chemical properties of the ILs.

Certain ILs were selected from the subset used in Taylor *et al* [30] and used for sizing bubbles for oscillatory flow as they had diverse liquid properties (viscosity, wettability) and chemical moieties present which would help determine the effects of the moieties present and the relationship between bubble formation (and size) with these properties and separate it from the effect of the interactions between chemical moieties. Although air was injected into the system in order to have the microbubbles act as proxies to the transport rates, it is our intention to develop a novel carbon dioxide capture system with IL mediated by microbubbles. Furthermore, the purpose of this study is to investigate bubbling with a fluidic oscillator to see if the limitations imposed by the moieties present can be suppressed, yet result in generation of smaller microbubbles, at a low energy cost *i.e.* lower pressure drop.

Taylor *et al.* [30] demonstrated an interesting and important ramification relevant to conventional bubble formation theory. Most of the papers that discuss bubble generation or formation dynamics

[28, 32, 35-37, 43-49] describe bubbling as a contest between viscous and buoyant forces. Consequently, the emergent bubble size and rise velocity depend on the viscosity of the liquid medium, wettability of the engendering surface, nature of the gas injected (viscosity and density of gas), inertial forces, inlet flow and orifice size. It was observed in Taylor *et al* [30], that the chemical moieties were interacting substantially, depending on their sigma moments, changing the bubble formation behaviour as compared to conventional bubbling with size being dependent on the influence of the chemical moieties present in the system. The chemical moieties can therefore pose a limitation on bubble size and formation characteristics which would not be a cause of concern for additives such as glycerol and tween [50]. Glycerol and tween are responsible for an increase in viscosity and add some charges on the interface but not the extent of the chemical moieties on the system as the ILs.

This paper with fluidic oscillation describes the increased throughput, the bubble size reduction and the novel interactions of the different moieties on the surface of the bubble following from Taylor *et al*. [30]. However, it also demonstrates energy efficient bubble generation and how the limitations imposed by the chemical moieties can be overcome for microbubble formation. Discussions on the change in properties affecting bubble formation for oscillatory flow over steady flow are also presented.

Materials and Method

Materials:

Chemicals used:

ILs used herein were selected from those previously synthesised and tested [30]. 1-ethyl-3-methylimidazolium dicyanamide [C₂mim][DCA] (98 %), 1-ethyl-3-methylimidazolium bis(trifluoromethylsulfonyl)imide [C₂mim][NTf₂] (≥97 %), and 1-butyl-3-methylimidazolium bis(trifluoromethylsulfonyl)imide [C₄mim][NTf₂] (≥98 %) were used as received from Merck. 1-Ethyl-3-methylimidazolium ethylsulfate ([C₂mim][EtSO₄]) was synthesised by dissolving diethylsulfate (Sigma-Aldrich, 98 %, 154.2 g, 1 mol) in ice cold toluene (Sigma-Aldrich, ≥99.5 %, 100 cm³) and adding this solution dropwise to 1-methylimidazole (Sigma-Aldrich, 99 %, 82.1 g, 1 mol) dissolved in water (500 cm³) in an ice bath under a nitrogen atmosphere. This solution was stirred overnight. The organic solvent was then removed and the former IL was then sequentially washed with toluene (100 cm³) and dried *in vacuo* five times. 1-Butyl-3-methylimidazolium trifluoroacetate [C₄mim][TFA] was synthesised from trifluoroacetic acid (Sigma-Aldrich, 99 %, 114.0 g, 1 mol) added dropwise to 1-butyl-3-methylimidazolium chloride

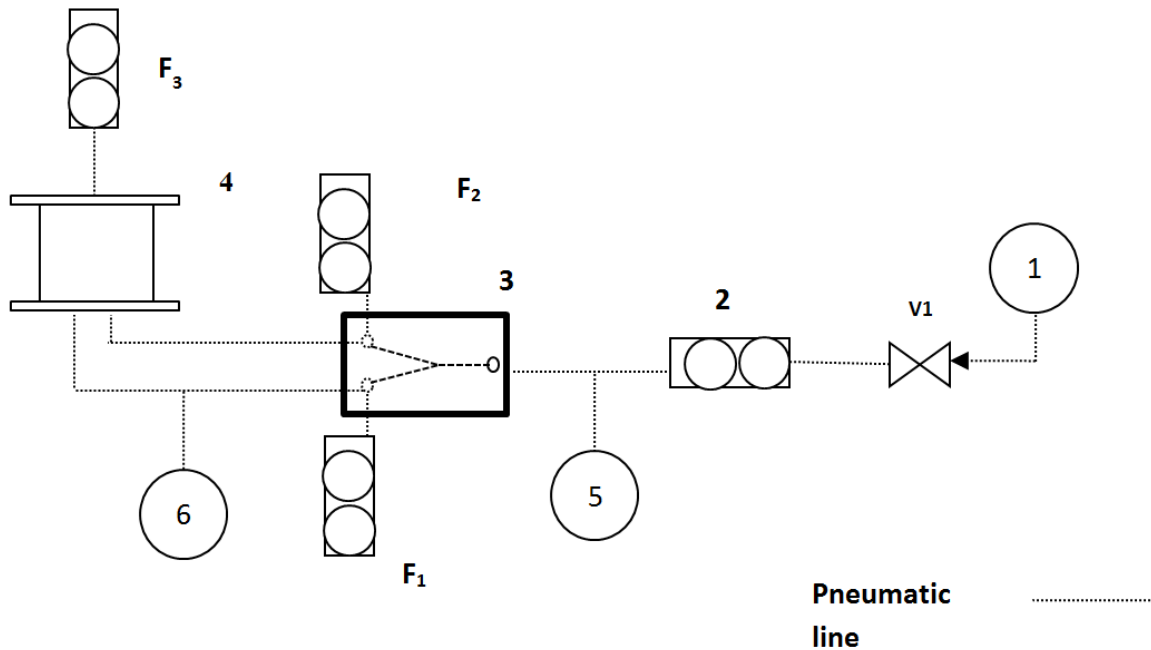
(174.7 g, 1 mol) dissolved in Milli-Q ultra-pure water (500 cm³) in an ice bath and allowed to stir overnight. The solvent was then removed using a rotary evaporator to obtain the IL. All ILs were dried *in vacuo* (< 10⁻² mbar @ 40 °C) for a minimum of 48 h and maintained under a flow of dry N₂ overnight before microbubble measurements were carried out. After drying, the water content of the ILs was measured using a Metrohm 787 KF Titrino Karl Fischer as < 0.1 wt% for all ILs. The purity of the synthesized ILs was analysed using ¹H NMR using a Bruker 300MHz Ultra shield Plus NMR spectrometer and the results were consistent with literature reports [51, 52].

Air was used, coming out of a pressurised compressor at 8 bar(g) which was then regulated by a pressure regulator down to the bubbling pressure required for the same.

Material Properties

Ionic Liquids	Viscosity (Pa.s)	Molecular Weight (g/mol)	Contact Angle (°)
[C ₂ mim][DCA]	0.01594	177.21	43.7
[C ₂ mim][EtSO ₄]	0.1204	236.29	53.5
[C ₂ mim][NTf ₂]	0.03249	391.31	56.4
[C ₄ mim][NTf ₂]	0.052	419.36	36.7
[C ₄ mim][TFA]	0.053	252.23	35.3

Experimental Setup



- | | |
|--------------------------------------|--|
| 1. Pressure Regulator for Air supply | V ₁ . Shutdown valve |
| 2. Mass Flow Controller | F ₁ . Vent Rotameter 1 |
| 3. Fluidic Oscillator | F ₂ . Vent Rotameter 2 |
| 4. Test Cell | F ₃ . Outlet Mass flowmeter |
| 5. Backpressure monitor | |
| 6. Pressure Transducer | |

Figure 90 Set up – shows the pneumatic set up for the system.

Pneumatic Set up

The experimental set up is shown in Figure 3 with the liquid placed inside the specially designed test cell for these sets of experiments. Gas (air in this instance) enters the system via the pressure regulator (1) which sends out a controlled, well-regulated gas supply into a mass flow controller(2). The mass flow controller(2) feeds in the appropriate amount of air to flow into the fluidic oscillator (3) to initialise oscillation. The fluidic oscillator in Zimmerman *et al* [9] needs a relatively large amount of air flow in order to initialise oscillations (60 litres per minute). The test cell (4) has been designed to work with low volume ILs and therefore low flow (millilitres per minute, rather than litres per minute required to initialise the oscillations) enters the test cell, whereas a much larger volume of gas enters the oscillator.

The appropriate amount of gas flow into the test cell is controlled using the vent rotameters (F1 and F2). Since a specific amount of flow is required for the fluidic oscillator to actuate, some of the gas flow is vented using rotameters. A pressure transducer (6) located at the outlet of the oscillator measures the amplitude and frequency of the oscillated air pulse. In addition, this measurement was

also used to calculate flow through the oscillator, prior to the sparger. This is so that oscillated air of an appropriate frequency, amplitude and flow rate can be delivered to the test cell(4). The pressure transducer (6) and backpressure monitor (5) help indicate the pressure and energetics of the system.

The flows for the system were monitored and adjusted using a mass flowmeter(F3)- (Bronkhorst model - Mini-CoriFlow) placed at the outlet of the system. The liquid layer in the system provided sufficient resistance which mitigated against any additional damping effects of the oscillatory flow by the mass flowmeter. Steady flow is achieved by bypassing the oscillator.

Test Cell

The 3D model of the test cell is shown in Figure 4 with an SEM image of the sparger used. It is a stainless-steel manifold with low pressure drop sparger (HP technical ceramic, sintered Alumina, 20 μm pore size and 40 mbar pressure drop) , with an active bubbling area for each outlet of the oscillator -1.5 cm x 3 cm. This test cell was designed because of the difficulty in preparing large volumes of IL. The cell was designed to hold 50 cm^3 -100 cm^3 of IL and leave some head space to account for any potential foaming. The visualisation window (quartz windows) helps in bubble size determination by optical imaging and the sparger can be changed in order to garner the best size distribution possible. Scanning electron microscopy (SEM) was carried out on a JEOL JSM 6300 SEM with an Agar MB7240 gold sputter coater. This sparger has a thickness of 5 mm and the pressure required to allow bubbling in an aqueous system is 40 mbar(g) at 298 K and 101.325 kPa.

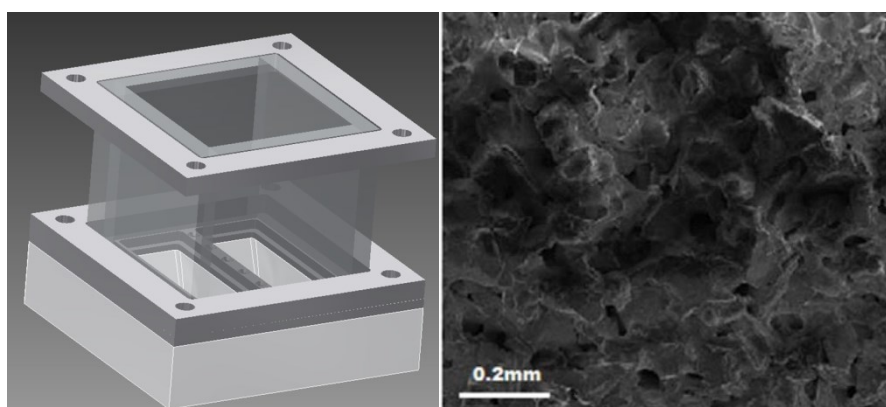


Figure 4 (left)Stainless steel test cell (labelled 4 in Figure 3) with quartz viewing windows which has the capability generating microbubbles in ILs. (right) SEM Image (JEOL JSM 6300 SEM with an Agar MB7240 gold sputter coater)

Frequency Measurement

The frequency of the oscillator was determined by using a bespoke code written in LabView. This could also be used to determine the magnitude of the pulse strength on the oscillatory wave. The code consisted of a Fast Fourier Transform (FFT) power spectrum for the raw data obtained from the pressure transducer at 128 kilo-samples per second. The FFT is a signal processing technique which, when respecting the Nyquist theorem with sufficient sampling rate for the wave power spectrum present, results in a peak formed for the various excited modes. Where there is a dominant frequency of oscillation, this is referred to as “the oscillation frequency” which helps to determine the amplitude of the wave jet generated from the oscillator outlet into the sparger.

Imaging Setup

The bubble sizing and imaging set up is described in Brittle *et al.* [53] with the camera and diffused light source placed opposite each other with the test cell placed in the centre.

The high-speed camera (Pixelink PL742 camera) is placed opposite to the diffused light source (Thorlabs LIU004- intensity - 1700 W/cm² and 450 nm - emission peak) with the test cell placed in the centre. The bright LED light source is diffused into a more uniform light using a white plastic translucent optical diffuser layer, placed before the test cell with the visualisation windows where the bubbles are imaged with the camera. Bubble sizes are determined by a bespoke code developed in LabView as described in [53]. Bubble size analysis was performed and histograms were generated with the code from the images captured. Mean, mode and median bubble sizes were calculated as described below.

Mean stands for the average bubble size and is calculated using

$$D[1,0] = \bar{D} = \frac{\sum_{i=1}^n D_i}{n} \quad (2)$$

Where $D[1,0]$ and \bar{D} is the mean bubble diameter, D_i is the diameter of bubble i in the distribution, and n is the total number of bubbles in the measured image. Mode stands for the maximum bubbles of the same size appear in the histogram or the bubble size that appears most times in the histogram.

Median stands for the middle value of bubble size in the histogram or the bubble size which lies right in the centre of the histogram. This value is also commonly denoted as D_{50} in particle sizing [54].

The difference among mean, mode and average of the bubble sizes characterises the major features of the bubble size distribution including the spread of a distribution [54].

The low air flow (millilitres per minute) into the test cell facilitated the use of the optical bubble sizing technique as a single plane can be observed and imaged, which minimises the magnitude of the error in the measurement technique. Three repeats were taken for the bubble sizes to get an average bubble size.

Since the test cell was designed for a low pressure drop to be able to compete with industrial processes in stark contrast to studies which were performed previously to study bubbling in ionic liquids [30] (and therefore the pore sizes were smaller and backpressure – higher, in order to reduce the effect of viscosity and wettability on formation dynamics), the pore sizes were increased (from 2.5 μm for a ceramic similar to PointFour (Pentair) Systems to HP Technical Ceramic, 20 μm pore size) and the pressure drop reduced (from 2.4bar(g) to 40 mbar(g))

The backpressure for this sparger and design is 40 mbar(g) and the oscillator operated at 100-110 mbar(g) bringing total system pressure drop to approximately 150 mbar. There are minor variations as this also depends slightly on the frequency of oscillation in the system.

Contact Angle Measurement

The contact angle measurements were made using an Attension pendant drop tensiometer for all the ILs. The methodology is described in [55].

The ILs were kept a dry environment and heated to 60°C for 24 hours in order to remove residual moisture whilst maintaining vacuum desiccation in the presence on CaCl_2 . The Attension pendant drop tensiometer is able to take precise measurements of the contact angle using a visualization setup similar to the bubble sizing visualization setup including a monochromatic light source, adjustable sample; and software able to recognize the drop and measure its contact angle. The ILs were pipetted onto the cleaned substrate stage, adjustable in three dimensions using micrometer screws. The droplet is then centered and an image taken for analysis using the software. An averaged contact angle is calculated from the recorded imaging taking the left and right angles into consideration (within 5% of each other or symmetry).

Results and Discussions

Runs were carried out for the different ILs at 50 millilitres per minute flow rates. Oscillatory flow was followed by a cleaning/flushing protocol involving flushing the system with water and ethanol and drying it with nitrogen. This was then followed by bubble injection into the IL with steady flow and bypassing the oscillator. The other conditions were kept the same. Different ILs of a fixed volume (50 cm³) were used throughout. Bubble imaging and image analysis was performed in order to garner the bubble size distribution for each condition. Bubble throughput was recorded as well.

The hypothesis of this paper was whether the bubble formation and bubble size for IL would change based on fluidic oscillator implementation and change in sparger characteristics such that microbubble generation is possible without significant impact on formation dynamics by chemical moieties. At the very least, suppression of the effect of the chemical moieties on the surface and improvement of the physico-chemical transport properties of the system is sought.

Bubble Size Analysis

Bubble size has conventionally been taken as the mean of the population. The mean is generally denoted by the quotient of the summation of the sizes of the bubbles in a given population over the total number of bubbles being formed. However, where cloud bubble dynamics are concerned, a major error is introduced when the assumption is that there is a monodisperse singular bubble population. Cloud bubble dynamics dictate bubble sizes to be polydisperse. Populations are distributed and rather unevenly for many cases and therefore there is a wide disparity in bubble sizes observed and a single figure cannot be used to describe the entire distribution. The presence of the focal plane to estimate bubble size is another source of error when bubble sizing is considered. This paper will use average bubble sizes (mean and median) initially and then discuss into individual bubble size distributions to better describe the effects of the chemical moieties on the bubble size.

Bubble Sizes

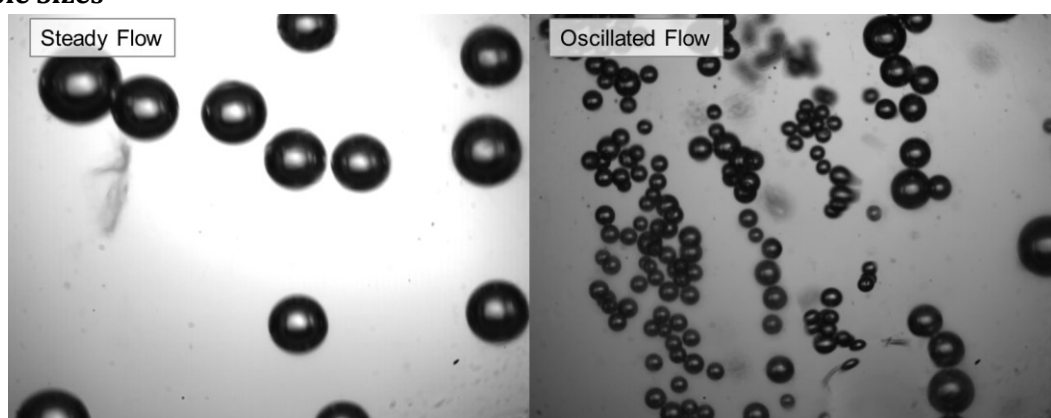


Figure 5 An example of the image captured in the test cell for steady flow (left) and oscillatory flow (right) for a single IL-[C₂mim][DCA] - at equivalent flowrate conditions (50 millilitres per minute).

Figure 5 shows an example of the image captured and the change of bubble size for the same conditions with fluidic oscillator implementation (right) and conventional steady flow (left) for the IL [C₂mim][DCA]. Similar size reductions were observed for all the ILs and the average size distributions are shown in Figure 6. Figure 6 shows the mean bubble size comparison for different ILs - [C₂mim][DCA], [C₂mim][EtSO₄], [C₂mim][NTf₂], [C₄mim][NTf₂], and [C₄mim][TFA] trialed in this paper. Fluidic oscillator mediated microbubble injection resulted in a substantial reduction in bubble size as seen in Figure 6. Bubble size reductions were observed for all of the ILs upon fluidic oscillator implementation with different levels of reduction due to the effect of the physico-chemical properties and effect of the moieties which will be discussed later.

Certain differences were observed for bubble size dependence on the actual mechanism and mechanics for bubble formation for oscillatory and steady flow.

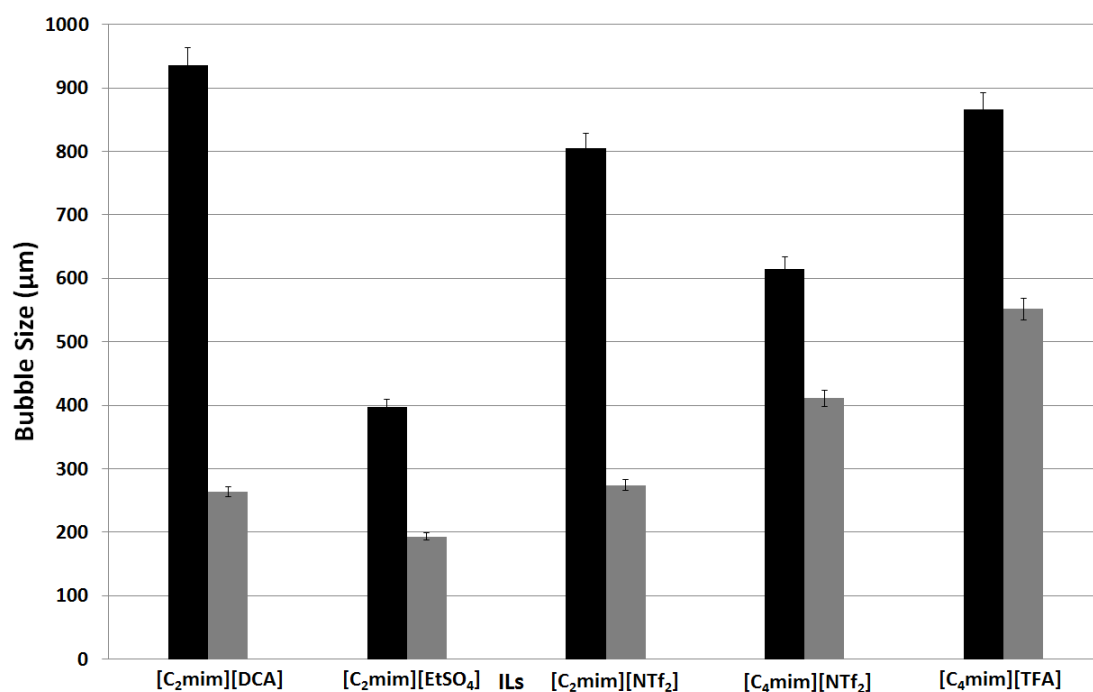


Figure 6 Average bubble sizes observed for different ILs for (■, Steady flow; ■, Fluidic oscillator).

The maximum difference (relative) in bubble size is observed for [C₂mim][DCA], is a factor of 3.65 reduction in size with fluidic oscillator implementation. This is fairly straightforward due to the low viscosity observed for the IL as compared to the other ILs. The oscillatory pulse, according to the hypothesis in this paper, especially the negative cycle, pulls in/ sucks the liquid into the wetted pore. The lower the viscosity of the IL, *i.e.* lower the liquid resistance, the easier it is to pull in/suck in the liquid in the negative cycle of the oscillatory pulse. This results in a greater wetting possible for the

inner pore thereby resulting in a more effective size reduction with fluidic oscillator implementation. This result agrees with the hypothesis and in accordance with the lubrication effect observed in Figure 11 and will be discussed further on.

The bubble sizes have been reduced for all the ILs upon fluidic oscillator implementation. The error bars were based on the 3 averages for the image analysis. The average bubble size depends on the IL – physico-chemical properties and the maximum size difference (relative) observed is for [C₂mim][DCA]- ≈260μm for fluidic oscillator as compared to ≈950μm for steady flow. The smallest bubble size observed is for [C₂mim][EtSO₄] at ≈200μm for fluidic oscillator as compared to ≈400μm for steady flow. This brings about a factor of 2 in bubble size with fluidic oscillator implementation. Relative differences for [C₂mim][NTf₂] are comparable with [C₂mim][DCA], *i.e.* ≈280μm for fluidic oscillator as compared to ≈830μm for steady flow, bringing it to a factor of 2.96.

There is a bubble size difference observed for each individual IL. The smallest bubble size (absolute) is observed for [C₂mim][EtSO₄] with ≈200μm for fluidic oscillator as compared to ≈400μm for steady flow. This concurs with the results obtained in Taylor *et al* [30] as it had the smallest bubble size in the study. The factor of 2 reduction in bubble size with the oscillator implementation is a good indication in terms of the potential for improvement in transport properties for this IL.

Relative differences for [C₂mim][NTf₂] are comparable with the relative differences seen in [C₂mim][DCA], *i.e.* ≈280μm for fluidic oscillator as compared to ≈830μm for steady flow, bringing it to a factor of 2.96. [C₄mim][NTf₂] shows the least relative bubble size difference between steady flow and oscillatory flow at relative difference of a factor of 1.45 *i.e.* with ≈430μm for fluidic oscillator as compared to ≈630μm for steady flow, with [C₄mim][TFA] , having a comparable viscosity , having a relative bubble size difference between steady flow and oscillatory flow of a factor of 1.55 *i.e.* with ≈570μm for fluidic oscillator as compared to ≈890μm for steady flow.

For oscillatory flow the following trend emerges:

[C₂mim][EtSO₄] < [C₂mim][DCA] ≈ [C₂mim][NTf₂] < [C₄mim][NTf₂] < [C₄mim][TFA]

For steady flow:

[C₂mim][EtSO₄] < [C₄mim][NTf₂] < [C₂mim][NTf₂] < [C₄mim][TFA] < [C₂mim][DCA]

By inspection, the fluidic oscillator implementation results in a bubble size reduction, with the maximum relative bubble size reduction for the low end viscosity ILs (in terms of relative difference - [C₂mim][DCA] and [C₂mim][NTf₂]). This is followed by the medium viscosity ILs -[C₄mim][NTf₂] and [C₄mim][TFA] in terms of relative change in bubble size. The anomaly is [C₂mim][EtSO₄] which shows

the lowest absolute bubble size observed and a larger relative size reduction observed as compared to the $[\text{C}_4\text{mim}][\text{NTf}_2]$ and $[\text{C}_4\text{mim}][\text{TFA}]$ - despite having a higher viscosity. Investigating the effect of the contact angle, i.e. wettability, and individual size distributions to know the effect of the chemical moieties will possibly clarify the anomalous behaviours.

Bubble Throughput

With the reduction in bubble size, the throughput of the system is increased. Figure 7 shows the throughput differences for various ILs for fluidic oscillator implementation. Generally speaking, there is a throughput increase for all the ILs upon fluidic oscillator implementation with significant observable increases in throughput for some ILs improving the transport properties substantially.

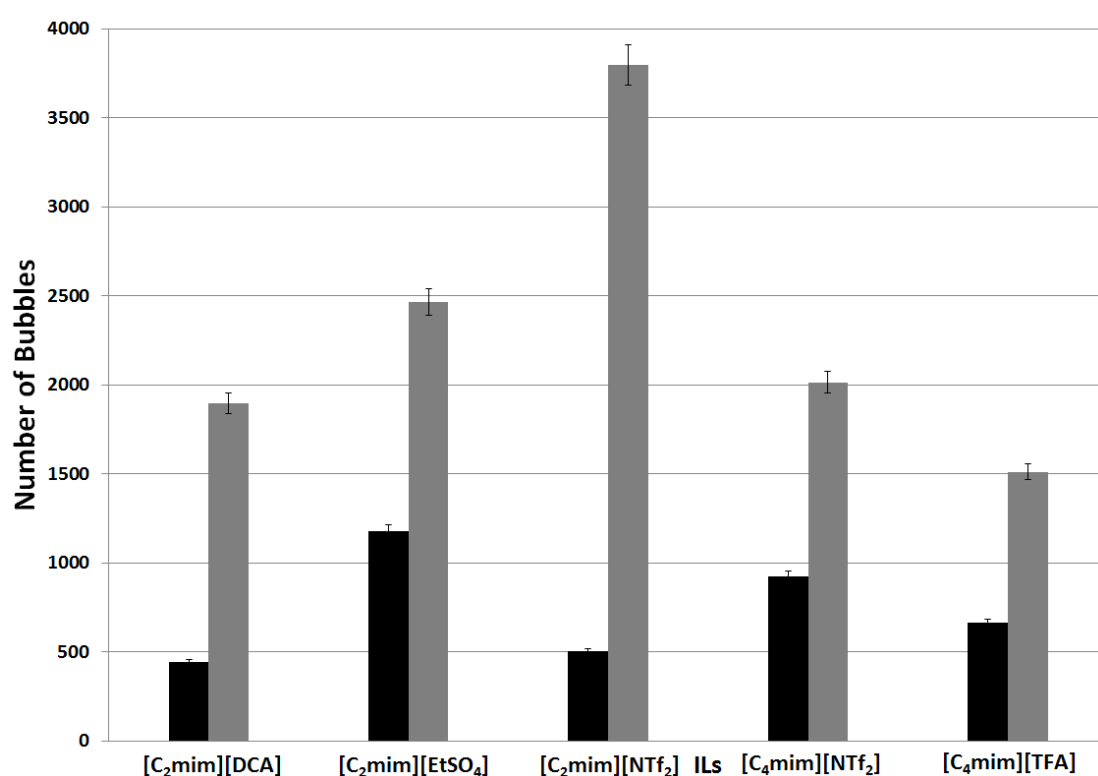


Figure 7 Bubbles throughput for the ILs used in the trial. (■ Steady flow ■ Fluidic oscillator).

The largest absolute throughput is observed for $[\text{C}_2\text{mim}][\text{NTf}_2]$, ≈ 3900 for fluidic oscillator as compared to 500 for steady flow which results in a factor of 8 difference. This is also the maximum relative throughput difference.

With the bubble size reduction for the gamut of ILs there is a resultant increase in throughput (since volumetric flow conditions remain the same). This agrees well with the hypothesis and aim to create greater surface area. The bubble throughputs increased for all the ILs upon fluidic oscillator implementation. The error bars were based on the 3 averages for the image analysis. The largest

absolute throughput is observed for [C₂mim][NTf₂], ≈3900 for fluidic oscillator as compared to 500 for steady flow which results in a factor of 8 difference. This is also the maximum relative throughput difference.

This is followed by [C₂mim][DCA] with ≈1900 for fluidic oscillator as compared to ≈490 for steady flow resulting in a factor of 3.8. The size and throughput behaviour in terms of relative factor remains constant for [C₂mim][EtSO₄] at ≈2550 for fluidic oscillator as compared to ≈1350 for steady flow and results in a factor of 1.8 in throughput with fluidic oscillator implementation. Likewise, [C₄mim][NTf₂] had a throughput of 2100 with fluidic oscillator implementation to 990 for steady flow resulting in a factor of 2.12 and [C₄mim][TFA] having a factor of 2.58 with a throughput of 1550 with fluidic oscillator implementation and 650 for steady flow.

The difference between the throughput and the bubble size trend and relative difference means that the histograms i.e. individual bubble size distributions for each IL need to be seen and the size distributions are affected by the chemical moieties on the surface of the bubble.

For oscillatory flow throughput, the following trend emerges for absolute terms:

[C₄mim][TFA] < [C₂mim][DCA] ≈ < [C₄mim][NTf₂] < [C₂mim][EtSO₄] < [C₂mim][NTf₂]

For steady flow, the following trend emerges for absolute terms:

[C₂mim][DCA] ≈ < [C₂mim][NTf₂] < [C₄mim][TFA] < [C₄mim][NTf₂] < [C₂mim][EtSO₄]

Figure 7 acts as corroborating evidence as there is a much higher bubble throughput due to the size reduction observed with fluidic oscillator implementation for [C₂mim][DCA], [C₂mim][EtSO₄], [C₂mim][NTf₂], [C₄mim][NTf₂], and [C₄mim][TFA]. The maximum difference between oscillatory flow and steady flow is observed for [C₂mim][NTf₂], an 8:1 ratio. This is due to the combination of the wettability, viscosity, and the effect of moieties on the system as will be discussed as the differences in behaviour (bubble size and throughput) cannot be directly explained by physico-chemical properties.

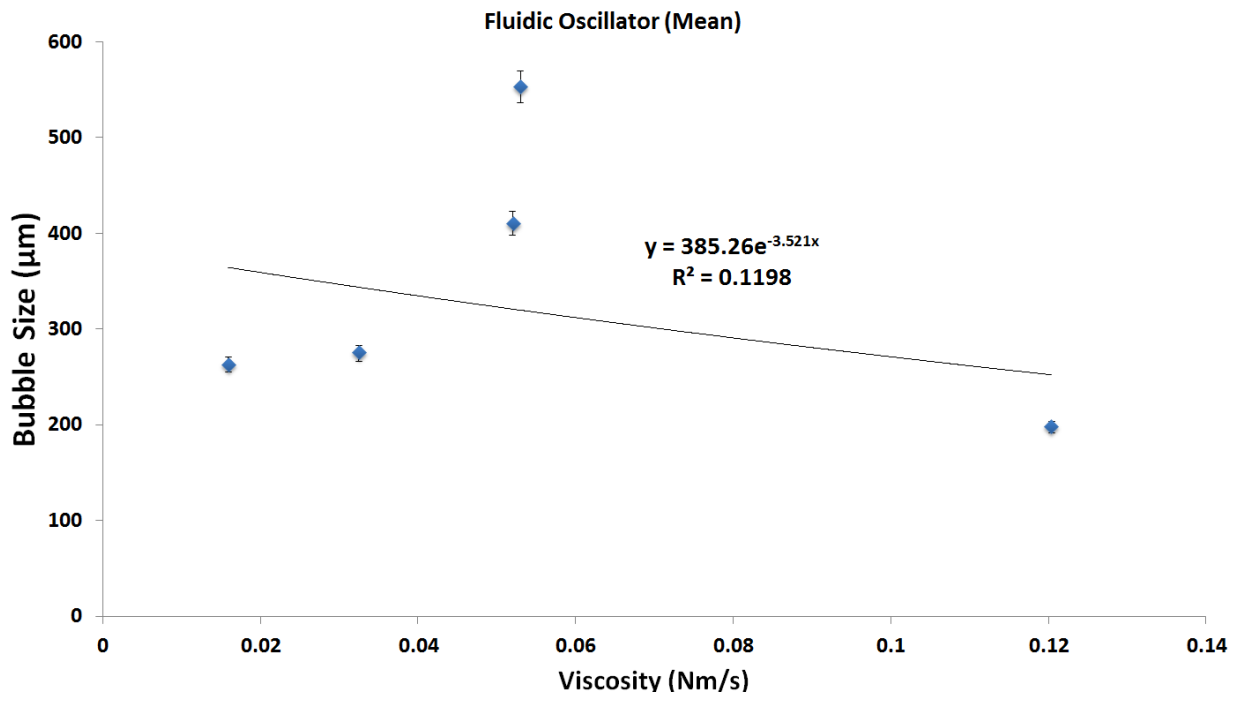
The example of the effects of moieties on the system can be seen using the example of [C₂mim][NTf₂] and [C₄mim][NTf₂] where the throughput variation changes from 8:1 to 2:1 with a change of the [C₂mim] and [C₄mim] moieties.

The behaviour is similar for the higher viscosity IL, [C₂mim][EtSO₄], with the differences in bubble size between fluidic oscillator and steady flow having a relative factor of 2 difference and the throughput between fluidic oscillator and steady flow having a relative factor of 1.8 difference. This shows a consistent behaviour in terms of size and throughput and this will be seen in the bubble size distribution / histogram.

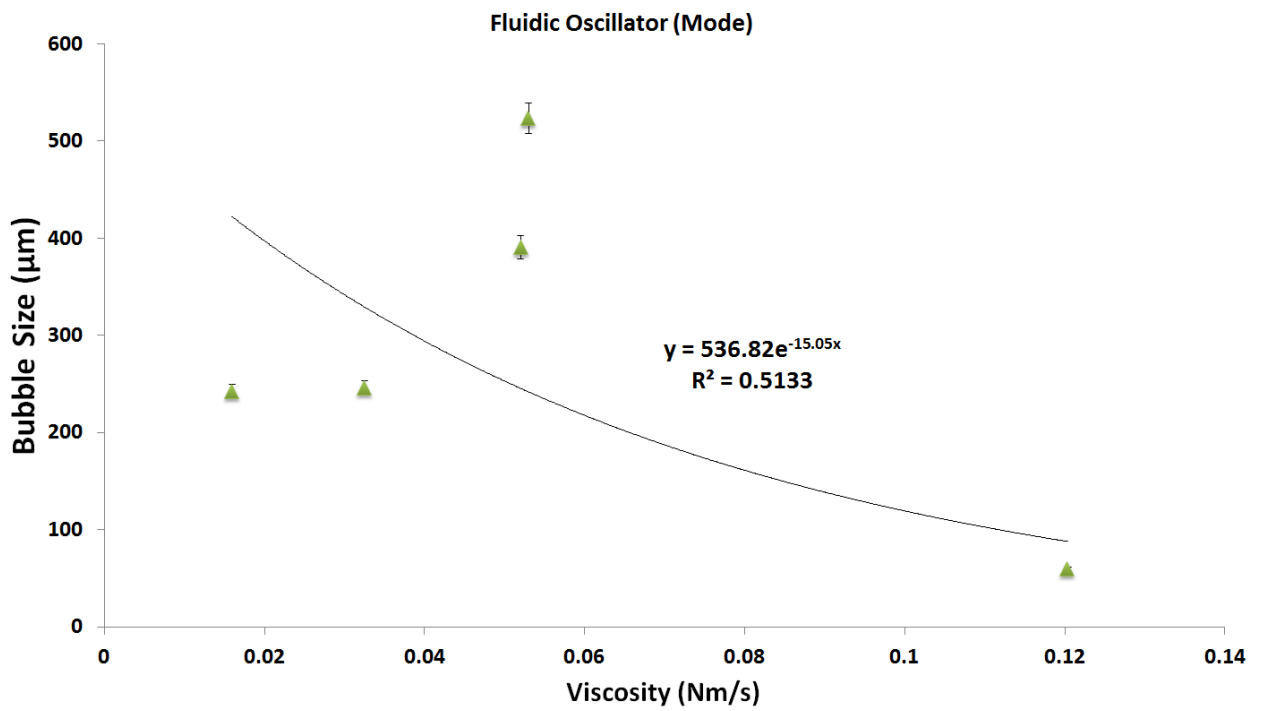
Effect of Viscosity

Figure 8 elucidates these results further when viscosity is compared to but remnants of the findings from [30], *i.e.* interactions between chemical moieties, do remain and are seen in the histograms and results below (Figure 8). Comparing the bubble size against viscosity for the two systems a strong trend emerges.

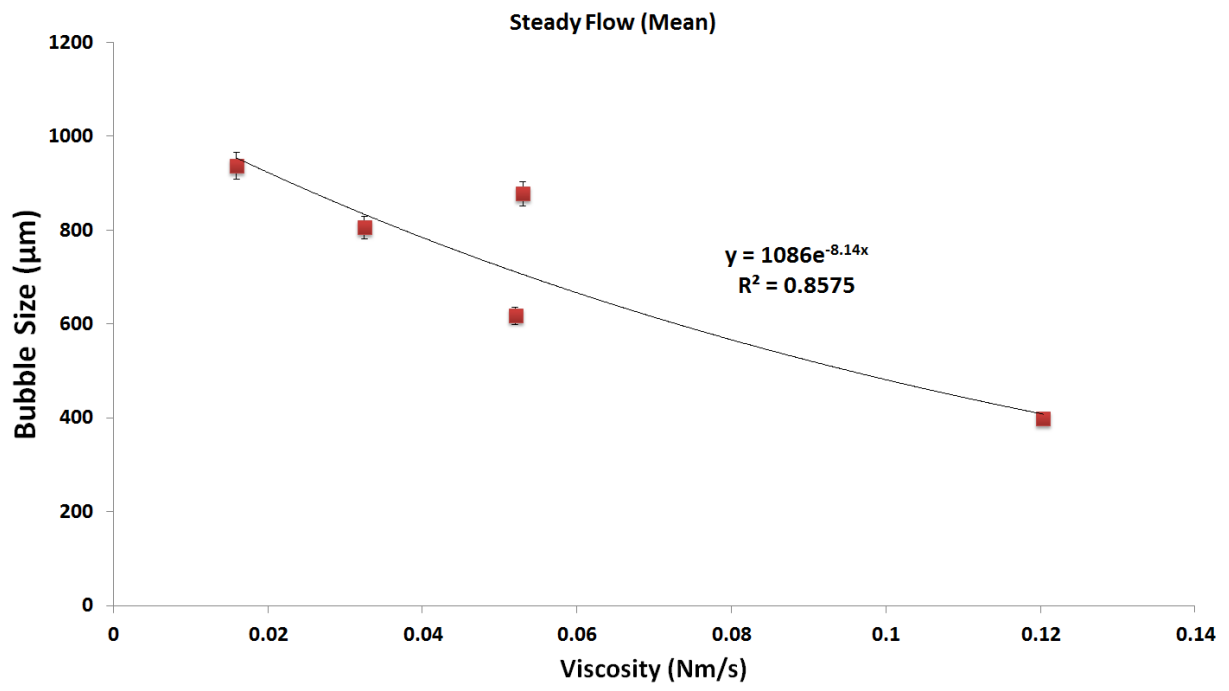
a.



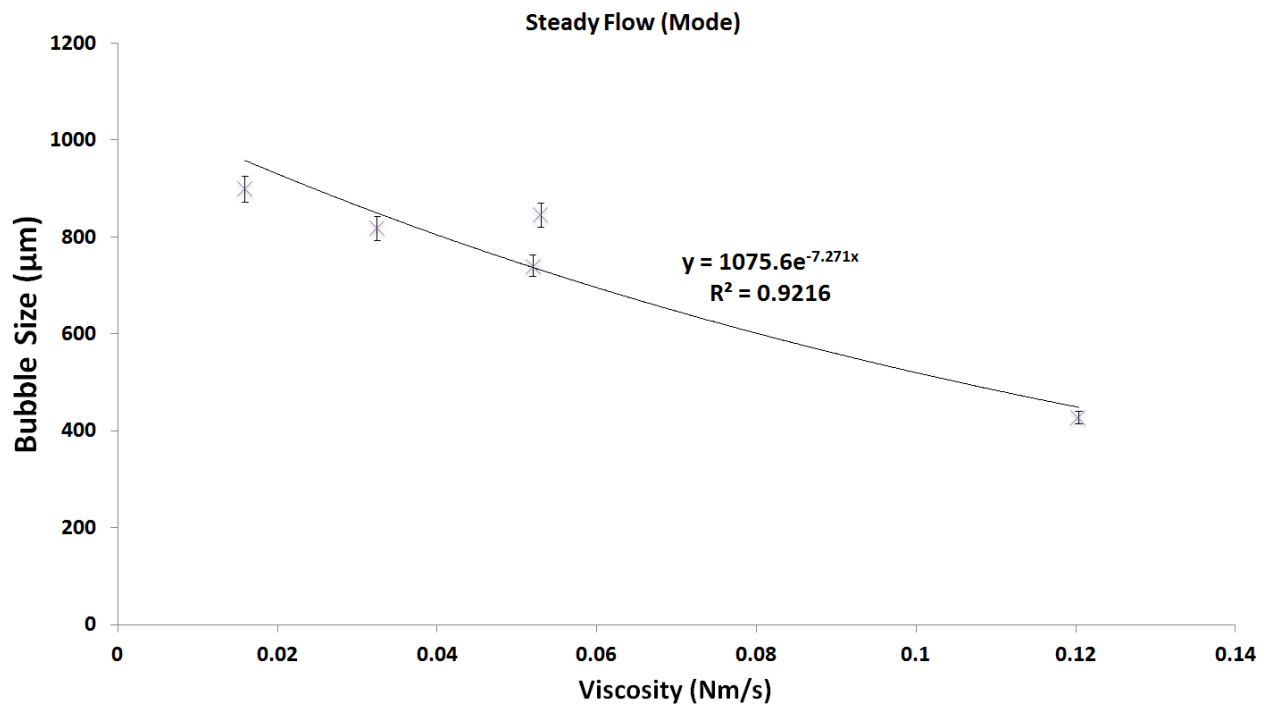
b.



c.



d.



e.

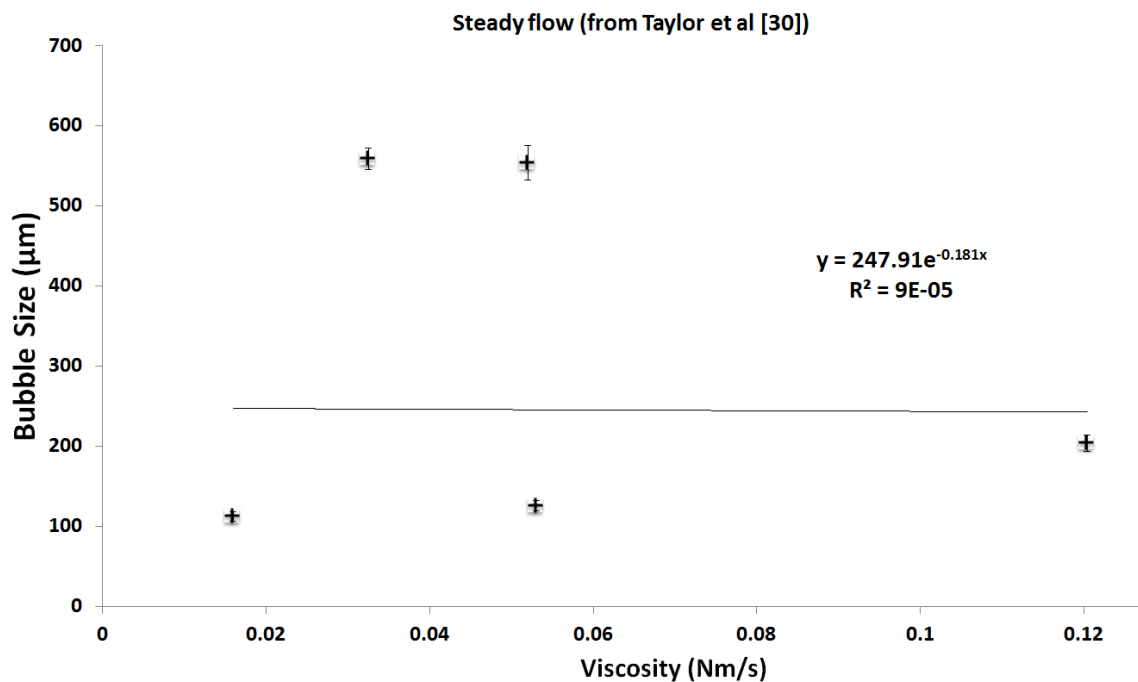


Figure 8 Viscosity plotted against bubble size (mean and mode) for fluidic oscillator and steady flow condition for different ILs - . Steady flow- \times (mode), \blacksquare (mean). Fluidic oscillator - \blacktriangle (mode) \blacklozenge (mean). Taylor *et al* [30] - \oplus (mean). The error bars were based on the 3 averages for the image analysis for data from this paper. Error bars for the work from Taylor *et al* data taken from [30].The trend lines are exponentials.

Figure 8 (a-d) shows the influence of the viscosity on the bubble sizes (mean and mode) formed for both steady flow and oscillatory flow and Figure 8e compares it with bubble sizes in Taylor *et al* [30]. It is observed that the bubble size *reduces* with increase in viscosity for steady flow (upon inspection). The trend line agrees well for steady flow for both mean and mode sizes (8 c and d), with R^2 values of 0.8575 and 0.9216 respectively. For oscillatory flow, there is an outlier ($[C_2mim][EtSO_4]$), which results in R^2 values of 0.1198 and 0.5133 respectively with the outlier included. If $[C_2mim][EtSO_4]$ is taken to be an outlier and ignored, then the trend line fits in reasonably well and R^2 values of 0.7965 and 0.7897 are observed, therefore reversing the findings from steady flow, *i.e.* greater the viscosity, larger the bubble size and in agreement with the hypothesis posed in this paper for fluidic oscillator mediated bubble formation in viscous liquids.

Typically, bubble size reduces with increase in viscosity for the system. The mean and mode of the system provide the variations within a bubble size distribution. For steady flow, especially at the higher viscosity, there has not been a substantial difference between mean and mode. The trend lines fit well for steady flow for both mean and mode sizes (c and d), with R^2 values of 0.8575 and 0.9216

respectively. However, for the fluidic oscillator, the differences between the mean and mode sizes for fluidic oscillator implementation due to the unusual behaviour exhibited by [C₂mim][EtSO₄]. The trend lines for fluidic oscillator flow for both mean and mode sizes (a and b), with R² values of 0.1198 and 0.5133 respectively for an exponential trend. If [C₂mim][EtSO₄] is taken to be an anomaly and ignored, then the trend line fits in well and R² values of 0.7965 and 0.7897 are observed. However, both the data sets are in contrast to the work done by Taylor *et al*, where the viscosity seems to have little or no effect on the bubble size with trend line (R² is 9E-05). This is because the pressure drop is high and the flow rate is low (3 millilitres per minute)

However, it is a combination of the physico-chemical properties and the interactions of the chemical moieties present on the bubble skin that affect the bubble size as seen Taylor *et al*. [30], which demonstrates that for a bubbling system there are features specific to ILs due to the chemical moieties present on the surface of the bubble. This has only been recently observed due to the bubbling in highly peculiar and specific ILs, which induces additional forces on the bubble forming in the system. It has been observed to some extent in systems where a surfactant or a salt has been added to the system (for example [57-66]). However it is not as prominent as that observed for the IL due to the varying sigma moments and subsequently the interactions between the anions and cations that are observed in IL.

In this paper, it is found, contrary to findings in [30], the increased membrane porosity (or rather decreased pressure drop of 40 mbar(g) as compared to 2.4 bar(g)) , larger pore size (20µm instead of 2.5µm), and higher flow rate (50 millilitres per minute instead of 3 millilitres per minute) that, the dynamics of bubble formation agree to the findings in [29].

The bubble size distribution for less viscous liquids has a greater impact by effect of fluidic oscillation as compared to higher viscosity liquids due to the 'resistance' to the oscillatory pulse offered by the liquid of greater viscosity.

It is evident from Figure 8 (c and d) steady flow that some of the results reported in literature [28] previously, especially for quiescent liquids. Surprisingly, although the system is not in any way a T-Junction device, there are similar observations here with respect to flow rates and higher viscosity liquids [32].

Since the [C₂mim][DCA] has a low viscosity, the interactions go against the QSPR and expected behaviour for [30] which does not show any correlation to viscosity as seen in Figure 8e. This is due to the removal of the higher pressure drop and therefore the suppression of the physico-chemical properties that had affected it in [30]. This is also similar to findings in [25,26, 27].

Bubble formation by fluidic oscillation in IL

The oscillator changes the dynamics of bubble formation and it is observed that detachment and bubble size depends on the viscosity (Figure 8a and 8b). However, the effect of the chemical moieties and the other physico-chemical properties is still high enough to counteract the effect of viscosity. This follows from the hypothesis presented in this paper that the amplitude of the oscillation needs to be matched with the liquid and membrane properties, in what is known as the fluidic circuitry (a similar concept to impedance matching in AC electric circuits).

Bubble generation in the positive cycle of the oscillator was first hypothesised and supported by Tesar *et al.* [8] and the paper found that the bubble detaches upon the completion of the oscillatory cycle in the positive cycle of the oscillatory pulse. This finding is then, upon modification of the circuitry for greater pulse strength (amplitude of flow in the oscillator) is then applied to the IL and a waveform is seen for an exemplar IL in Figure 9.

The waveform of the oscillator with the appropriate bubble growth dynamics observed is seen in Figure 9. Tesar *et al.* [8] previously described the mechanism for cases with aqueous media but not in highly viscous liquids. It is not a big leap to conjecture that for a similar effect to be observed in highly viscous liquids the amplitude of this oscillatory wave needs to be larger in order to impart a greater momentum (translated into a greater rise velocity) so as to be able to leave the engendering surface and not coalesce with the next bubble generated.

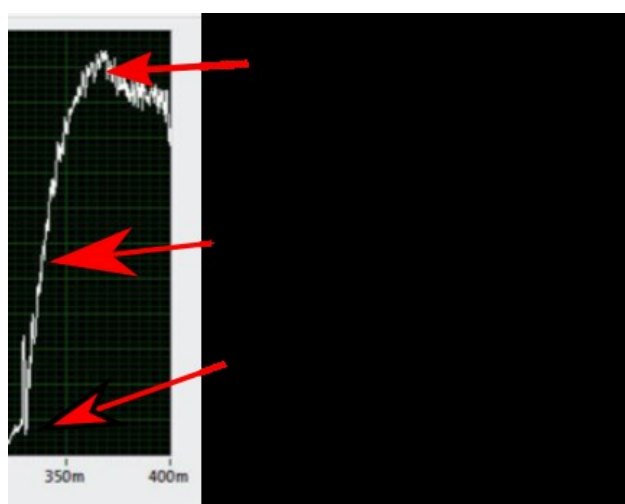


Figure9 Exemplar oscillatory waveform and bubble formation dynamics for IL ($[C_2mim][DCA]$). This is based on work by Tesar *et al* [8] for aqueous media and suitably adapted for higher viscosity liquids (ILs)

with accompanying increase in the pulse strength to account for the detachment force. The formation forces and the pulse strength can be seen in Figure 17.

Figure 9 shows the bubble formation mediated by fluidic oscillation during the ON pulse, *i.e.* positive cycle of the oscillatory pulse. Subsequently, the negative cycle can be seen on the waveform. The frequency is the inverse of the time step for each pulse, which means that the time step is the width of this pulse. The width of the pulse determines the onset of the negative cycle, and that results in the bubble pinch off [8, 9] which results in bubble growth termination and subsequent release. Once the bubble is detached, it has been imparted momentum [12] from the impinging jet from the oscillator. The rise velocity of the bubble and its dependence on the viscosity of the medium is the difficulty with IL and other viscous liquids. A liquid with higher viscosity will have a bubble with a slower rise velocity and the bubble wake (of the previously generated bubble) will have a greater impact on the concatenated bubble due to the viscosity of the medium. The moieties on the surface of the bubble repel each other, further adding to the effect of the bubble wake and reducing coalescence [57-66].

Taking this into account, the bubble formed with the oscillator demonstrates a greater dependence on viscosity than the effect of chemical moieties (which will still contribute to the shape and nature of the bubble size distribution). It is therefore observed that for all the IL save one, the bubble size increases with increase in viscosity.

Effect of Contact Angle

The viscosity was one of the major physico-chemical properties and contact angle (and therefore, its proxy, wettability/surface tension) is the other. Since bubbling is the combination of three interfaces (gas (impinging jet), liquid (IL in this case), and solid (sparger generating the bubble)), contact angle is the easiest measurable property that can act as a proxy to the wettability/surface tension characteristics. As hypothesised in this paper, the wettability was an important factor observed with fluidic oscillator implementation. Greater contact angle means greater wetting, and therefore, the pore imbibition possible during the negative cycle of the oscillator increases, *i.e.* the lubrication effect is more prominent. $[C_2mim][EtSO_4]$ seems to agree well with this trend and this could be another reason why there was a discrepancy observed when only the viscosity was taken into account. The higher wettability of this IL ensures that although the 'resistance' offered to the liquid is high by the liquid, the increased wetting aids the lubrication effect and the interactions between the chemical moieties add to this, which then ensures that the bubble size for this IL is reduced and the effect of the oscillator implementation is suppressed due to the higher viscosity but enhanced due to the increased wetting.

[C₂mim][NTf₂] is a discrepancy here and this is described by the interactions of the chemical moieties on the surface as although there is wetting, the charge is concentrated within the moieties and therefore there is a ‘repulsion’ factor due to the moieties that comes into play. This will be seen when the individual bubble size distributions are seen. Figure 10 shows the contact angle versus the bubble size for different ILs at steady flow and oscillatory flow conditions.

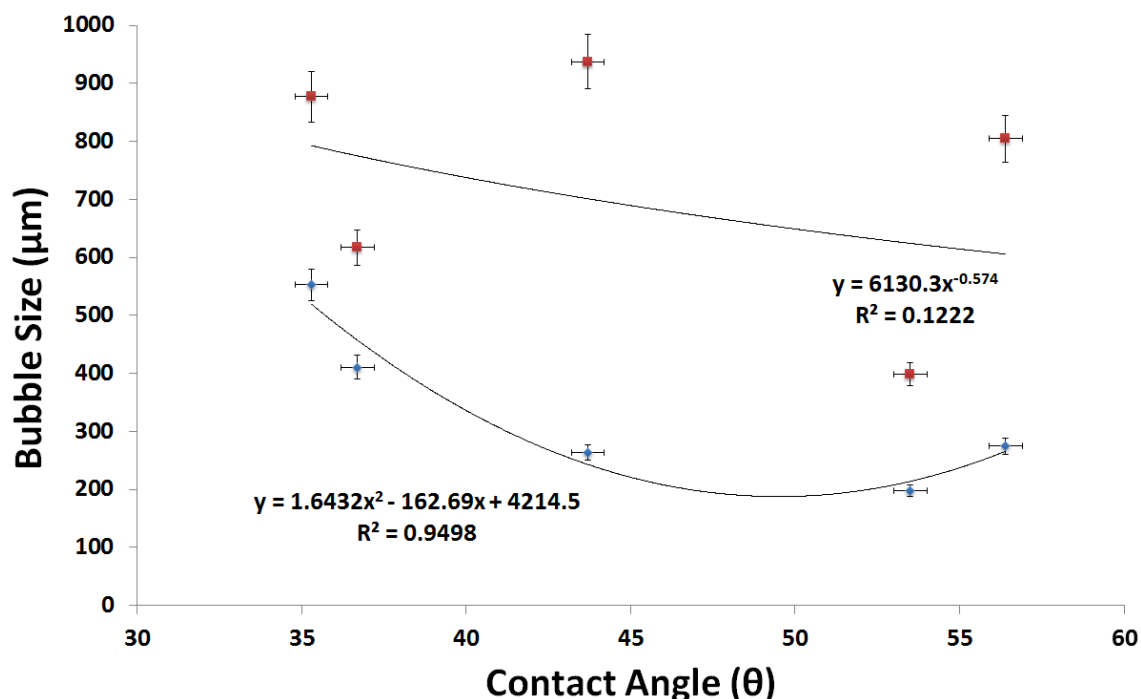


Figure 10 Contact Angle versus Bubble Size – it is observed that the contact angle plays an important role in the fluidic oscillator mediated bubble size. ■ -Steady flow, ◆ - Fluidic Oscillator

The error bars for bubble size were based on the 3 averages for the image analysis and errors in contact angle have been obtained as described in the methods section. As hypothesised, there is a good correlation of bubble size performance with fluidic oscillator implementation (R^2 is 0.9498 for equation and R^2 is 0.7279 for a logarithmic trend line), due to the increased wetting which aids the lubrication effect. Wetting does not seem to have a large effect on the steady flow dynamics (R^2 is 0.1222). This shows good agreement with the hypothesis posed in this study and partially explains the anomalous behaviour observed for [C₂mim][EtSO₄].

For oscillatory flow, there is a good correlation between the wettability and bubble size as expected for the oscillatory flow, (R^2 is 0.9498 for the equation) due to the agreement with the hypothesis except for one point ([C₂mim][NTf₂]). As discussed, this is due to the effect of the chemical moieties which will be observed when individual bubble size distributions are taken into account. Additionally,

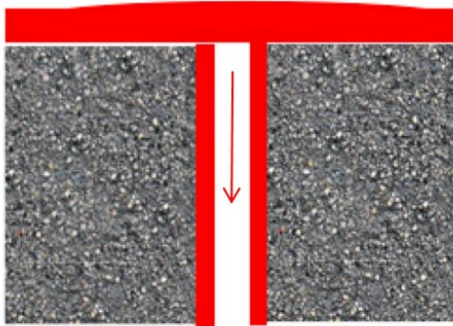
[C₂mim][NTf₂] has a higher density and therefore lower amount of free volume available for the bubbles to form easily especially when one considers the spread of charge on the [NTf₂]⁻ anion. When the [NTf₂]⁻ anion is compared with the combinations of [C₂mim]⁺ and [C₄mim]⁺ cations. The possible reason for the different bubble sizes might be seen with the individual bubble size distributions as it is highly likely that this is due to the effect of the chemical moieties on the system.

There is a difference observed in the mean and median size distribution for [C₂mim][EtSO₄] when compared with viscosity and surface tension which is likely due to the interactions between ions in solution. The bubble size distribution is shifted to the left and this is what reduced the bubble size but the histogram shape remains the same noting it as a property of the IL. This reduction in bubble size is achieved by a variety of factors, the most important of them is highly likely the wetting property and by proxy, the contact angle that the liquid makes on the bubble engendering surface. This significantly reduces bubble size as has been observed in [56].

Lubrication Effect

Figure 11 is a graphic which illustrates the effect of the wetting of the liquid on the membrane on the bubble formation. For the steady flow configuration, the bubbles are formed in a disordered fashion with seemingly no particular relationship to the wetting angle properties, contrary to observed literature. However, for the fluidic oscillator mediated microbubbles, the bubble size is highly dependent on the amount of wetting *i.e.* contact angle made for the IL on the orifice. The liquid weeps into the orifice that engenders the bubble during the “OFF” phase/ negative cycle of the oscillatory pulse. This is because the surface is wetted more by liquids with a higher wetting angle and the liquid weep helps create a layer inside the orifice wall. This further reduces the size of the orifice as well as substantially changing the wetting anchor force. The oscillator then pushes the liquid out, along with the gas thereby forming smaller bubbles. The liquid velocity and momentum are what push the bubble faster since the gas bubble itself has no mass or momentum associated with it *per se* (relative to the highly viscous IL). The lubrication makes bubbles smaller when the wettability is matched even when the oscillator is not utilised as observed in [56]. This shows that a higher wetting liquid should generate smaller bubbles despite other additional ‘hindrances’ to small bubble formation as can be seen for [C₂mim][EtSO₄] which has a smaller bubble size despite the higher viscosity and effect of the chemical moieties.

Red denotes liquid, which is 'sucked in' or pore imbibition due to liquid wettability and the negative cycle of the oscillatory pulse. The amount imbibed depends on the pulse strength or wettability of the liquid



Sparger with a channel for bubble generation

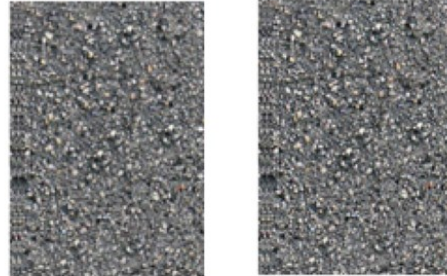


Figure 11 Lubrication Effect – The grey area is the sparger with the blank space (right) representing the pore/channel with the red representing the liquid weep into the orifice thereby providing lubrication like effect(left).

This lubrication effect is further enhanced thanks to the negative suction or backflow observed for the oscillator. The fluidic oscillator can reduce bubble size due to the increased backflow and the associated liquid momentum of the jet diverted into the medium. This backflow has an amplitude that can be controlled by tuning the fluidic oscillator.

The oscillator pushes this liquid coupled with the gas in order to generate the bubble. The negative cycle of the oscillatory pulse 'sucks' the liquid into the pore/channel and the positive cycle of the pulse generates the bubble. Originally, the effect of backflow due to the negative cycle of the pulse was enumerated in Tesar *et al* [9]. The results so far agree well with this hypothesis. The interesting finding is that wettability adds to this effect and results in an even smaller bubble size.

Tesar elucidates the dynamics of the class of hybrid synthetic jets [67, 68], resulting from fluidic oscillation in a single fluid phase and its characteristics, with a key feature being that they induce a net positive wave with a magnitude slightly higher than the negative cycle.

Higher wetting liquid-surface combinations result in smaller bubbles for steady flow [56] if other conditions remain the same. Other properties also effect a change to the bubble size. Lubrication effect results in liquid imbibition and keeps the difference of bubble size high when fluidic oscillator is

implemented. High wetting would result in smaller bubbles, whereas the fluidic oscillator induces a high wetting of the liquid artificially.

Individual Bubble Size Distributions

From consideration of individual bubble size distributions for the ILs, several different behaviours and patterns emerge. Generally speaking, the fluidic oscillator actuates to produce a significantly smaller bubble size as has been seen in Figure 6 and has been observed for all the ILs tested. The size difference is substantial and is between 40%- 400% in size. However, the average bubble size, and even the mean and median bubble sizes do not adequately describe the bubble formation dynamics especially the effect of the chemical moieties easily.

The individual bubble size distributions provide a better idea on the bubble formation dynamics. Figure 12 shows the bubble size distribution for $[\text{C}_2\text{mim}][\text{DCA}]$.

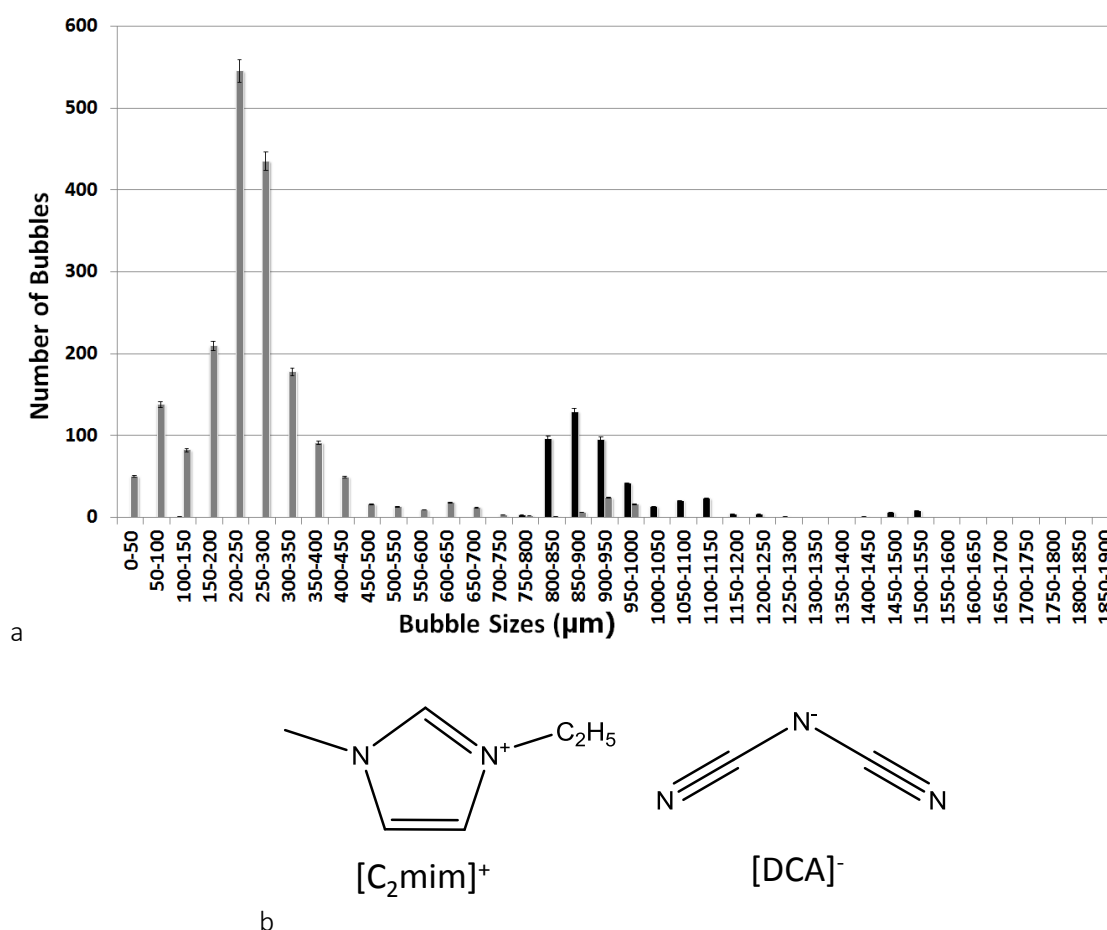


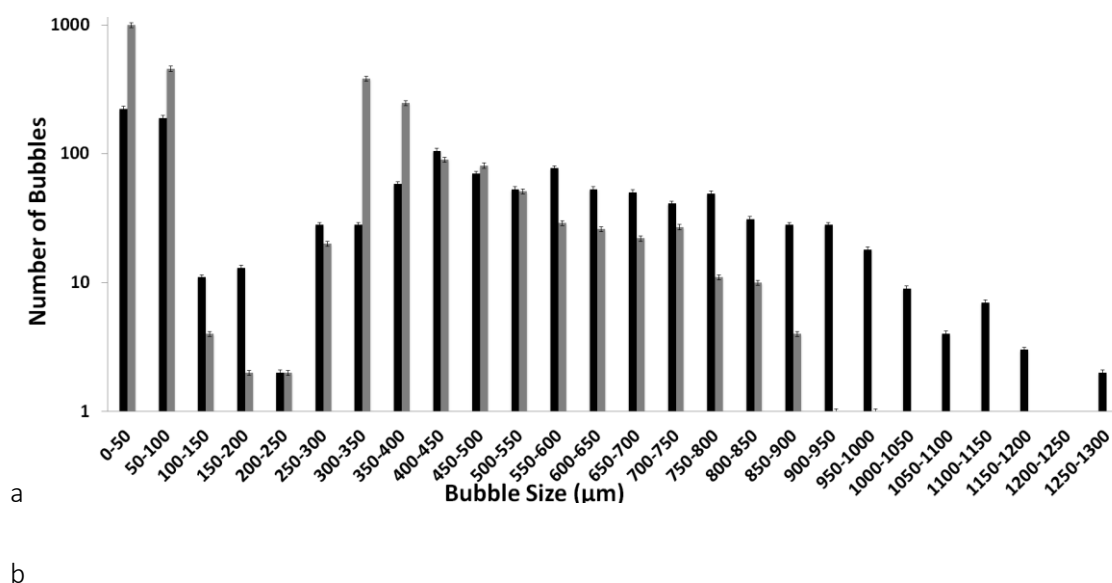
Figure 12 Bubble size distribution comparison for ($[\text{C}_2\text{mim}][\text{DCA}]$) (a) - (■ Steady flow ■ Fluidic oscillator) and structures (b). The error bars were based on the 3 averages for the image analysis.

Figures 6, 7, and 8 provided the average bubble size and the effect of viscosity on the bubble size. Figure 10 showed the effect of the surface tension on the average bubble size. However, in order to reconcile the anomalies for the physico-chemical properties and garner the differences due to the chemical moieties on the bubble size, the entire distribution has to be seen. The findings supported the hypothesis of the paper and how the fluidic oscillator had a different impact on bubble formation for fluidic oscillator mediated bubbles and steady flow mediated bubbles in ILs. The bubble size distribution seen in Figure 12 for [C₂mim][DCA] shows resulting reduction in bubble size due to fluidic oscillator implementation and the similarity in shape of the size distribution is observed, but the distribution obtained with the fluidic oscillator implementation is shifted to the left (smaller bubbles) with much higher throughput. As per the hypothesis, this should be the maximum effect (relative difference wrt steady flow) observed with fluidic oscillator implementation for this IL and it is in good agreement with 4 times the throughput and 1/3.6 times the size.

Figure 13 shows the comparison of bubble size distribution for oscillatory and steady flow for [C₂mim][EtSO₄]. Anomalous size for [C₂mim][EtSO₄] can also be seen in its bubble size distribution (log scale), (normal scale graph in supplementary information).

There are two regions in the size distribution and this is exhibited in both steady flow and oscillatory flow which is similar to the bubble size distribution for [C₂mim][DCA] as in the steady flow and oscillatory flow have similar distributions but the throughput and bubble generation for smaller bubbles is much higher for fluidic oscillator implementation (5 fold more throughput for 0-50 μm and 2.5 times greater throughput for 50-100 μm, and over 40 times for the median bubble size for the distribution for 300-350 μm).

This is seen in Figure 13.



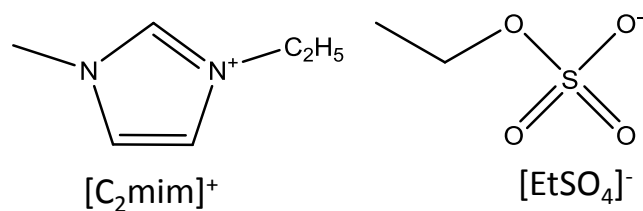


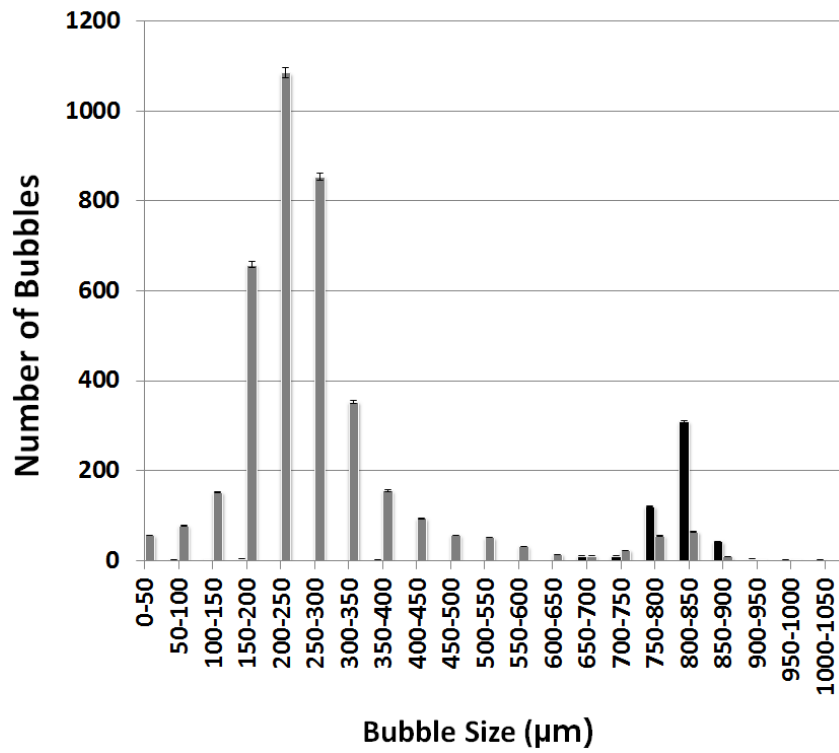
Figure 13 Comparison of Bubble size distribution for $[C_2mim][EtSO_4]$ (a) (■ Steady flow ■ Fluidic oscillator) (log scale) and structures of the moieties (b). The error bars were based on the 3 averages for the image analysis

The size and throughput behaviour in terms of relative factor remains constant for $[C_2mim][EtSO_4]$ at ≈ 2550 for fluidic oscillator as compared to ≈ 1350 for steady flow and results in a factor of 1.8 in throughput with fluidic oscillator implementation. The smallest bubble size observed is for $[C_2mim][EtSO_4]$ at $\approx 200\mu m$ for fluidic oscillator as compared to $\approx 400\mu m$ for steady flow. This brings about a factor of 2 in bubble size with fluidic oscillator implementation. The bubble size distribution for fluidic oscillator and steady flow are similar to each other. However, both these distributions are broad and this is the effect of the chemical moieties wherein the delocalisation across the moieties results in a wider distribution similar to that observed in Taylor *et al*, [30].

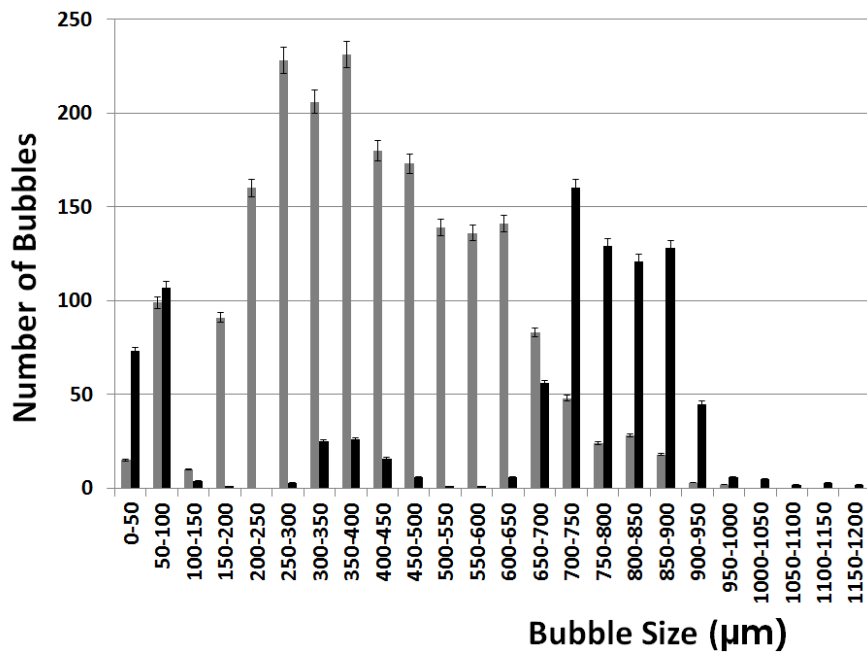
A bubble size reduction with increase in throughput is observed with approximately twice the throughput and half the bubble size observed with fluidic oscillator implementation. However, the size distribution observed is broad which might explain the discrepancy in the trend for fluidic oscillator implementation in Figure 8 (a and b). The charge is highly delocalised for $[C_2mim][EtSO_4]$ which can be seen in the sigma profiles for this IL [30]. This could potentially be the reason for why this IL behaves in such a manner. Interestingly, the bubble throughput is significantly different with a five-fold improvement in bubble throughput at 0-50 μm and 50-100 μm level for oscillatory flow as compared to steady flow. This diffuse charge, coupled with the higher viscosity of ILs, results in the difference in bubble size. The skew in the bubble distribution is due to the implementation of the oscillator but the overall distribution is similar for both conditions, thus demonstrating the effect of the chemical moieties on the bubble formation system and the bubble size distribution (at least indicative and influencing the shape of the distribution).

Differences in the bubble size distributions for different moieties - [C₂mim][NTf₂] and [C₄mim][NTf₂] will be seen in Figure 13.

a



b



c

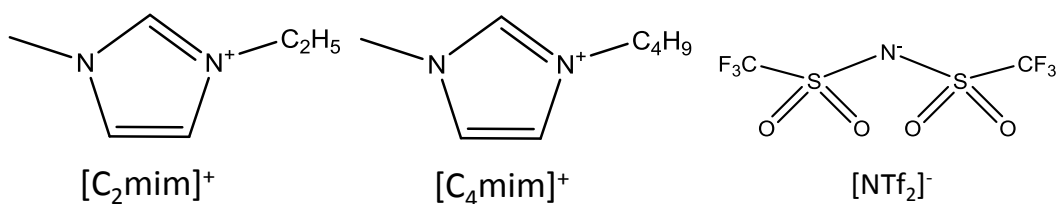


Figure 14 Bubble size distribution between $[C_2mim]$ (a) and $[C_4mim]$ (b) (■ Steady flow ■ Fluidic oscillator) with $[NTf_2]$ moiety and structures of the three moieties (c).

The bubble size distribution for the $[C_2mim]$ is tightly packed and narrow. This is best seen in the steady flow distribution for $[C_2mim][NTf_2]$. $[C_4mim][NTf_2]$ shows a broader distribution and a much larger bubble size. Oscillator implementation shifts the size distribution for both these liquids and reduces it. The effect of the chemical moieties is better observed in the steady flow and Figure 15 shows the polarisation charge on the two moieties.

$[C_2mim][NTf_2]$ has a higher density and therefore lower amount of free volume available for the bubbles to form easily especially when one considers the spread of charge on the $[NTf_2]^-$ anion. When the $[NTf_2]^-$ anion is compared with the combinations of $[C_2mim]^+$ and $[C_4mim]^+$ cations. The bubble sizes for these two ILs are different this could possibly be explained by their polarisation charge. For the same anion, the difference in the peak strength changes the relative attraction and repulsion within the system and results in the bubble size formation observed in Figure 14.

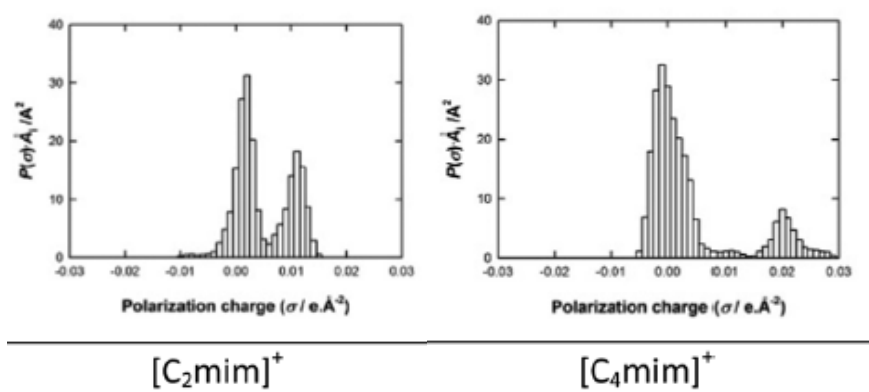


Figure 15 The charge distribution for the two cations (Taylor *et al* , [30])

Figure 15 shows the charge distribution or polarization charge for the two cations, $[C_2mim]^+$ and $[C_4mim]^+$ which might elucidate the differences in the bubble size distributions generated and the difference in bubble sizes obtained. The effect of the moieties is stronger for the steady flow bubbles whereas physico-chemical properties dominate largely for the oscillator mediated bubble size distributions.

The $[C_2mim]^+$ moiety has a two substantial peaks whilst $[C_4mim]^+$ has one substantial peak and another minor peak with a larger area. The anion constant i.e. $[NTf_2]^-$, is constant. This possibly results in a closer bond between the two and leads to repulsion between the different moieties when the bubbles are formed which results in a broad size distribution. This is also seen in Figure 16, where the bubble size distribution for $[C_2mim][TFA]$ is broad.

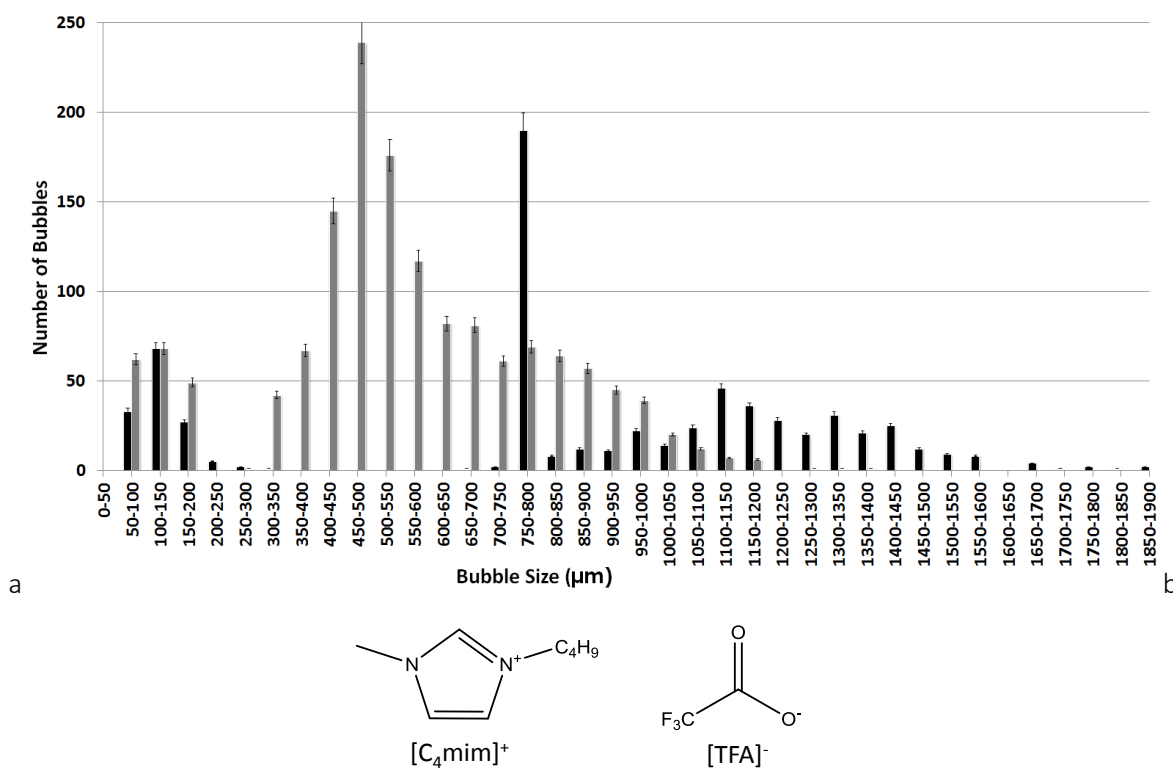


Figure 16 Bubble size distribution for $[C_4mim][TFA]$ (a) and structures for $[C_4mim]^+$ and $[TFA]^-$ (b) moieties. (■ Steady flow ■ Fluidic oscillator).

Figure 16 shows the size distribution for $[C_4mim][TFA]$. The spread of the size distribution shows a diffused and broad size distribution. This is due to the combination of viscosity, wettability and the moieties present. The viscosity is in the middle of the other ILs tested. The contact angle is low, implying greater wetting, which will result in a reduced relative effect of fluidic oscillation as per the lubrication theory, (900 μm (steady flow) reduced to 550 μm (fluidic oscillation)) as a comparison between the two since the lubrication effect is observed for steady flow and oscillatory flow due to

the wettability. Since the wettability is high, the lubrication effect is observed, which results in a relative reduced effect of oscillator compared to steady flow.

The overall bubble size distribution again is broad as seen for $[C_4mim][NTf_2]$. The bubble size distribution is narrower for the oscillatory bubble formation (compared to steady flow but less so than a typical oscillatory bubble formation and the effect of the oscillator is low for this IL.

Oscillatory Waveforms

The oscillation cycle can be seen in Figure 17. The oscillatory pulse is comprised of the positive cycle and the negative cycle. The positive cycle results in bubble formation and the negative cycle results in liquid imbibition into the orifice. The net positive pressure of the hybrid synthetic jet prevents substantial backflow into the oscillator but keeps the membrane ‘lubricated’. This ensures that the orifice size is reduced slightly and the bubble formed is much smaller than what would normally be the case. This is then controlled by the frequency and amplitude of the oscillator.

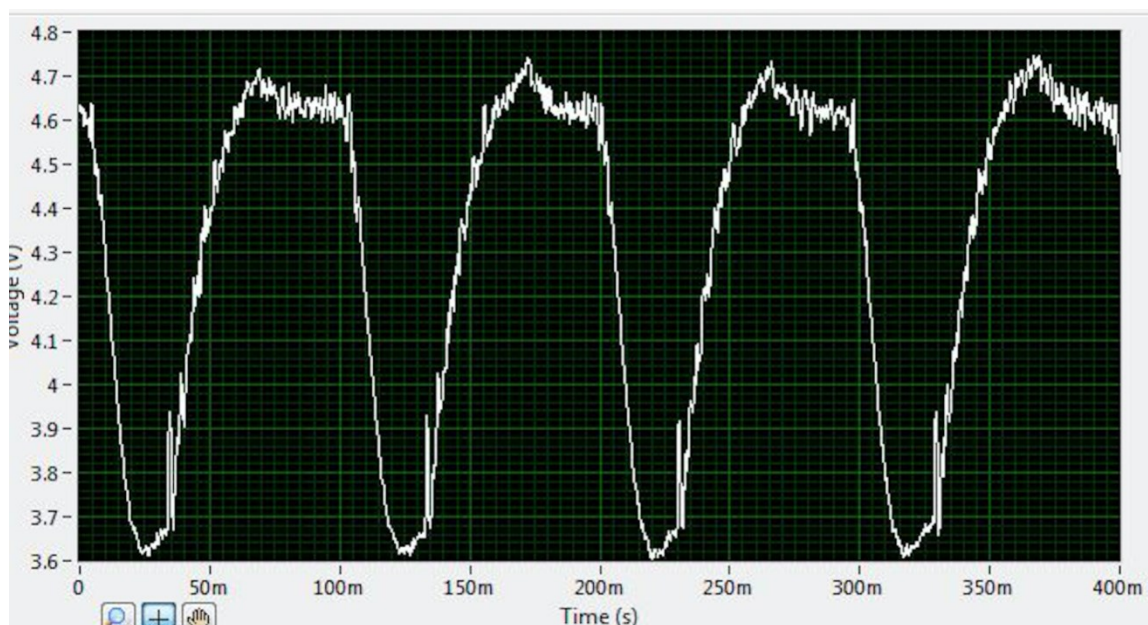


Figure 17 Exemplar of the oscillator waveform used in this paper – Fluidic Oscillator Waveform, IL- $[C_2mim][DCA]$

The pressure transducer measures the voltage between 0-10 V which correlates to 0-1 bar pressure. The oscillator introduces a force equivalent of 100 mbar for each pulse (4.6 V – 3.6V, which results in an equivalent of 100 mbar for a 0-10V equivalent pressure transducer- 0-1 bar). This pulse strength

can be seen in Figure 17. This is the reason for bubble detachment and the reason why wettability and viscosity play such a huge factor in bubble size. This results in a substantial translation of momentum into the bubble but can be further tuned depending on the liquid in question. This, coupled with the lubrication theory, explains why the oscillator reduces the bubble size for all the ILs tested.

Conclusions

Fluidic oscillator actuated microbubbles shift the bubble size distribution to a smaller size, compared to steady flow, with an accompanying *increase* in throughput for all ILs (viscous liquids) tested for the same pressure drop.

There is a substantial decrease in comparative bubble, size up to 400 %, for the ILs when compared for the same system with oscillator and with steady flow, with the oscillator changing the formation dynamics and essentially improving the associated transport phenomena. This can now be used with other ILs specifically targeted for carbon capture or catalysis. There is an almost 8 times increase in throughput observed for the same pressure drop with fluidic oscillator implementation.

In previous studies, such as [30], it was found that bubble size in ILs depended on a variety of properties for steady flow. The effect of chemical moieties was seen on bubble size. This study showed that for a lower pressure drop system as well, the steady flow bubbles concur with these findings. Both studies show little or no dependence on viscosity of liquid for steady flow bubble formation and wettability shows more of an effect on bubble size.

For oscillatory flow, there is a bubble size reduction with oscillator implementation. There is a correlation related for bubble size with wettability and viscosity with bubble size reducing with increase in wettability (relatively reduced effect with higher wettability), and bubble size reduction with increase in viscosity.

The bubble size distribution shows characteristics of the moieties and retains features for both oscillatory and steady flow but has greater impact on steady flow as opposed to oscillatory flow. The physico-chemical properties are dominant on bubble size for oscillatory flow.

The size of the bubble reflects broadly on the ionic liquid property as well as the chemical moiety present. However, this is not a significant factor when oscillation is introduced as wettability and the 'lubrication' effect becomes more dominant and therefore physico-chemical effects come into play. Each pulse generates a bubble, and the oscillatory flow throughput is significantly improved over steady flow throughput of the system. Contact angles, viscosity and liquid-gas- surface interactions play a significant part in bubble formation dynamics upon oscillator implementation as compared to steady flow for which surface kinetics and interaction between chemical moieties dominate bubble generation dynamics. In this study, the following trends were observed for the average bubble size :

For oscillatory flow:



For steady flow:



In Taylor *et al*, [30], experimentally, it comes out to be:



This is due to the differences in the experimental approaches (higher pressure drops with smaller pore sizes and lower flow rates) as compared to the current paper.

In summary, this paper reports on the following achievements and features of fluidic oscillation generated bubbles in ILs:

1. A low cost (energy in terms of pressure drop) has been developed for contacting with ILs for potential use in catalysis or CO₂ capture/release systems.
2. Oscillatory flow, with equivalent fluidic circuit matching, has resulted in a significant increase in transport properties for viscous ILs with an approximately 4 fold size reduction and 8 times throughput increase.
3. For oscillatory flow, physico-chemical properties dominate in determining size dependency. For steady flow, chemical moieties show a greater relative effect and the physico-chemical properties are not at prominent.
4. For both conditions, the effect of chemical moieties has been observed on bubble size and formation characteristics and can be gleaned from their respective bubble size distributions.

Acknowledgements

This work was carried out as part of the “4CU” programme grant, aimed at sustainable conversion of carbon dioxide into fuels, led by The University of Sheffield and carried out in collaboration with The University of Manchester, Queens University Belfast and University College London. The authors acknowledge gratefully the Engineering and Physical Sciences Research Council (EPSRC) for supporting this work financially (Grant no. EP/K001329/1). Pratik Desai would like to acknowledge R3 Water FP7 for this work. Pratik Desai would like to acknowledge Dr. Michael Hines, Professor Ray Allen & Jevgenija Manerova for useful discussions. The authors would also like to acknowledge the support provided by Elliot Gunard and Andy Patrick from the technical workshop at the Department of Chemical & Biological Engineering, University of Sheffield.

References

1. Zimmerman, W.B., V. Tesař, and H.C.H. Bandulasena, *Towards energy efficient nanobubble generation with fluidic oscillation*. *Current Opinion in Colloid & Interface Science*, 2011. **16**(4): p. 350-356.
2. Lee, J.-W.K., Hyeon-Woo; Sohn, Jong-In; Yoon, Gil-Sang, *A Study on Micro Bubbles Influence on Human Skin Cleaning*. *Advanced Science Letters*, 2013. **19**(9): p. 5.
3. Mears, S. and A. Alonso, *Ultrasound, microbubbles and the blood–brain barrier*. *Progress in Biophysics and Molecular Biology*, 2007. **93**(1–3): p. 354-362.
4. Cai, X., *Applications of Magnetic Microbubbles for Theranostics*. *Theranostics*, 2012: p. 103.
5. Dharmakumar, R., D.B. Plewes, and G.A. Wright, *A novel microbubble construct for intracardiac or intravascular MR manometry: a theoretical study*. *Physics in Medicine and Biology*, 2005. **50**(20): p. 4745-4762.
6. Sirsi, S.R. and M.A. Borden, *Microbubble compositions, properties and biomedical applications*. *Bubble Science, Engineering & Technology*, 2009. **1**(1): p. 3-17.
7. Suzuki, R., et al., *Gene delivery by combination of novel liposomal bubbles with perfluoropropane and ultrasound*. *Journal of Controlled Release*, 2007. **117**(1): p. 130-136.

8. Tesař, V., C.-H. Hung, and W.B. Zimmerman, *No-moving-part hybrid-synthetic jet actuator*. Sensors and Actuators A: Physical, 2006. **125**(2): p. 159-169.
9. Zimmerman WB., Tesar, V., Butler, S. & Bandalusena, H.C.H., *Microbubble Generation*. Recent Patents on Engineering, 2008. **2**(1): p. 1-8.
10. Tesař, V., *Microbubble generation by fluidics. part i: Development of the oscillator*, in *Colloquium Fluid Dynamics 2012*: Prague, Czech Republic. p. 13.
11. Tesař, V., *Mechanism of pressure recovery in jet-type actuators*. Sensors and Actuators A: Physical, 2009. **152**(2): p. 182-191.
12. Tesař, V. and H. Bandalusena, *Bistable diverter valve in microfluidics*. Experiments in Fluids, 2011. **50**(5): p. 1225-1233.
13. Tesař, V. and J. Kordík, *Two forward-flow regimes in actuator nozzles with large-amplitude pulsation*. Sensors and Actuators A: Physical, 2013. **191**: p. 34-44.
14. Agarwal, A., W.J. Ng, and Y. Liu, *Principle and applications of microbubble and nanobubble technology for water treatment*. Chemosphere, 2011. **84**(9): p. 1175-1180.
15. Al-Mashhadani, M.K.H., H.C.H. Bandulasena, and W.B. Zimmerman, *CO₂ Mass Transfer Induced through an Airlift Loop by a Microbubble Cloud Generated by Fluidic Oscillation*. Industrial & Engineering Chemistry Research, 2011. **51**(4): p. 1864-1877.
16. A. Al-Yaqoobi , WBJ Zimmerman., *Microbubble distillation studies of a binary mixture in USES - University of Sheffield Engineering Symposium 2014*, Z.L. Pratik Desai, Dr. Rachael Elder, Dr. Dmitriy Kuvshinov, Editor. 2014 Sheffield p. 9.
17. Coward, T., J.G.M. Lee, and G.S. Caldwell, *The effect of bubble size on the efficiency and economics of harvesting microalgae by foam flotation*. Journal of Applied Phycology, 2014.
18. F Rehman, G.M., HCH Bandalusena , WBJ Zimmerman *Fluidic oscillator-mediated microbubble generation to provide cost effective mass transfer and mixing efficiency to the wastewater treatment plants*. Environmental Research, 2015. **137**: p. 32-39.
19. Hanotu, J., H.C. Bandulasena, and W.B. Zimmerman, *Microflotation performance for algal separation*. Biotechnol Bioeng, 2012. **109**(7): p. 1663-73.
20. Hanotu, J., H.C. Bandulasena, Chiu, Tze Yen and W.B. Zimmerman, *Oil emulsion separation with fluidic oscillator generated microbubbles*. International Journal of Multiphase Flow, 2013. **56**: p. 119-125.
21. Hanotu, J., Karunakaran, E. Bandulasena, HCH., Biggs, C., Zimmerman, WBJ., *Harvesting and dewatering yeast by microflotation*. Biochemical Engineering Journal, 2014. **82**: p. 174-182.

22. Kezhen Ying, D.J.G., Yuzhen Shi, William B. Zimmerman, *Growth Enhancement of Dunaliella salina by Microbubble Induced Airlift Loop Bioreactor (ALB)—The Relation between Mass Transfer and Growth Rate*. Journal of Biomaterials and Nanobiotechnology, 2013. **4**(2A): p. 1-9.
23. Kezhen Ying, M.K.H.A.-M., James O. Hanotu, Daniel J. Gilmour, William B. Zimmerman, *Enhanced Mass Transfer in Microbubble Driven Airlift Bioreactor for Microalgal Culture*. Engineering, 2013. **5**(9): p. 735-743.
24. Duhar, G.r. and C. Colin, *Dynamics of bubble growth and detachment in a viscous shear flow*. Physics of Fluids, 2006. **18**(7): p. 077101.
25. Calderbank, P.H., *Transactions of the Institute of Chemical Engineers and the Chemical Engineer*. Transactions of the Institute of Chemical Engineers and the Chemical Engineer, 1958. **36**: p. 443.
26. Hassan, I.T.M., *Stirred tank mechanical power requirement and gas hold-up in aerated aqueous phases*. AIChE journal., 1977. **23**(1): p. 48-56.
27. Yung, C.N., C.W. Wong, and C.L. Chang, *Gas Holdup And Aerated Power Consumption In Mechanically Stirred Tanks*. Canadian Journal of Chemical Engineering, 1979. **57**(6): p. 672-676.
28. A.A.Kulkarni , J.B.Joshi., *Bubble Formation and Bubble Rise Velocity in Gas-Liquid Systems: A Review*. Industrial & Engineering Chemistry Research, 2005. **44**: p. 59.
29. Vlaev, S.D. and M. Fialova, *Bubble Column Bioreactors: Comparison with Stirred Fermenters Based on Local Gas Hold-up Distribution*. The Canadian Journal of Chemical Engineering, 2003. **81**(3-4): p. 535-542.
30. Taylor, S. F. R.; Brittle, S. A.; Desai, P.; Jacquemin, J.; Hardacre, C.; Zimmerman, W. A., *Factors affecting bubble size in ionic liquids*. Physical Chemistry Chemical Physics, 2017. **19**(22): p. 14306-14318.
31. Makuta, T., Takemura, F., Hihara, E., Matsumoto, Y. & Shoji, M. *Generation of micro gas bubbles of uniform diameter in an ultrasonic field*. Journal of Fluid Mechanics, 2006. **548**: p. 113-131.
32. Pancholi, K., E. Stride, and M. Edirisinghe, *Dynamics of Bubble Formation in Highly Viscous Liquids*. Langmuir, 2008. **24**(8): p. 4388-4393.
33. Tsuge, H., Terasaka, K., Tozawa, K. & Hibino, S.-I. *Bubble Formation from an Orifice Submerged in Highly Viscous Liquids*. Kagaku Kogaku Ronbunshu, 1987. **13**(6): p. 857-860.
34. Weber, D.B.a.M.E., *Bubbles in viscous liquids: shapes, wakes and velocities*. Journal of Fluid Mechanics, 1981. **105**: p. 24.
35. Khurana, A.K. and R. Kumar, *Studies in bubble formation — III*. Chemical Engineering Science, 1969. **24**(11): p. 1711-1723.

36. Ramakrishnan, S., R. Kumar, and N.R. Kuloor, *Studies in bubble formation-I bubble formation under constant flow conditions*. Chemical Engineering Science, 1969. **24**(4): p. 731-747.
37. Satyanarayan, A., R. Kumar, and N.R. Kuloor, *Studies in bubble formation—II bubble formation under constant pressure conditions*. Chemical Engineering Science, 1969. **24**(4): p. 749-761.
38. Abdulrazaq, N., Al-Sabbagh, B., Rees, J. M., Zimmerman, W. B. *Separation of azeotropic mixtures using air microbubbles generated by fluidic oscillation*. AIChE Journal, 2015. **62** (4), 1192-1199.
39. Zimmerman, W.B., M.K.H. Al-Mashhadani, and H.C.H. Bandulasena, *Evaporation dynamics of microbubbles*. Chemical Engineering Science, 2013. **101**(0): p. 865-877.
40. Earle, M. J.; Esperanca, J. M.; Gilea, M. A.; Lopes, J. N.; Rebelo, L. P.; Magee, J. W.; Seddon, K. R.; Widegren, J. A. *The distillation and volatility of ionic liquids*. *Nature* **2006**, 439 (7078), 831-4.
41. Bier, M.; Dietrich, S. Vapour pressure of ionic liquids. *Molecular Physics* **2010**, 108 (2), 211-214.
42. Arebi, B.a.D., W.M., *Bubble formation at two adjacent submerged orifices in inviscid fluids*. Journal of Engineering Research, 2008(10): p. 10.
43. Tesař, V. Fluidic Generator Of Microbubbles – Oscillator With Gas Flow Reversal For A Part Of Period. *Acta Mechanica et Automatica* **2015**, 9 (4).
44. Byakova, A. V., Gnyloskurenko, S. V., Nakamura, T., Raychenko, O. I., *Influence of wetting conditions on bubble formation at orifice in an inviscid liquid: Mechanism of bubble evolution*. Colloids and Surfaces A: Physicochemical and Engineering Aspects, 2003. **229**(1–3): p. 19-32.
45. Gray, J., *A Model Of Bubble Growth In Wetting And Non-Wetting Liquids*. Chemical Engineering Science, 1988. **43**(12): p. 12.
46. Marmur, A. and E. Rubin, *A theoretical model for bubble formation at an orifice submerged in an inviscid liquid*. Chemical Engineering Science, 1976. **31**(6): p. 453-463.
47. Pinczewski, W.V., *The formation and growth of bubbles at a submerged orifice*. Chemical Engineering Science, 1981. **36**(2): p. 405-411.
48. Shirota, M., Sanada, T., Sato, A. & Watanabe, M., *Formation of a submillimeter bubble from an orifice using pulsed acoustic pressure waves in gas phase*. Physics of Fluids, 2008. **20**(4): p. 043301-11.
49. Tsuge, H. and S.I. Hibino, *Bubble formation from an orifice submerged in liquids*. Chemical Engineering Communications, 1983. **22**(1-2): p. 63-79.

50. Samaras, K., Kostoglou, M., Karapantsios, T. D. & Mavros, P., *Effect of adding glycerol and Tween 80 on gas holdup and bubble size distribution in an aerated stirred tank*. Colloids and Surfaces A: Physicochemical and Engineering Aspects, 2014. **441**: p. 815-824.
51. W. Lu, J. Ma, J. Hu, J. Song, Z. Zhang, G. Yang and B. Han, *Efficient synthesis of quinazoline-2,4(1H,3H)-diones from CO₂ using ionic liquids as a dual solvent-catalyst at atmospheric pressure*. Green Chemistry, 2014. **16**(1): p. 221-225.
52. J. D. Holbrey, W. M. Reichert, R. P. Swatloski, G. A. Broker, W. R. Pitner, K. R. Seddon and R. D. Rogers, *Efficient, halide free synthesis of new, low cost ionic liquids: 1,3-dialkylimidazolium salts containing methyl- and ethyl-sulfate anions*. Green Chemistry, 2002. **4**(5): p. 407-413.
53. Brittle, S., Desai, P., Ng, W. C., Dunbar, A., Howell, R., Tesař, V. & Zimmerman, W. B. *Minimising microbubble size through oscillation frequency control*. Chemical Engineering Research and Design. **104**: p. 357-366.
54. Allen, T., *Particle Size Measurement: Volume 1: Powder sampling and particle size measurement*. 1996: Springer Netherlands.
55. S. Brittle, A.S., W. B. Zimmerman, *Atmospheric Moisture Content Effects on Ionic Liquid Wettability of Alumina*, in *University of Sheffield Engineering Symposium, 2014*, Z.Y.L. Pratik Desai , Dr. Rachael Elder, Dr. Dmitriy Kuvshinov, Editor. 2014, WhiteRose Press: Sheffield. p. 7-8.
56. Wesley, D. J., Smith, R. M., Zimmerman, W. B. & Howse, J. R., *Influence of Surface Wettability on Microbubble Formation*. Langmuir, 2016. **32**(5): p. 1269-1278.
57. Efremov, G.I. and I.A. Vakhrushev, *Formation of bubbles of gas in different liquids from cylindrical nozzles*. Chemistry and Technology of Fuels and Oils, 1968. **4**(6): p. 441-447.
58. Kukizaki, M. and Y. Baba, *Effect of surfactant type on microbubble formation behavior using Shirasu porous glass (SPG) membranes*. Colloids and Surfaces A: Physicochemical and Engineering Aspects, 2008. **326**(3): p. 129-137.
59. Browne, C., Tabor, R. F., Chan, D. Y., Dagastine, R. R., Ashokkumar, M. & Grieser, F., *Bubble coalescence during acoustic cavitation in aqueous electrolyte solutions*. Langmuir, 2011. **27**(19): p. 12025-32.
60. Laskowski, Y., *Bubble Coalescence and Its Effect on Dynamic Foam Stability*. The Canadian Journal of Chemical Engineering, 2002. **80**: p. 7.
61. Li Chen, Y.L., *The Coalescence Of Bubbles - A Numerical Study*, in *Third International Conference on Multiphase Flow, ICMF'98*. 1998: Lyon.

62. Samanta, S. and P. Ghosh, *Coalescence of Bubbles and Stability of Foams in Brij Surfactant Systems*. Industrial & Engineering Chemistry Research, 2011. **50**(8): p. 4484-4493.
63. Srinivas, A. and P. Ghosh, *Coalescence of Bubbles in Aqueous Alcohol Solutions*. Industrial & Engineering Chemistry Research, 2012. **51**(2): p. 795-806.
64. Vincent S.J. Craig, B.W.N., Richard M. Pashley, *The Effect of Electrolytes on Bubble Coalescence in Water*. Journal of Physical Chemistry, 1993. **97**: p. 5.
64. Yaminsky, V. V., Ohnishi, S., Vogler, E. A. & Horn, R. G., *Stability of aqueous films between bubbles. Part 1. The effect of speed on bubble coalescence in purified water and simple electrolyte solutions*. Langmuir, 2010. **26**(11): p. 8061-74.
66. Zieminski, R., *Bubble Coalescence and Gas Transfer in Aqueous Electrolytic Solutions*. Industrial & Engineering Chemistry Fundamental, 1971. **10**(2): p. 10.
67. Tesař, V., *Configurations of fluidic actuators for generating hybrid-synthetic jets*. Sensors and Actuators A: Physical, 2007. **138**(2): p. 394-403.
68. Tesař, V., *Effective hydraulic resistance of actuator nozzle generating a periodic jet*. Sensors and Actuators A: Physical, 2012. **179**: p. 211-222.

Molecular Weight

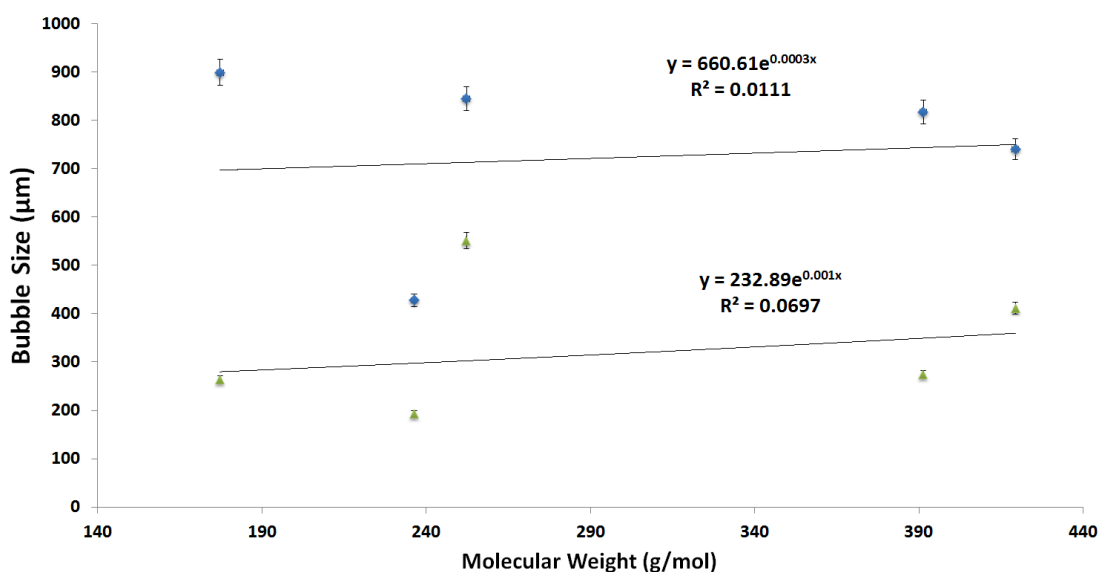




Figure 1 Molecular weight plotted against bubble size for fluidic oscillator and steady flow condition for different ILs - . Steady flow-  ; Fluidic oscillator -  . No correlation to Molecular weight

There is no significant correlation with molecular weight for either of the cases.

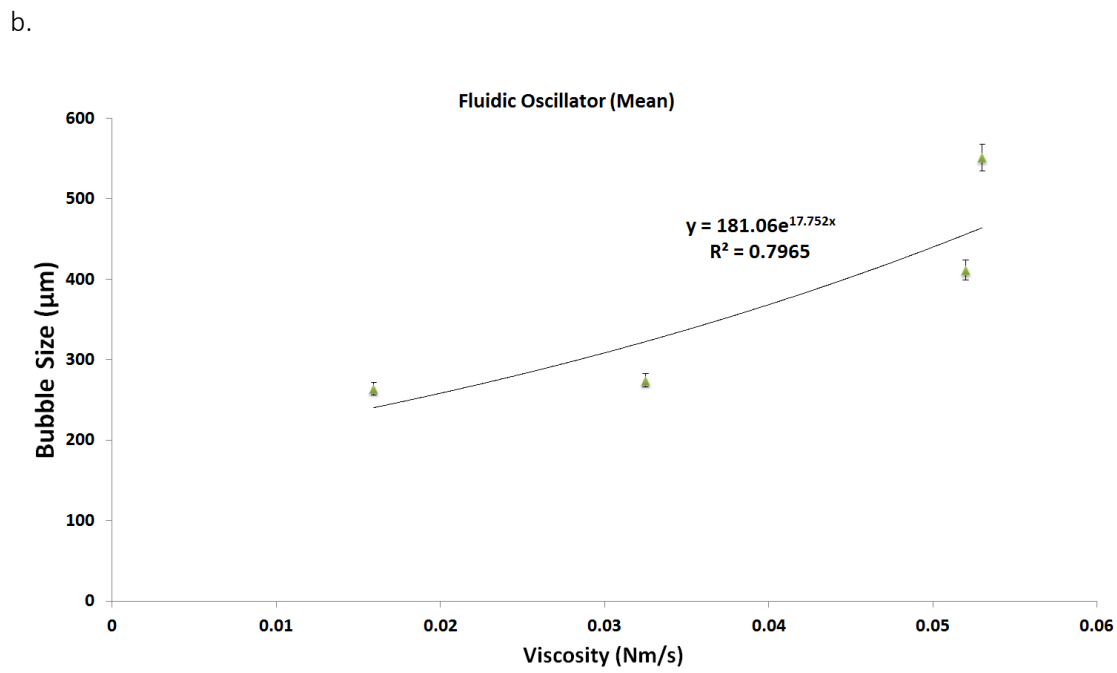
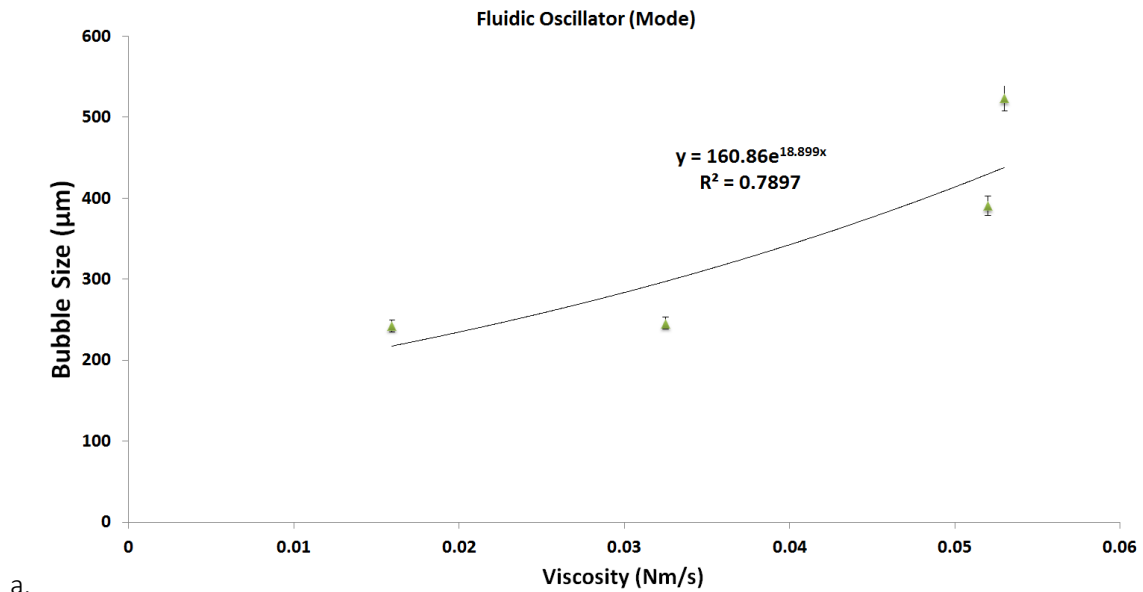


Figure2 Viscosity plotted against bubble size for fluidic oscillator and steady flow condition for different ILs, for mean (a) and median (b) sizes.

Shows the difference to the mean and median bubble sizes for viscosity upon oscillator implementation.

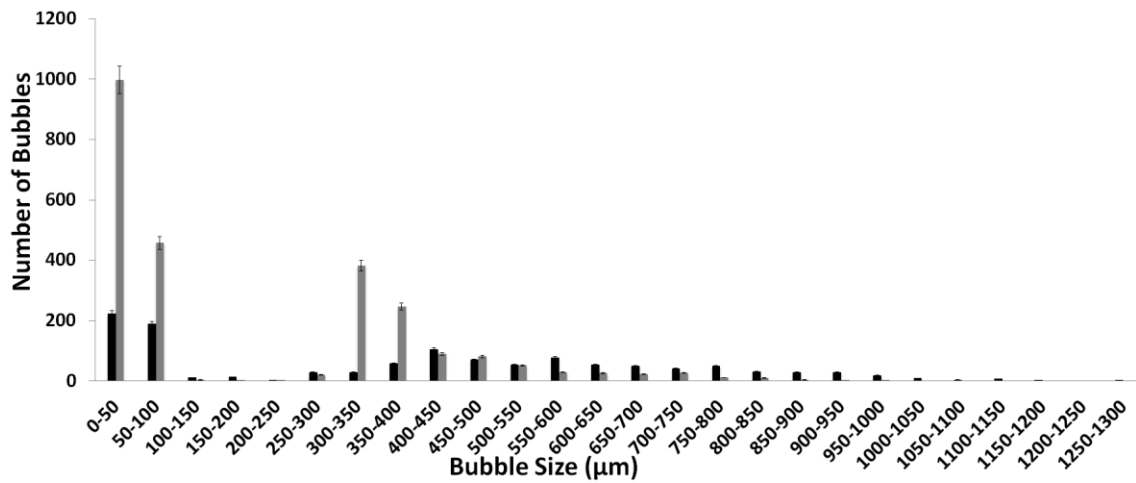


Figure3 Bubble size distribution for [C₂mim][EtSO₄] on a normal scale.

The Effect of Staging of Fluidic Oscillation on Microbubble Generation in Viscous Liquids

Pratik Desai^{a,d}, Sarah FR Taylor^{b,c}, Johan Jaquemin^c, Christopher Hardacre^{b,c}, William B Zimmerman^{a*}

*corresponding author – w.zimmerman@sheffield.ac.uk

a – Department of Chemical and Biological Engineering, Mappin Street, University of Sheffield, Sheffield, S1 3JD, United Kingdom

b – School of Chemical Engineering & Analytical Science, The Mill, University of Manchester Manchester, M13 9PL, United Kingdom

c – School of Chemistry and Chemical Engineering, Queen's University Belfast, David Keir Building, 39 Stranmillis Road, Belfast, BT9 5AG, United Kingdom

d – Perlemax Ltd., 40 Leavygreave Road, S3 7RD, Sheffield, United Kingdom

Abstract (232 words)

Microbubbles are gas-liquid interfaces smaller than 1mm and larger than 1 μ m. Microbubble clouds exhibit very high rates of transport phenomena due to their large surface area to volume ratio. Conventional generation (ultrasound, ablative technologies, and electrolytic mechanisms) of microbubbles requires large amounts of energy and generates a wide distribution of microbubbles. Fluidic oscillation is an energy efficient technique used for microbubble generation capable of generating a fairly monodisperse population of microbubbles compared to conventional bubbling. The hypothesis for the paper was based on the ability of the fluidic oscillator to suction the flow and cause liquid imbibition which would temporarily change the membrane dynamics and wet it with the liquid. Therefore, using steady flow post this operation would result in a similar behaviour (smaller bubble size) temporarily. This paper refers to the bubble generation using fluidic oscillation and the ability of the bubble generating surface to temporarily retain the memory of fluidic oscillator application and generate smaller bubbles. This results in an interesting interplay between the two conditions - conventional bubbling (steady flow) and oscillatory flow, thereby presenting an intermediate condition with an associated reduction in bubble size when staged appropriately i.e. for steady flow bubbling post fluidic oscillator application. The resultant average bubble size is 25% lower than the steady flow bubbling prior to fluidic oscillation application but is dependent on physico-chemical properties, viscosity and wetting angle being primary ones.

Introduction

Microbubbles are bubbles (gas-liquid interfaces) sized between 1 μ m - 999 μ m. This size offers a large interfacial area, which greatly increases the surface area to volume ratio (SA/V) associated with

them. This increased SA/V is responsible for them being extremely good vectors for gas-liquid transfer operations and other associated transport phenomena (Brittle et al., 2015, Abdulrazzaq et al., 2015, Al-Mashhadani et al., 2011, AlYaqoobi, 2014, Rehman, 2015, Zimmerman et al., 2013, Zimmerman, 2014). Economically feasible generation of microbubbles has been difficult to achieve and this has hampered their extensive use in industry. With the advent of fluidic oscillation for microbubble generation, substantial headway has been made for a feasible large-scale energy and economically efficient microbubble generation system (Zimmerman, 2008, Zimmerman et al., 2011).

Figure 91 shows the effect of the bubble surface area to volume ratio. To the left are three bubbles of unit radii 1, 5, and 10 respectively. The volumes and surface area can be seen therein. 1000 bubbles of unit radii 1 would be required to occupy the same volume as that of a single bubble of unit radius 10. – The figure on the right shows how bubble volume affects the surface area and the figure on the left shows how unit radii of 1, 5 and 10 have for bubble surface area and volume.

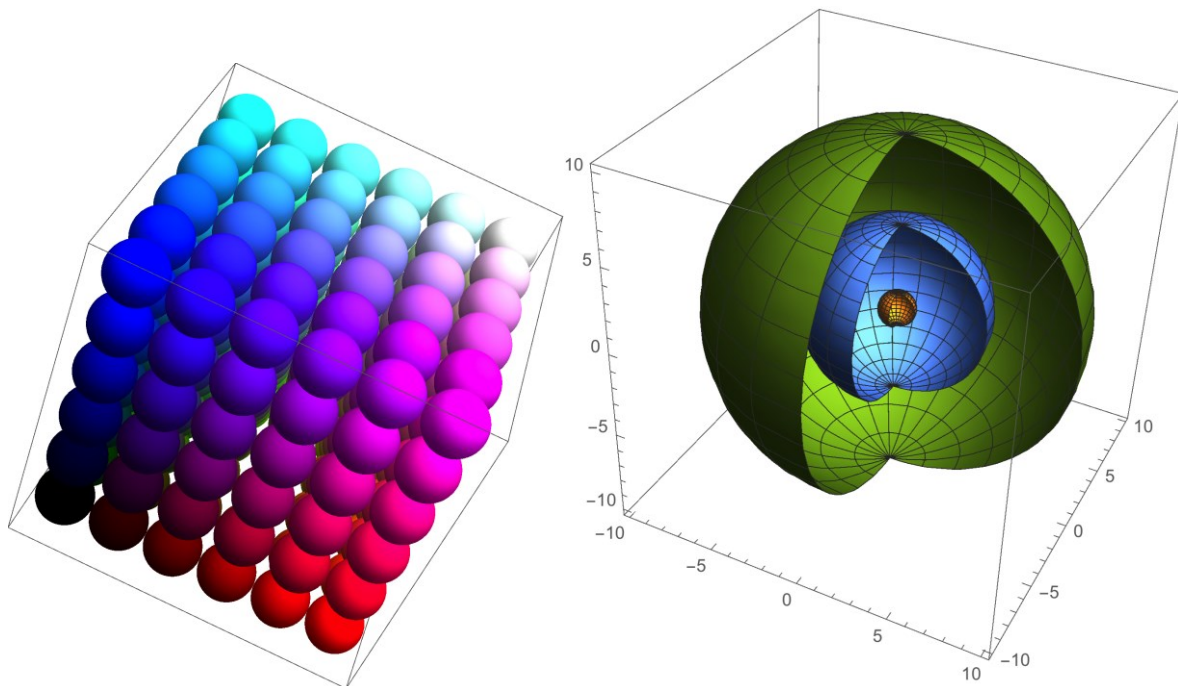


Figure 91 Bubble Volume and Surface Area Connotations Figures are made using Mathematica 11.

With three surfaces (gas inside, liquid outside as well as the gas liquid interface) on offer, an extremely large residence time, increased interior convective current, ability to acquire charge on the surface by using the right combination of gas and liquid, microbubbles can be extremely versatile and utilised in a variety of ways (Agarwal, 2011, Christiansen et al., 1994, Lindner, 2004, Liu et al., 2006, Agarwal et al., 2011, Al-Mashhadani et al., 2011, AlYaqoobi, 2014, Hanotu et al., 2012, Hanotu et al., 2013, Janssen et al., 1999, Lee, 2013, Meairs and Alonso, 2007).

Microbubble Generation

Different ways for microbubble generation are discussed in Zimmerman *et al*, 2011(Zimmerman et al., 2011) and Stride *et al*(Stride and Edirisinghe, 2008). The major cost associated with microbubble generation is that they cost in terms of surface energy. Smaller the bubble, larger is the bubble surface energy required to generate it and this is governed by the Young-Laplace equation

$$\Delta P = \frac{2\sigma}{R} \quad - (1)$$

The reduction in bubble size, results in a large increase in the surface area to volume ratio and an example has been shown Figure 91 to showcase this effect.

With the advent of fluidic oscillation, the generation of inexpensive and energy efficient microbubbles is now a possibility bringing about the possibility for ubiquitous use in industrial applications and processes.

The fluidic oscillator is a no-moving part, hybrid synthetic jet engendering fluidic device that can generate bubbles of the order of the orifice used to engender the bubbles(Tesař et al., 2006, Zimmerman, 2008, Zimmerman et al., 2009, Tesař, 2012, Tesař, 2014, Tesař and Bandalusena, 2011). This y-type bistable valve is able to switch the flow supplied to it in to its two outlets based on the principle of the Coanda effect. The Coanda effect refers to the phenomenon observed of the tendency of the jet to adhere to the wall. Figure 92 is taken from Tesař *et al* (Tesař, 2012), which show the most popular configurations of fluidic oscillators used.

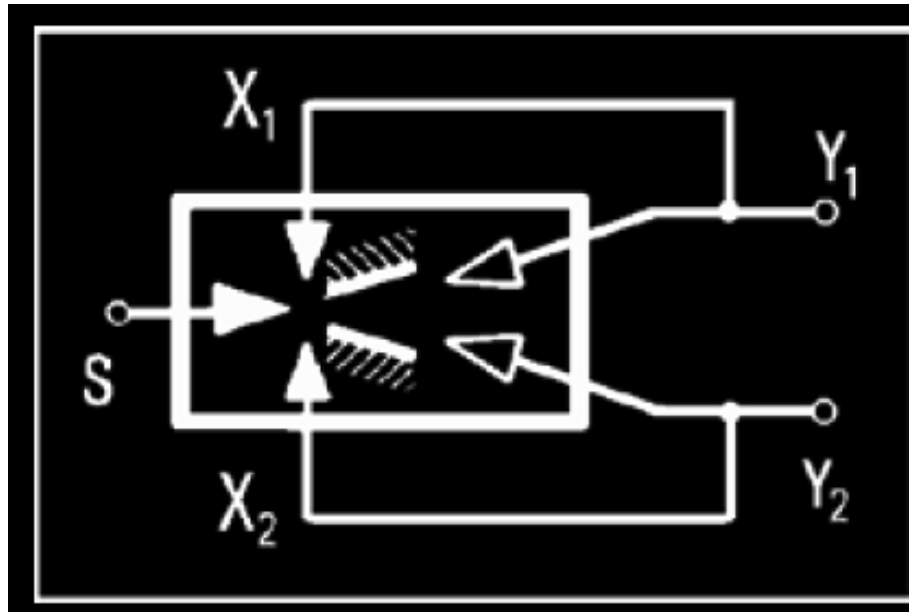


Figure 92 Spyropolous type fluidic oscillator(Tesař, 2012). S (supply nozzle), X1 and X2 (control terminals) and Y1 and Y2 (outlets).

The configuration used in this paper is based on the Spyropolous loop type configuration wherein a feedback loop is attached at the control terminals of the oscillator in order to induce a frequency change. S is the supply nozzle, X1 and X2 are the control terminals and Y1 and Y2 are connected to the membrane based diffusers and are the designated outlets for this oscillator.

This frequency is dependent on the inlet flow, the length of the control terminal (akin to introduction of negative feedback) and the outlet terminals which are then connected to the membrane diffusers. These diffusers are placed in the liquid of interest. This can be quantified into a dimensionless quantity known as the Strouhal number which is used to calculate the performance of the oscillator. The Strouhal number is what the oscillator performance and frequency are based on and the change in the frequency is possible by affecting a change in any of these parameters.

$$St = \frac{f l}{v} \quad - (2)$$

Where f is the frequency [Hz], l is the length of feedback loop (amount of negative feedback) [m] and v is the exit velocity of outlet [m/s].

Bubble generation normally depends on the balancing of forces for the Navier-Stokes equation for steady flow and various studies and models have been developed for the same (Amol A. Kulkarni 2005, Arebi, 2008, Bozzano and Dente, 2001, Byakova et al., 2003, Efremov and Vakhrushev, 1968, GRAY, 1988, Khurana and Kumar, 1969, Loubière and Hébrard, 2003, Pancholi et al., 2008, Pinczewski, 1981, Ramakrishnan et al., 1969, Satyanarayan et al., 1969, Tsuge and Hibino, 1983, Tsuge et al., 1987, Tsuge et al., 2006) whereas it depends (under appropriate conditions and momentum injected), on the switching frequency of the fluidic oscillator and the amplitude of the pulse (Tesař, 2012, Zimmerman, 2008)

Assumptions:

1. Bubble are spherical in shape (since the bubbles being formed are less than 2mm , they can be assumed to be spherical)
2. Bubble detaches from the orifice when the distance between the bubble and the nozzle reaches a certain value (when upwards force = downwards force) for conventional steady flow and during the 'OFF' stage for the fluidic oscillator generated bubble where the bubble pinch off occurs then during the oscillatory cycle.

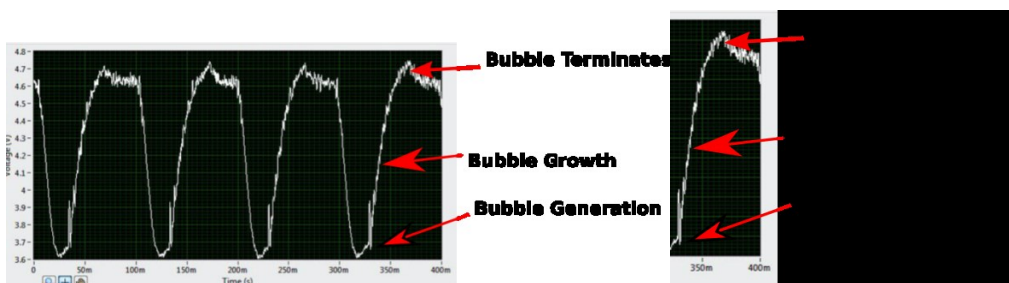


Figure 93 Bubble pinch-off for oscillatory flow

Bubble growth and detachment is governed by the frequency of oscillation and the flow cut off induced by the oscillatory flow, due to it being a synthetic hybrid jet, results in bubble detachment comparable to the size of the orifice in question. Hanotu *et al* (Hanotu et al., 2012) showed the generation of 90 μm bubbles from a 45 μm orifice facilitated by fluidic oscillation with 1069 μm bubbles being generated from the same orifice via conventional steady flow. The engendered jet is a hybrid synthetic one which is the major hypothesis that is going to be used herein to demonstrate the staging effects of the oscillator on bubble generation. A hybrid synthetic jet as described by Tesař *et al* (Tesař et al., 2006) and demonstrates how bubble generation via fluidic oscillation is unique and

cannot be simply replicated using an acoustic/electronic system without compromising fidelity. However, this net positive property of the jet is to be used for the experiments performed herein.

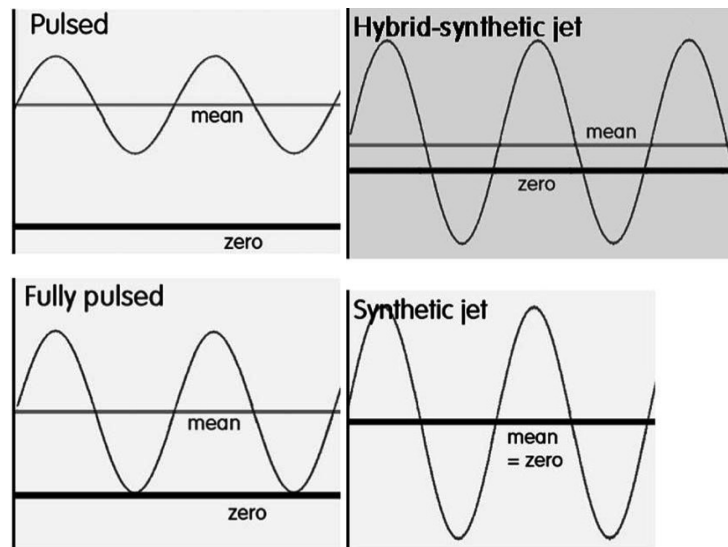


Figure 94 Different types of jets as described by Tesar(Tesař, 2007, Gottfried et al., 1966, Tesař et al., 2006).

This paper investigates microbubble generation via fluidic oscillation in highly viscous liquids and the staging effects observed which changes the dynamics of bubble formation. It is hypothesised that the bubble formation mechanism which determines the cut off of the flow to ensure the bubble pinch-off results in an improvement in the conventional mechanism of bubble generation as well if staged in the right order with the caveat that it is for viscous liquids. This is because the other factors that determine viscous forces become more dominant and responsible for bubble size(Li, 1998, Pancholi et al., 2008). The negative pressure, i.e. the backflow, generated by the oscillator is an extremely important factor to the bubble generation mechanism and this causes the substantial decrease in bubble size.

The hypothesis for this paper is that the negative flow i.e. backflow/suction, of the oscillator should result in a high wetting of the orifices engendering the bubbles that results in smaller bubble size even post oscillator removal for conventional steady flow when compared to conventional steady flow bubble formation before oscillator application.

Methods and Materials

Optical visualisation set up with ionic liquids is to be used in conjunction with a bespoke bubble size sparger set up, and bubble sizes are to be taken optically using conventional flow, then oscillatory

flow followed by conventional flow. To amplify the effect of negative backflow into the system, the chambre was sealed and maintained as a closed system. This would reduce errors induced by external effects. The flow was measured at the outlet which coupled with the sizing would provide the control required for the set up.

Materials

Chemicals used:

ILs used herein were selected from those previously synthesised and tested (Taylor et al., 2017). 1-ethyl-3-methylimidazolium dicyanamide [C₂mim][DCA] (98 %), 1-ethyl-3-methylimidazolium bis(trifluoromethylsulfonyl)imide [C₂mim][NTf₂] (≥97 %), and 1-butyl-3-methylimidazolium bis(trifluoromethylsulfonyl)imide [C₄mim][NTf₂] (≥98 %) were used as received from Merck. 1-Ethyl-3-methylimidazolium ethylsulfate ([C₂mim][EtSO₄]) was synthesised by dissolving diethylsulfate (Sigma-Aldrich, 98 %, 154.2 g, 1 mol) in ice cold toluene (Sigma-Aldrich, ≥99.5 %, 100 cm³) and adding this solution dropwise to 1-methylimidazole (Sigma-Aldrich, 99 %, 82.1 g, 1 mol) dissolved in water (500 cm³) in an ice bath under a nitrogen atmosphere. This solution was stirred overnight. The organic solvent was then removed and the former IL was then sequentially washed with toluene (100 cm³) and dried *in vacuo* five times. 1-Butyl-3-methylimidazolium trifluoroacetate [C₄mim][TFA] was synthesised from trifluoroacetic acid (Sigma-Aldrich, 99 %, 114.0 g, 1 mol) added dropwise to 1-butyl-3-methylimidazolium chloride (174.7 g, 1 mol) dissolved in Milli-Q ultra-pure water (500 cm³) in an ice bath and allowed to stir overnight. The solvent was then removed using a rotary evaporator to obtain the IL. All ILs were dried *in vacuo* (< 10⁻² mbar @ 40 °C) for a minimum of 48 h and maintained under a flow of dry N₂ overnight before microbubble measurements were carried out. After drying, the water content of the ILs was measured using a Metrohm 787 KF Titrino Karl Fischer as < 0.1 wt% for all ILs. The purity of the synthesized ILs was analysed using ¹H NMR using a Bruker 300MHz Ultra shield Plus NMR spectrometer and the results were consistent with literature reports (Holbrey et al., 2002, Lu et al., 2014).

Air was used, coming out of a pressurised compressor at 8bar (g) which was then regulated by a pressure regulator down to the bubbling pressure required for the same.

Two setups have to be used for this with one connection maintained with a back flow. The systemic pressure is controlled using a pressure regulator and the flow is controlled using a mass flow controller. The oscillator is then connected into the bespoke diffuser set up. There is a limited amount of flow allowed through the system in order to not allow for pressurised system but it is maintained

which results in as close an approximation to a closed system as reasonably possible. Flow matching is performed using a mass flow controller (Bronkhorst - miniCoriFlow) placed at the outlet.

The light source and camera are placed opposite each other with the rig in the centre in order to obtain maximum contrast and garner the best images possible. Conventional steady flow is used first in order to generate bubbles at the fixed flow rate.

Maintaining similar conditions, the oscillator is then introduced to the system and the bubbles are sized again. This is then replicated with conventional steady flow. The former defines the staging effect we are investigating, while the latter is the control for comparison purposes of the influence of the active principle of staging oscillation before steady flow for bubble generation.

Bubble Generating System

The test cell has been described there. Membrane used - HP Technical Ceramic (fused alumina, 20 μ m average pore size, 2 off - 50x25mm² area), The test cell has been designed for low flow systems with a maximum liquid volume of 100cm³ and flowrates in mlpm. This is why venting is required in order to initiate the oscillation for the fluidic oscillator whilst maintaining appropriate flow across the membrane.

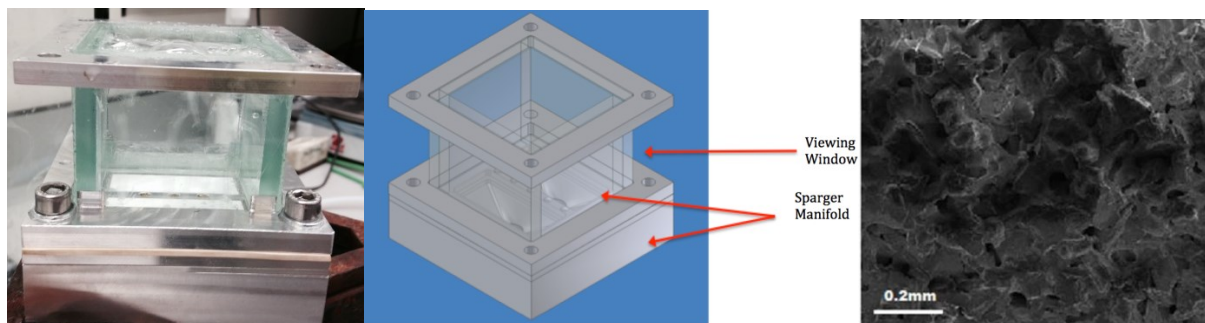
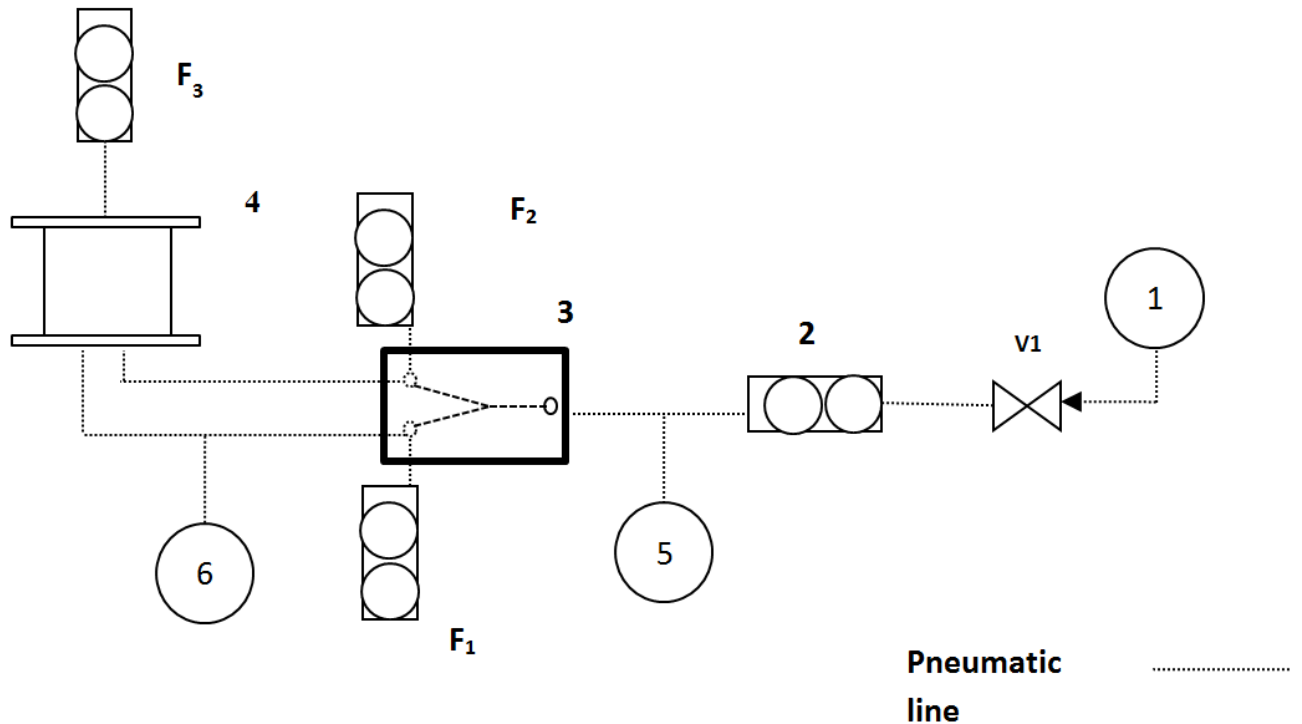


Figure 95 Test Cell – Stainless steel test cell for trialling small amounts of viscous liquids, which has the capability of bubble sizing the bubble cloud formed using optical techniques.

Pneumatic Set up



- | | |
|--------------------------------------|--|
| 1. Pressure Regulator for Air supply | V ₁ . Shutdown valve |
| 2. Mass Flow Controller | F ₁ . Vent Rotameter 1 |
| 3. Fluidic Oscillator | F ₂ . Vent Rotameter 2 |
| 4. Test Cell | F ₃ . Outlet Mass flowmeter |
| 5. Backpressure monitor | |
| 6. Pressure Transducer | |

Figure 96 Schematic of the Set up.

Gas enters the system via the pressure regulator which sends out a controlled, well-regulated gas supply into a mass flow controller. The mass flow controller feeds in the appropriate amount of air to flow into the fluidic oscillator to initialise oscillation. Pressure sensors and backpressure monitors help indicate the pressure and energetics of the system.

As discussed previously, the Test Cell has been designed to work with low volume liquids and therefore low flow (cubic cm i.e. millilitres per minute, rather than litres per minute required to initialise the oscillations) enters the test cell, whereas a much larger volume of gas enters the oscillator.

The appropriate amount of gas flow into the Test Cell is controlled using the vent rotameters. Since a specific amount of flow is required for the fluidic oscillator to actuate, some of the gas flow is vented using rotameters. A pressure transducer located at the outlet of the oscillator measures the

amplitude and frequency of the oscillated air pulse. In addition, this measurement was also used to calculate flow through the oscillator, prior to the diffuser. This is so that oscillated air of an appropriate frequency, amplitude and flow rate can be delivered to the Test Cell.

The flows for the system were monitored and adjusted using a mass flow meter (Bronkhorst model - Mini-CoriFlow) placed at the outlet of the system. The liquid layer in the system provided sufficient resistance which mitigated against any additional damping effects of the oscillatory flow by the mass flow controller.

Frequency Measurement

The frequency of the oscillator was determined by using a bespoke code written in LabView. This could also be used to determine the magnitude of the pulse strength on the oscillatory wave. The code consisted of a Fast Fourier Transform (FFT) power spectrum for the raw data obtained from the pressure transducer at 128 kilo-samples per second. The FFT is a signal processing technique which, when observed with the Nyquist theorem and with sufficient sampling results in a sampling averaged frequency of a wave spectrum resulting in a peak formed for the various systems in use. The frequency of oscillation would help determine the amplitude of the wave jet engendering from the oscillator outlet into the sparger.

Imaging Setup

The bubble sizing and imaging set up is described in Brittle *et al* (Wesley et al., 2016a). The Test Cell is a specially designed bubble generator and described in Figure 95. It is placed in the centre with the camera and diffused light sourced placed opposite each other in order to obtain maximal contrast. This has been described well in (Brittle et al., 2015, Wesley et al., 2016a).

The high-speed camera (Pixelink PL742 camera) is placed antipodal to the diffused light source (Thorlabs LIU004- intensity - 1700 W/cm² and 450 nm - emission peak) with the Test Cell placed in the middle. The bright LED light source is diffused into a more uniform light using a white plastic translucent optical diffuser layer, placed before the Test Cell with the visualisation windows where the bubbles are imaged with the camera. Bubble sizes are determined by a bespoke code developed in LabView. Bubble size analysis was performed and histograms were generated with the code from the images captured. Mean, mode and median bubble sizes were calculated as described below.

Mean stands for the average bubble size and is calculated using

$$D[1,0] = \bar{D} = \frac{\sum_{i=1}^n D_i}{n} \quad - \quad (13)$$

Where $D[1,0]$ is the mean, D_i is the diameter of the bubble i , and n is the number of bubbles.

Mode stands for the maximum bubbles of the same size appear in the histogram or the bubble size that appears most times in the histogram.

Median stands for the middle value of bubble size in the histogram or the bubble size which lies right in the centre of the histogram. This value is also commonly denoted as D_{50} in particle sizing (Allen, 1996).

The low air flow into the system also facilitated the use of the optical bubble sizing technique as a single plane can be observed and imaged, which minimises the magnitude of the error in the measurement technique. Three repeats were taken.

Contact Angle Measurement

The contact angle measurements were made using an Attension pendant drop tensiometer for the IL. The methodology is described in (S. Brittle, 2014). The ILs were kept a dry environment and heated to 60°C for 24 hours in order to remove residual moisture whilst maintaining vacuum desiccation in the presence on CaCl_2 . The Attension pendant drop tensiometer is able to take precise measurements of the contact angle using a visualisation setup similar to the bubble sizing visualisation setup including a monochromatic light source, adjustable sample; and software able to recognise the drop and measure its contact angle. The ILs were pipetted onto the cleaned substrate stage, adjustable in three dimensions using micrometer screws. The droplet is then centred and an image taken for analysis using the software. An averaged contact angle is calculated from the recorded imaging taking the left and right angles into consideration (within 5% of each other or symmetry).

Bubble Size Analyses

Two factors are readily computable for the bubble size analysis- average bubble size in terms of number of bubbles and average bubble size in terms of void fraction contribution (volume contribution) of the bubble. Depending on the application, bubble sizing is usually reported using either of these two factors. Since number contributions are more relevant for this paper and generally more widely used, all discussions related to bubble sizes except when specifically stated are in terms of number contributions. Table 19 provides an exemplar for a case wherein there are 3 classes of bubbles – Class A- with a size of 1 μm and 600 in number, Class B with size of 100 μm and 200 in number and Class C of size 500 μm and 200 in number. This would lead to a total of 1000 bubbles. The surface area of the bubbles is measured and so is the volume. The bubble size can be computed by either using average bubble size in terms of numbers i.e. weighted bubble size divided by total numbers, or in terms of average bubble size in terms of volume contribution i.e. weighted bubble volume divided by total bubble volume.

Average bubble size in terms of number:

$$N_{av} = \sum_{i=1}^n \frac{n_i x_i}{n} \quad - (14)$$

where n is the total number of bubbles, n_i is bubble contribution for each bubble of size x_i .

The average bubble size in terms of volume contribution is

$$N_{vc} = \sum_{i=1}^n \frac{n_i V_i}{nV} \quad - (15)$$

with

$$V_i = \frac{4}{3} \pi x_i^3 \quad - (16)$$

where n is the total number of bubbles and n_i is the bubble contribution for volume of each bubble of size x_i represented by V_i

Table 19 Exemplar

S.No.	Bubble	Size	Number	Volume of individual bubble	Total Volume Contribution	Surface Area	Total Surface Area	Surface Area/Volume
1	A	1	600	5.24E-01	3.14E+02	3.14E+00	1.88E+03	6.00E+00
2	B	100	200	5.24E+05	1.05E+08	3.14E+04	6.28E+06	6.00E-02
3	C	500	200	6.54E+07	1.31E+10	7.85E+05	1.57E+08	1.20E-02
			1000		1.32E+10			
N_{Av}	120.6	N_{vc}	200	μm				

This also means that 1 million 1 μm bubbles occupy the same volume as a single 100 μm bubble. This brings about a massive disparity in bubble size in terms of volume contribution. However, the volume contribution would be a useful tool for estimating any transport phenomena exercise over number contribution.

Generally speaking, size distributions collated from membranes are narrow and the difference in the two averages is lower. A large difference in bubble sizes is observed for a highly dispersed distribution and it is beneficial to the system to have a narrower size distribution. This exemplar demonstrates how these two values need not be the same and their dispersity results in the width of the bubble size

distribution. Work by Allen (Allen, 1996) and Merkus (Merkus, 2009) explain the nuances associated with particle sizing and statistical calculations performed for them in detail.

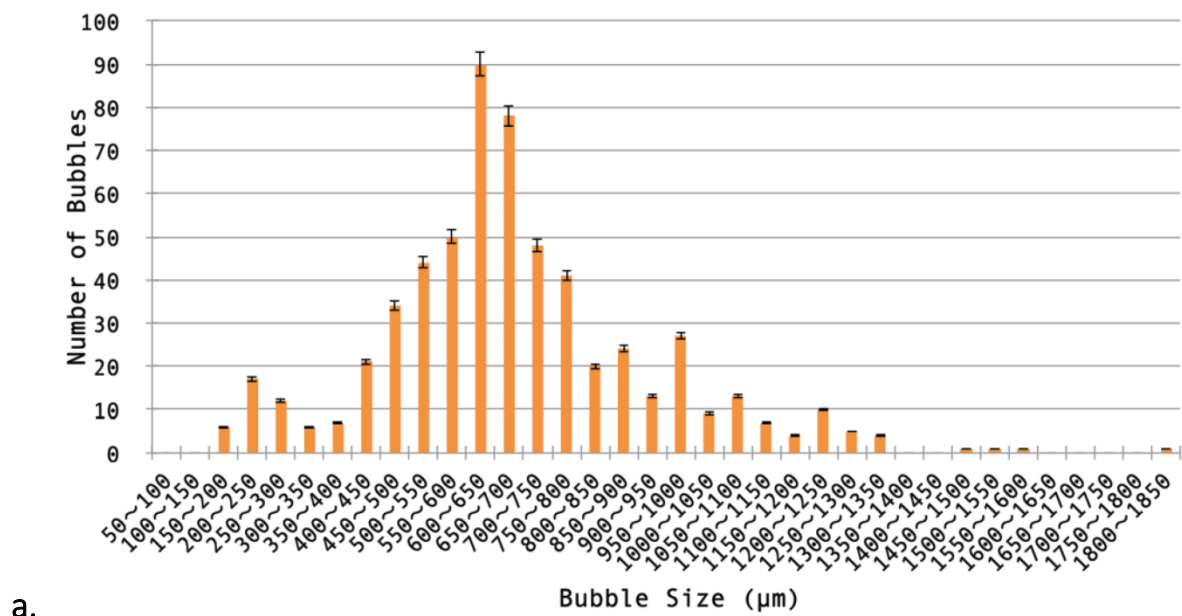
Results

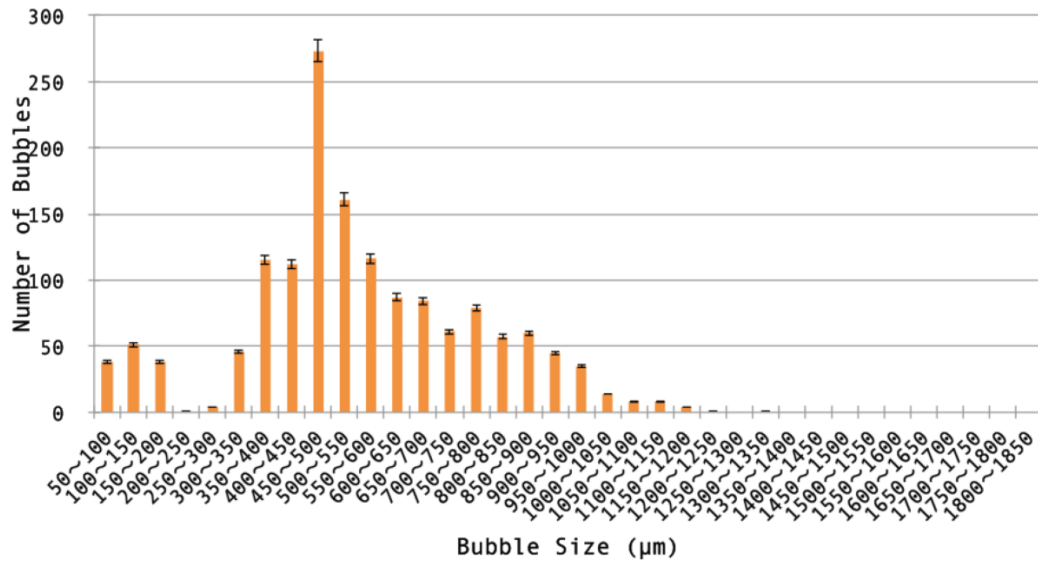
Bubble size distributions were measured for the various conditions and for the different ionic liquids. Fluidic oscillator application resulted in a bubble size reduction for all the cases. A general result is provided for the gamut of ILs studied here but detailed discussions are made for an exemplar.

The graphs herein show the bubble size variations for the three conditions and follow the staging order.

Steady Flow is the first one, followed by fluidic oscillator flow and then by Steady Flow Post Fluidic Oscillation.

The bubble size variations and the effect of the oscillator can be observed and the differences are within experimental errors (less than 5%). There is not only a substantial decrease in bubble size observed due to the introduction of the fluidic oscillator, but there is also a concomitant increase in bubble throughput as well as an even bubble generation across the membrane.





b.

Figure 97 Bubble size distribution for steady flow (a) and for fluidic oscillator generated bubbles in [C₄mim][TFA] (b).

Figure 97 demonstrates the difference between steady flow and oscillatory flow. The number of bubbles (bubble throughput) is increased significantly for oscillatory flow,

The bubble size distribution is wide and since larger bubbles are formed, fewer bubbles are formed for the same throughput for conventional steady flow. The bubble size distribution is narrower and far more numerous bubbles are formed and the size distribution can be seen to shift to the left for fluidic oscillator mediated microbubbles in [C₄mim][TFA].

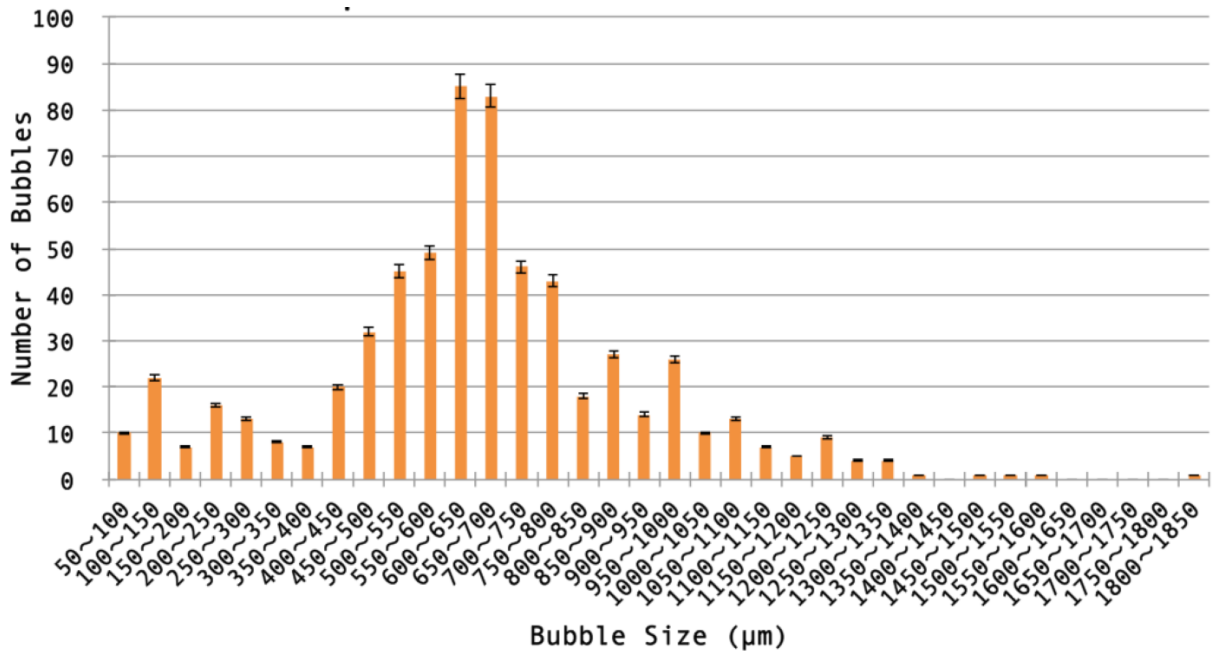


Figure 98 Bubble size distribution for conventional steady flow post FO in [C₄mim] [TFA].

Figure 98 shows a 'morphing' of the two bubble size distributions. The bubble size distributions are merged and there is a slight shift to the left compared to the steady flow originally.

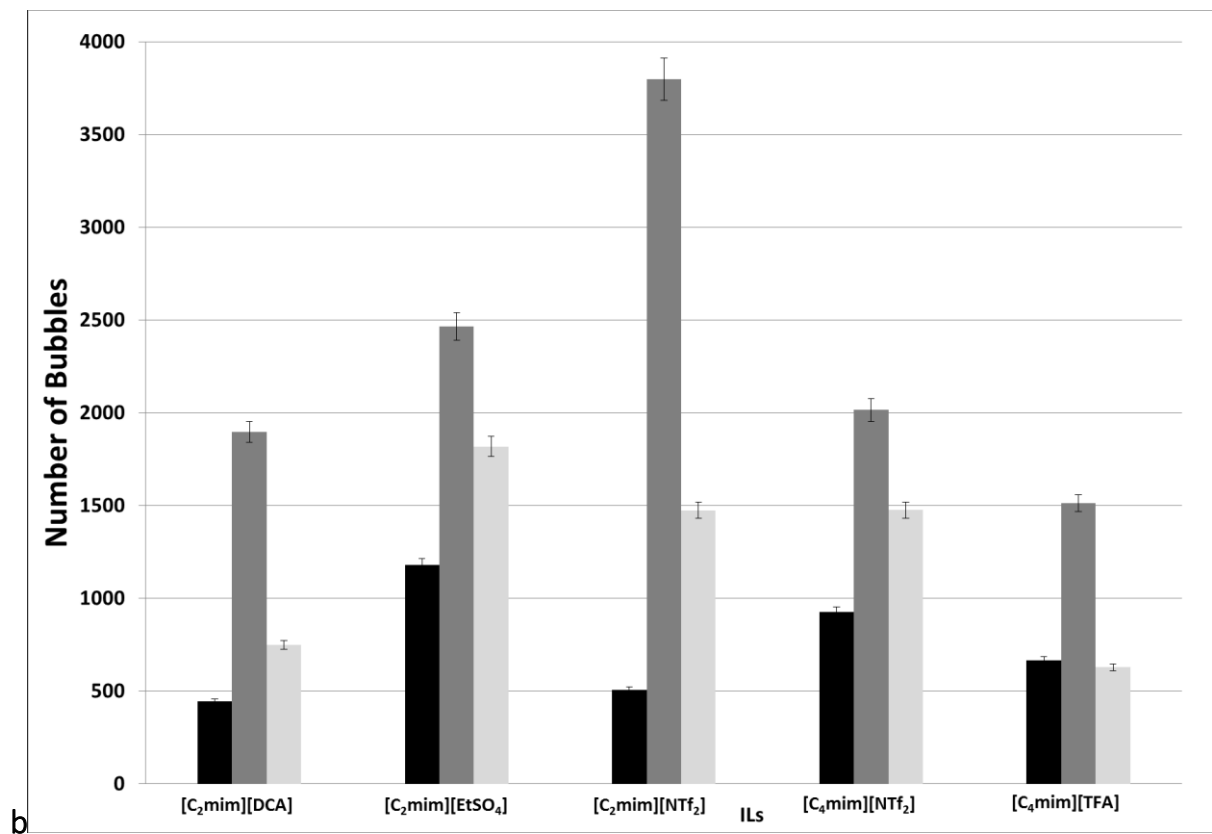
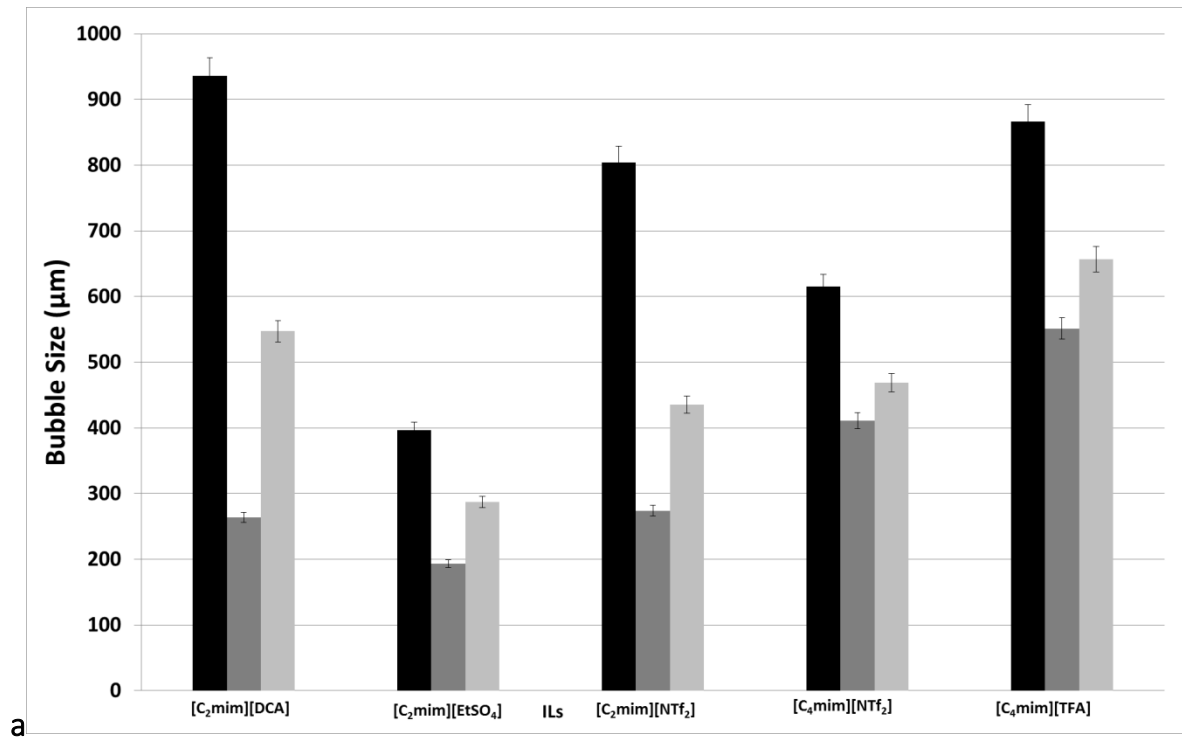


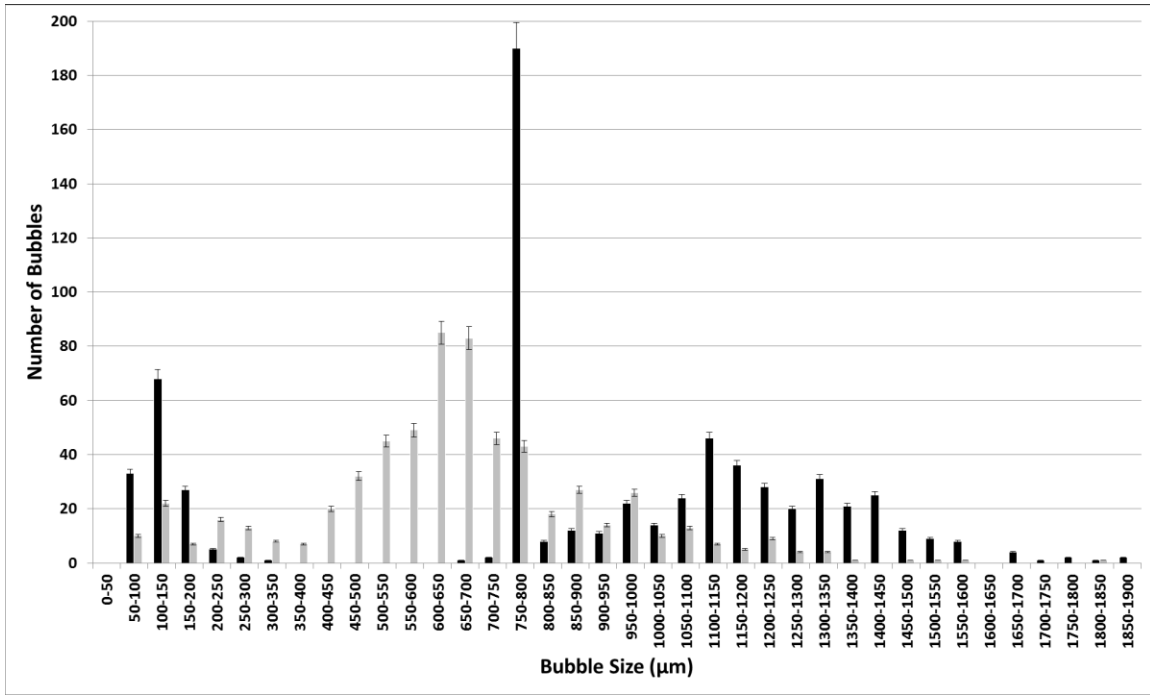
Figure 99 Bubble size distribution (a) and throughput (b) for the various IL exhibiting the staging effect observed. ■- Steady flow, ■ - Fluidic oscillator, and ■- Steady flow post fluidic oscillator implementation

Figure 99 shows the average bubble size and throughput for the various ILs. The throughput is seen to increase substantially upon fluidic oscillation and matches the results in the Desai et al, 2017 (oscillatory flow paper) with the fluidic oscillator and steady flow. The bubble size has reduced by 50% for most cases with [C₂mim][DCA] showing an almost 3.5-fold reduction in bubble size and 4-fold increase in throughput. Upon subsequent implementation of steady flow post oscillation for [C₂mim][DCA], there was a combination of oscillatory flow and steady flow behaviour observed, which results in a 50% reduction in bubble size compared to steady flow or 50% increase in bubble size compared to oscillatory flow and likewise for throughput. This behaviour is seen for all the ILs tested. The interesting behaviour to note is for [C₂mim][NTf₂] where the staging effect observed (steady flow post FO) is closer in size to the steady flow than the FO and can be seen as a direct consequence in the throughput chart. Viscosity and other physico-chemical parameters will be considered in the discussions. The important aspects can be seen in the individual bubble size distributions for the three conditions. . The bubble size decreases and corresponding throughput increases with fluidic oscillator implementation compared to steady flow. The corresponding bubble size and throughput agrees with the hypothesis for steady flow post fluidic oscillator implementation. The steady flow post fluidic oscillator condition displays a mid-range value of the oscillator and steady flow condition and retains this for a short period of time (≈500-600 seconds). Once the system is flushed/cleaned, this feature is not retained.

Discussions

Figure 100 and Figure 101 show the BSD for an exemplar IL [C₄mim][TFA] being superimposed. This shows a much clearer picture of the bubble formation dynamics. The BSDs show how the steady flow formation post fluidic oscillator implementation is a mixture of fluidic oscillator induced BSD and steady flow induced BSD. The fluidic oscillator induced BSD is substantially better than steady flow induced BSD and there is a significant reduction in the bubble size for steady flow post oscillator implementation due to the morphed behaviour observed in Figure 101. However the pseudo-oscillator induced behaviour can be gleaned from this BSD and the pore activation due to which the bubble throughput has increased concomitant with size reduction.

a.



B

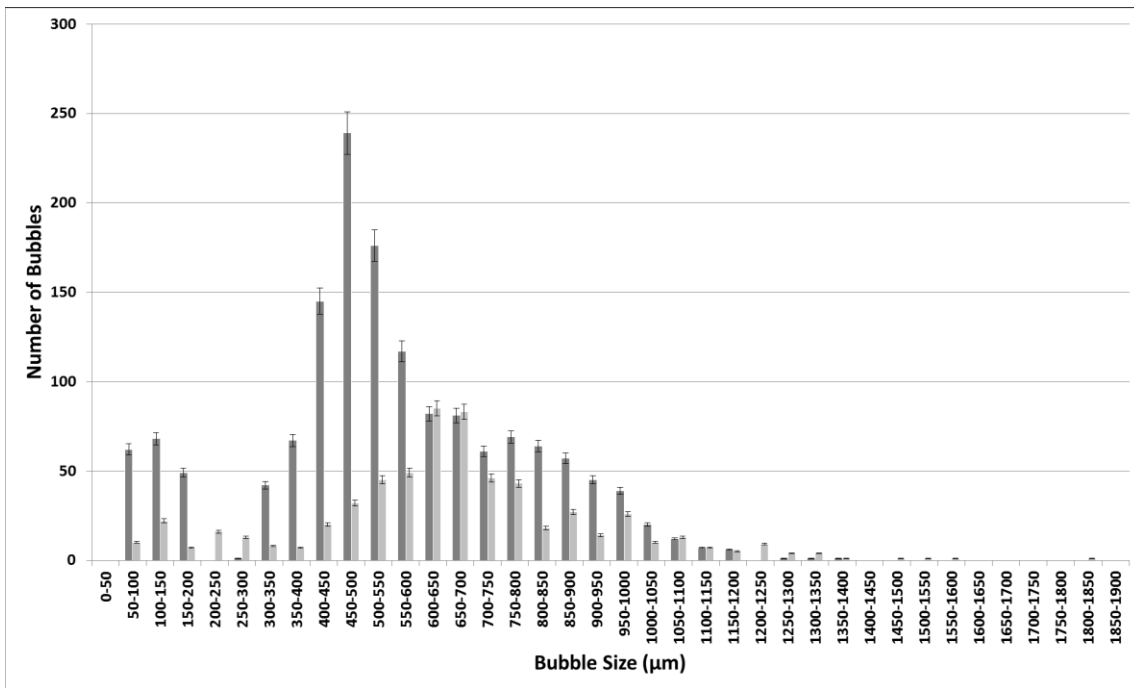


Figure 100 Bubble size distributions for steady flow pre and post FO. The similar characteristics can be seen and observed. The smaller bubbles for post FO steady flow resemble FO bubbles. The figure here shows the morphed characteristics of FO and Steady flow post FO. ■- Steady flow, ■ - Fluidic oscillator, and ■ - Steady flow post fluidic oscillator implementation

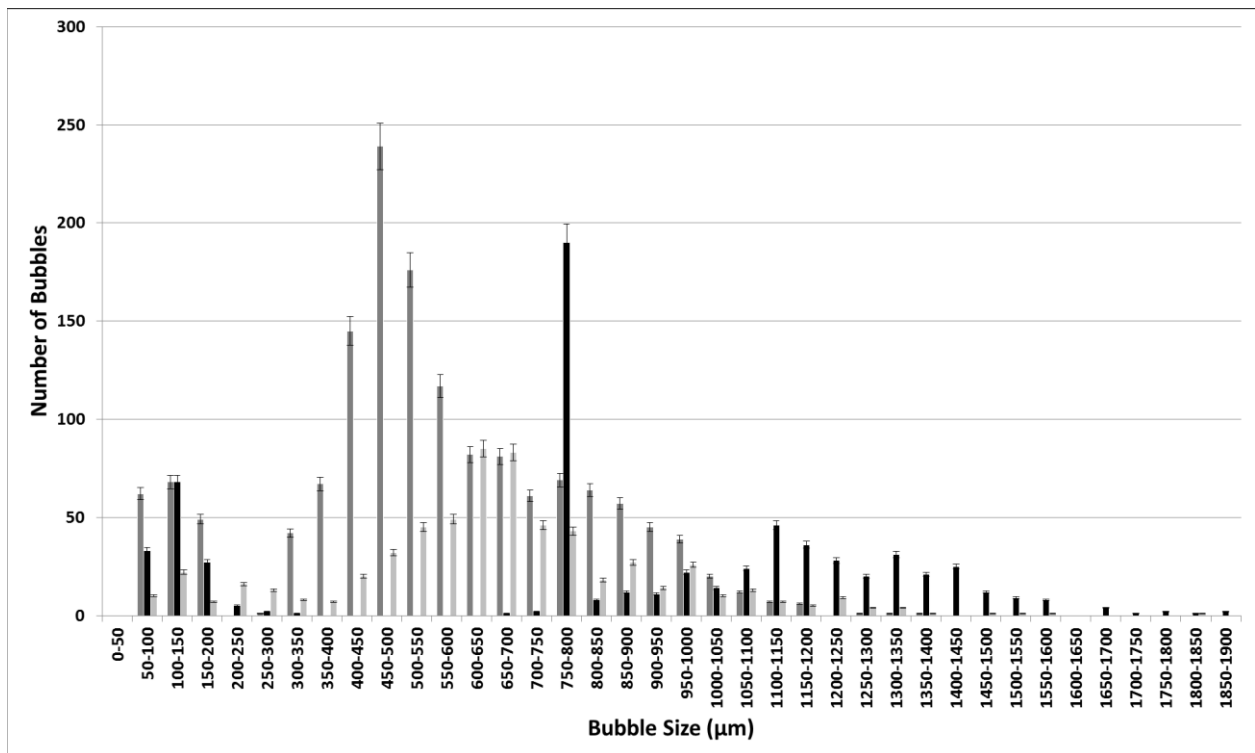
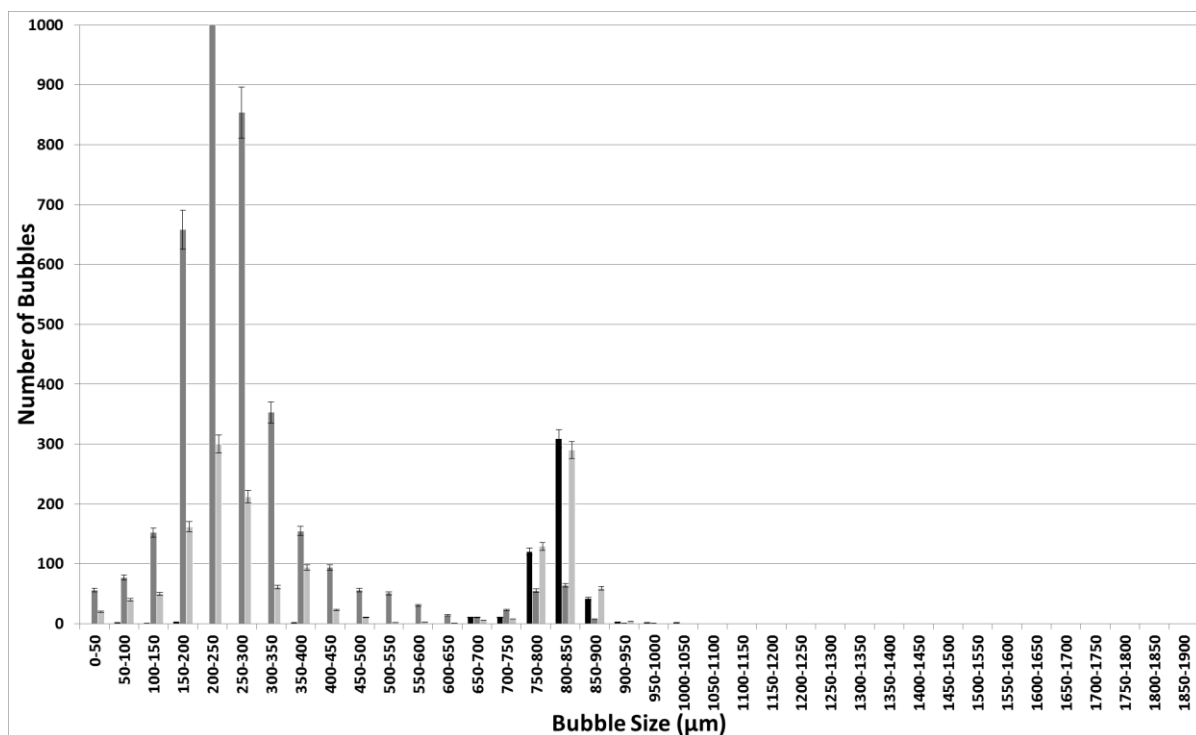


Figure 101 The juxtaposition of three conditions. ■- Steady flow, ■ - Fluidic oscillator, and ■ - Steady flow post fluidic oscillator implementation.

Figure 101 discusses . FO application results in a substantially higher number of bubbles formed as compared to both the steady flow conditions. Similarities and the morphing of the bubble size distributions for steady flow post FO to a condition between FO and Steady flow is observed. The pseudo condition retains properties of both fluidic oscillator and steady flow conditions and this results in an average bubble size smaller than the steady flow condition but larger than the oscillator mediated condition.

a



b

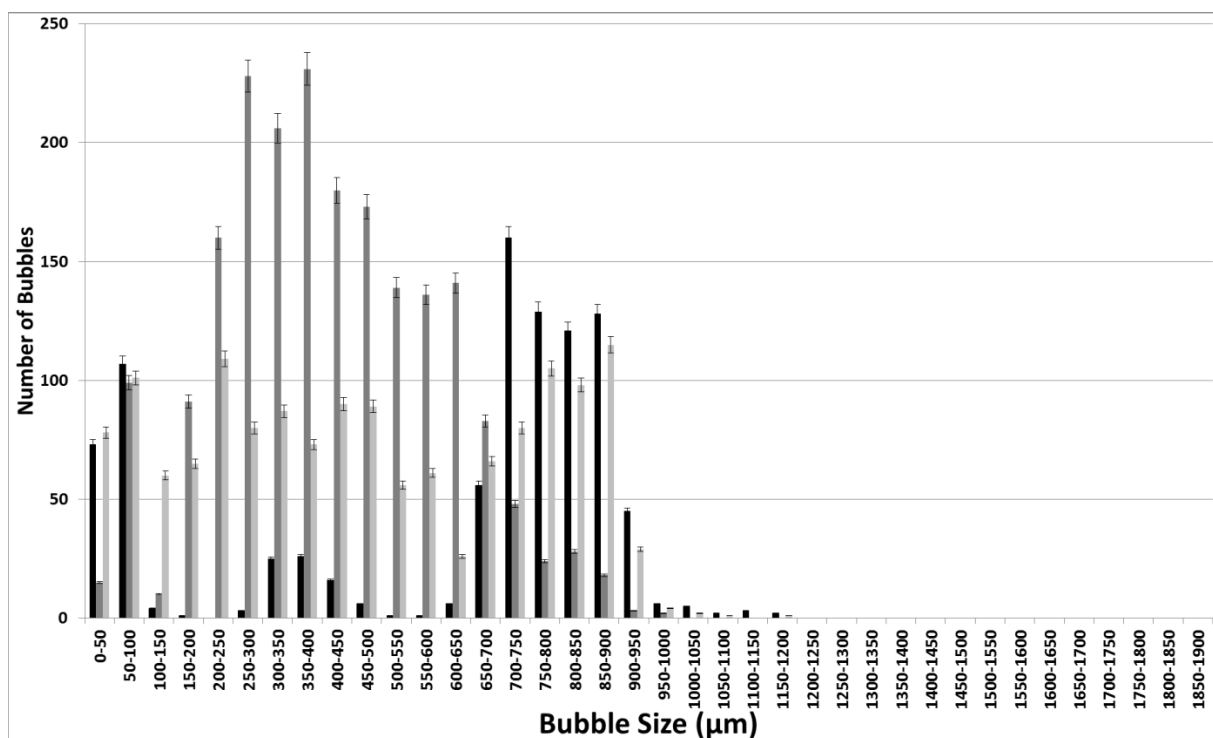


Figure 102 Bubble size distributions comparing steady and oscillatory flow ■- Steady flow, ■ - Fluidic oscillator, and ■- Steady flow post fluidic oscillator implementation.

Figure 102 shows the difference between the BSD obtained by changing the moieties. The diffused structure due to the reduced polarisation observed for [C₄mim] over [C₂mim]. This leads to a broader

BSD and a more diffused structure. This also reduces the difference between the FO and steady flow as well as the staging effect. FO application results in a substantially higher number of bubbles formed as compared to both the steady flow conditions for $[C_2mim][NTf_2]$ (a) and $[C_4mim][NTf_2]$ (b) - The change in the moieties $-[C_2mim]$ and $[C_4mim]$ – changes the bubble size distribution as well as the impact of steady flow post FO implementation. The distributions are varied and the bubble size is substantially different.

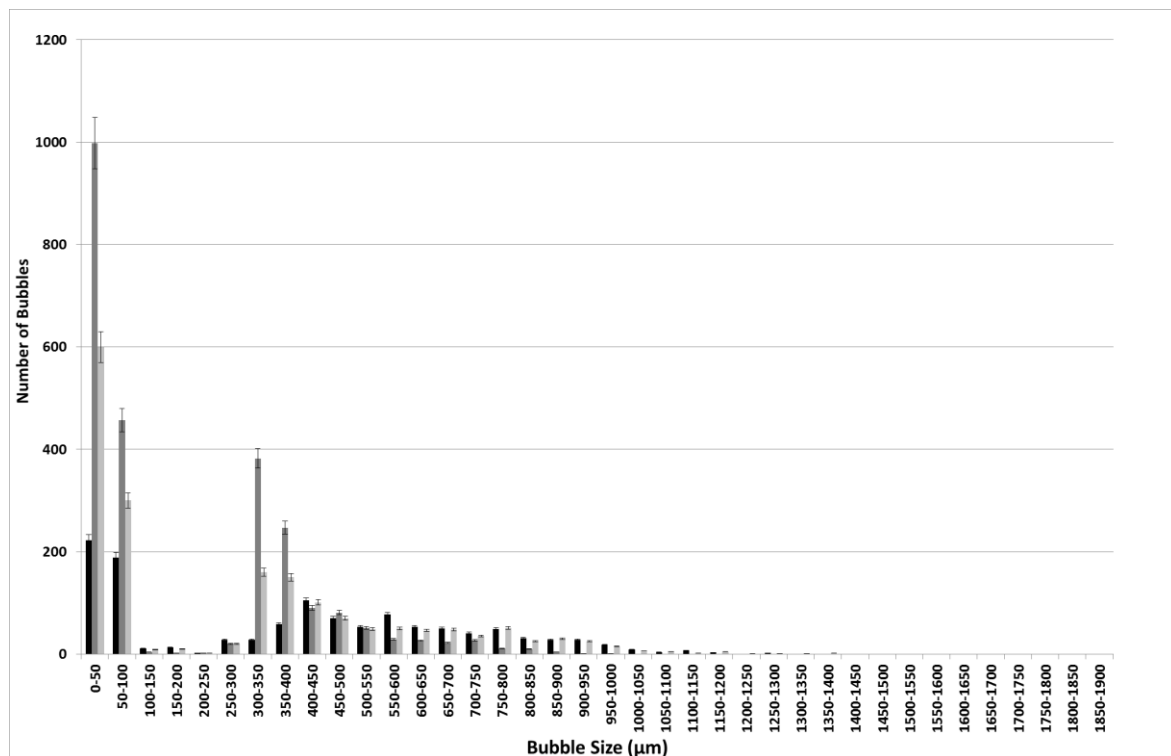


Figure 103 FO application results in a substantially higher number of bubbles formed as compared to both the steady flow conditions for $[C_2mim][EtSO_4]$. ■- Steady flow, ■ - Fluidic oscillator, and ■ - Steady flow post fluidic oscillator implementation.

$[C_2mim][EtSO_4]$ shows a distinctly similar approach due to the high polarisation between the moieties which then results in a similar BSD as for all three cases but just with an increased throughput due to the pore activation and residual FO effects for staging. This ensures that the BSD is the same for all three cases but with slightly larger bubbles (at the tail end) for the steady flow and staging effect which ensures volume conservation but more importantly, the smaller bubble throughput is increased for the FO implementation case over 5-fold – 1000 for FO, 200 for steady flow, and 600 for steady flow post FO (staging effect). Table 2 has collated information on bubble throughput and sizes for the three conditions.

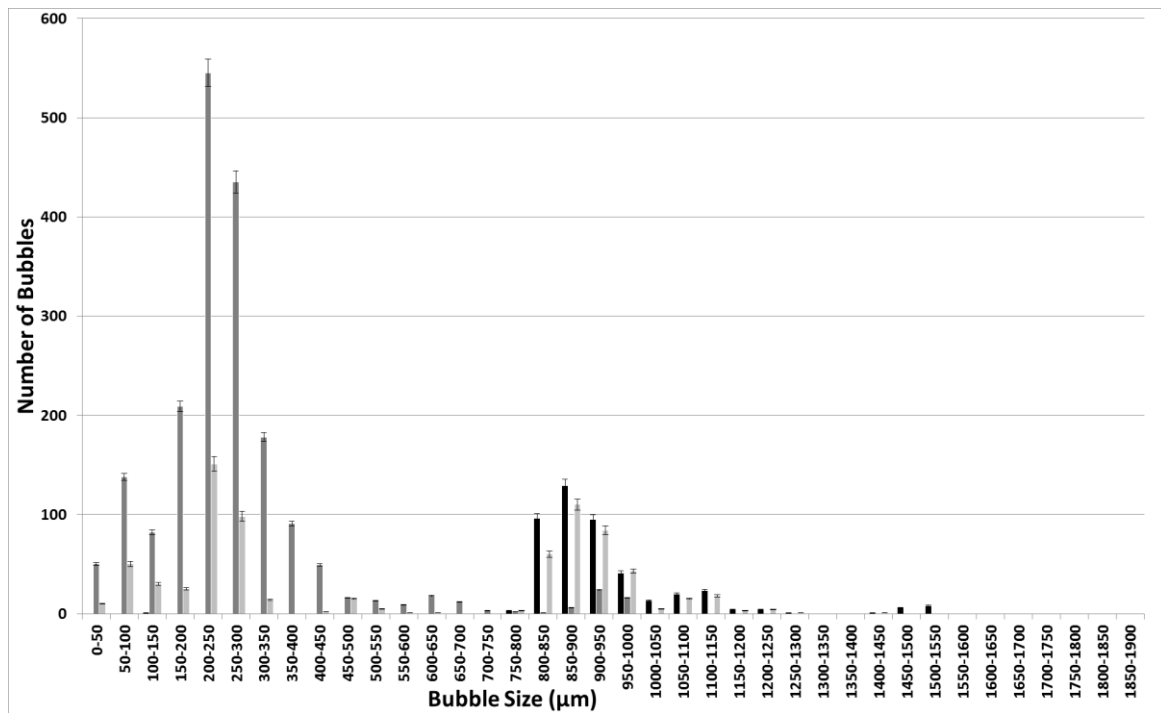


Figure 104 FO application results in a substantially higher number of bubbles formed as compared to both the steady flow conditions for [C₂mim][DCA]. ■ - Steady flow, ▀ - Fluidic oscillator, and ▁ - Steady flow post fluidic oscillator implementation.

The [C₂mim] [DCA] is distinctive due to the physical properties of the system. The BSD is fairly distinct between the FO and steady flow and the staging effect observed is disparate. Once again, the oscillator throughput is high(≈6000). The steady flow bubbles are larger with the steady flow post FO bearing , once again, similarities to both systems as a hybrid BSD.

The size difference thus observed has been so for all the different systems tested out and the system only returns to normal performance after bubbling it dry or removing the liquid and drying out the system entirely.

The bubble size variations observed herein coincide with hypothesis about the staging effect of the oscillator as proposed. That backflow is introduced into the system due to the negative cycle of the synthetic hybrid jet engendered by the oscillator has been explicitly demonstrated by Tesar(Tesař, Tesař, Tesař, 2012, Tesař, 2013, Tesař et al., 2006). However, the backflow results in pore wetting and subsequent pore activation for the membrane used in conjunction with the oscillator. This results in

an increased wetting of the membrane by the liquid of interest. This increased wetting not only results in a reduction in bubble size, but also an increase in throughput via the pore activation.

We propose that wetting of the liquid across the membrane and into the orifice(liquid weeping) causes the decrease in bubble size(Wesley et al., 2016b). This is the theory that we propose for this and an explanation.

Red denotes liquid, which is 'sucked in' or pore imbibition due to liquid wettability and the negative cycle of the oscillatory pulse. The amount imbibed depends on the pulse strength or wettability of the liquid

Sparger with a channel for bubble generation

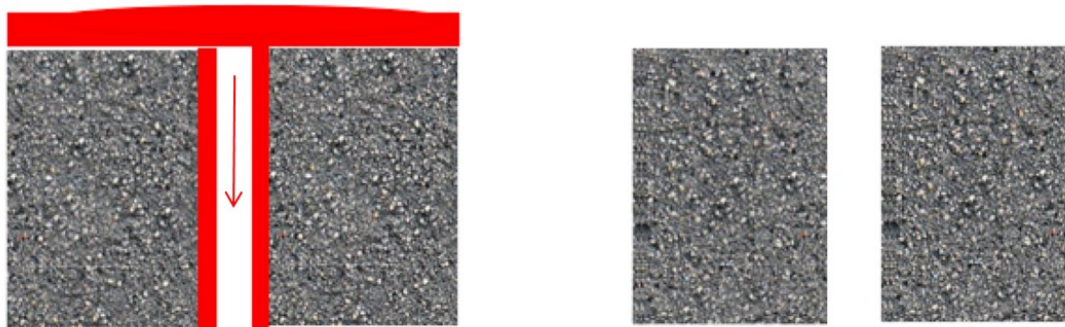


Figure 105 Lubrication Effect – The grey area is the sparger with the blank space (right) representing the pore/channel with the red representing the liquid weep into the orifice thereby providing lubrication like effect(left).

Figure 16 elucidates the lubrication effect and the liquid weeping and this is determined by the liquid wetting across the surface of the membrane. However, in order to satisfy the hypothesis, the viscosity ought to play an important part too. Viscosity can be seen to be acting analogous to the inertial medium that ensures bubble formation. Therefore, coupled with the liquid height above the membrane, it is the 'resistance' to bubble formation. The oscillator pushes this liquid coupled with the gas in order to generate the bubble. The negative cycle of the oscillatory pulse 'sucks' the liquid into the pore/channel and the positive cycle of the pulse generates the bubble. Originally, the effect of backflow due to the negative cycle of the pulse was enumerated in Tesar *et al* [9]. The results so far agree well with this hypothesis. The interesting finding is that wettability adds to this effect and results in an even smaller bubble size.

With the oscillatory flow, although the contact angle i.e. liquid wetting would be appropriate at the start for bubble formation it would be the viscosity that would be more important for the staging effect to take place effectively in conjunction with the wetting angle.

Figure 93 shows the bubble formation under oscillatory flow for an exemplar liquid. The negative pulse is important for the bubble formation and for causing this staging effect.

For τ , being the time constant,

At $\tau_0 - \tau_{1/2}$, i.e. positive half cycle or 'ON' condition, helping the buoyancy forces, the bubble detaches if the amplitude matches the detachment force required and the forces are balanced.

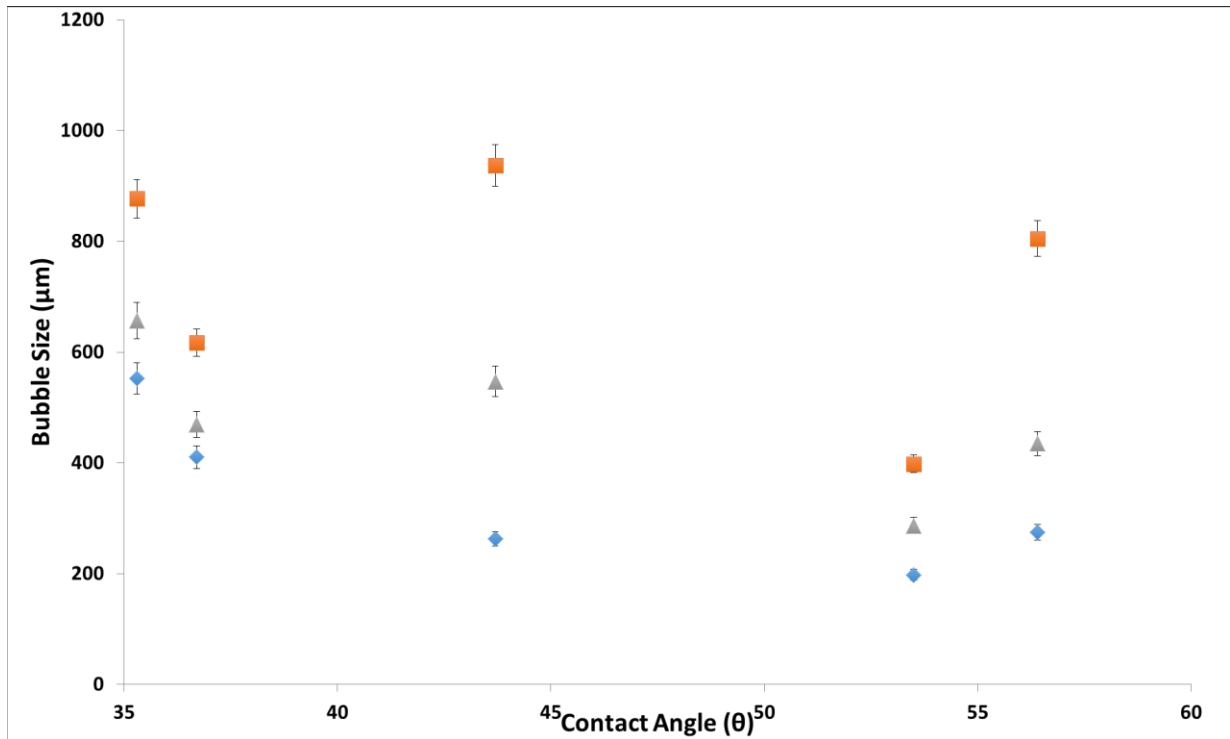
$\tau_{1/2} - \tau_1$, i.e. negative half cycle or 'OFF' condition with a negative force in place opposed to the buoyancy force, this forces the liquid to imbibe into the porous channels. Suddenly there is an evenly distributed liquid 'lubrication' for the pores which then evens the flow through by equalising the force across the membrane due to the liquid. The next positive cycle, smaller bubbles are formed. Once the liquid wet, the lubrication effect ensures that there is complete wetting observed in the system. This lubrication effect results in a tremendous narrowing of the engendering orifice and therefore resulting in a temporary reduction in bubble size. This is where the wetting of the liquid is important for the bubble formation. This could have several implications on the bubbling process. The FO generates smaller bubbles at the expense of back pressure *i.e.* the pressure drop across the fluidic oscillator required to initiate the oscillation. The backpressure is extremely low - 0.2 bar. However, if some performance can be expended at the expense of operating costs, then pulsed use of the oscillator might be possible reducing the operating costs of the plant whilst maintaining required bubble size.

When the oscillator is removed, and steady flow is applied, the behaviour observed is similar to a mixture of the steady flow and the oscillatory flow. The 'memory' retained is temporary but also only relative to the viscosity of the liquid and is between 500-600 seconds. Lower the viscosity, there is an effect of the staging on the system and the morphed character observed has a smaller bubble size. The staging observed has smaller bubble sizes and retains the characteristics of the steady flow and oscillatory flow. Higher is the viscosity, greater is the bubble size for all conditions. However, the difference in size is minimised. One can think of this as the inertia to the bubble formation for the jet to ensure bubble pinch off. The oscillator results in a negative pulse which is able to weep and coat the orifices with the negative or 'OFF' pulse (Tesař, Tesař et al., 2006)

This is most prominently seen in liquids with a higher viscosity as for liquids with a viscosity similar to water or lower, other forces tend to dominate, and the question of pore activation does not arise.

The effect of staging continues as long as bubbling continues and once the liquid is removed, the lubrication effect is no longer in place and this then does not arise and reverts to simple steady flow behaviour.

a.



b.

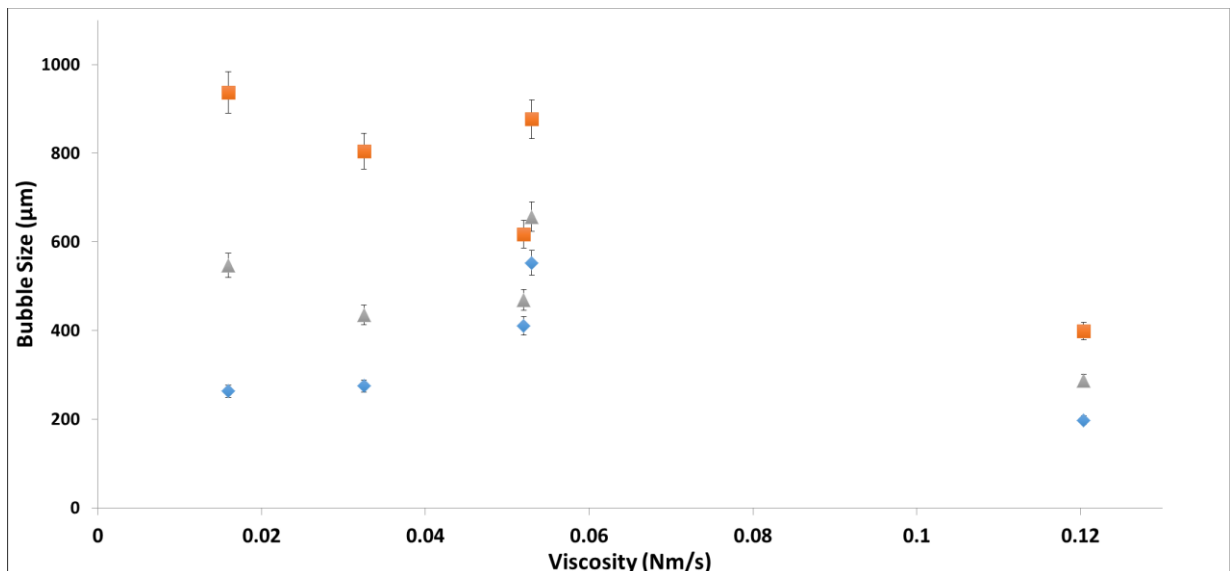


Figure 106 Contact angle vs bubble sizes(left (a)) and Viscosity vs bubble size(right (b)) for various ILs at the three conditions ■ - Steady flow, ◆ - Fluidic Oscillator, and ▲ - Steady flow post FO

The figures seen in the results section demonstrate the level of changes observed in the system when the FO is introduced. For differences in bubble size with respect to physical properties, they have been dealt with in the Taylor et al study(Taylor et al., 2017)and the Desai et al paper (oscillatory flow paper) for FO and steady flow. Interestingly, the staging effect is observed here and conforms closely with the hypothesis about the negative pulse of the fluidic oscillator. The negative pulse, pulls in the liquid as described in the lubrication effect and this effect can be seen herein with a substantial reduction in bubble size and a large difference in bubble size observed for lower viscosity liquids with FO implementation and staging effect. The higher viscosity liquids tend to have a smaller difference observed.

This relationship between the wettability of the liquid for the surface used to engender the bubbles is elucidated when the bubble size is plotted against wettability are plotted. This is observed in Figure 106 where there is no discernible effect seen on the system. This is due to the larger effect observed when viscosity of the system is plotted.

[C₂mim][DCA] is an example about the difference in the size reduction (maximum pulse transfer and therefore maximum size reduction observed) and the viscosity. The differences in size observed for the other ILs reduces due to the increase in viscosity. The liquid back flow is further increased due to the close system approximation placed herein. The increased wetting of the liquid results in an even distribution of bubble size via even flow distribution as for any case of membrane; equal responsiveness can only be an assumption. Effectively, there is no such thing as an equally responsive membrane and therefore, when there is an increased pressure head (due to a highly viscous liquid for example), the wettability increase offered by the negative cycle of the oscillator helps in the decrease in bubble size and concomitant increase in throughput / effective utilisation of the membrane.

As discussed in equation 14, N_{av} is the average bubble size due to the number of bubbles.

The steady flow size for each liquid as the divisor results in

$$\frac{N_{avSF}}{N_{avx}} \quad - (17)$$

Where x is for Steady flow, Fluidic oscillator and Steady flow post fluidic oscillator application.

Table 20 Table summarising bubble sizes, bubble flux and properties of the ionic liquids used at various conditions

Ionic Liquid	Conditions	Bubble Sizes (μm)	Number of Bubbles	Viscosity (N.s/m^2)	Contact Angle ($\theta,^\circ$)
[C₂mim][DCA]	Average Bubble Size (SF)	936	445		
	Average Bubble Size (FO)	264	1897	0.01594	43.7
	Average Bubble Size (SF post FO)	547	749		
[C₂mim][ETSO₄]	Average Bubble Size (SF)	397	1179		
	Average Bubble Size (FO)	193	2465	0.1204	53.5
	Average Bubble Size (SF post FO)	287	1819		
[C₂mim][NTf₂]	Average Bubble Size (SF)	804	506		
	Average Bubble Size (FO)	274	3798	0.03249	56.4
	Average Bubble Size (SF post FO)	435	1474		
[C₄mim][NTf₂]	Average Bubble Size (SF)	615	926		
	Average Bubble Size (FO)	411	2015	0.052	36.7
	Average Bubble Size (SF post FO)	469	1476		
[C₄mim][TFA]	Average Bubble Size (SF)	866	666		
	Average Bubble Size (FO)	551	1512	0.053	35.3
	Average Bubble Size (SF post FO)	657	628		

Table 20 summarises the bubble sizes for the various conditions achieved coupled with throughput, viscosity and contact angle.

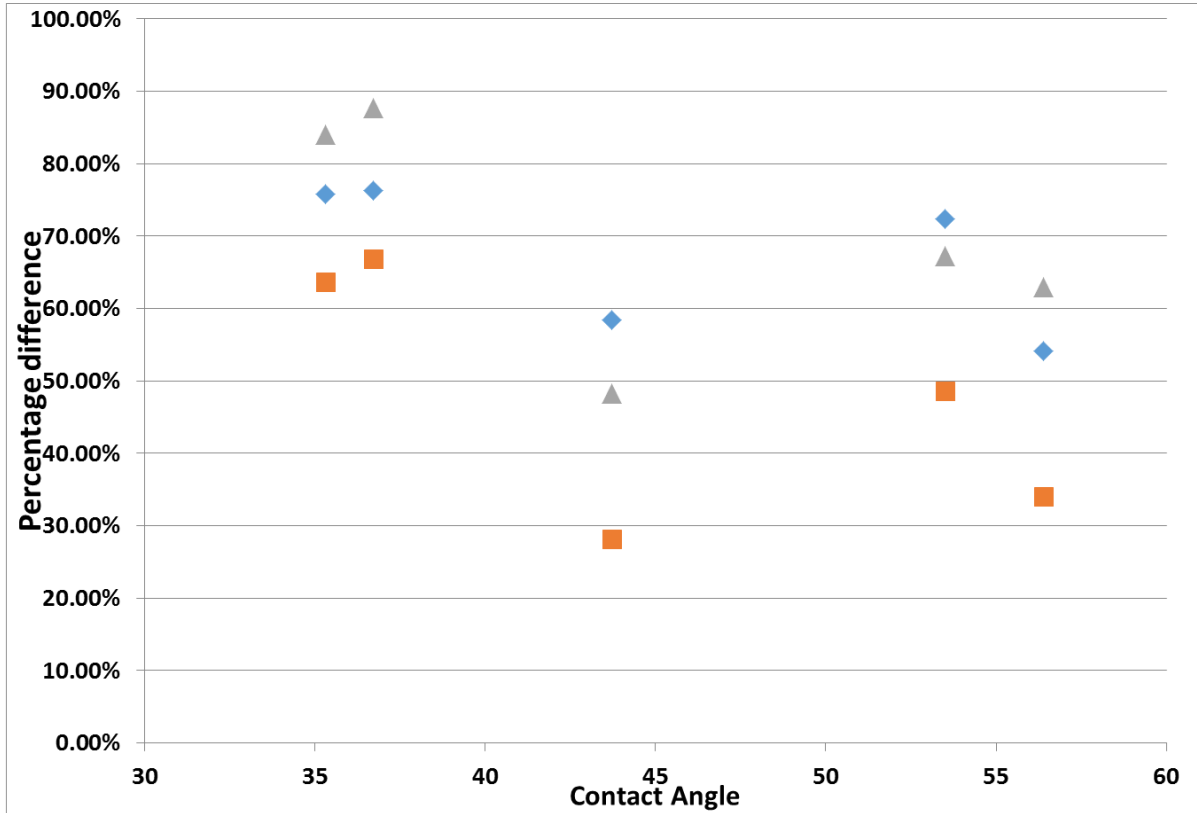
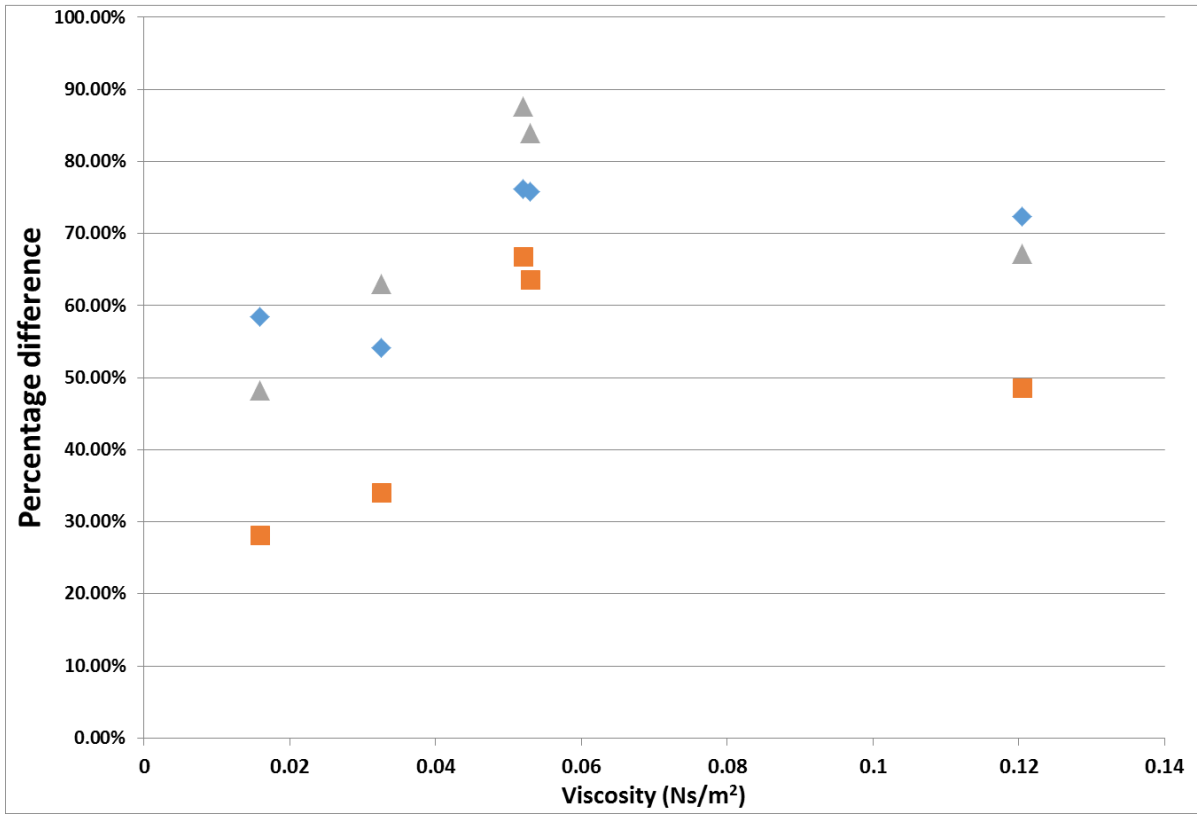


Figure 107 Percentage difference for bubble sizes at various conditions in various liquids versus their viscosities and contact angle. $\blacklozenge - \frac{\text{steady flow post FO}}{\text{steady flow}}$, $\blacksquare - \frac{FO}{\text{steady flow}}$ and $\blacktriangle - \frac{FO}{\text{steady flow post FO}}$

Steady flow post FO/Steady flow is roughly between 50-80% of the steady flow bubble size. This is the staging effect taking place and this demonstrates how the viscosity and wettability play an integral part in the sizing.

When FO/Steady flow ratio is plotted, it provides a strong relationship between wetting and bubble size with the viscosity playing a supplementary role in this thereby resulting in reduced bubble size. This is an important conclusion as this is not apparent but agrees well with the hypothesis for the lubrication effect and previous studies ((Taylor et al., 2017) and Desai *et al*).

The FO/Steady flow post FO demonstrates the ‘character’ percentage observed for the morphed system and how much the steady flow post FO is compared to the FO. Here, the lower viscosity means that there will be a lower value. Higher the viscosity, higher is this value, which means there is a greater staging observed.

Conclusions

Bubble size depends on a variety of factors as determined by (Taylor et al., 2017) and the oscillator produces a smaller bubble size (Desai et al) but viscous forces and wetting forces dominate.

Hypothesis of staging is effective and positively indicated, i.e. negative pulse of the fluidic oscillator results in bubble size reduction based on wettability and viscosity of the liquid and is additionally responsible for the ‘memory’ of the membrane.

Bubble size distribution for the bubbles for steady flow post fluidic oscillation is a morph between steady flow and oscillatory flow conditions. This combines the two conditions and results in a mixture of oscillatory and steady flow bubble size distributions.

Acknowledgements

This work was carried out as part of the “4CU” programme grant, aimed at sustainable conversion of carbon dioxide into fuels, led by The University of Sheffield and carried out in collaboration with The University of Manchester, Queens University Belfast and University College London. The authors acknowledge gratefully the Engineering and Physical Sciences Research Council (EPSRC) for

supporting this work financially (Grant no. EP/K001329/1). PD would also like to thank R3 Water FP7 grant. The authors would also like to acknowledge the support provided by Elliot Gunard and Andrew “Andy” Patrick from the technical workshop at the Department of Chemical & Biological Engineering, University of Sheffield. PD would like to thank Dr. Michael Hines and Professor Ray Allen for interesting discussions and GK for inspiration.

References

- ABDULRAZZAQ, N., AL-SABBAGH, B., REES, J. M. & ZIMMERMAN, W. B. 2015. Separation of azeotropic mixtures using air microbubbles generated by fluidic oscillation. *AIChE Journal*, 62, 1192-1199.
- AGARWAL, A., NG, W. J. & LIU, Y. 2011. Principle and applications of microbubble and nanobubble technology for water treatment. *Chemosphere*, 84, 1175-1180.
- AGARWAL, A., NG, W. J., LIU, Y. 2011. Principle and applications of microbubble and nanobubble technology for water treatment. *Chemosphere*, 84, 1175-80.
- AL-MASHHADANI, M. K. H., BANDULASENA, H. C. H. & ZIMMERMAN, W. B. 2011. CO₂ Mass Transfer Induced through an Airlift Loop by a Microbubble Cloud Generated by Fluidic Oscillation. *Industrial & Engineering Chemistry Research*, 51, 1864-1877.
- ALLEN, T. 1996. *Particle Size Measurement: Volume 1: Powder sampling and particle size measurement*, Springer.
- ALYAQOOBI, A. Z., W.B. 2014. Microbubble distillation studies of a binary mixture. In: PRATIK DESAI, Z. L., DR. RACHAEL ELDER, DR. DMITRIY KUVSHINOV (ed.) *USES - University of Sheffield Engineering Symposium 2014*. Sheffield: WhiteRose Consortia.
- AMOL A. KULKARNI , J. B. J. 2005. Bubble Formation and Bubble Rise Velocity in Gas-Liquid Systems: A Review. *Industrial & Engineering Chemistry Research*, 44, 59.
- AREBI, B. A. D., W.M. 2008. Bubble formation at two adjacent submerged orifices in inviscid fluids. *Journal of Engineering Research*, 10.
- BOZZANO, G. & DENTE, M. 2001. Shape and terminal velocity of single bubble motion: a novel approach. *Computers & Chemical Engineering*, 25, 571-576.
- BRITTLE, S., DESAI, P., NG, W. C., DUNBAR, A., HOWELL, R., TESAŘ, V. & ZIMMERMAN, W. B. 2015. Minimising microbubble size through oscillation frequency control. *Chemical Engineering Research and Design*, 104, 357-366.
- BYAKOVA, A. V., GNYLOSKURENKO, S. V., NAKAMURA, T. & RAYCHENKO, O. I. 2003. Influence of wetting conditions on bubble formation at orifice in an inviscid liquid: Mechanism of bubble evolution. *Colloids and Surfaces A: Physicochemical and Engineering Aspects*, 229, 19-32.
- CHRISTIANSEN, C., KRYVI, H., SONTUM, P. C. & SKOTLAND, T. 1994. Physical and biochemical characterization of Albunex, a new ultrasound contrast agent consisting of air-filled albumin microspheres suspended in a solution of human albumin. *Biotechnology and applied biochemistry*, 19 (Pt 3), 307-20.

- EFREMOV, G. I. & VAKHRUSHEV, I. A. 1968. Formation of bubbles of gas in different liquids from cylindrical nozzles. *Chemistry and Technology of Fuels and Oils*, 4, 441-447.
- GOTTFRIED, B. S., LEE, C. J. & BELL, K. J. 1966. The leidenfrost phenomenon: film boiling of liquid droplets on a flat plate. *International Journal of Heat and Mass Transfer*, 9, 1167-1188.
- GRAY, J.-L. L. A. N. B. 1988. A Model Of Bubble Growth In Wetting And Non-Wetting Liquids. *Chemical Engineering Science*, 43, 12.
- HANOTU, J., BANDULASENA, H. C. & ZIMMERMAN, W. B. 2012. Microflotation performance for algal separation. *Biotechnol Bioeng*, 109, 1663-73.
- HANOTU, J., BANDULASENA, H. C. H., CHIU, T. Y. & ZIMMERMAN, W. B. 2013. Oil emulsion separation with fluidic oscillator generated microbubbles. *International Journal of Multiphase Flow*, 56, 119-125.
- HOLBREY, J. D., REICHERT, W. M., SWATLOSKI, R. P., BROKER, G. A., PITNER, W. R., SEDDON, K. R. & ROGERS, R. D. 2002. Efficient, halide free synthesis of new, low cost ionic liquids: 1,3-dialkylimidazolium salts containing methyl- and ethyl-sulfate anions. *Green Chemistry*, 4, 407-413.
- JANSSEN, A. J. H., LETTINGA, G. & DE KEIZER, A. 1999. Removal of hydrogen sulphide from wastewater and waste gases by biological conversion to elemental sulphur: Colloidal and interfacial aspects of biologically produced sulphur particles. *Colloids and Surfaces A: Physicochemical and Engineering Aspects*, 151, 389-397.
- KAWAHARA, A., SADATOMI, M., MATSUYAMA, F., MATSUURA, H., TOMINAGA, M. & NOGUCHI, M. 2009. Prediction of micro-bubble dissolution characteristics in water and seawater. *Experimental Thermal and Fluid Science*, 33, 883-894.
- KHURANA, A. K. & KUMAR, R. 1969. Studies in bubble formation — III. *Chemical Engineering Science*, 24, 1711-1723.
- LEE, J.-W. K., HYEON-WOO; SOHN, JONG-IN; YOON, GIL-SANG 2013. A Study on Micro Bubbles Influence on Human Skin Cleaning. *Advanced Science Letters*, 19, 5.
- LI, C. L., YUGUO.; MANASSEH, RICHARD. 1998. The Coalescence of Bubbles - A Numerical Study. *Third International Conference on Multiphase Flow, ICMF'98*. Lyon.
- LINDNER, J. R. 2004. Microbubbles in medical imaging: current applications and future directions. *Nat Rev Drug Discov*, 3, 527-533.
- LIU, Y., MIYOSHI, H. & NAKAMURA, M. 2006. Encapsulated ultrasound microbubbles: Therapeutic application in drug/gene delivery. *Journal of Controlled Release*, 114, 89-99.
- LOUBIÈRE, K. & HÉBRARD, G. 2003. Bubble formation from a flexible hole submerged in an inviscid liquid. *Chemical Engineering Science*, 58, 135-148.
- LU, W., MA, J., HU, J., SONG, J., ZHANG, Z., YANG, G. & HAN, B. 2014. Efficient synthesis of quinazoline-2,4(1H,3H)-diones from CO₂ using ionic liquids as a dual solvent-catalyst at atmospheric pressure. *Green Chemistry*, 16, 221-225.
- LUO, X., MCCREARY, E. I., ATENCIO, J. H., MCCOWN, A. W. & SANDER, R. K. 1998. Bubble chamber as a trace chemical detector. *Applied Optics*, 37, 5640-5646.

- MEAIRS, S. & ALONSO, A. 2007. Ultrasound, microbubbles and the blood–brain barrier. *Progress in Biophysics and Molecular Biology*, 93, 354-362.
- MERKUS, H. G. 2009. *Particle Size Measurements: Fundamentals, Practice, Quality*, Springer.
- PANCHOLI, K., STRIDE, E. & EDIRISINGHE, M. 2008. Dynamics of Bubble Formation in Highly Viscous Liquids. *Langmuir*, 24, 4388-4393.
- PINCZEWSKI, W. V. 1981. The formation and growth of bubbles at a submerged orifice. *Chemical Engineering Science*, 36, 405-411.
- RAMAKRISHNAN, S., KUMAR, R. & KULLOOR, N. R. 1969. Studies in bubble formation-I bubble formation under constant flow conditions. *Chemical Engineering Science*, 24, 731-747.
- REHMAN, F., MEDLEY, G., BANDALUSENA, HCH., ZIMMERMAN, W.B. 2015. Fluidic oscillator-mediated microbubble generation to provide cost effective mass transfer and mixing efficiency to the wastewater treatment plants. *Environmental Research*, 137, 32-39.
- S. BRITTLE, A. S., W. B. ZIMMERMAN 2014. Atmospheric Moisture Content Effects on Ionic Liquid Wettability of Alumina. In: PRATIK DESAI, Z. Y. L., DR. RACHAEL ELDER, DR. DMITRIY KUVSHINOV (ed.) *University of Sheffield Engineering Symposium, 2014*. Sheffield: WhiteRose Press.
- SADATOMI, M., KAWAHARA, A., KANO, K. & OHTOMO, A. 2005. Performance of a new micro-bubble generator with a spherical body in a flowing water tube. *Experimental Thermal and Fluid Science*, 29, 615-623.
- SATYANARAYAN, A., KUMAR, R. & KULLOOR, N. R. 1969. Studies in bubble formation—II bubble formation under constant pressure conditions. *Chemical Engineering Science*, 24, 749-761.
- STRIDE, E. & EDIRISINGHE, M. 2008. Novel microbubble preparation technologies. *Soft Matter*, 4, 2350-2359.
- TAYLOR, S. F. R., BRITTLE, S. A., DESAI, P., JACQUEMIN, J., HARDACRE, C. & ZIMMERMAN, W. A. 2017. Factors affecting bubble size in ionic liquids. *Phys Chem Chem Phys*.
- TESAŘ, V. Mechanisms of fluidic microbubble generation Part I: Growth by multiple conjunctions. *Chemical Engineering Science*.
- TESAŘ, V. Mechanisms of fluidic microbubble generation part II: Suppressing the conjunctions. *Chemical Engineering Science*.
- TESAŘ, V. 2007. *Pressure-Driven Microfluidics*, Artech House.
- TESAŘ, V. 2012. Microbubble generation by fluidics. part i: Development of the oscillator. *Colloquium FLUID DYNAMICS 2012*. Prague, Czech Republic.
- TESAŘ, V. 2013. Microbubble smallness limited by conjunctions. *Chemical Engineering Journal*, 231, 526-536.
- TESAŘ, V. 2014. Mechanisms of fluidic microbubble generation part II: Suppressing the conjunctions. *Chemical Engineering Science*.
- TESAŘ, V. & BANDALUSENA, H. 2011. Bistable diverter valve in microfluidics. *Experiments in Fluids*, 50, 1225-1233.

- TESAŘ, V., HUNG, C.-H. & ZIMMERMAN, W. B. 2006. No-moving-part hybrid-synthetic jet actuator. *Sensors and Actuators A: Physical*, 125, 159-169.
- TSUGE, H. & HIBINO, S. I. 1983. BUBBLE FORMATION FROM AN ORIFICE SUBMERGED IN LIQUIDS. *Chemical Engineering Communications*, 22, 63-79.
- TSUGE, H., TERASAKA, K., TOZAWA, K. & HIBINO, S.-I. 1987. Bubble Formation from an Orifice Submerged in Highly Viscous Liquids. *KAGAKU KOGAKU RONBUNSHU*, 13, 857-860.
- TSUGE, H., TEZUKA, Y. & MITSUDANI, M. 2006. Bubble formation mechanism from downward nozzle—Effect of nozzle shape and operating parameters. *Chemical Engineering Science*, 61, 3290-3298.
- WESLEY, D. J., BRITTLE, S. A. & TOOLAN, D. T. 2016a. Development of an optical microscopy system for automated bubble cloud analysis. *Appl Opt*, 55, 6102-7.
- WESLEY, D. J., SMITH, R. M., ZIMMERMAN, W. B. & HOWSE, J. R. 2016b. Influence of Surface Wettability on Microbubble Formation. *Langmuir*, 32, 1269-1278.
- ZIMMERMAN, W. B., AL-MASHHADANI, M. K. H. & BANDULASENA, H. C. H. 2013. Evaporation dynamics of microbubbles. *Chemical Engineering Science*, 101, 865-877.
- ZIMMERMAN, W. B., HEWAKANDAMBY, B. N., TESAŘ, V., BANDULASENA, H. C. H. & OMOTOWA, O. A. 2009. On the design and simulation of an airlift loop bioreactor with microbubble generation by fluidic oscillation. *Food and Bioproducts Processing*, 87, 215-227.
- ZIMMERMAN, W. B., TESAŘ, V. & BANDULASENA, H. C. H. 2011. Towards energy efficient nanobubble generation with fluidic oscillation. *Current Opinion in Colloid & Interface Science*, 16, 350-356.
- ZIMMERMAN, W. B. J. 2014. Mass transfer processes with limited sensible heat exchange. Google Patents.
- ZIMMERMAN, W. B. T., V. ; BUTLER, S.; BANDULASENA, H.C.H. 2008. Microbubble Generation. *Recent Patents on Engineering*, 2, 1-8.

Appendix B Desai-Zimmerman MMARP – Microbubble mediated Ammonia Recovery Processes – ‘Waste Factory’

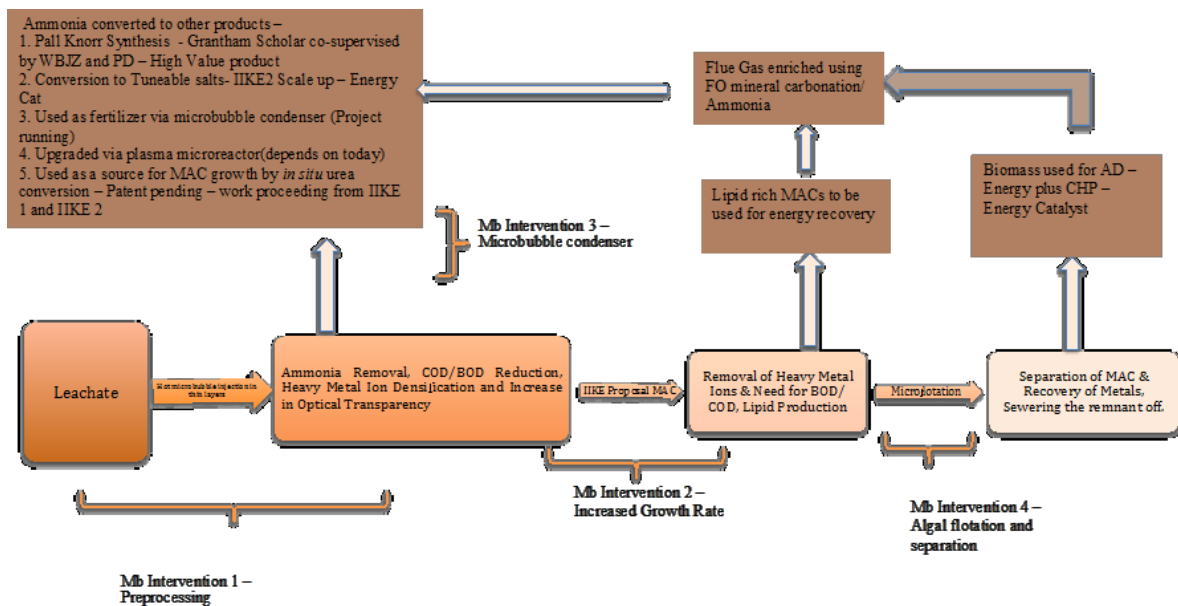


Figure 108 Example of Desai-Zimmerman MMARP. This is an example of the MMARP as there are other methods that can be used and other techniques added and removed to make this work.

This is an example of the cycle with certain components. Each component has been proven on the lab scale by the author and advisor and we are proceeding with pilot scale design and implementation for the same. The leachate has had the ammonia stripped out using the method described in Chapter 7. The ammonia is recovered and converted into several products.

1. As we saw in the CO₂ absorption case, that dissolution can be sped up tremendously in thin liquid layers, so this ammonia can be dissolved in water and converted into ammonium hydroxide. This is the simplest route.
2. The ‘dirty ammonia’ can also be converted to high value commodity chemicals such as the ones seen in Figure 109.
3. These can be reacted and converted into tuneable salts of carbamate and carbonate of ammonia in an energy efficient manner. This work underpins the biogas sweetening part of the £300,000 InnovateUK Energy Catalyst grant led by the author.
4. There are several other routes such as upgrading via plasma microreactors, converting it into ammonia –rich straw pellets, converting it into an acid source via *in situ* product conversion, and other methods.

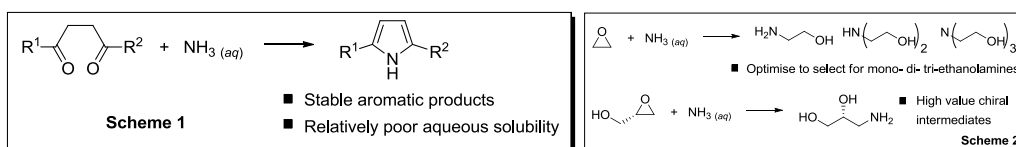


Figure 109 Dirty Ammonia being converted into a high value product. Work has been done using pure chemicals but not for 'dirty' off gasses. This work was awarded a Grantham Scholarship to Professor Harrity, Professor Zimmerman, and Pratik Desai.

The liquid left over after ammonia has been stripped off from the leachate is now lighter as seen in Figure 108. The heavy metals have densified and the COD/BOD has reduced significantly. The ammonia has been reduced below inhibitory levels. Pandhal and Desai won an IIKE award demonstrating the ability to engineer microbial algal communities (MAC) that could withstand the liquid but also be able to uptake the heavy metal ions. Additionally, since leachate is not their natural environment, the environmental stress leads to higher lipid production. Ammonia is inhibitory at high levels (> 70ppm) but not for lower levels (< 50ppm) which can be used by these communities as a nutrient and an N Source. This results in a relaxation in the process requirements for Chapter 7 and in agreement with the Pareto principle type of approach (also known as principle of factor sparsity), the energetics involved in the microbubble stripping process are greatly reduced. Dr. Pandhal won the NERC scale up grant to this problem with Co-Is Professor Zimmerman and Dr. Brown and P.Desai as the Industrial lead. The microflotation as explored initially by (Hanotu *et al.*, 2012) and worked on now for scale up with industrial partners by Desai (employing Chapters 2,3, and 4) can be employed to separate the MAC out. The bacterial consortia are actually useful for wiping out the COD/BOD and as a nutrient source for the algal communities and for their protection. This process can also be intensified using CO₂ microbubbles (Kezhen Ying, 2013b) resulting in better growth rates (utilising Chapter 2 and Chapter 3 for better bubbling) in order to improve performance by up to 160%. This now leaves the liquid which can be sewerred off. The algal biomass can be fed into anaerobic digestion which the other is underpinning innovation being intensified in the Energy Catalyst grant and discussed in the next appendix. The biodiesel work by the author is too far out of the remit to discuss but will be published shortly.

References

- HANOTU, J., BANDULASENA, H. C.H., & ZIMMERMAN, W. B. 2012. Microflotation performance for algal separation. *Biotechnol Bioeng*, 109, 1663-73.
- KEZHEN YING, AI MASHHADANI, M. K. H., HANOTU, J.O., GILMOUR, D.J., ZIMMERMAN, W.B., 2013. Enhanced Mass Transfer in Microbubble Driven Airlift Bioreactor for Microalgal Culture. *Engineering*, 5, 735-743.

Appendix C InnovateUK Energy Catalyst Grant - Enhancing The Methane Generation From Food Waste Anaerobic Digestion Mediated By Fluidic Oscillator Generated Microbubbles

Project lead – Pratik Desai, University PI – Professor William B Zimmerman

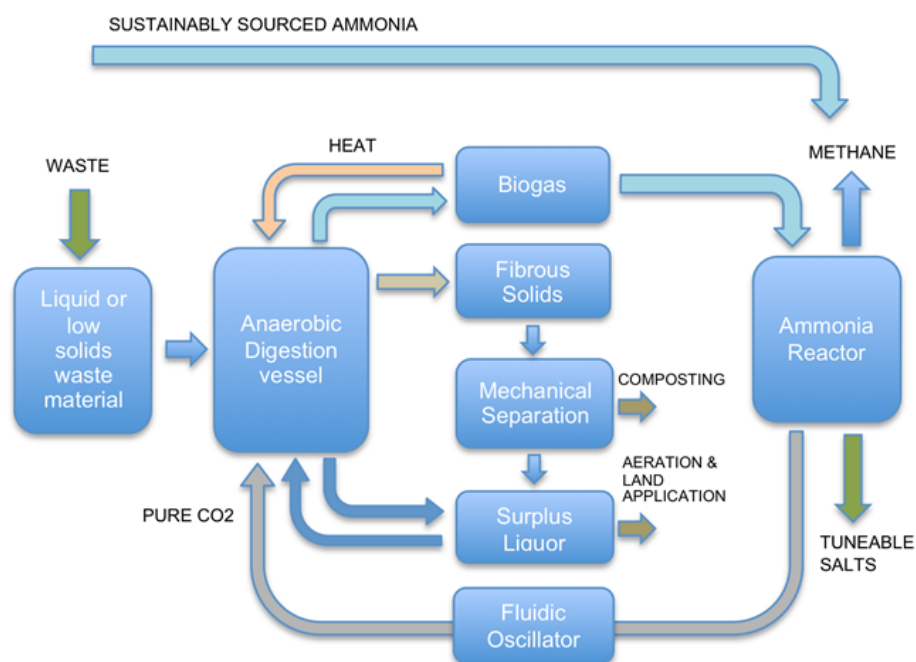


Figure 110 The Energy Catalyst Cycle – Aimed at intensifying Anaerobic Digestion, concomitant with biogas sweetening via sustainable ammonia stripping from ammonia-rich liquors

This work relies on three major innovations.

Firstly, intensification of anaerobic digestion by periodic (5 minutes) CO₂ microbubble injection in untreated wet food waste which would pre-treat it and release biogas approximately 100-110% faster. This reduces the batch rate substantially and therefore the CAPEX and OPEX.

Ammonia is a major environmental liability and also a known inhibitor for microbes. This reduces the solids loading that an AD plant can handle which significantly reduces capital efficiencies.

Here comes the second innovation, the ammonia is sustainably recovered either from the digestate (which increases capital efficiencies) or leachate (which remediates a liability and sustainably produces ammonia). Both cases are highly beneficial- fiscally, sustainably, and in terms of energetics.

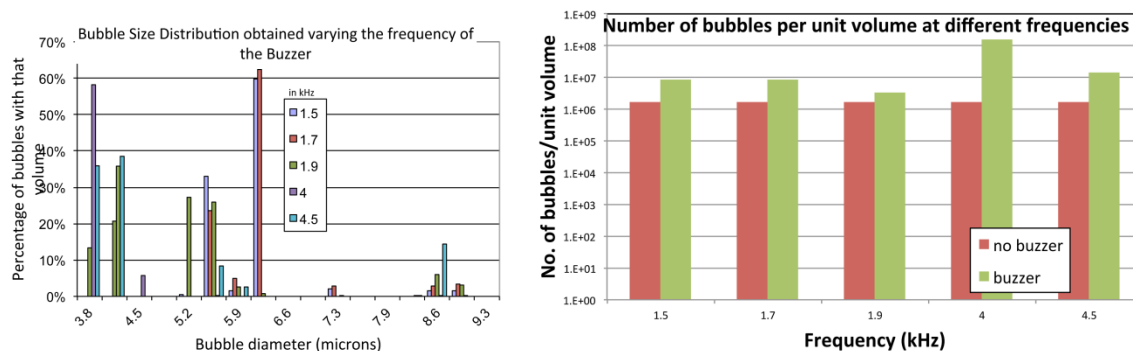
Thirdly, an important work carried out by the author and advisor was based on the use of the 'infinite catalyst'. The CO_2 and NH_3 have been reacted to form a combination of tuneable salts of carbonate and carbamate of ammonia. Carbonate formation is straightforward but carbamate is less so. The surface of the microbubble acts as a scaffold where the chemicals react on the surface forming a covalent bond. This enables the formation of equal quantities of carbamate and carbonate and at room temperature and pressure. Typically, urea formation is accompanied by 200 bar (g) pressure and a temperature of 200°C in the presence of a catalyst. The ability to do this at room temperature due to the presence of the microbubble as a catalyst is the novelty.

Covalent bonds are stable and CO_2 being a highly stable molecule, precludes it from being used as a commodity chemical at relaxed conditions. But much of organic chemistry can be conducted using CO_2 as a building block and this opens up a large avenue for organic chemistry.

It is proposed to react the recovered NH_3 and CO_2 from the biogas to concomitantly sweeten the biogas and generate these tuneable salts in an economic manner. The exothermic nature of this process is also used to provide some of the heating requirements for the AD process.

Appendix D Supplementary Data – Chapter 3 – Peractuation of fluidic oscillation for controlled microbubble generation

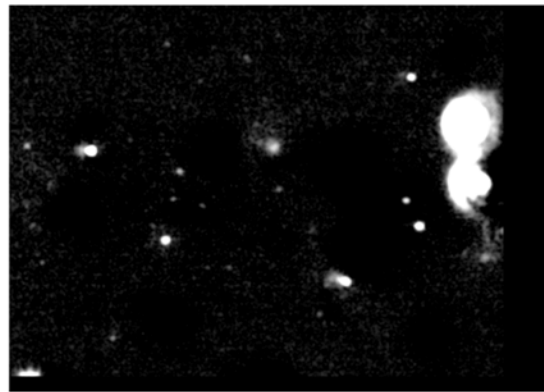
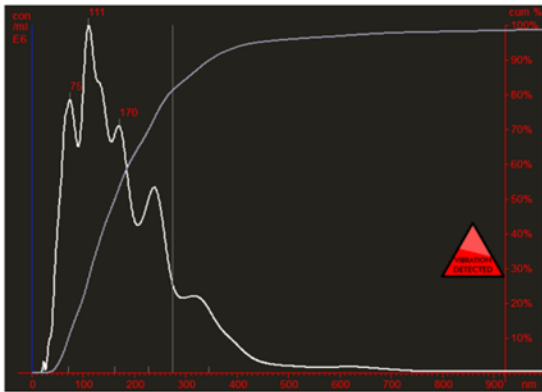
For small scale purposes, upon per-actuation of the fluidic oscillator, the author has, in his previous work, engendered bubbles 3.4 μm in size (60% population of that size , $\pm 0.5\mu\text{m}$) and increased the total bubble flux by a 100 fold for nominally oscillated flow. However, since it is patent pending, publications will happen once the patent is in place. Since this work was for production of medical microbubbles (extremely expensive end product), scale up was not imperative at the time. This work was performed in collaboration with the National Physical Laboratory.



This result is still highly relevant, as the volume production (unit volume was 1 mL), is still 2 magnitudes higher than the higher possible (with concomitant specificity) as stated in the conclusions in (Fiabane *et al.*, 2016):

The device capable of generating microbubbles with mean diameter as low as 2.6 μm and standard deviation of $\pm 0.4 \mu\text{m}$, at a concentration of $30 \times 10^6 \text{ mL}^{-1}$ is reported here. The produced microbubbles were as small as one-fortieth of the orifice and their mean diameter can be controlled by varying liquid flow rate and nitrogen gas pressures.

This work was further expanded on by the author as a pro bono consultant to the Wellcome Trust Grant – Investigation into Micro/Nanobubble generation for biomedical applications with Professor Chris Newman and Professor William B Zimmerman wherein he was able to generate 200-300nm size nanobubbles which were uncoated. This makes us the only research group in western hemisphere capable of generating uncoated, air –water interface stable nanobubbles.



Particle Size / Concentration

Sample Video Frame

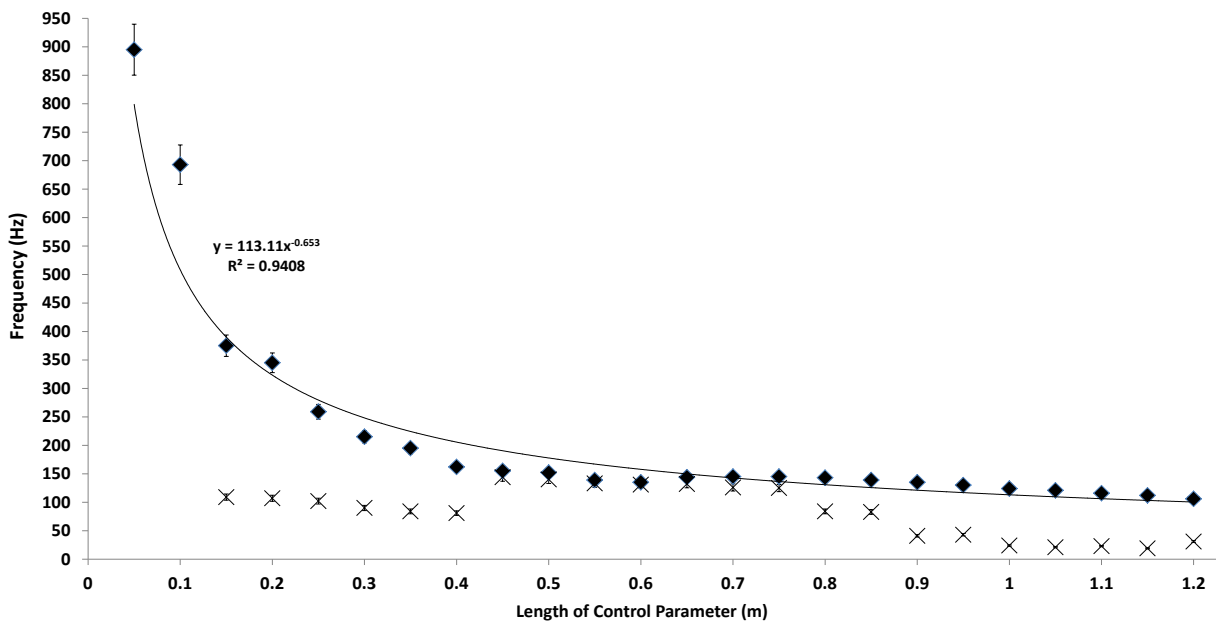
Operator:		RESULTS:	
Sample:		Size Distribution:	Mean: 207 nm, Mode: 111 nm, SD: 190 nm
Video File:	Bubble3_3_ax10.avi analysis no: 001	Cumulative Data (nm):	D10: 72, D50: 162, D90: 346, D70: 229
Date/Time of Report:	16/04/2013 17:09:09	User Lines:	274 nm, 0 nm
Dispersant/Diluent:		Total Concentration:	11.97 particles / frame, 0.45E8 particles / ml

Figure 111 The peak measured using DLS (Dynamic Light Scattering)

This work needs some justification in terms of bubble and particle since DLS cannot differentiate between the two. However, inferences were made using secondary observations.

Frequency responses for the different oscillators as exemplars since the frequencies will change with the set up and other conditions

Frequency Curves for the 4 types of oscillators:



a

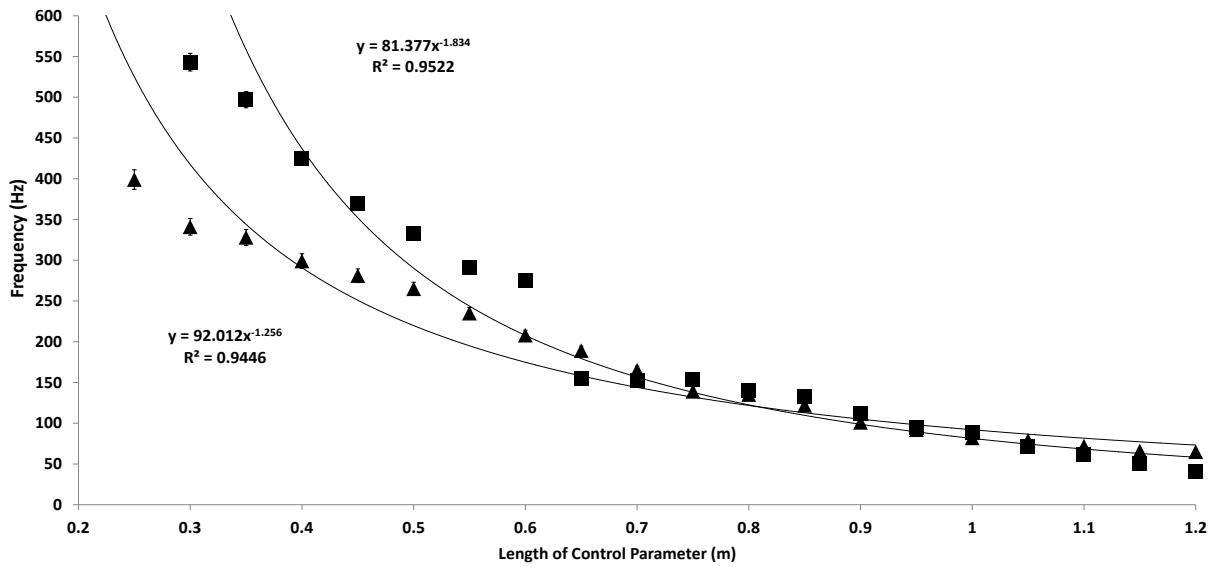






Figure 112 Frequency response:  - DZFO,  - TZFO,  - MS TZFO,  - TCFO

The DZFO, Microscaled TZFO, and TZFO obey the power law for the frequency response whereas the TCFO does not. These are all exemplar frequencies as depending on the Strouhal number, everything will change.